Computational Models of Cerebral Hemodynamics

Samara Samir Alzaidi

A thesis presented for the degree of
Doctor of Philosophy
in
Bioengineering
at the
University of Canterbury,
Christchurch, New Zealand.

1 April 2009

To my mother, Nidhal.
Because the science of being a loving mother is the most difficult of all.

Acknowledgements

I would like to express my sincere gratitude to my supervisor, Prof Tim David for his constant guidance and excellent supervision. I want to thank him for giving me the opportunity to be part of this interesting and exciting research. Thanks to my co-supervisor Prof Geoff Chase for his valuable advice and guidance especially during the first year of my research.

I would like to thank previous and current members of the Brain Group for being part of a supportive research team; Katherine Moorhead, Steve Moore, Jade Arnold, Svava Kristinsdottir, Hannah Farr, Boudewijn Deurloo, Iain McIver, Fabian Herzog, Navid Safaeian and Mohsin Shaikh. Thanks to Prof Ken Brodlie and his student Robert Hayford at the University of Leeds for the work done on the collaborative environment visualisation.

I would like to thank all my friends for always saying the right thing to inspire me to do my best throughout this wonderful journey. Thanks to Judy Zhou, Amelia Rushbrook, Sanitta Thongpang, William Lee, Anthony Hii, Alan Wright, Miharu Yamamoto, Nicolas Buchmann and everyone at the Centre of Bioengineering.

My family has always been an endless source of unconditional love. Thanks to my father, Samir, for the constant support and encouragement since I was little, for never getting tired of answering my questions, especially during those long road trips. To my mother and best friend, Nidhal, for being the perfect model of a patient, supportive and loving mother. To my affectionate and caring brothers, Mustafa and Mohammad, for being there and for always drawing a smile on my face. I love you and I cannot imagine life without you.

Contents

List of Figures

List of Tables

Nomenclature & Abbreviations

0D	Zero-dimensional.
1D	One-dimensional.
2D	Two-dimensional.
3D	Three-dimensional.
$\boldsymbol{\alpha}$	Scaling factor to calculate first daughter vessel's radius in arterial binary tree.
$\boldsymbol{\alpha_{Ca}}$	Parameter in the myogenic model.
$\boldsymbol{\beta}$	Scaling factor to calculate second daughter vessel's radius in arterial binary tree.
$\boldsymbol{\beta_e}$	Parameter in the myogenic model.
$\boldsymbol{\gamma}$	Bifurcation (or asymmetry) index.
$\boldsymbol{\delta}$	Membrane shear modulus.
$\boldsymbol{\varepsilon}$	Multiplication factor for testing the metabolic model with different $CMRO_2$.
$\boldsymbol{\zeta}$	Short term memory parameter.
$\boldsymbol{\eta}$	Area ratio.
$\boldsymbol{\theta}$	Angle of bifurcating or combining vessels.
$\boldsymbol{\vartheta}$	Scaling factor for the myogenic mechanism.
$\boldsymbol{\lambda}$	Time constant for PI controller.

$\boldsymbol{\lambda_n}$	Statistical parameter in the myogenic model.
$\boldsymbol{\mu}$	Blood viscosity.
$\boldsymbol{\mu_e}$	eNOS-caveolin association rate.
$\boldsymbol{\nu}$	Blood kinematic viscosity.
$\boldsymbol{\xi}$	Characteristic time for smooth muscle relaxation.
$\boldsymbol{\xi'}$	Non-dimensional ξ.
$\boldsymbol{\rho}$	Blood density.
$\boldsymbol{\rho_{Ca}}$	Parameter in the myogenic model.
$\boldsymbol{\varrho}$	No-load channel constant.
$\boldsymbol{\sigma_0^\#}$	Hoop stress at the maximum muscle activation.
$\boldsymbol{\sigma_u}$	The hoop stress associated with the series elastic component in a Maxwell model.
$\boldsymbol{\sigma_u'}$	Non-dimensional σ_u.
$\boldsymbol{\sigma_x}$	The hoop stress associated with the parallel elastic component in a Maxwell model.
$\boldsymbol{\sigma_x'}$	Non-dimensional σ_x.
$\boldsymbol{\sigma_y}$	The hoop stress associated with the contractile component in a Maxwell model.
$\boldsymbol{\sigma_y'}$	Non-dimensional σ_y.
$\boldsymbol{\sigma_{y0}}$	The hoop stress σ_y at optimum length of y0.
$\boldsymbol{\sigma_{y0}^\#}$	Parameter in the myogenic model.
$\boldsymbol{\varsigma}$	The oxygen consumption per tissue cylinder.
$\boldsymbol{\tau}$	Wall shear stress.

$\boldsymbol{\phi_n}$	Parameter in the myogenic model.
$\boldsymbol{\varphi}$	Relative strength of the Ca2+-dependent.
$\boldsymbol{\chi}$	The number of groups the terminal vessels' flowrate distribution is divided into.
$\boldsymbol{\psi}$	Parameter to model the sigmoidal function for the dependence of phosphorylation on
$\boldsymbol{\psi_m}$	Parameter in the myogenic model.
$\boldsymbol{\omega}$	The fraction of crossbridges.
$\boldsymbol{\omega_{ref}}$	The reference fraction of crossbridges.
$\boldsymbol{\Gamma}$	Parameter used for metabolic model in Chapter 7.
$\boldsymbol{\Pi}$	Parameter used for metabolic model in Chapter 7.
$\boldsymbol{\Omega}$	Oxygen content in blood.
$\boldsymbol{\Omega_B}$	Oxygen carrying capacity in blood.
$\boldsymbol{a'}$	Parameter in the myogenic model.
$\boldsymbol{a_k}$	Bend curvature radius.
$\mathbf{A}$	Matrix containing the CoW vessel resistances in equation $A\tilde{x} = \tilde{b}$.
ACA1	Anterior cerebral artery - segment one.
ACA2	Anterior cerebral artery - segment two.
AChA	Anterior choroidal artery.
ACoA	Anterior communicating artery.
$\boldsymbol{A_{cs}}$	Cross sectional area.
AD	Alzheimer's disease.

ANN	Artificial neural networks.
$\boldsymbol{AUT_{CVR}}$	Cerebrovascular resistance actuator.
$\boldsymbol{AUT_{OEF}}$	Oxygen extraction factor actuator.
b	Vector in equation $A\tilde{x} = \tilde{b}$ containing input and output pressures.
$\boldsymbol{b'}$	Parameter in the myogenic model.
BA	Basilar artery.
BA1	Basilar artery - segment one.
BA2	Basilar artery - segment two.
BBB	Blood-brain barrier.
$\boldsymbol{B_T}$	Constant for cell calcium-buffer systems.
c	Sigmoidal function for AUT_{CVR}.
$\boldsymbol{c'}$	Parameter in the myogenic model.
C	Cell capacity.
C'	Non-dimensional oxygen concentration in tissue.
$\boldsymbol{Ca^{2+}}$	Calcium.
$\boldsymbol{Ca_3}$	Parameter in the myogenic model.
$\boldsymbol{Ca_4}$	Parameter in the myogenic model.
$\boldsymbol{CaCO_2}$	Arterial carbon dioxide concentration.
$\boldsymbol{Ca_i}$	Cytosolic calcium ion concentration.
$\boldsymbol{Ca_{i,ref}}$	A reference cytosolic calcium ion concentration.

$Ca_i m$	Parameter in the myogenic model.
CaO_2	Arterial oxygen concentration.
CBF	Cerebral blood flow.
CBF'	Non-dimensional cerebral blood flow.
CBF_{sp}	Cerebral blood flow set point.
CBV	Cerebral blood volume.
CC	The contractile component in a Maxwell model.
CCO	Constrained constructive optimisation.
CEVCoW	Collaborative environment for visualisation of the circle of willis.
CFD	Computational fluid dynamics.
C_L	Pressure losses constant.
$CMRO_2$	Metabolic rate of oxygen consumption.
CO_2	Carbon dioxide.
CoW	Circle of Willis.
CPP	Cerebral perfusion pressure.
CSF	Cerebrospinal fluid.
$CtCO_2$	Tissue carbon dioxide concentration.
$CtCO_{2,sp}$	Tissue carbon dioxide concentration set point.
CVA	Cerebrovascular accident.
CvO_2	Venous oxygen concentration.

CVP	Central venous pressure.
CVR	Cerebrovascular resistance.
$\boldsymbol{CVR_h}$	Resistance of the healthy section of a vessel with stenosis.
$\boldsymbol{CVR_s}$	Resistance of the stenosed section of a vessel with stenosis.
$\boldsymbol{CVR_{ll}}$	Lower limit of cerebrovascular resistance.
$\boldsymbol{CVR_{sp}}$	Cerebrovascular resistance set point.
$\boldsymbol{CVR_{ul}}$	Upper limit of cerebrovascular resistance.
$\boldsymbol{d'}$	Parameter in the myogenic model.
$\boldsymbol{d_v}$	Vessel diameter.
$\boldsymbol{d_s}$	Vessel diameter at the stenosed section.
DoS	Degree of stenosis.
EEG	Electroencephalographic.
eNOS	Endothelial nitric oxide synthase.
$\mathbf{err(t)}$	Error used in the PI controller.
$\boldsymbol{f_{\Delta p}}$	The systemic blood pressure force normal to a longitudinal section of a vessel wall.
$\boldsymbol{f_u}$	The hoop force experienced by the series elastic component in a Maxwell model.
$\boldsymbol{f_x}$	The hoop force experienced by the parallel elastic component in a Maxwell model.
$\mathbf{F(x)}$	A set of equations.
$\boldsymbol{F(\tau)}$	A function of the wall shear stress acting on the endothelial cell membrane.
$\boldsymbol{g_{Ca}}$	Maximum membrane conductance for calcium current.

$\boldsymbol{g_K}$	Maximum membrane conductance for potassium current.
$\boldsymbol{g_L}$	Maximum membrane conductance for leak current.
$\boldsymbol{g_{max}}$	Maximum WSS-induced eNOS activation.
$\mathbf{G}$	Conductance.
$\boldsymbol{G_{CO_2}}$	Metabolic gain.
$\mathbf{h}$	Time step.
$\boldsymbol{H}$	Hill equation exponent.
$\boldsymbol{H^+}$	Hydrogen ions.
$[\boldsymbol{Hb}]$	Haemoglobin concentration.
ICA	Internal carotid artery.
ICP	Intracranial pressure.
$\mathbf{J(x)}$	Jacobian matrix.
$\mathbf{k}$	Power law index.
$\boldsymbol{k_\psi}$	Parameter in the myogenic model.
$\boldsymbol{k_{Ca}}$	Ratio of calcium outflux to cytosolic calcium.
$\boldsymbol{k_{dis}}$	eNOS-caveolin disassociation rat.
$\boldsymbol{k_e}$	Parameter in the myogenic model.
$\boldsymbol{K^+}$	Potassium.
$\boldsymbol{K_2}$	Gain for the AUT_{CVR} differential equation.
$\boldsymbol{K_3}$	Gain for the AUT_{OEF} differential equation.

$\boldsymbol{K_d}$	Parameter in the myogenic model.
$\boldsymbol{K_i}$	Integral gain of the PI controller.
$\boldsymbol{K_L}$	Pressure losses coefficient.
$\boldsymbol{K_o}$	Krogh diffusion coefficient.
$\boldsymbol{K_p}$	Proportional gain of the PI controller.
$\boldsymbol{l_v}$	Length of a vessel.
$\boldsymbol{l_s}$	Length of the stenosed section of a vessel.
LACA1	Left anterior cerebral artery - segment one.
LACA2	Left anterior cerebral artery - segment two.
LAChA	Left anterior choroidal artery.
LICA	Left internal carotid artery.
LLA	Lower limit of autoregulation.
LMA	Leptomeningeal arteries.
LMCA	Left middle cerebral artery.
LPCA1	Left posterior cerebral artery - segment one.
LPCA2	Left posterior cerebral artery - segment two.
LPCoA	Left posterior communicating artery.
LSCbA	Left superior cerebellar artery.
$\boldsymbol{m_\infty}$	Ca^{2+} channel distribution of open states.
MAP	Mean arterial pressure.

$\boldsymbol{MAP_{sp}}$	Mean arterial pressure set point.
MCA	Middle cerebral artery.
MLC	Myosin Light Chain.
$\boldsymbol{M_o}$	Oxygen demand.
$\boldsymbol{M(P_t)}$	Oxygen consumption rate per unit volume of the tissue volume.
MRA	Magnetic resonance angiography.
MRI	Magnetic resonance imaging.
$\boldsymbol{M_t}$	Mass transfer coefficient.
n	The time course of the fraction of Ca^{2+}-dependent K^+ open channel states.
$\boldsymbol{n_\infty}$	K^+ channel distribution of open states.
$\boldsymbol{N(i)}$	K^+ channel distribution of open states.
NO	Nitric Oxide.
o	Sigmoidal function for AUT_{OEF}.
$\boldsymbol{O_2}$	Oxygen.
ODE	Ordinary differential equation.
OEF	Oxygen extraction factor.
pH	A measure of concentration of hydrogen ions.
$\boldsymbol{\Delta p}$	Transmural pressure.
P	Pressure.
$\boldsymbol{P_{50}}$	Oxygen partial pressure at which hemoglobin is 50% saturated.

$\boldsymbol{P_a}$	Arterial pressure.
$\boldsymbol{P_{a_{sp}}}$	Arterial pressure set point.
$\boldsymbol{P_b}$	Oxygen partial pressure in blood.
PC	Phase contrast (a MRA technique)..
PCA1	Posterior cerebral artery - segment one.
PCA2	Posterior cerebral artery - segment two.
$\boldsymbol{PCO_2}$	Carbon dioxide partial pressure.
PCoA	Posterior communicating artery.
PEC	The parallel elastic component in a Maxwell model.
PI	Proportional integral.
$\boldsymbol{P_{Loss}}$	Pressure losses (minor losses).
$\boldsymbol{P_o}$	Oxygen partial pressure at which consumption is half of demand.
$\boldsymbol{PO_2}$	Oxygen partial pressure.
$\boldsymbol{P_t}$	Oxygen partial pressure in tissue cylinder at radial distance r.
$\boldsymbol{P_v}$	Venous pressure.
PVL	Periventricular leukomalacia.
$\boldsymbol{q}$	Power index for phosphorylation dependence on calcium.
Q	Flowrate.
r	Radius.
$\boldsymbol{r'}$	Non-dimensional radius.

r_c	Capillary radius.
r_t	Tissue cylinder radius.
r_v	Vessel radius.
R	Resistance.
RACA1	Right anterior cerebral artery - segment one.
RACA2	Right anterior cerebral artery - segment two.
RAChA	Right anterior choroidal artery.
Re	Reynolds number.
RHS	Right hand side.
RICA	Right internal carotid artery.
RMCA	Right middle cerebral artery.
RPCA1	Right posterior cerebral artery - segment one.
RPCA2	Right posterior cerebral artery - segment two.
RPCoA	Right posterior communicating artery.
R_r	Ratio of inner to outer radius.
R_s	Resistance of a straight vessel (non-linear).
RSCbA	Right superior cerebellar artery.
R_t	Resistance of a tortuous vessel (non-linear).
s	A function to reproduce the stress-length relationship asymmetry.
S	Longitudinal section of a vessel wall.

$\boldsymbol{SaO_2}$	Oxygen saturation factor.
SCbA	Superior cerebellar artery.
SEC	The series elastic component in a Maxwell model.
$\boldsymbol{S_{Hb}}$	Oxyhemoglobin saturation.
SMC	Smooth muscle cell.
$\boldsymbol{S_R}$	Sensitivity of resistance to oxygen.
t	Time.
t'	Non-dimensional t.
T	Temperature.
TCD	Transcranial doppler.
$\boldsymbol{TC_{O_2}}$	Total oxygen consumption per unit length.
TIA	Transient ischemic attack.
TOF	Time-of-flight (a MRA technique).
u	Blood velocity. Also used as the length of the series elastic component in a Maxwell model.
u'	Non-dimensional u in the myogenic model.
$\boldsymbol{u_1'}$	Parameter in the myogenic model.
$\boldsymbol{u_4'}$	Parameter in the myogenic model.
$\boldsymbol{u_3'}$	Parameter in the myogenic model.
$\boldsymbol{U(t)}$	Controller input of the PI controller.

ULA	Upper limit of autoregulation.
V	Average blood velocity.
$\boldsymbol{v1}$	Voltage associated with the opening of half the population of the Ca^{2+} open states.
V2	Measure of the Ca^{2+} open states distribution.
V3	Measure of the K^{+} open states distribution.
V5	Parameter in the myogenic model.
V6	Parameter in the myogenic model.
VA	Vertebral arteries.
$\boldsymbol{v_{Ca}}$	Nernst reversal calcium potential.
$\boldsymbol{v_K}$	Nernst reversal potassium potential.
$\boldsymbol{v_L}$	Nernst reversal leak potential.
$\boldsymbol{v'_{ref}}$	Normalised zero load velocity of the CC at reference level.
VSM	Vascular smooth muscle.
$\boldsymbol{w_e}$	Weight representing electrical contribution to hoop forces.
$\boldsymbol{w_m}$	Weight representing muscular contribution to hoop forces.
$\boldsymbol{W_0}$	Shear gating constant.
$\boldsymbol{W(\tau)}$	Boltzmann dependence on the strain energy density in the membrane.
x	Vector in equation $A\tilde{x} = \tilde{b}$ containing flowrates and pressures of the CoW. Also used as the circumferential distance of an artery wall in the myogenic model representing the parallel elastic component in a Maxwell model.
x'	Non-dimensional x in the myogenic model.

$\boldsymbol{x'_1}$	Parameter in the myogenic model.
$\boldsymbol{x'_2}$	Parameter in the myogenic model.
$\boldsymbol{x'_3}$	Parameter in the myogenic model.
$\boldsymbol{x'_4}$	Parameter in the myogenic model.
$\boldsymbol{x'_5}$	Parameter in the myogenic model.
$\boldsymbol{x'_6}$	Parameter in the myogenic model.
$\boldsymbol{x'_7}$	Parameter in the myogenic model.
$\boldsymbol{x'_8}$	Parameter in the myogenic model.
$\boldsymbol{x'_9}$	Parameter in the myogenic model.
$\mathbf{y}$	The length of the contractile component in a Maxwell model.
$\mathbf{y'}$	Non-dimensional y in the myogenic model.
$\boldsymbol{y'_0}$	Parameter in the myogenic model.
$\boldsymbol{y'_1}$	Parameter in the myogenic model.
$\boldsymbol{y'_2}$	Parameter in the myogenic model.
$\boldsymbol{y'_3}$	Parameter in the myogenic model.
$\boldsymbol{y'_4}$	Parameter in the myogenic model.
$\mathbf{Y}$	Admittance.
$\mathbf{z}$	Distance along vessel.

Glossary

Actin — One of the two main proteins of muscle. Myosin and actin are the proteins involved in contraction of muscle fibers. Contraction occurs when the two protein bundles slide over one another.

Admittance — The inverse of impedance.

Adrenergic fiber — A nerve fiber of the autonomic nervous system that releases the neurotransmitter norepinephrine.

Afferent — Carrying blood towards an organ.

Astrocytes — Are characteristic star-shaped glial cells in the brain and spinal cord. They perform many functions, including biochemical support of endothelial cells which form the blood-brain barrier.

Atheromatous — A deposit or degenerative accumulation of lipid-containing plaques on the innermost layer of the wall of an artery.

Atrophy — A wasting or decrease in the size of an organ or tissue, as from death and reabsorption of cells, diminished cellular proliferation, pressure, ischemia, malnutrition, decreased function, or hormonal changes.

Bilateral — Having, or relating to, two sides. Bilateral is as opposed, for example, to unilateral (which means having, or relating to, one side).

Calmodulin — A calcium-binding protein which can bind to and regulate a number of different protein targets, thereby affecting many different cellular functions by modifying the activity of specific calcium-sensitive enzymes (an abbreviation for CALcium MODULated proteIN).

Contralateral Pertaining to, situated on, or affecting the opposite side Proximal Distal Penumbra Hypoplastic.

Corpus callosum The arched bridge of nervous tissue that connects the two cerebral hemispheres, allowing communication between the right and left sides of the brain.

Cytosolic Existing in the cytosol, which is the intracellular fluid (fluid component of cytoplasm, excluding organelles and the insoluble cytoplasmic components. Cytoplasm is the parts of a cell that are enclosed within the plasma membrane.)

Dementia A loss of mental ability severe enough to interfere with normal activities of daily living, lasting more than six months, not present since birth, and not associated with a loss or alteration of consciousness.

EEG Electroencephalography. Is the recording of electrical activity along the scalp produced by the firing of neurons within the brain.

Efferent Carrying blood away from an organ.

Endothelial cells Cells lining the lumen of blood vessels.

Excitotoxicity A pathological process by which nerve cells are damaged and killed by glutamate and similar substances.

Gestational The period of development in the uterus from conception until birth; pregnancy.

Glutamate A neurotransmitter in mammalian nervous system. It is a key molecule in cellular metabolism. In humans, dietary proteins are broken down by digestion into amino acids; glutamate is produced as a result.

Herniation Abnormal protrusion of an organ or other body structure through a defect.

Hyperemia An increase in the quantity of blood flow to a body part; engorgement.

Hyperoxia A higher than normal oxygen tension, such as that produced by breathing air or oxygen at greater than atmospheric pressures.

Hypertrophy The increase of the size of an organ or in a select area of the tissue.

Hypoplastic A condition in which tissue or an organ of the body fails to grow to normal size.

Hypoxia Insufficient levels of oxygen in blood or tissue.

Hematocrit A measure of the proportion of blood volume that is occupied by red blood cells. Its normally 45% $\pm$ 7%. Also called packed cell volume (PCV).

Impedance The opposition to the flow of alternating current in a circuit. It is the combination of resistance, inductance and capacitance of the circuit.

Ipsilateral Located on or affecting the same side of the body.

Kinase An enzyme that catalyzes the conversion of a proenzyme to an active enzyme (alternatively known as a phosphotransferase).

Mesentery The peritoneal fold attaching the small intestine to the posterior body wall.

Morphometry Measurement of the form of organisms or of their parts.

Murray's law The cube of the radius of a parent vessel equals the sum of the cubes of the radii of the daughters.

Myosin One of the two main proteins of muscle. Myosin and actin are the proteins involved in contraction of muscle fibers. Contraction occurs when the two protein bundles slide over one another.

Myosin light chains each molecule of smooth muscle cell myosin contains two pairs of light molecular weight chains (MLCs), one alkali MLC and one regulatory MLC.

Neonate A newborn infant, especially one less than four weeks old.

Occlusion An obstruction or closure of a passageway in the body.

pH A measure of the acidity or alkalinity of a solution, numerically equal to 7 for neutral solutions, increasing with increasing alkalinity and decreasing with increasing acidity. The pH scale commonly in use ranges from 0 to 14.

Pial artery An artery that runs along the pia mater, which is the delicate innermost membrane enveloping the brain and spinal cord.

Protein synthesis Process in which cells build proteins. A multi-step process beginning with amino acid synthesis and transcription, which are then used for translation.

Rheological The study of blood flow, pressure, and velocity through the vascular system.

Sarcoplasmic reticulum The endoplasmic reticulum found in striated muscle fibers.

Spasm A sudden involuntary contraction of a muscle or group of muscles.

Stenosis The narrowing of an opening or passage-way in the body.

Synapse a specialized junctions through which neurons signal to each other and to non-neuronal cells such as those in muscles or glands.

Transmural pressure Pressure across the wall of a blood vessel.

Unilateral Having, or relating to, one side.

Vasospasm A sudden constriction of a blood vessel that reduces the blood flow.

Vasoconstriction Narrowing of the blood vessels resulting from contracting of the muscular wall of the vessels. The opposite of vasodilation.

Vasodilation Widening of blood vessels resulting from relaxation of the muscular wall of the vessels. The opposite of vasoconstriction.

Abstract

The cerebral tissue requires a constant supply of oxygen and nutrients. This is maintained through delivering a constant supply of blood. The delivery of sufficient blood is preserved by the cerebral vasculature and its autoregulatory function. The cerebral vasculature is composed of the Circle of Willis (CoW), a ring-like anastomoses of arteries at the base of the brain, and its peripheral arteries. However, only 50% of the population have a classical complete CoW network. This implies that the route of blood flow through the cerebral vasculature is different and dependent on where the blood is needed most in the brain. Autoregulation is a mechanism held by the peripheral arteries and arterioles downstream of the CoW. It ensures the delivery of the essential amount of cerebral blood flow despite changes in the arterial perfusion pressure, through the vasoconstriction and vasodilation of the vessels. The mechanisms that control the vessels' vasomotion could be attributed to myogenic, metabolic, neurogenic regulation or a combination of all three. However, the variations in the CoW structure, combined with different pathological conditions such as hypertension, a stenosis or an occlusion in one or more of the supplying cerebral arteries may alter, damage or abolish autoregulation, and consequently result in a stroke. Stroke is the most common cerebrovascular disease that affects millions of people in the world every year. Therefore, it is essential to understand the cerebral hemodynamics via mathematical modelling of the cerebral vasculature and its regulation mechanisms.

This thesis presents the developed model of the cerebral vasculature coupled with the different forms of autoregulation mechanisms. The model was developed over multiple stages. First, a linear model of the CoW was developed, where the peripheral vessels downstream of the CoW efferent arteries are represented as lumped parameter variable resistances. The autoregulation function in the efferent arteries was modelled using a PI controller, and a metabolic model was added to the lumped peripheral variable resistances. The model was then modified so the pressure losses encountered at the CoW bifurcations, and the vessels' tortuosity are taken into account resulting in a non-linear system.

A number of cerebral autoregulation models exist in the literature, however, no model combines a fully populated arterial tree with dynamic autoregulation. The final

model presented in this thesis was built by creating an asymmetric binary arterial vascular tree to replace the lumped resistance parameters for the vasculature network downstream of each of the CoW efferent arteries. The autoregulation function was introduced to the binary arterial tree by implementing the myogenic and metabolic mechanisms which are active in the small arteries and arterioles of the binary arterial tree. The myogenic and metabolic regulation mechanisms were both tested in the model. The results indicate that because of the low pressures experienced by the arterioles downstream of the arterial tree, the myogenic mechanism, which is hypothesised by multiple researchers as the main driver of autoregulation, does not provide enough regulation of the arterioles' diameters to support autoregulation. The metabolic model showed that it can provide sufficient changes in the arterioles' diameters, which produces a vascular resistance that support the constancy of the autoregulation function.

The work carried out for this research has the potential of being a significant clinical tool to evaluate patient-specific cases when combined with the graphical user interfaces provided. The research and modelling performed was done as part of the Brain Group of the Centre of Bioengineering at the University of Canterbury.

Chapter 1

Anatomy and Pathology

1.1 Introduction

All body structures of organs and tissues work together in harmony to maintain homeostasis. Homeostasis is the maintenance of constant conditions in the circulatory system of the body. Each functional structure provides its share to maintain the homeostasis conditions. If one of these structures loses its ability to perform its share, all parts of the body suffer. Moderate dysfunction leads to sickness while extreme dysfunction leads to death.

The circulatory system is the body's means to deliver its metabolic needs to its tissues. These needs include the delivery of oxygen and other nutrients such as glucose and amino acids, removal of carbon dioxide and hydrogen ions, maintenance of suitable concentrations of other ions, and transport of hormones and other substances to the tissues. Body tissues and organs perform local control to supply their own metabolic needs. Hence, the higher the metabolic needs of an organ, the higher the blood flow. The local control of blood flow aims to sustain a constant amount of oxygenated blood flow despite arterial pressure variations. This is called *Autoregulation*. For a certain range of arterial pressure, autoregulation of blood flow is maintained. However, in cases of very low or high arterial pressure, the autoregulation property is lost (Figure 1.1).

The brain is one of the organs that is critically dependent on its blood supply. It is not very surprising, then, that the blood flow to various parts of the brain is very specific and highly regulated. The human brain accounts for approximately 2% of total body weight, yet it uses 15% of the blood supply and consumes 20% of the oxygen supplied to the body. Interruption of blood flow supply to cerebral mass for several seconds will result in unconsciousness [47]. If this lasts for more than five minutes, permanent damage to the affected area in the brain will most likely occur [51].

Stroke is the most common cerebrovascular disease, which affects 17 million people worldwide every year [121]. Other diseases that might arise as a result of cerebrovas-

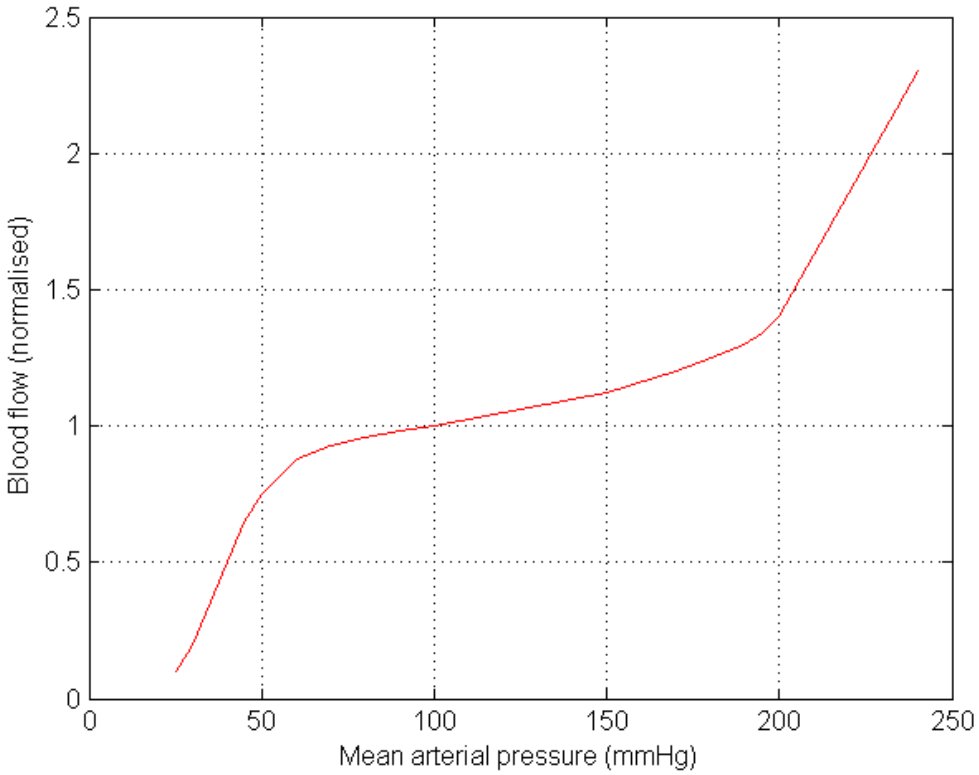

Figure 1.1 Autoregulation of blood flow [47].

cular dysfunction include moyamoya, periventricular leukomalacia (PVL), and even alzheimer's disease[1]. Understanding the circulation system in the cerebral mass and how the brain regulates its blood supply is essential for clinicians to recognize causes of cerebrovascular disease and design preventions. It is also important to gain better insight into the state of the patient to establish whether it is in the patient's best interests to undergo surgery. However, the circular collateral arterial network, termed Circle of Willis (CoW), in the cerebral mass differs from one person to another, which makes it difficult to identify how the blood is regulated and, therefore, determine better planned treatments.

In medicine, the ultimate goals are detection and prevention of diseases. As technology advances, it is expected that causes of a high mortality disease will be analysed, understood, and consequently, prevented from occurring in the future. This is appealing because preventative medicine is the cheapest form of cure. Worldwide, cardiovascular disease and stroke are the leading disease causes of mortality; examining them is essential. Assessment of blood flow in cerebral masses and its effects is one of the challenging problems in medicine. The aim of this work is to create a model that replicates the au-

[1]See disease, Section 1.3

toregulation response for the different anatomical variations of the CoW in the cerebral mass; investigate how close this model is to the real physiology of individual patients; and transform it into a tool to be used by clinicians. This will aid in recognising future stroke episodes, especially re-occurring ones.

1.1.1 The Problem

In the literature, there is no available description of a comprehensive cerebrovascular system that includes cerebrovascular variations as well as major auto-regulatory mechanisms. These include:

- Patient-specific parameters, such as mean arterial pressure (MAP)
- Variations in the CoW geometry, such as missing arterial segments
- Rate of change of arterial vessels' diameter as a function of transmural[2] pressure (termed *myogenic* response)
- Rate of change of arterial vessels' diameter as a function of metabolites in blood (termed *metabolic* response)
- Oxygen, carbon dioxide and other metabolite exchange between capillaries and brain tissue that affects arteriole walls upstream of the capillaries.

A complete cerebrovascular system must consist of all levels and sizes of arterial vessels, from the major arteries supplying the brain down to the capillaries. These can be represented in a model designed for a clinical environment to shed light on cerebrovascular behaviour.

1.1.2 The model

The model developed in this thesis can create an arterial branching tree down to the capillary level for each of the main efferent[3] arteries that supply blood to the brain. It can replicate the artery and arteriole vasoconstriction and vasodilation[4] behaviour to maintain autoregulation. The vasoconstriction and vasodilation of vessels is based on myogenic as well as metabolic algorithms. The oxygen diffusion from blood capillaries to brain tissue is then modelled. The above mechanisms have a significant effect on cerebrovascular behaviour and autoregulation.

[2]Transmural pressure: pressure across the wall of a blood vessel.
[3]Efferent: carrying blood away from an organ.
[4]See Glossary

In order to have a valid model for patient use, it is essential that the model is patient specific. This means inclusion of arterial network dimensions, total cerebral blood flow, cerebral perfusion pressure, anatomical variations in the cerebral arterial network, and pathological conditions of stenosis[5], occlusion[6], or lack of oxygen in the blood. This will greatly benefit people who have had or might have a stroke, moyamoya disease, periventricular leukomalacia disease, or alzheimer's disease.

1.2 Anatomy

A thorough understanding of brain anatomy and blood circulation physiology must be presented in order to explain how the computational models of cerebral hemodynamics work. The first two chapters of this thesis are dedicated to this.

1.2.1 The Brain

The human central nervous system consists of the brain and the spinal cord. The brain is one of the most complex organs in the body and it is remarkable in terms of what it allows us to do. The cerebrum, cerebellum, diencephalon, and brain stem are the main parts of the brain (Figure 1.2).

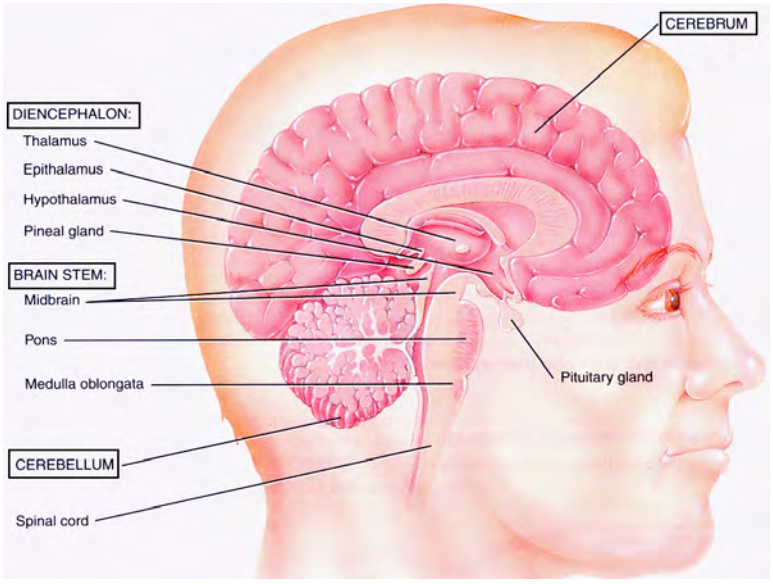

Figure 1.2 The main parts of the brain [120].

Each part of the brain is in charge of many functions. Only the basic and most important functions are discussed here. The cerebrum contains the Basal ganglia and

[5]Stenosis: the narrowing of an opening or passageway in the body.
[6]Occlusion: an obstruction or closure of a passageway in the body.

the limbic system. It interprets sensory impulses, controls conscious motor activity, emotion, and intellectual processes. The basal ganglia control muscle activity and posture while the limbic system controls autonomic response to smell, emotion, and mood. The right and left halves of the brain are the cerebral hemispheres (Figure 1.3). Each hemisphere is divided into four lobes: the frontal, parietal, occipital, and temporal lobes (Figure 1.4).

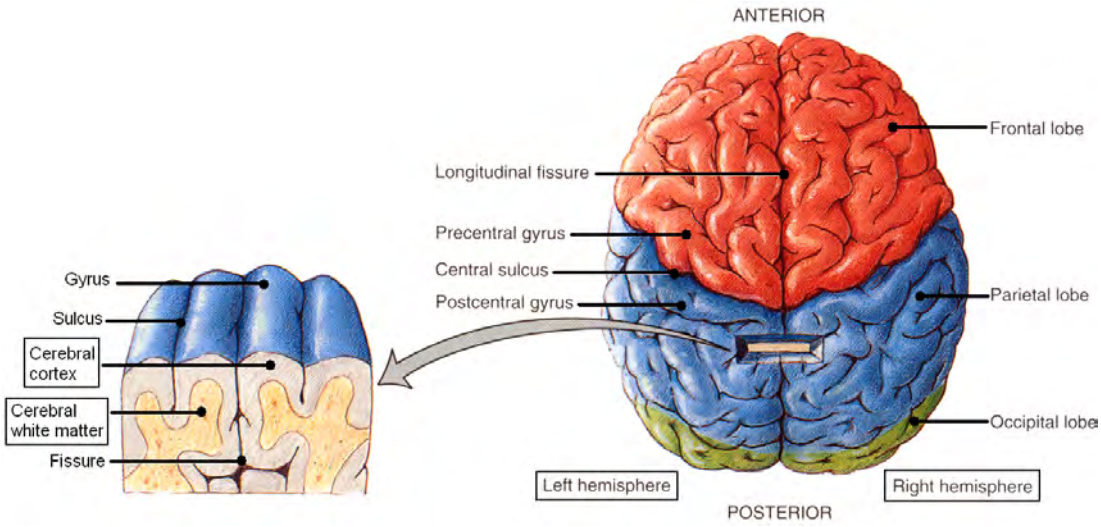

Figure 1.3 The right and left hemispheres of the cerebrum [120].

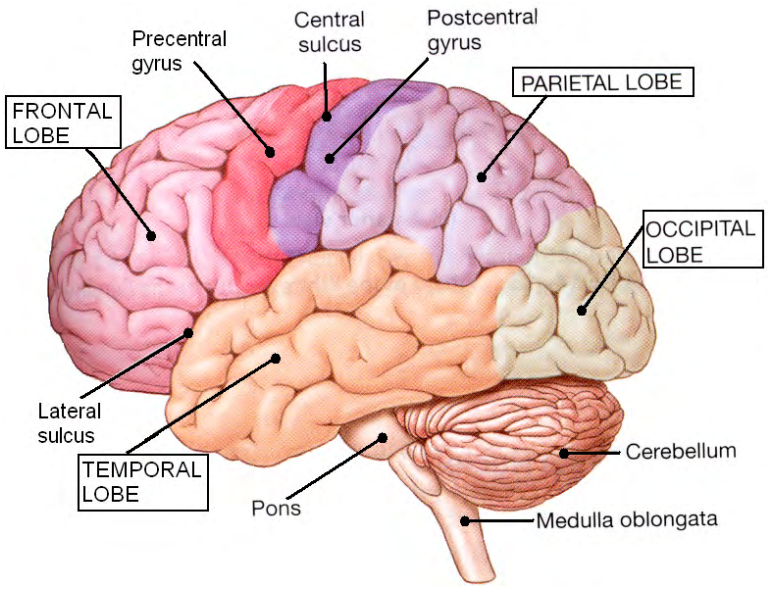

Figure 1.4 The four lobes of the cerebrum [120].

The cerebellum controls muscle movement and tone, regulates the extent of intentional movement, and regulates posture and balance.

The diencephalon consists of the thalamus, which relays almost all sensory input

to the cerebral cortex and influences mood and movement; the subthalamus, which contains nerve tracks and nuclei; the epithalamus, which contains nuclei responding to olfactory stimulation; and the hypothalamus, which is the major centre for maintaining homeostasis. It also controls and integrates the activities of the autonomic nervous system.

The brain stem is a pathway for ascending and descending nerve tracts. It consists of the midbrain, pons, and medulla oblongata. The midbrain contains visual reflex and part of the auditory pathway. The pons relays impulses between the cerebrum and cerebellum, and from one side of the cerebellum to the other. The medulla oblongata is the centre for multiple important reflexes, such as heart rate, breathing, and swallowing.

Neurons and neuroglia are the cellular building blocks of the nervous system. There are about 100 billion neurons in the human brain. The neuron consists of three main parts: a cell body, dendrites, and an axon (Figure 1.5). The cell body contains the nucleus and typical cell organelles. It is where most protein synthesis[7] occurs. The dendrites are cellular extensions, which receive signals from other neurons. The axon propagates nerve impulses from the cell body to the axon terminal where the signal is transmitted to other neurons. Most axons are surrounded by a myelin sheath (Figure 1.5). The neuroglia are non-neuronal cells that do not generate or propagate signals. Their function is to provide nutrition, support, and protection for neurons. They outnumber the neurones by 5 to 50 times.

The outer part of the cerebrum, the cerebral cortex where most conscious behaviour is processed, is made of grey matter; the inner part is made of white matter (Figure 1.3). Grey matter is grey because it consists of nerve cell bodies, unmyelinated fibre, and capillaries; white matter is white because it consists of myelin-coated nerve cell fibre. The cerebral cortex occupies 77% of the total brain volume.

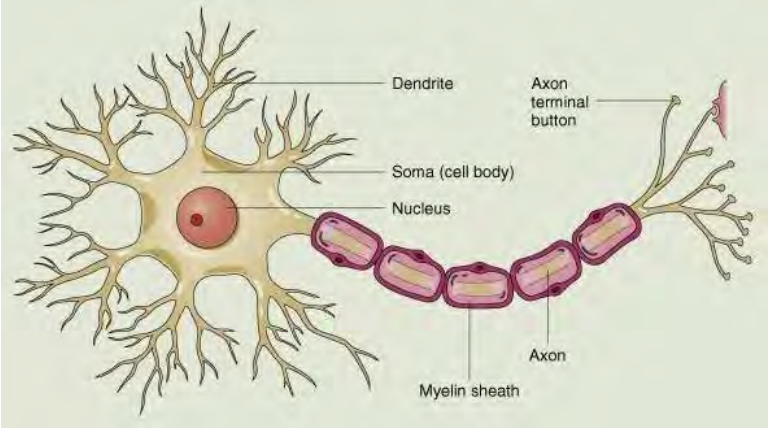

Figure 1.5 The neuron.

[7]See Glossary

1.2.2 Cerebral Circulation

The brain is a highly vascularised organ due to its high blood flowrate and high oxygen demand. Figure 1.6 shows a lateral view of a corrosion cast for the arterial circulation.

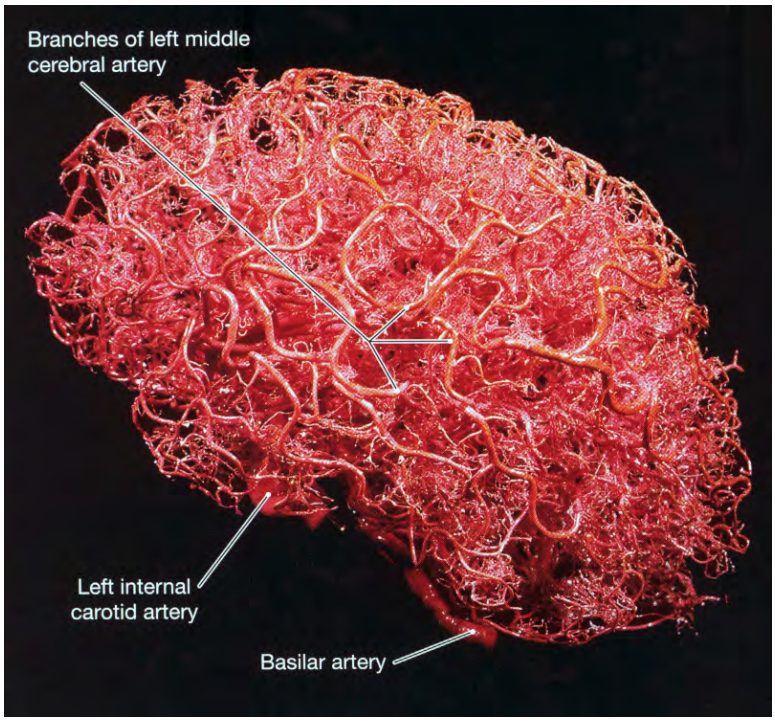

Figure 1.6 Corrosion cast of the arterial circulation in the brain [82].

The cerebral mass is the only organ that is supplied by four arteries, the two Vertebral Arteries (VA) and the two Internal Carotid Arteries (ICA) (Figure 1.7). The Vertebral Arteries join together to form the Basilar Artery (BA). The afferent[8] arteries, BA and ICAs, anastomose together to form the Circle of Willis (CoW). The CoW is a ring-like structure at the base of the brain whose main function is to distribute the incoming oxygen-rich blood to the cerebral mass. This is done through the major efferent arteries: Anterior Cerebral Arteries (ACA), Middle Cerebral Arteries (MCA), and Posterior Cerebral Arteries (PCA). This section will give a detailed description of the cerebral vasculature, along with the areas of the brain supplied by it [31, 92, 108, 113].

[8] Afferent: carrying blood towards an organ.

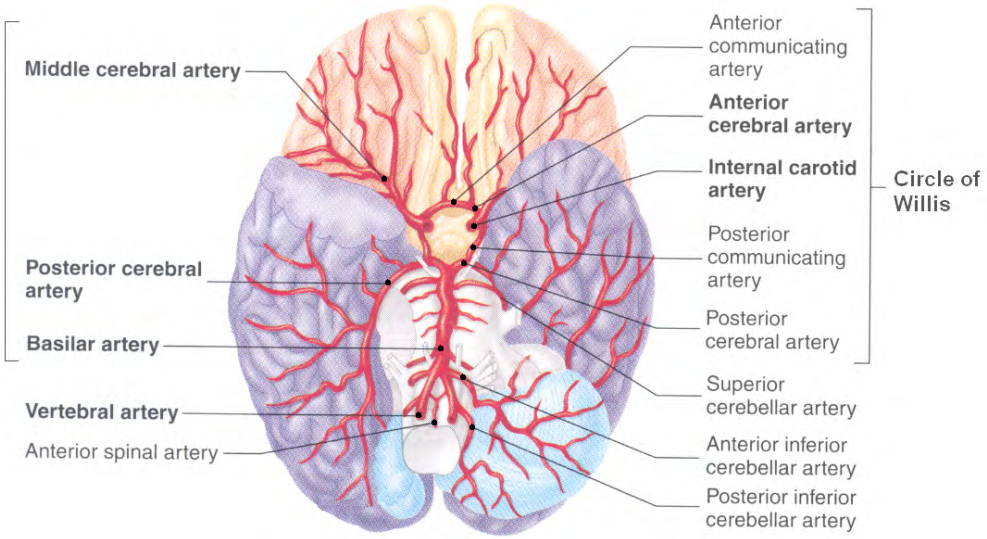

Figure 1.7 Arteries of the brain [110].

1.2.2.1 From Aorta To Brain: The Route To The CoW

Three arteries originate from the aortic arch to deliver blood to the head, neck, shoulders and upper limbs. These are the brachiocephalic trunk, the left common carotid artery, and the left subclavian artery (Figure 1.8). The brachiocephalic trunk ascends for a short distance then branches into the right common carotid artery and right subclavian artery. The subclavian arteries give rise to the vertebral arteries, which ascend until joining to form the basilar artery (BA). The common carotid artery divides into the external and internal carotid arteries. The right and left internal carotid arteries (ICA) and the BA anastomose together to form the CoW. See Figure 1.9 for a flow chart of the cerebral vasculature from the aorta to the CoW.

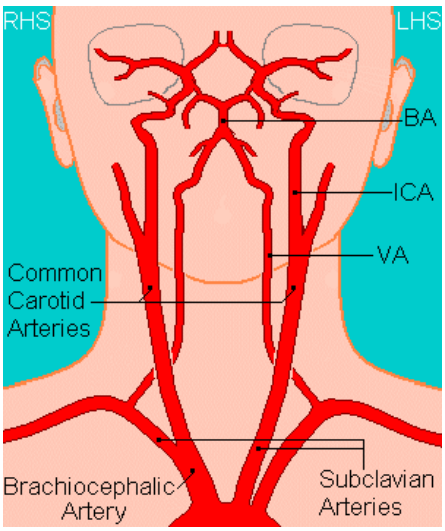

Figure 1.8 Aorta to CoW arteries.

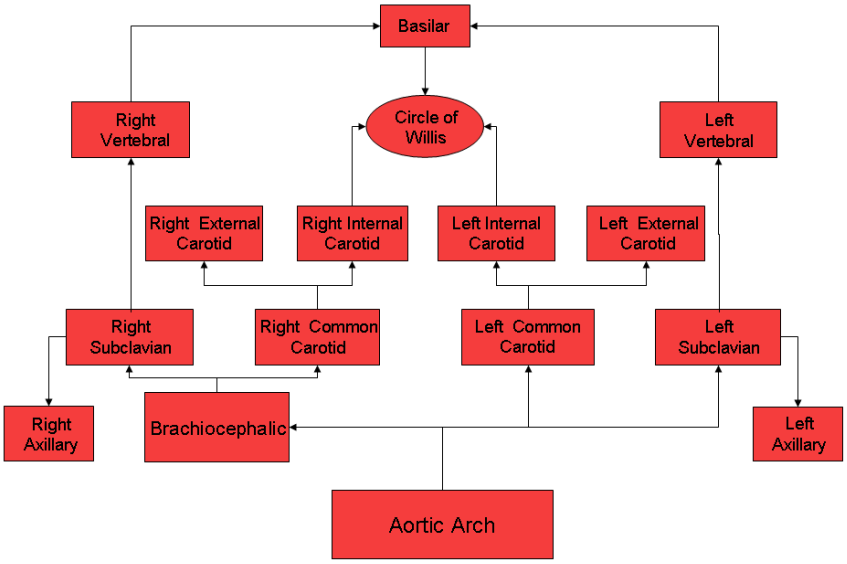

Figure 1.9 Head arteries flowchart.

1.2.2.2 Afferent Arteries

Internal Carotid Arteries (ICA)

The common carotid arteries divide into the external and internal carotid arteries at the level of the thyroid cartilage. The external carotid arteries supply the face, scalp, dura mater, skull, and structures of the neck. The ICAs supply most of the cerebrum (about 80%) and the diencephalon.

Before joining the CoW network, the superior hypophyseal artery and the ophthalmic artery branch off the ICA, as do small branches to the optic nerve, chiasm, and hypothalamus. The ophthalmic artery splits into seven smaller arteries, and it supplies the eyes, orbits, forehead, and nose.

Vertebral Arteries And The Basilar Artery (VA & BA)

The VAs and BA supply the brainstem, cerebellum, parts of the diencephalon, occipital and temporal lobes, and spinal cord.

The VAs run along the medulla oblongata and fuse to form the BA at the junction between the medulla and the pons. Before forming the BA, the VAs give off multiple arteries: the posterior spinal arteries; the medial branches, which join together to form the single anterior spinal artery; the posterior inferior cerebellar artery; and the bulbar

branches.

The BA is the main artery that supplies the PCAs. It is approximately 2.5 cm in length and gives off multiple arteries: the anterior inferior cerebellar artery, the superior cerebellar artery, and the pontine branches that supply the pons and the internal auditory artery (which may also originate from the anterior inferior cerebellar artery).

1.2.2.3 CoW Arteries

As mentioned above, the BA and ICAs anastomose together to form the CoW (Figure 1.10). This is named after the professor of natural physiology at Oxford, Thomas Willis (1621-1675), whose work on the nervous system and anatomy made him one of the greatest scientists of the seventeenth century. Thomas Willis presented the first detailed description of this arterial circle in the base of the brain and was first to recognize its importance [143]. The CoW encircles the pituitary gland and optic chiasma. The ring-like structure in the CoW consists of the Anterior Communications Artery (ACoA), Anterior Cerebral Arteries (ACA), Posterior Communications Arteries (PCoA), and Posterior Cerebral Arteries (PCA).

The CoW is the most extraordinary collateral circulatory system in the human body. It provides alternative routes for blood to reach the brain tissue if some arteries are occluded or stenosed. In a complete CoW, the collateral circulation is very adaptable to any changes in flow as a result of afferent artery occlusions, even if they are sudden. The CoW is versatile even with missing segments such as the ACA1 or PCoA. These variations in the CoW are presented in Section 1.2.3. The description given here is for a classical and complete CoW structure.

Each of the ACA and PCA vessels are divided into two trunks, the proximal trunk, which is part of the ring-like structure of the CoW (segment one, e.g. ACA1), and the distal trunk (segment two, e.g. ACA2), which branches off the ring-like structure and goes on to supply the cerebral mass.

Anterior Cerebral Arteries - Segment One (ACA1)

The ACA1 is the part of the CoW that delivers all the blood flow from the ICA to the ACA2 in a complete CoW. The two ACA1s are linked to each other via the ACoA. Each ACA1 gives off a medial striate artery.

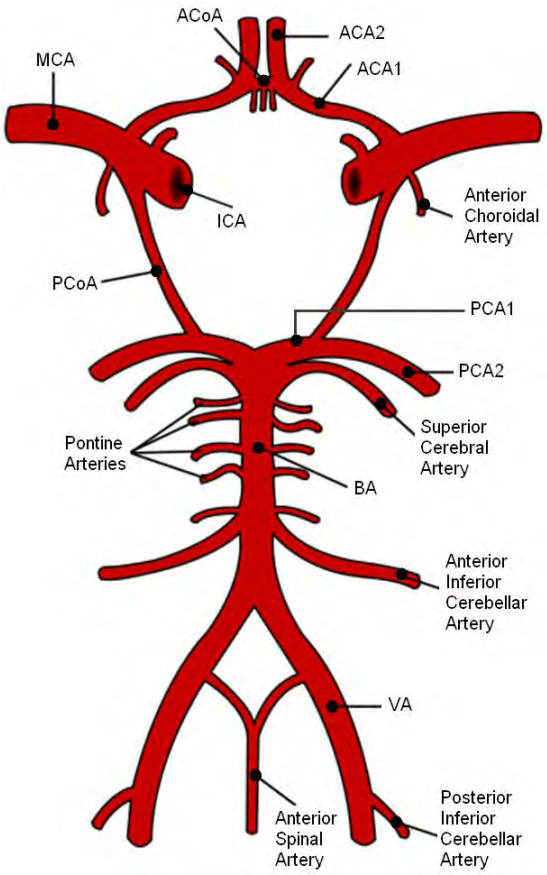

Figure 1.10 The Circle of Willis (CoW), [45].

Anterior Communicating Artery (ACoA)

The main anastomotic function of the ACoA in the CoW overshadows the fact that it may distribute blood, and its branches are neglected in many cerebrovasculature studies. The reason for that is probably the variability in the existence of branching vessels, which supply the corpus callosum[9].

Posterior Communicating Arteries (PCoA)

The PCoA joins the PCA to the ICA/MCA. In a complete CoW, it is relatively small in diameter. This is because in the complete CoW case the arterial pressure in the ICA is about the same as that in the PCA1. Therefore, the BA supplies the distal PCA (here named PCA2) through the PCA1 segments, and the ICAs supply the middle and anterior cerebral arteries. This means that blood flow through the PCoA is low, hence the small diameter. The PCoA gives rise to several vessels that supply various parts of the diencephalon.

[9]See Glossary

Posterior Cerebral Arteries - Segment One (PCA1)

This section of the PCA gives rise to brain stem branches. These are the perforating, quadrigeminal, thalamic, posterior choroidal, premammillary, and peduncular arteries. The posterior choroidal is a group of arteries most commonly identified in anatomy books, and it supplies some of the choroidal plexus[10].

1.2.2.4 Efferent Arteries

Anterior Cerebral Artery - Segment Two (ACA2)

The ACA2s supply most of the anterior cerebral parts of the brain, the medial surface of the cerebrum (frontal and parietal lobes), and deep masses of grey matter within the cerebrum (Figure 1.12). The ACA2 lies at bottom of the cerebral longitudinal fissure. It courses medially and anteriorly to cerebral hemispheres, curves around the genu of corpus callosum, and then extends posteriorly. The continuation of the ACA2, after it arches around the genu of corpus callosum, is called the pericallosal artery. The frontobasilar, frontopolar, callosomarginal, and posterior frontal arteries branch off the ACA2/pericallosal artery (Figure 1.13).

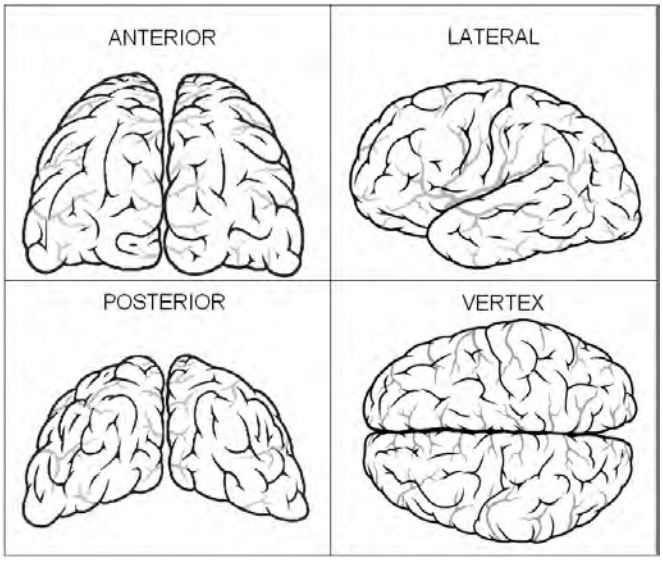

Figure 1.11 Guide to views in Figures 1.12, 1.14, and 1.16 [31].

[10]Choroidal plexus: sites of cerebrospinal fluid production.

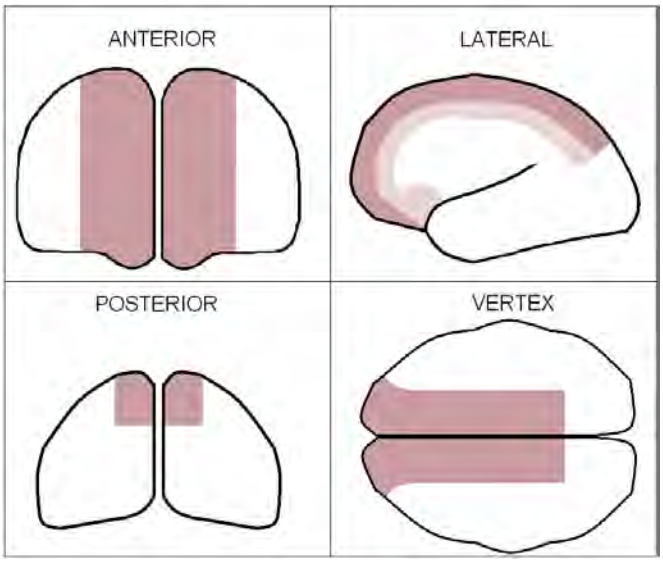

Figure 1.12 Anterior, posterior, lateral, and vertex views of the cerebral areas supplied by the ACA [31].

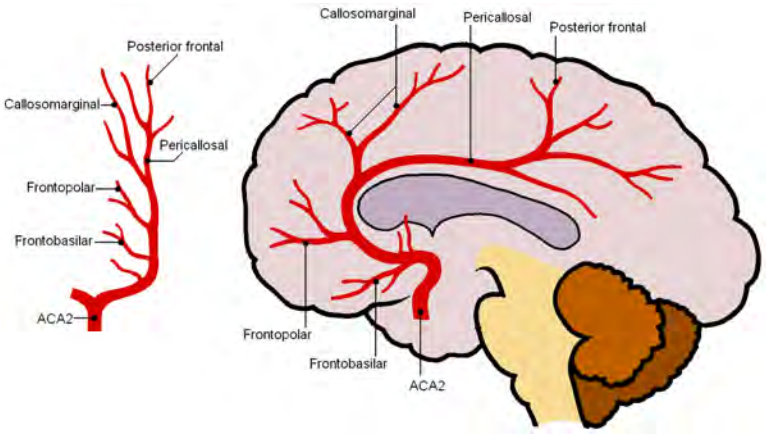

Figure 1.13 The ACA arteries [31].

Middle Cerebral Artery (MCA)

The MCA is the largest efferent artery in CoW in terms of size and amount of blood it delivers. It can be assumed to be a continuation of the ICA. The MCAs supply most of the lateral surface of the cerebrum. Superficial branches deliver blood to the temporal lobe and large parts of the frontal and parietal lobes. Deep branches supply the basal nuclei and parts of the thalamus (Figure 1.14).

The MCA gives rise to many arteries. One of the major arteries is the anterior choroidal artery, which may in many cases branches off the PCoA, or the ICA at the point that connects the ICA to the MCA [108]. The lateral striate arteries, 10-20 in number, branch off the first segment of the MCA. Many other major arteries branch off

the MCA to supply the lateral cortex of the frontal, parietal, occipital, and temporal lobes. These major arteries have relatively consistent areas of distribution. These are orbitofrontal, prerolandic, rolandic, anterior and posterior parietal, anterior, middle and posterior temporal, and angular arteries (Figure 1.15).

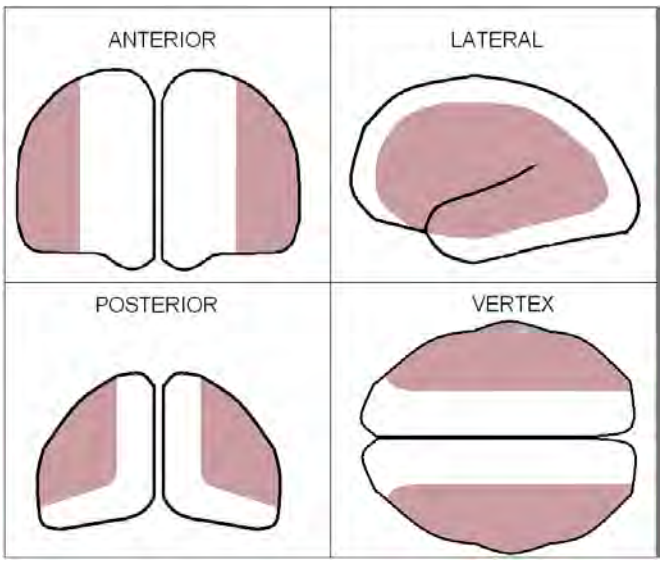

Figure 1.14 Anterior, posterior, lateral, and vertex views of the cerebral areas supplied by the MCA [31].

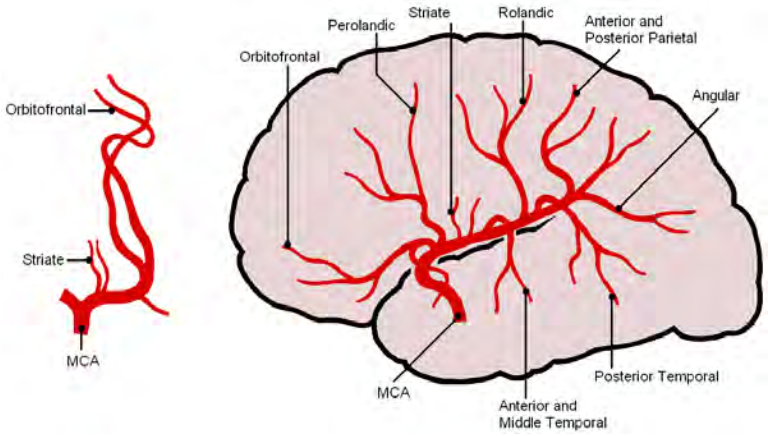

Figure 1.15 The MCA arteries [31].

Posterior Cerebral Artery - Segment Two (PCA2)

The PCA2 curves around the midbrain and gives rise to posterior choroidal arteries and cortical branches, which include the parieto-occipital, lateral temporal, and calcarine arteries. The PCA2 supplies the inferolateral surface of the temporal lobe, lateral and medial surfaces of the occipital lobe, deep masses of grey matter within the cerebrum, and the midbrain. (Figures 1.16 and 1.17).

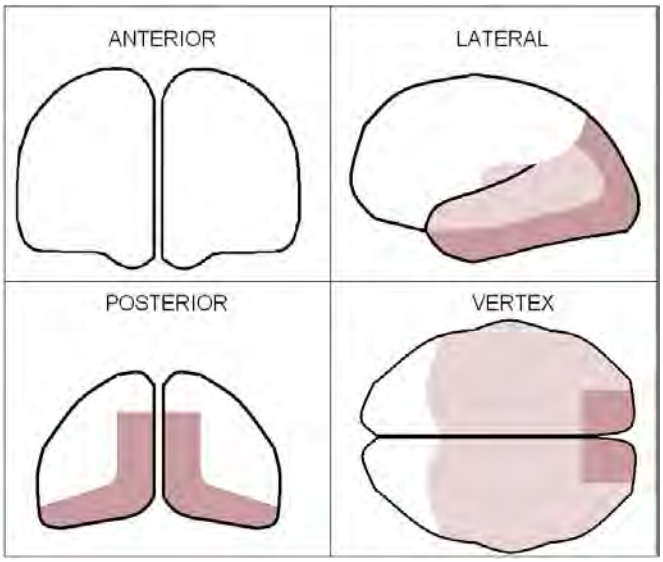

Figure 1.16 Posterior, lateral, and vertex views of the cerebral areas supplied by the PCA [31].

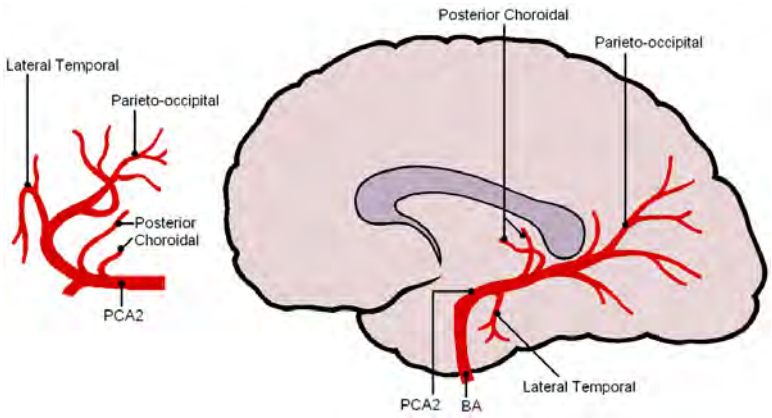

Figure 1.17 The PCA arteries [31].

It is important to note here that there is a variability of the territories supplied by the major efferent cerebral arteries. A study by Hillen et al. [133] showed that there is asymmetry in the territorial patterns in both hemispheres intra-individually. In addition, there is a time dependent change in individual territorial distribution as a result of altering hemodynamic circumstances such as variation of mean arterial pressure as a result of an individual moving from a seating position to a standing position.

1.2.3 CoW Variation

With the help of the CoW, flow can be maintained in the case of impaired or decreased flow being delivered to one of the major efferent cerebral arteries. This depends heavily on the presence and/or size of the CoW vessels. There are large morphologic

variations in the CoW configurations in both patients with cerebrovascular diseases as well as healthy individuals. These variations play an important role in an ischemic stroke outcome.

Approximately 42-52% of the population have an incomplete CoW [5, 70]. In addition, complete CoW configurations have other anatomical variations compared with the classical and complete CoW described in Section 1.2.2.3. The study done by Krabbe-Hartkamp et al. looks into the CoW morphologic variation in detail using three-dimensional time-of-flight (TOF) magnetic resonance Angiography (MRA). The data was based on 150 people divided into two groups. The younger group consisted of 50 healthy individuals between the ages of 20 and 25. The older group consisted of individuals between the ages of 60 and 88. Out of the 100 older individuals, 51 had one of the following conditions: cerebrovascular accident, myocardial infarction, diabetes mellitus, transient ischemic attack (TIA), hypertension, and meningitis. The anterior and posterior parts of the CoW were assessed separately. Figures 1.18 and 1.19 show the variations in the anterior and posterior parts of the CoW respectively.

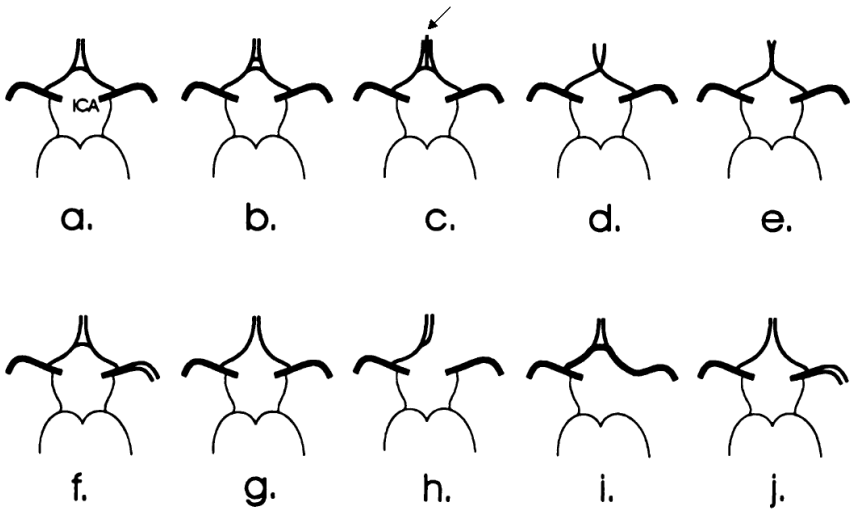

Figure 1.18 Anatomic variations in the anterior part of the CoW [70]. Variants a-f are complete, whereas variants g-j are incomplete. a) a single ACoA. b) Two (or more) ACoAs. c) Medial artery of the corpus callosum arises from the ACoA. d) Fusion of the anterior cerebral arteries over a short distance. e) Anterior cerebral arteries form a common trunk and split distally into two segments. f) MCA originates from the ICA as two separate trunks. g) Absence of the ACoA (most common variant). h) One ACA1 is absent, the other ACA1 segment gives rise to both ACA2s. i) Absence of an ICA. The contralateral ACA1 gives rise to both ACA2s and supplies retrograde flow to the ipsilateral ACA1 segment, which, in turn, gives rise to the ipsilateral MCA (both ACAs and both MCAs are supplied by a single ICA). j)Absence of an ACoA and the MCA arises as two separate trunks.

The occurrence percentage of each of the configurations in the anterior and posterior parts of the CoW are shown in Table 1.1. Statistically, there were no significant age or sex differences in the anatomical variations. However, there is an age-related difference in vessel diameters. The afferent arteries (ICAs and BA) supplying the CoW were larger in diameter while efferent arteries supplying the cerebral mass (ACA2s, MCAs

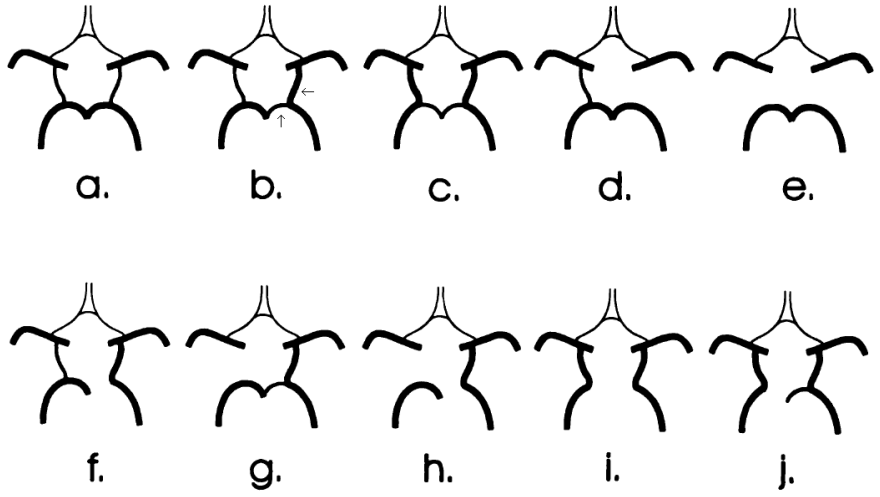

Figure 1.19 Anatomic variations in the posterior part of the CoW [70]. Variants a-c are complete, whereas variants d-j are incomplete. a) Bilateral PCoAs present. b) Unilateral fetal case where the diameter of the PCoA is larger than the PCA1 (arrows). c) Bilateral fetal case. d) Unilateral PCoA absence (most common variant). e) Absence of both PCoAs and isolation of the anterior and posterior parts of the circle at this level. f) Unilateral fetal case and absence of ipsilateral PCA1. g) Unilateral fetal case and absence of the contralateral PCoA. h) Unilateral fetal case and absence of both a PCA1 and the PCoA. i) Bilateral fetal case with absence of both PCA1s. j) Bilateral fetal case with absence of one PCA1.

and PCA2s) were smaller in older subjects.

The most common anterior variant, apart from a complete anterior, was the absence of the ACoA while the most common posterior variants, apart from a complete posterior, were the unilateral absence of a PCoA followed by a unilateral fetal case. The fetal case is where the diameter of a PCoA is larger than the ipsilateral PCA1. The main supply to the distal PCA (PCA2) is, therefore, delivered by the ICA via the PCoA rather than by the BA via the PCA1. It is called fetal because in the early embryonic stage (8 weeks) the PCA2 is a continuation of the PCoA, which is a continuation of the ICA. However, when the vertebro-basilar system develops at a later stage, the PCA1 develops and overtakes the function of the PCoA, which now resembles the adult configuration, becoming insignificant in terms of blood flow through it, and therefore, smaller in diameter [134]. In cases of a major CoW vessel slowly occluding, the small-diameter PCoA will slowly enlarge and allow flow to compensate for the occlusion [92].

Table 1.1 *Percentages of CoW anterior and posterior variants [70].*

CoW part	a	b	c	d	e	f	g	h	i	j
Anterior	60.7	8.0	1.3	1.3	1.3	1.3	18	6.7	0	1.3
Posterior	28.7	18	5.3	28.7	10.7	1.3	4.7	0.7	0.7	1.3

ACoA is the most common site of anomalies of the CoW. It may be hypoplastic[11] but more often duplicated or triplicated, retaining its embryonic form. Another common variant in the anterior part of the CoW is having a unilateral hypoplastic ACA1. In such cases, the contralateral ACA1 supplies both ACA2s: the ACA2 directly connected to it as well the opposite ACA2 via the ACoA, if it exists.

1.2.4 Collateral Circulation

Collateral circulations in general are alternative supply systems that substitute in case of a deficiency. Collateral circulation maintains a degree of cortical perfusion, protecting the tissue from irreversible cell death. The causes that bring collateral channels or anastomoses into action are temporary or permanent insufficiency of an arterial channel. These anastomoses are developed during fetal growth. However, any permanent change of arterial circulation is usually due to disease.

1.2.4.1 CoW collateral circulation

Aspects of the CoW collateral circulation and its adaptability were presented in Sections 1.2.2.3 and 1.2.3 above.

1.2.4.2 Non-CoW collateral circulation

Collateral circulation outside the CoW is different. In this case, the vessels, which have been very inactive, become highly active as a result of one of the major arteries becoming occluded. They are also much smaller in diameter compared with CoW arteries and, therefore, cannot adapt as well as the CoW under a sudden increase in blood flow [39]. The opening of pre-existing collaterals is the first bodily response of an occlusion of a major artery.

The collateral system is better developed if the stenosis or occlusion began slowly. If the occlusion develops over time, collateral vascularity adapts better to the gradual increase in flowrate. Therefore, individuals who suffer a sudden occlusion, by embolism for example, will suffer greatly because the collateral arterial wall will not adjust very well to the sudden increase in flowrate. The collateral circulation, if available, may not adjust rapidly enough to prevent episodes of transient ischemic attacks (TIA) where alterations occur in the systemic blood pressure. This means that recovery is possible if blood pressure does not fall below a specific range. However, if the CoW is incomplete, permanent damage may result.

[11] Hypoplastic: a condition in which tissue or an organ of the body fails to grow to normal size.

The effectiveness of collateral vessels dependents on a number of variables: the calibre of the vessel, the size and location of the occlusion, the time of the occlusion's development, the cardiovascular system, and the condition of collateral vessel walls. The walls must be healthy to accommodate the increase in flow. With aging, vessel walls become less elastic and less responsive to vasomotion[12].

There are several examples of collateral circulation in the cerebral vasculature; a few are demonstrated here [31, 39, 144].

ICA occlusion

If an ICA is occluded, parallel circulation may be established through several routes (Figure 1.20). The ICA is then supplied by the external carotid artery through the internal maxillary and ophthalmic arteries. There are several collateral routes (up to 15) that can be followed to link the internal maxillary artery to the ophthalmic artery. Three of the most common are the external maxillary, superficial temporal, and middle meningeal arteries.

VA and BA occlusion

When a BA occlusion occurs proximal to the superior cerebellar arteries, collateral anastomoses between the inferior cerebellar arteries and the superior cerebellar arteries may form (Figure 1.21).

If a unilateral occlusion of the vertebral artery (VA) occurs, the spinal branches of the VA will participate in collateral circulation. However, the most important anastomosis in that case is the one between a branch off the external carotid artery and a branch off the VA. In the case of bilateral VA occlusion proximal to the anterior spinal artery, an anastomosis between the VA and the anterior spinal artery will bypass the occlusion to supply blood to the BA.

Common carotid artery occlusion

Seldom is there neurological damage due to a common carotid artery occlusion. This is because there are several collateral circulations that blood can travel through in this case (Figure 1.22). The most significant are collateral circulation from the contralateral external carotid artery branches, ipsilateral costocervical and thyrocervical vessels, and anastomoses between the ipsilateral external carotid artery and VA branches. In

[12] See Section 2.2.5

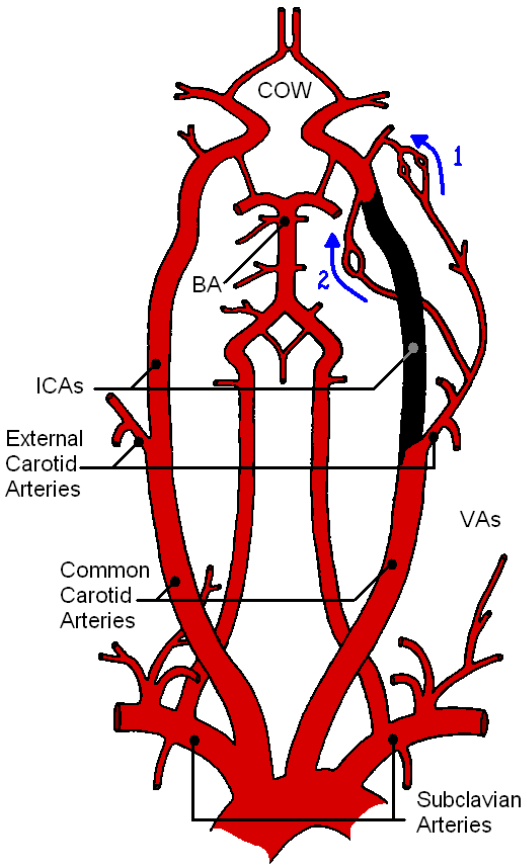

Figure 1.20 The collateral circulation in the ICA occlusion case [39]. 1,2) Collateral circulation between the ICA and the external carotid artery.

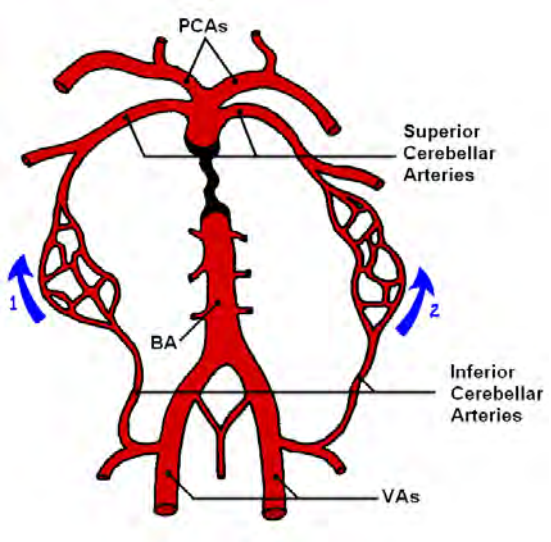

Figure 1.21 The collateral circulation in the BA occlusion case [31]. 1,2) Collateral circulation between the inferior cerebellar arteries and the superior cerebellar arteries.

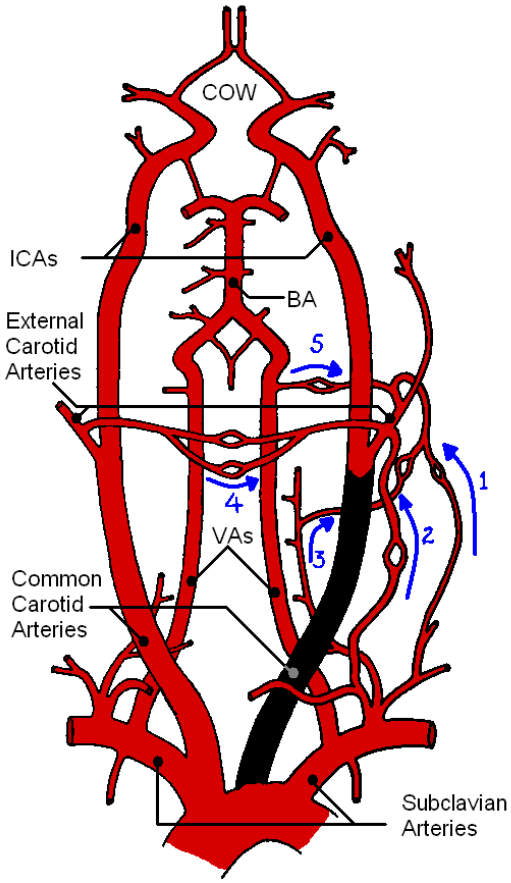

Figure 1.22 The collateral circulation in the common carotid artery occlusion case [39]. 1,2,3) Collateral circulation from ipsilateral costocervical and thyrocervical vessels. 4) Collateral circulation from the contralateral external carotid artery branches. 5) Collateral circulation between the ipsilateral external carotid artery and VA branches.

addition, there is further collateral circulation through the CoW as a result of reduced arterial blood pressure in the distal intra-cranial branches of the carotid system.

Principle cerebral artery occlusion

The major efferent arteries in the cerebral vasculature, namely ACA, MCA and PCA, have collateral circulation over the surface of the brain (termed the *leptomeningeal* arteries).

A leptomeningeal artery (LMA) is a pial[13] artery that connects two major cerebral arteries supplying two cortical territories, for example the MCA and ACA. The LMA may be important in understanding stroke; however, the literature shows no consensus between statements on the existence of leptomeningeal anastomoses and compensatory capacity. In recent years, both anatomic and angiographic studies confirmed the pres-

[13]See Glossary

ence of the LMA in every brain. Van der Zwan and Hillen [16, 132] studied the variability of the vascular territories in human cadaver brains and observed anastomosis as large as 1 mm.

The leptomeningeal arteries can flow in either direction. However, since thrombotic occlusion occurs more frequently in the MCA, the flow is usually from the ACA and PCA to the MCA. Figures 1.23-1.25 show the LMA between the ACA and MCA, MCA and PCA, and ACA and PCA. The precuneal arteries originate from either the middle of pericallosal artery or the posterior of callosomarginal artery.

There are also several anastomoses between the two ACA2 sections along the corpus callosum that become active if one of the two becomes inadequate (Figure 1.26).

Occlusions in the arteries to the brainstem and basal ganglia usually result in infarctions because they are end-arteries and do not have collateral circulation.

1.2.4.3 Microcirculation

The most important aspects of circulation are the exchange of nutrients and the removal of wastes. This occurs through the capillary walls, which consist of one layer of endothelial cells (Figure 1.27). Capillaries do not function independently; they form interconnected networks called capillary beds. A single arteriole gives rise to a capillary bed that empties into a venule. The precapillary arterioles, termed terminal arterioles or metarterioles, have a structure midway between a capillary and an arteriole.

The number of capillaries is higher if the tissue has a high metabolic rate. For example, the metabolic rate of grey matter is four times the metabolic rate of white matter. The number of capillaries in grey matter are, therefore, four times the number of capillaries in white matter. The regulation through resistance is made of arteries and arterioles segments. Arteriole walls are lined with smooth muscle cells as well as endothelial cells (Figure 1.27). The local conditions in the tissue control the diameters of the arterioles, which in turn control blood flow to the tissue using the smooth muscles in the walls. This local control ensures that there is enough blood supply to meet the demand.

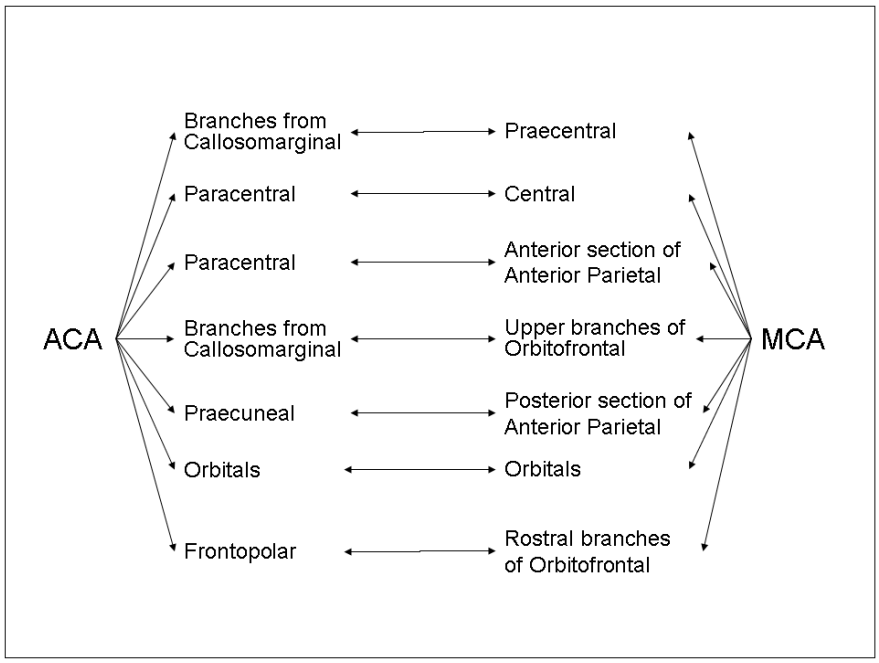

Figure 1.23 The leptomeningeal arteries between the ACA and MCA [16].

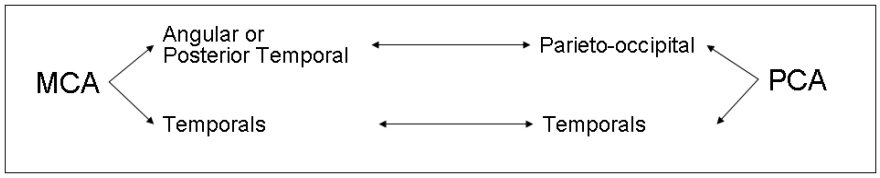

Figure 1.24 The leptomeningeal arteries between the MCA and PCA [16].

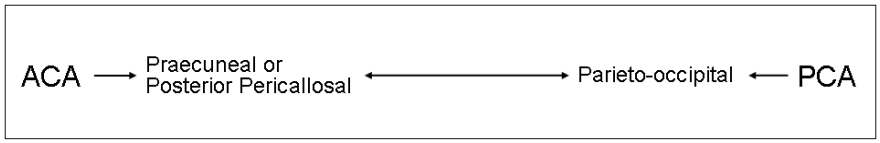

Figure 1.25 The leptomeningeal arteries between the ACA and PCA [16].

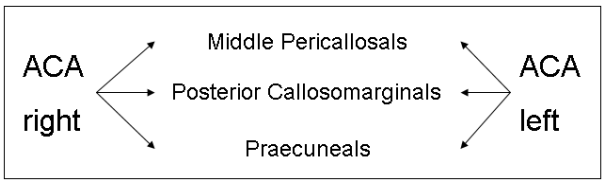

Figure 1.26 The leptomeningeal arteries between the ACAs along the corpus callosum [16].

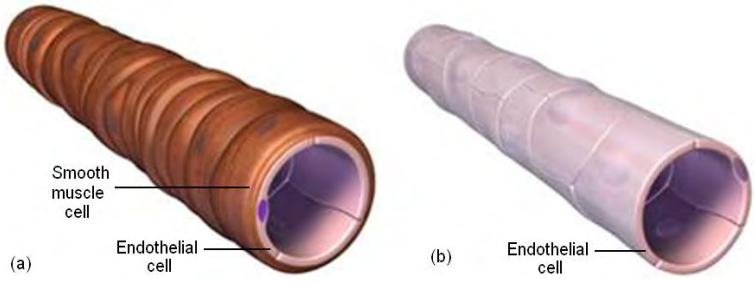

Figure 1.27 a) An arteriole. b) A capillary.

1.3 Pathology

1.3.1 Stroke

A stroke, also known as cerebrovascular accident (CVA), is an acute neurologic injury in which the blood supply to a part of the brain is interrupted by rupture or blocking of a blood vessel. Stroke involves sudden loss of neuronal function caused by disturbance in cerebral perfusion. This disturbance in perfusion is commonly arterial, but can be venous. The part of the brain with disturbed perfusion no longer receives adequate oxygen, causing vital brain and nerve cells to die. Strokes that affect the lower brain stem are almost always fatal [82]. Diversity of clinical outcome of stroke is attributed to the variability of collateral circulation which may vary in size, number and location. The collateral circulation availability is very important in the prognosis of ischemic disease.

1.3.1.1 Stroke Statistics

Stroke carries a high risk of death. Survivors may suffer paralysis, loss of speech and vision. Previous stroke significantly increases the risk of having further incidents. The statistics below [52, 80, 121] and the high cost of treatment of stroke show that a high priority should be given to preventive strategies, or at least to preventing further episodes:

- In New Zealand, stroke is the third biggest killer and greatest cause of major disability.
- Worldwide, stroke is the third leading cause of death from disease exceeded only by coronary heart disease and cancer.
- Worldwide, 17 million people suffer a stroke each year: 5.5 million cases result in death and 5 million are left permanently disabled.

- Of all stroke cases, 22% of men and 25% of women die within a year.
- Approximately 50% of all stroke patients die from a stroke.
- 8-12% of ischemic strokes and 37-38% of haemorrhagic strokes result in death within 30 days.
- 8% of men and 11% of women will have a stroke within six years after a heart attack.
- 14% of people who have a stroke or TIA will have another within a year.
- 28% of people who suffer a stroke in a given year are under the age of 65.
- About 47% of stroke deaths occur out of hospital.
- On average, individuals have a 1:8 chance of having a stroke in their lifetime.
- Stroke accounts for a higher proportion of deaths among women than men.

1.3.1.2 Stroke Types and Causes

There are two major types of stroke, ischemic and haemorrhagic (defined below). Stroke is caused by either defective blood flow or defective blood vessels [31]. Blood flow can be defective as a result of multiple phenomena such as presence of extravascular blood, use of vasospastic drugs which cause the vessels to constrict, or particles that deposit on the inner arterial wall (e.g. atheroma, endarterial blood clot and fibrin deposits). Defective blood vessels can happen as a result of events such as inflammations (polyarteritis, syphilis, meningitis and radiation), arteriovenous malformations, and aneurysms.

Ischemic Stroke

Ischemic stroke (Figure 1.28) is where the artery is blocked by a blood clot, which interrupts the brain's blood supply ("ischemia" means to restrain blood in Greek). This means that not enough blood is getting to the brain cells in that area. Cells cannot live without oxygen, so if the blood supply is cut off, nerve cells die and that part of the brain stops working and some body functions are impaired. Ischemic stroke is the most common type of stroke with approximately 85% of all stroke and it has a mortality rate of 40%. It can occur due to two main reasons:

Thrombotic stroke happens when a blood clot forms in the main artery leading to the brain. Disease (atherosclerosis) causes the inside walls of the artery to thicken

up due to atheromatous and fatty degeneration of connective tissue so the lumen is too narrow for enough blood to get through. 50% of all strokes are thrombotic with 30% happening in large vessels such as the ICA or MCA and 20% happening in relatively small vessels.

Embolic stroke - happens when a blood clot forms elsewhere in the body and is swept into the arteries perfusing the brain (Figure 1.29). For example, a clot can form in the heart, break off and travel with the blood until it gets jammed in a small or narrowed artery in the brain. Emboli are composed of aggregated platelets with strands of fibrin and few red and white cells. Emboli large enough to block one of the major cerebral arteries usually originate from a lesion in the heart. 30% of all strokes are due to an embolism.

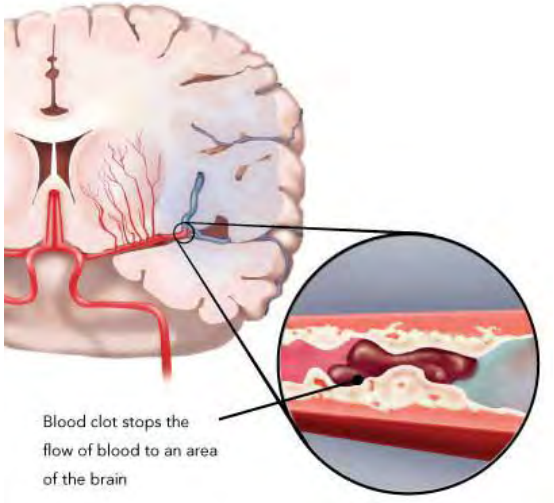

Figure 1.28 Ischemic Stroke [1].

Figure 1.29 Formation of emboli [2].

Hemorrhagic Stroke

In the second type of stroke, blood bursts through the walls of an artery and leaks into the brain (intra-cerebral hemorrhage) or on to the surface of the brain (subarach-

noid haemorrhage). The part of the vessel that experiences a wall weakness, causing it balloon out, or rupture is called an aneurysm (Figure 1.30).

It is triggered by either a congenital cause or hypertension. The most common aneurysms are due to a congenital cause, when people are born with a faulty artery [1]. These account for 70-80% of cases. Aneurysms can also form over time as a result of hypertension, which drives the artery walls to become thin and brittle.

Blood is forced into brain tissue and, because there is not much space around the brain in the skull cavity, the build up of blood presses on the part of the brain where the bleeding occurred, damaging the nerve cells so that area of the brain cannot function. Only 15% of strokes are hemorrhagic; however, they have a high mortality rate of 80%.

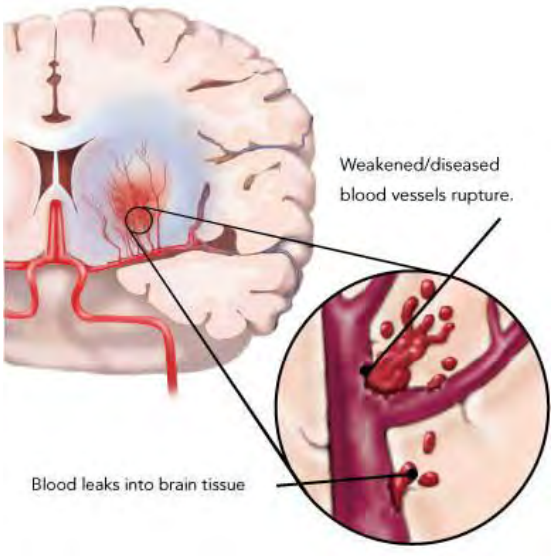

Figure 1.30 Hemorrhagic Stroke [1].

1.3.1.3 Common Sites of Stroke

Stenosis and occlusion in one of the ICAs due to thrombosis is very common, especially where the ICA bifurcates off the common carotid artery. Since the MCA is the largest efferent artery in the CoW, it is the most common site of stroke. If stroke occurs in the left MCA, the individual will experience aphasia (partial or total loss of the ability to articulate ideas or comprehend spoken or written language) and sensory and motor paralysis of the right side of the body will result. If however, a stroke occurs in the right MCA, the individual will experience difficulty drawing or interpreting spatial relationships and paralysis in the left side of the body will result.

Infarction in the PCA territory is not infrequent. It may occur as a result of embolism or thrombosis, or may be secondary to BA occlusion. In case of temporal

lobe herniation[14], the PCA can close resulting in infarction.

The VA is a common site for thrombosis. It is common to have a VA that is larger in size than the other side. In that case, blood flow can be seriously compromised by occlusion of the larger artery.

For aneurysms, the ACoA is the most common and most complex site of aneurysms constituting up to 30% of all cerebral aneurysms [97]. The point of origin of the PCoA from the ICA is another very common site of aneurysms.

The lateral striate arteries that branch off the MCA have narrow thin wall and are frequently involved in hypertensive cerebral hemorrhage. The origin of the lateral striate from or near the point of bifurcation of the MCA is also the most common site of MCA aneurysms.

1.3.2 Moyamoya Disease

Moyamoya disease is a unique cerebrovascular disease with much higher incidents in the Japanese and asian races. It is characterized by the bilateral occlusion of the ICAs with spontaneous development of a collateral vascular network at the base of the brain which is somtimes called moyamoya vessels [41, 116]. From the epidemiologic data in Japan, the disease is distributed among all age groups but predominates in the age group below 10 years.

1.3.3 Periventricular leukomalacia (PVL) in Neonate

Periventricular leukomalacia (PVL) is a neurological disability that occurs most commonly in the very premature infant. It affects the immature white matter of cerebral hemispheres and increases the risk of developing a variety of neurological disorders such as motor dysfunction, delayed cognitive development, visual impairment, and epilepsy [40, 67].

Minimal white matter is present in the 29 gestational[15] weeks infant. This increases five-fold between 35 and 40 gestational weeks (40 is full term pregnancy). If the cerebral white matter has not reached complete maturation, it becomes very vulnerable to PVL, which is the case for the very premature infant. The major cause of PVL is considered to be the cerebral ischemia in the premature infant with cerebral vascular immaturity and arterial end-zones in the periventricular region, coupled with the tendency for impaired vascular autoregulation. The total blood flow volume and mean blood pressure are

[14]Herniation: abnormal protrusion of an organ or other body structure through a defect.
[15]Gestational: the period of development in the uterus from conception until birth; pregnancy.

significantly lower in the infants with PVL compared to normal infants. PVL can also be caused by a bacterial infection in the mother and/or the fetus [40, 67].

1.3.4 Alzheimer's Disease (AD)

Alzheimer's is a neurodegenerative disease. It is the most common cause of dementia[16], accounting for about 50% of all cases. It occurs mostly in individuals over 65 years of age and currently has no cure. AD is characterized by progressive dementia with memory disturbances and decline in senses [28]. Pathologically, it is characterized by loss of neurons and their synapses[16] in cerebral cortex which results in atrophy[16] in various lobes of the brain. Latest research suggests that it may be caused by lack of oxygen [104].

Prolonged oxygen deprivation (chronic hypoxia), which may occur as a result of cardiovascular or cerebrovascular disorders, leads to significant cell remodeling. The cell remodeling is a result of change to regulation of the oxygen sensitive ion channels. Hypoxia leads to cell depolarisation which may account for excitotoxicity[16] associated with excessive glutamate[16] release of central hypoxia. This results in alterations in protein expression of cell, i.e. cell remodeling. This cell remodeling is strongly associated with the production of Amyloid Beta Peptide of alzheimer's disease.

[16]See Glossary

Chapter 2

Physiology of Autoregulation

The focus of this chapter is to view the different physiological aspects of blood delivery to the cerebral mass and to examine the different mechanisms that the vessels possess to maintain a constant blood supply.

The brain derives most of its energy from oxygen and glucose supplied via the bloodstream. Under normal conditions, cerebral blood flow (CBF) and energy use are tightly coupled, and the brain must adapt to local alterations in energy requirement by regulating the amount of blood flow accordingly. The anterior, middle and posterior arteries of the CoW divide into pial arteries. These run over the surface of the brain, and subdivide into short arterioles which give rise to a high density of capillaries. This vascular network supplies the nerve cells with the essential nutrients. A constant blood supply is maintained by the vascular network through the autoregulation function described below. Autoregulation is achieved by the vasodilation and vasoconstriction of smaller arteries and arterioles in the cerebral vasculature, which give rise to changes in the cerebral vascular resistance. The mechanisms that drive the constriction and dilation of these vessels can be metabolic, myogenic and/or neurogenic, which are described further in detail below.

2.1 Autoregulation Mechanisms

Homeostasis refers to the body's maintenance of constant conditions in the internal environment. All tissues and organs in the body perform functions to maintain these constant conditions. The circulatory system is one of the major systems that works to sustain homeostasis.

The blood circulation in the body enables each tissue or organ to control its own local blood supply in relation to its metabolic needs. This is sometimes called *Autoregulation*. When refereing to cerebral circulation, autoregulation refers to the capacity of cerebral blood flow (CBF) to remain constant despite changes in the arterial blood

perfusion pressure. It is a homeostatic mechanism that ensures adequate blood perfusion to the cerebral mass. Without autoregulation, CBF increases or decreases with changes in arterial pressure, which may result in cerebral edema or ischemia. Respectively, the local control of blood flow can be divided into two mechanisms: acute control and long-term control.

Acute control is achieved through local vasodilation and vasoconstriction of small arteries, arterioles and precapillary sphincters occurring within seconds to minutes. For example, an acute increase in arterial blood pressure results in immediate increase in blood flow. This blood flow decreases back to normal level within a minute even though the arterial blood pressure is still elevated. This is called *Autoregulation*. Long-term control represents the slow changes in blood flow occurring over days, weeks or months. The developments carried out for this thesis research addresses only the acute control of blood circulation by the autoregulation function.

2.1.1 Metabolic Mechanism

The mechanisms of how the autoregulation function is regulated are not completely understood; however, it is most likely related to the responsiveness of the small arteries and arterioles to the concentrations of various chemicals in the blood [65]. When the arterial blood pressure is elevated, the blood flow delivers too much oxygen and nutrients to the tissues. The nutrients cause the vessels to constrict resulting in an increase of vasculature resistance, which forces the blood flow to return to its normal level despite the elevated pressure. The metabolic regulation can be induced by the concentration of the different chemicals in the blood, which are coupled with the cerebral metabolism and local increase of neuronal activity.

2.1.1.1 Chemical Regulation

The different components of the blood have major effects on the cerebral circulation. The main components are oxygen (O_2), carbon dioxide (CO_2) and blood pH[1].

CO_2 and hydrogen ions (H^+) have a relaxant effect on the cerebral vascular muscle, which results in changes in the vascular resistance, and consequently, CBF [55]. The effect of CO_2 increase on pial arterioles depends on the vessel size, where the increase produces a greater percentile increase in the calibre of small vessels compared to larger vessels. This may be explained by the fact that during moderate CO_2 increase, the dilator effect of CO_2 in larger vessels is attenuated by vasoconstriction induced by increased

[1] pH: a measure of the acidity or alkalinity of a solution.

activity of adrenergic fibres[2]. Hydrogen ions have a direct relaxant effect on cerebral vascular muscle. Several mechanisms may explain this relaxant effect. The interactions of H^+ and Ca^{2+} are suggested as a potential mechanism, where the increased Ca^{2+} concentration inhibits pial arteriolar dilation caused by acidosis [55]. The magnitude of the response as a result of CO_2 changes varies in different regions of the brain. Increases in blood flow are more marked in cerebral gray matter than in white matter [55].

O_2 generally has a constrictive effect on the cerebral vascular muscle. Arterial hypoxia[3] induced by inhaling gas mixtures with low O_2 concentration results in pial arteriolar dilation. Increases in the oxygen partial pressure (PO_2) levels above normal induce modest pial arteriolar constriction. The mechanism by which tissue hypoxia leads to pial arteriolar vasodilation is not fully understood. One hypothesis is that the response is mediated by the release of adenosine, which is a strong vasodilator of pial arterioles. Other potential mediators are K^+, H^+, and prostaglandins. The response to arterial hypoxia is more marked in the gray matter than white matter. In contrast to effects in other vascular beds, hypoxia appears to affect CBF primarily by local mechanisms rather than reflex mechanisms [55]. Changes in cerebral metabolism during hypoxia may influence the hyperemic[4] response. In humans, arterial hypoxia causes no change in cerebral O_2 consumption. In dogs, mild arterial hypoxia causes increase cerebral O_2 consumption [55]. Prolonged hypoxia may result in different effects than acute hypoxia of comparable magnitude. This is because the concentration of HCO_3^- in the cerebral spinal fluid (CSF) decreases during chronic hypoxia, which results in complex changes in CBF that can occur during prolonged exposure to high altitude. Initially there is an increase in CBF, which later returns to a normal value because of an increase of HCO_3^- in the CSF resulting in cerebral vascular vasoconstriction. Hyperoxia[5] induced by inhalation of 100% O_2 in humans produces mild cerebral vasoconstriction, while inhalation of 100% O_2 at 3.5 atm in humans causes severe cerebral vasoconstriction [55].

The small arteries and arterioles in the cerebral vascular system can be assumed to be responsive to the concentration of oxygen in the venous blood. This is possible because arteries and veins tend to to run side by side. Therefore, the venous concentrations may regulate arterial resistance by release and diffusion of regulatory substances [65].

[2]Adrenergic fiber: a nerve fiber of the autonomic nervous system that releases norepinephrine.
[3]Hypoxia: insufficient levels of oxygen in blood or tissue.
[4]Hyperemia: an increase in the quantity of blood flow to a body part; engorgement.
[5]Hyperoxia: a higher than normal oxygen tension.

2.1.1.2 Cerebral Metabolism

The brain depends heavily on a continuous supply of blood flow because of its high metabolism. Therefore, there is a tight coupling between CBF and cerebral metabolism. Reductions in the CBF equal to 34%-60% of the normal resting value results in cerebral function disturbances. However, measurements of total CBF during various activities, such as intense mental activity, exercise, apprehension and sleep, showed a reasonably stable level of blood flow [55]. This result does not agree with the vascular physiology principle, where functional activity of tissues and organs result in appropriate increases in their blood flow. However, instead of increases in *total* blood flow, increases in *local* blood flow during increased activity of parts of the brain were observed [55]. There is a close relationship between regional CBF and the activity of areas of the cerebral cortex. This was supported by the correlations between blood flow and electroencephalographic (EEG) activity. The EEG frequency is related to the metabolic rate of the brain. However, the local metabolic rate increases are usually not sufficient to increase the total CBF. This is because these local increases in CBF are considered to be too small.

The changes in cerebral function and metabolism may alter CBF by reflex mechanism or by vasodilator metabolites [55]. The reflex mechanisms hypothesis is based on the assumption that active neurons release signals to adjacent pre-capillary vessels through astrocytes[6] [102]. Astrocytes are considered to be the pivotal mediators between the neurons and brain microcirculation providing a link between the neuronal activation and vasodilation. Astrocytes detect the level of glutamate-dependent synaptic activity and then signal to adjacent cerebral vessels to cause vasodilation. Another hypothesis is the release of vasodilator metabolites from active neural cells. The metabolites are presumed to reach the blood vessels by diffusion, which will have a direct relaxant effect on the vascular wall. The vascular muscle tone of the pre-capillary vessel is assumed to be constantly dependent on the metabolites' concentration. Several metabolites are suggested to be the mediation of the coupling between the CBF and metabolism. These include adenosine, potassium ions (K^+), hydrogen ions, oxygen and carbon dioxide (see Chemical Regulation section above) and calcium ions (Ca^{2+}) [55].

2.1.2 Endothelial Nitric Oxide Synthase (eNOS)

The endothelium-derived factors may be of importance to cerebral autoregulation. Some studies show that endothelial cells may cause relaxation of the vascular smooth muscle through the release of an endothelium-derived relaxing factor. Studies in vitro suggest that the endothelium may function as a pressure transducer by releasing or suppressing myogenic factors [36]. The endothelium may also act as a flowrate transducer

[6] See Glossary

by sensing changes in shear stress and releasing factors that modulate vascular smooth muscle tone.

Nitric oxide (NO) plays an important role in vascular autoregulation mechanism. NO diffuses into the vascular smooth muscle from the endothelium, resulting in vasodilation as required. NO is formed by nitric oxide synthesis in the endothelium, called eNOS. The eNOS activity is modulated by calcium released from the subsarcolemmal storage sites in response to the binding of certain ligands to their receptors. Another important mechanism regulating the release of NO is shearing forces acting on the laminal surface of vascular endothelium. The increase in flow velocity stimulates calcium release and increased eNOS activity [36]. Arterial regions that experience low wall shear stress correspond to regions with impaired eNOS signalling in the endothelial cells. This results in reduced amounts of NO. It is believed that an increase in the arterial blood pressure causes smooth muscle cells to contract, while an increase in wall shear stress causes the arterial walls to dilate [27, 105].

2.1.3 Myogenic Mechanism

The myogenic theory is based on the observation that a sudden stretch of blood vessels results in the smooth muscle cells of the wall to contract. When the arterial blood pressure is elevated, the increase in blood flow stretches the vessel and produces a constriction in the vessel's wall. This causes an increase in vasculature resistance, which forces the blood flow back to its normal condition.

A rapid change in the transmural pressure alters the state of the actin[7] and myosin[7] filaments in the smooth muscle cells which results in a change in the vessel's radius [44]. The transmural pressure determines a hoop stress which changes the calcium flux across the smooth muscle cell membrane via the Ca^{2+} ion channels. The variations of the Ca^{2+} concentration are coupled to the variation in cross bridge links to the myosin light chain (MLC[7]) kinase[7].

The increase in the cytosolic calcium concentration results in the crossbridges formation between overlapping myosin and actin filaments. The calcium first combines with calmodulin[7]. The combination then activates the MLC kinase, which as a result phosphorylates the myosin. Actin interacts with the phosphorylated myosin to form crossbridges and develop stress. This results in smooth muscle cell contraction. The decrease in the cytosolic calcium concentration results in dissociation of calcium and calmodulin from the MLC kinase, which becomes inactive. As a result, the myosin dephosphorylates causing muscle relaxation.

[7]See Glossary

One of the factors that favors the myogenic mechanism hypothesis is the rapidity of the autoregulation response. Vasodilation is initiated within few seconds of the change in pressure, and is completed within 15-30 seconds. However, if cerebral autoregulation depends mainly on the myogenic mechanism, cerebral vessels would be expected to constrict in response to intravascular pressure increases, even under conditions where further constriction would impair the CBF autoregulation. One suggestion is that the myogenic mechanism may dominate the autoregulation response under circumstances where the metabolic mechanism is weak, such as low cerebral metabolism [36], or it may be a way of filtering out effects of sharp changes in perfusion pressure.

2.1.4 Neuronal Regulation

In addition to the main regulation systems described above, the nervous system provides additional control to the circulation. However, the neuronal regulation contributes to the more global functions of circulation such as providing rapid control of arterial pressure [47]. Cerebral vessels are highly innervated[8]; however, neuronal regulation of CBF has been highly controversial.

The autonomic nervous system consists of the sympathetic and parasympathetic parts. The most important for the regulation of the circulation is the sympathetic nervous system. The parasympathetic contribution to the circulation is mainly the regulation of the heart function[47, 55]. Cerebral vessels receive sympathetic innervation primarily from the superior cervical ganglion. Large and small cerebral arteries, pial arteries, and veins receive sympathetic innervation. The innervation density varies in different parts of the brain. Innervation in the internal carotid system appears to be more extensive than in the vertebral system [55] (see below for baroreceptors in the internal carotid arteries). The electrical simulation of sympathetic nerves constrict pial arteries. The reduction of the arteries' diameters was only 7-12 % in cats and confined primarily to large vessels [55]. Intense electrical simulation of sympathetic nerves under normal conditions showed little or no effects in cats and dogs, and modest effects in rabbits and monkeys [55].

There is strong evidence that sympathetic nerves protect cerebral vessels under sudden increases in arterial pressure [55]. Increases in blood flow during severe hypertension and the sympathetic simulation protective effects are more pronounced in gray matter than white matter. The mechanisms that result in the increased cerebral vascular responses to sympathetic stimulation during acute hypertension are not clear.

As mentioned above, one of the most important functions of the nervous regulation of circulation is its capability to cause very rapid increases in arterial pressure, which

[8]Innervation: the supply of nerves and distribution of nerve fibers to an organ or body region.

is controlled by the baroreceptor reflex. The baroreceptors are located in the walls of the large systemic arteries and they are extremely abundant in the walls of each internal carotid artery slightly above the carotid bifurcation (called the *carotid sinus*), and the wall of the aortic arch. When the baroreceptors are stretched as a result of a pressure rise, they transmit signals into the central nervous system, where feedback signals are then sent back through the autonomic nervous system to the circulation to reduce arterial pressure to the normal level.

Similarly to the baroreceptor reflex, the chemoreceptor reflex is associated with the pressure control system. Chemoreceptors are chemosensitive cells sensitive to hypoxia, carbon dioxide excess, or hydrogen ion excess located in the bifurcation of each internal carotid arteries and adjacent to the aorta. Stimulation of the carotid chemoreceptors produces acute increases in arterial pressure. When there is a fall in arterial pressure below a critical level, the chemoreceptors become stimulated due to a drop in blood flow, and therefore, lower availability of oxygen and excess of carbon dioxide and hydrogen ions. The chemoreceptors transmit signals to the vasomotor center, this elevates pressure.

In this thesis, only the metabolic and myogenic mechanisms are modelled and tested to examine their affects on maintaining the autoregulation function by the cerebral vasculature. The exact effects of neuronal regulation of CBF are still debateable and more research is required to understand its function fully.

2.2 Autoregulation Characteristics

2.2.1 Autoregulation Limits

The cerebrovascular resistance changes through the dilation and constriction of cerebral vessels, mainly arterioles, to adapt to changes in the perfusion pressure in order to keep a relatively constant CBF delivery. The lower and upper limits of CBF autoregulation do not occur at fixed points of the arterial blood pressure. Many factors may affects these limits, such as sympathetic nerve activity, arterial CO_2 tension, chronic arterial hypertension, and various pharmacologic agents [36]. In the conditions of extreme hemorrhage, CBF is maintained more effectively compared to the blood flow in other organs of the body. Cerebral arteries and arterioles dilate as the perfusion pressure decreases to keep CBF constant until a critical level of perfusion pressure (lower limit of autoregulation), where the CBF decreases with further reductions in pressure. The lower limit of autoregulation (LLA) for CBF is between 50 and 60 mmHg. However, maximal arteriolar dilation is observed at 40 mmHg [36]. This indicates that the autoregulation limit is reached before maximal dilation. Reduction of cerebral perfusion

pressure below the LLA results in hypoperfusion of the brain. However, this results in an increase in the oxygen extraction from the blood flow. Autoregulation during increases in the cerebral perfusion pressure results in vasoconstriction in not only the arterioles but also the larger cerebral vessels [36].

The autoregulation curve by Guyton [47] shows that autoregulation is active between 75 and 175 mmHg. Gao et al. [43] reviewed autoregulation studies focusing on the lower and upper limits. The summarised data give 50 to 145 mmHg as the values for the LLA and ULA, respectively. The differences in defining the lower and higher limits of autoregulation may be due to the different methods of measurement.

2.2.2 Autoregulation Plot Flatness

Many studies examined autoregulation to identify its characteristics. A substantial review of these studies were carried out by Panerai [98]. Some studies assessed the autoregulation curve based on each subject's data examined individually, while others assessed the autoregulation curve based on pooled data for groups of patients. The former assessment is preferred because in general, each subject may have a different autoregulation curve based on their own control. Many studies provided in Panerai's review show that the autoregulatory curve can shift from one individual to another based on changes in metabolism, carbon dioxide partial pressure (PCO_2), hypertension and other factors. The variability in individual static autoregulation curves can be observed in the examples provided by Strandgaard's study [114] shown in Figure 2.1. These autoregulation curves show that the autoregulation region is flat with no slope. Pooling data for a group of patients can produce inaccurate representation of the autoregulation curve as demonstrated in Figure 2.2. The resultant averaging of the data in Figure 2.2 produces a slope in the autoregulation region, which is the outcome reported by some studies. However, the autoregulation curve is a population characteristic. The population autoregulation curve can be assessed more accurately based on the average CBF at each perfusion pressure, which would result in a flat autoregulation region.

2.2.3 Steal Phenomena

Intracerebral steal is a hemodynamic phenomena where the blood intended to be delivered to a particular part of the brain is re-routed for another part. When the local vasculature dilates, its resistance decreases and a redistribution of the blood flow between the different parts of the brain takes place. The blood flow is *stolen* to the disadvantage of one part and to the advantage of other parts, where the disadvantaged area may experience an ischemia.

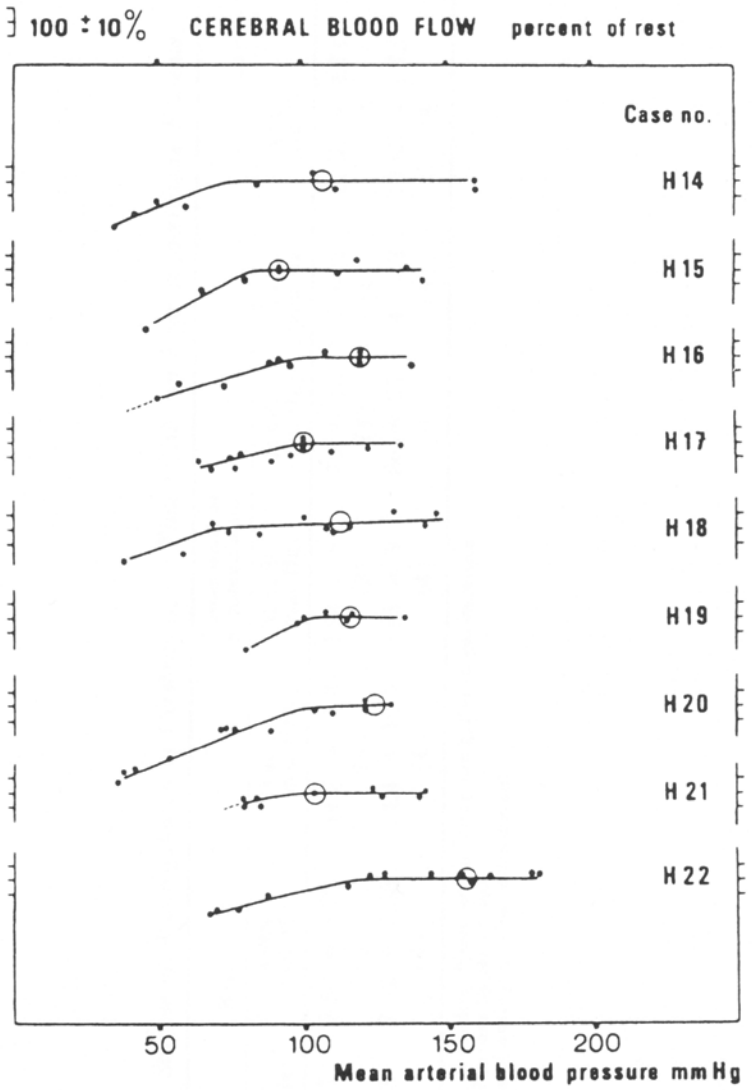

Figure 2.1 Individual curves of CBF autoregulation from nine patients with a formerly severe hypertension by Strandgaard [114].

The intracerebral steal phenomena has been demonstrated in pathological conditions. There are several mechanisms that may result in the intracerebral steal phenomena. It may occur in patients with arterio-venous malformations. In other cases, a shift of blood supply to other cerebral areas may be experienced because of a drop in local perfusion pressure below a lower limit compatible with an efficient cerebral autoregulation. The intracerebral steal phenomena becomes effective when the local autoregulation is already compromised by subtle changes in vascular reactivity. Cerebral vessels cannot always alter their diameter to adapt to changes in the systemic pressure, or to changes in other vascular areas of the brain. Therefore, cerebral ischemia can take place even in absence of arterial occlusions [144] as a result of the steal phenomena.

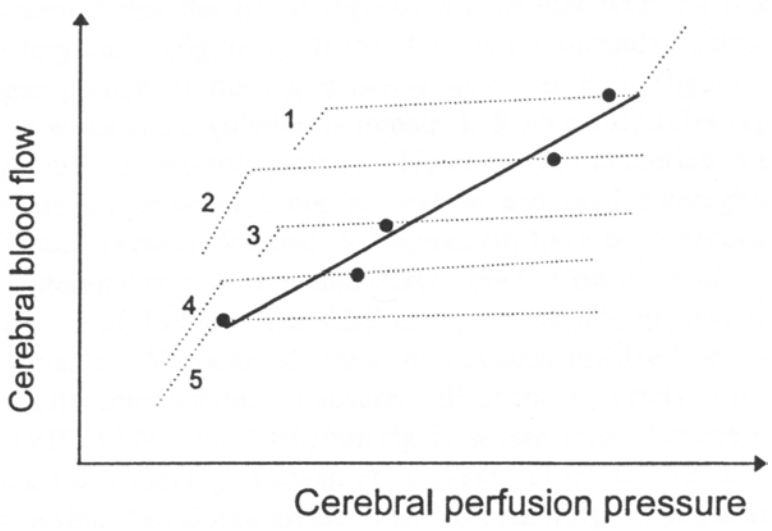

Figure 2.2 Pooling a number of measurements from a group of subjects with normal static autoregulatory curves (1-5) may produce misleading results due to individual variability [98].

2.2.4 Hypertension

Hypertension is a medical condition in which the blood pressure is chronically elevated in the arteries. There are many effects that are generated as a result of prolonged hypertension such as an aggravation of atherosclerosis and facilitating aneurysm development.

In the hypertensive patient with no neurological deficits, the resting CBF value is the same as in healthy individuals. This is because in both cases, the CBF is autoregulated [114]. However, the autoregulation curve in hypertensive patients demonstrates a horizontal shift to higher blood pressure levels. The lowest tolerated blood pressure at which symptoms develop is higher in hypertensive patients than healthy individuals, where the lower limit of autoregulation is on average 120 mmHg [115] as demonstrated in Figure 2.3. This is much higher than the lower limit in healthy individuals. The shift may be caused by hypertrophy[9] of the arteriolar walls.

The degree of CBF autoregulation adaptation is correlated with the severity of hypertension. When the blood pressure increases, the arterioles constrict to maintain same CBF value. The failure of autoregulation beyond the upper pressure limit may provoke arteriole spasm at very high blood pressures, which causes critical hypoperfusion resulting in brain tissue ischemia [115].

[9]Hypertrophy: the increase of the size of an organ or in a select area of the tissue.

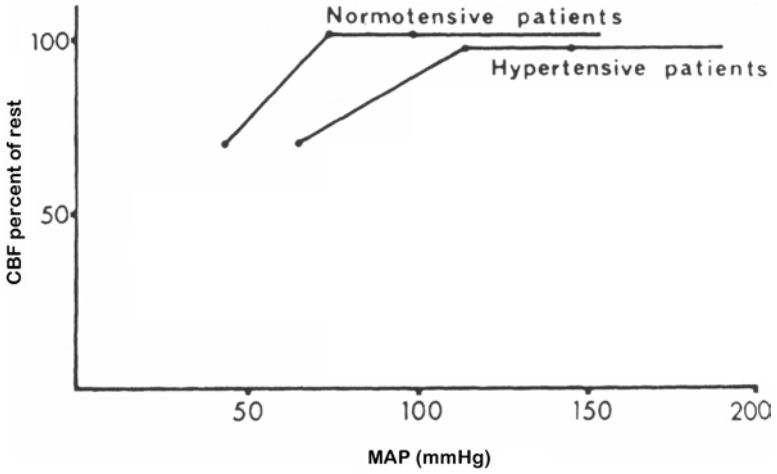

Figure 2.3 The autoregulation curve in healthy and hypertensive patients [114].

2.2.5 Aging

As we age, the vessels in our bodies become stiffer. The ageing process may affect the cerebral vasculature responsiveness and the autoregulation function. Age may also affect the response to CO_2 concentration increase in the cerebral circulation. CBF in newborn lambs and dogs respond to changes in CO_2 as vigorously as in adult animals. However, responsiveness in newborn monkeys is reduced. A small decrease in CBF responsiveness was observed with increasing age in humans [55].

In terms of CBF autoregulation, studies in rats and humans reviewed by Edvinsson et al. [36] demonstrated that aging results in the shift of the lower limit of autoregulation to higher level of arterial pressure. This may be caused by a decrease in distensibility after atrophy in the cerebral arterioles' walls. The shift of the lower limit of autoregulation may induce episodes of cerebral ischemia without symptoms, which could result in the development of vascular dementia[10] [36].

2.3 Measurement of Cerebral Circulation

The methods to measure the cerebral blood flow have developed over the years to advanced non-invasive continuous measurement methods. There are many different techniques that has been used or are currently used to measure the CBF and autoregulation. Only the most common methods are described in detail in this section.

Autoregulation is not a physical quantity with directly measurable quantities. It is

[10]Vascular dementia: a type of dementia caused by problems in the supply of blood to the brain.

rather a characteristic of the vasculature derived from complex relationships between several variables. The cerebral autoregulation can be evaluated by measuring alterations in CBF as a result of steady state changes in arterial pressure (static), or in response to a rapid change in blood pressure (dynamic). Static measurements evaluate the efficiency of the autoregulation function in response to changes in arterial pressure but do not address the time taken to change the cerebrovascular resistance which will force the CBF back to its normal value. Dynamic measurements evaluate the responsiveness of the cerebro-vasculature.

2.3.1 Arteriovenous Oxygen Difference

The arteriovenous oxygen difference method is based on the assumption that the cerebral metabolic rate of oxygen consumption ($CMRO_2$) is constant [115]. The CBF can be calculated from the cerebral arteriovenous oxygen difference defined by

$$CBF = \frac{CMRO_2}{CaO_2 - CvO_2} \tag{2.1}$$

where CaO_2 and CvO_2 are the arterial and venous oxygen concentrations respectively [115]. Under local anaesthesia, a catheter is placed in the jugular bulb from an arm vein under fluoroscopic control. Another catheter is placed in the brachial or femoral artery and an intravenous drip is set up in an arm vein. Oxygen content in arterial and jugular venous blood is found through spectrophotometric measurement of the oxygen saturation of the hemoglobin. Blood samples are taken at various blood pressure levels to find the arterial and venous oxygen content. This method was used in the past to evaluate static autoregulation response [93, 114, 115].

2.3.2 Transcranial Doppler

Transcranial doppler (TCD) is a technique used to measure the blood flow velocity. A high-pitched sound wave from the ultrasound probe is emitted, which then reflects off different materials then get measured by the same probe, as in Figure 2.4. A specific frequency is used and the speed of the blood flow in relation to the probe causes a phase shift. The velocity of blood flow is recorded electronically by directly correlating the frequency change with the speed of blood. Because the the bones of the skull may block the ultrasound transmission, TCD is performed through skull regions with thinner walls, such as the temporal region. The TCD method has been used to measure relative changes in the cerebral blood flow velocity in the MCA, which reflects the relative changes in CBF. This method has the advantage of being non-invasive and able

to perform continuous measurement of the autoregulatory response.

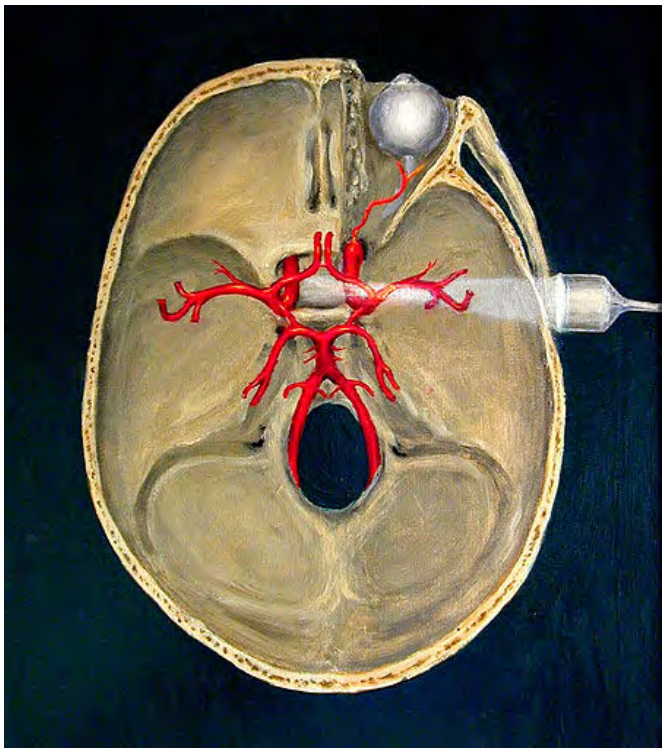

Figure 2.4 The transcranial doppler technique.

The TCD method has been used to determine the static and dynamic autoregulatory responses [36, 91, 98, 119]. A study by Tiecks et al. [119] compared the static and dynamic autoregulation responses using TCD and found a good correlation between the two methods in individuals with normal and impaired autoregulation functions. Static autoregulation was examined by the use of phenylephrine to increase the blood pressure. Dynamic autoregulation was examined by the use of the thigh cuff technique, where a rapid deflation of a blood pressure cuff around one thigh was used as a stimulus.

2.3.3 Magnetic Resonance Angiography

Magnetic Resonance Angiography (MRA) is a type of magnetic resonance imaging (MRI) scan that uses a magnetic field and pulses of radio wave energy to provide pictures of blood vessels inside the body. MRA is now considered one of the most advanced methods to measure CBF. The two main types of MRA are time-of-flight (TOF) and phase contrast (PC). The description of how MRA techniques work is not provided in this thesis but can be found easily in the literature [18].

The main advantage of MRA over other techniques is the ability to determine blood flow in all of the major cerebral vessels of the CoW non-invasively. Other techniques

which has been used in the past do not provide quantitative blood flow in individual vessels. For example, TCD provides only blood velocity information in some accessible arteries at the base of the brain, such as the MCA. This is because the ultrasound transmission needs to be in a suitable angle in relation to the blood flow direction, in addition to the need of a thin skull wall, such as the temporal region.

Other techniques that have been used to measure CBF include the indicator-dilution method, where a gas such as xenon 133 (^{133}C) is inserted into the blood stream, near infrared spectroscopy, PET, SPECT, and thermal diffusion flowmetry [36, 55].

Chapter 3

Literature Review

3.1 Introduction

Models of cerebrovascular hemodynamics have to address two main challenges: they must efficiently represent all major physiological mechanisms that take place in the cerebral vessels; and they should be patient-specific in terms of geometry and pathological conditions. There is a significant body of literature on the field of cerebrovascular hemodynamics. Different aspects of hemodynamics have been identified, investigated, and simulated.

In this chapter, these aspects are studied and summarised in three sections: modelling of the cerebral vasculature system, autoregulation modelling, and oxygen diffusion into tissue. Owing to the nature of cerebrovascular hemodynamics modelling, there is some overlap between these sections. These particular aspects of cerebral hemodynamics are reviewed here because of their association with the research topic of this thesis. Several aspects of the reviewed models are adopted in the current research.

3.2 Vascular Models

The cerebrovasculature can be roughly divided into two parts: the CoW, and peripheral vascular beds. The CoW vasculature is identified by all vessels described in Sections 1.2.2.2 - 1.2.2.4. It is important to capture the main CoW vasculature and its blood distribution because of the variations between individuals in its geometry. A peripheral vascular bed is defined as all the vessels branching from a CoW efferent artery down to, and including, the capillaries. The arterial tree representing the vascular bed is significant because of its role in representing the autoregulation. This is described further below.

3.2.1 CoW Models

The majority of published cerebrovascular models are zero dimensional (0D) or one-dimensional (1D). This is due to their great advantage of simplicity and because fewer computations are required compared to two-dimensional (2D) and three-dimensional (3D) models. The models are created for different aims. Some models only capture the basic CoW geometry while others' purpose is to examine a specific cerebrovascular abnormality or disease.

One of the earliest works of modelling the CoW is the 0D non-linear mathematical model by Hillen et al. [57, 58]. The initial geometry of the model includes only part of the CoW (VA, BA, PCA, PCoA and ICA) [57]. The hemodynamics are represented using two non-linear partial differential equations for the pressure and velocity of each segment. These were based on conservation of mass and conservation of momentum equations. The elastic properties of the vessel walls are modelled using a linear relationship between pressure and cross-sectional area. The model examines the flowrate variations in PCoA as a result of changes in VA and PCoA diameters. The model was modified in later work to represent the whole CoW [58]. The efferent arteries (ACAs, MCAs and PCAs) are terminated by resistance blocks representing the arterial branches and capillary network. The values of peripheral resistances are determined using a fixed ratio of 6:3:4 for ACA:MCA:PCA and imposing a total CBF of $12.5cm^3s^{-1}$. This is roughly inversely proportional to the brain masses perfused by corresponding vessels.

Hudetz et al. developed a simple linear mathematical model that describes the regional flowrate and tissue oxygenation for the system of cerebral vessels. The latter consists of main CoW arteries, coupled peripheral arteries at the end of main out-flowing arteries, and anastomotic connections (pial arteries) between distal ACAs, MCAs, and PCAs [59]. The model also includes an autoregulation mechanism based on local control of pressure and flow in the pial and intra-cerebral arteries, respectively. However, no detailed description of the autoregulation mechanisms, or CVR calculation is given. The oxygen partial pressure (PO_2) is calculated using a Krogh cylinder model, described further in Section 3.4. The model is used to study flowrates in the case of MCA occlusion, with diameter variations of the pial arteries.

Zagzoule et al. created a non-linear mathematical model of cerebral circulation [140]. The stenoses of ICAs were analysed using the model; however, the the model did not take into account any form of autoregulation. The cerebral vasculature includes the arterial, microcirculation and venous systems. Zagzoule et al. simulated the network by the use of unsteady fluid mechanics equations including conservation of mass, conservation of momentum, and the tube law. These equations form a first order quasi-linear hyperbolic system. The tube law describes the relation between the transmural pressure

and the cross-sectional area of a vessel, which produces a purely elastic relation. This model was used by Cassot et al. [19] to simulate the effect that the diameter of ACoA has on cerebral hemodynamics in the case of ICA disease. In later work, Cassot et al. [20] created a linear model with a small number of parameters to reduce the complexity of the model and minimise the amount of computations required. The model assumes a linear relation between the blood flowrate in a vessel and the pressure gradient. It also applies the conservation of mass principle at every node of the network.

Similar models based on conservation of mass, conservation of momentum, and lumped peripheral impedances[1] were also created. The algorithms of these models are similar but they have different purposes. Basing their work on Cassot and Zagzoule's model, Viedma et al. examined a wider range of arteries supplying the cerebral mass [137]. The 1D unsteady periodic pulse flow is modelled in the CoW and the collateral circulation between ICA and external carotid artery, through the periorbital artery. TCD measurements are used as input conditions of the model. Charbel et al. investigated the possibility of identifying patients in whom the balloon occlusion test would not be tolerated [25]. The study compares a patient-specific blood flow computer model with the current evaluation of a balloon occlusion test. Patient-specific parameters were measured using phase contrast MR angiograms.

In the work of Lodi and Ursino [79], the CoW was represented in part of a model that analysed the hemodynamic effect of cerebral vasospasm[2]. They divided the cerebral arterial hemodynamics into with-spasm and without-spasm territories, with collateral circulation between them. The overall cerebral hemodynamics are represented using a hydraulic model (Figure 3.1). The hydraulic model uses Ohm's law for pressure drop along a vessel as a function of blood flowrate, and equations for elasticity of the vessel through a lumped parameter compliance. Autoregulation is reproduced by assuming that the pial artery compliances are actively modulated by changes in local CBF. The dependence of compliance on flowrate includes a sigmoidal dimensionless static relationship and first order low-pass dynamics with a time constant. This work was later developed to study the CO_2 cerebral hemodynamics response in patients with ICA occlusion [131]. It also takes into account the CoW ability to redistribute blood to where it is needed most, as well as a distinction of the anterior, middle, and posterior cerebral arteries.

Despite the fact that most authors use a linear pressure-flowrate relation in their models, this relation is in fact non-linear. There are two main reasons for this. First, the physical nodes in the CoW cause flow disturbances, which result in velocity development along outgoing branches. Second, tortuosity of vessels gives rise to centripetal forces,

[1] See Glossary

[2] Vasospasm: a sudden constriction of a blood vessel that reduces the blood flow.

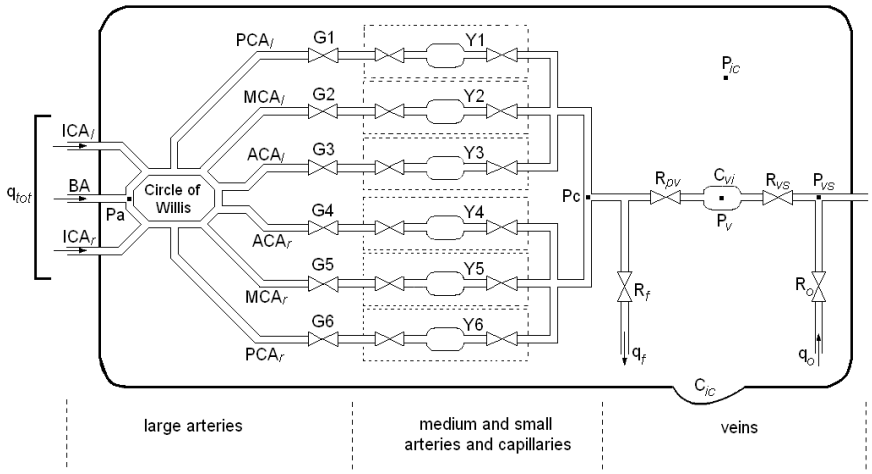

Figure 3.1 Hydraulic model by Ursino et al. [79]. CBF enters skull at systemic arterial pressure of P_a. Each of the six efferent arteries is characterised by a hydraulic conductance (G).The sections downstream of the large arteries include pial circulation and intra-cerebral arterioles and are described by hydraulic admittance (Y). P_c is capillary pressure, R_{pv} is proximal venous resistance, C_{vi} is intra-cranial venous compliance, R_{vs} is terminal venous resistance, P_v is cerebral venous pressure, and P_{vs} is pressure at dural sinuses. The rates of CSF formation and outflow are q_f and q_o, respectively. R_f is the CSF formation resistance and R_o is the CSF outflow resistance.The whole compartment is enclosed in a rigid space where C_{ic} represents the craniospinal storage capacity and P_{ic} is the intra-cranial pressure.

which result in secondary flows in plane perpendicular to the main stream. Cieslicki et al. investigated the flowrate and pressure disturbances in a physical model of the CoW [26]. Cieslicki states that non-linearity of flow characteristics of the vessels is mainly caused by tortuosity of the vessels as well as the small length of vessels in relation to their diameters. These non-linearities are analysed and modelled. A vascular phantom was prepared based on microsurgical antomy of a large number of specimens of the CoW. The phantom was used in an experiment shown in Figure 3.2. Here, the inlet pressure was secured within a specific range of normal values; outlet pressure is maintained by six small reservoirs at the end of out-flowing vessels; and pressure at various places in the CoW is monitored using pressure transducers. The non-linearities are captured using simple formulae defining the non-linear resistance of vessels. In the model, neither the compliance nor the autoregulation mechanism of peripheral arterial beds was considered. The formulae created were used in the model utilised in this thesis research as described in Section 6.2.

One of the latest CoW models was created by Alastruey et al. [3, 4]. 1D equations of pressure and flow wave propagation are used to model the hemodynamics in the CoW. Again, conservation of mass and conservation of momentum equations are used to model all arteries supplying the cerebral mass from the aorta to the CoW. The model ignores the peripheral arteries' autoregulatory mechanisms such as vasodilation, vaso-constriction, and wall remodelling. The peripheral impedances are assumed constant in all simulations. The model is used to study the collateral ability of the complete CoW

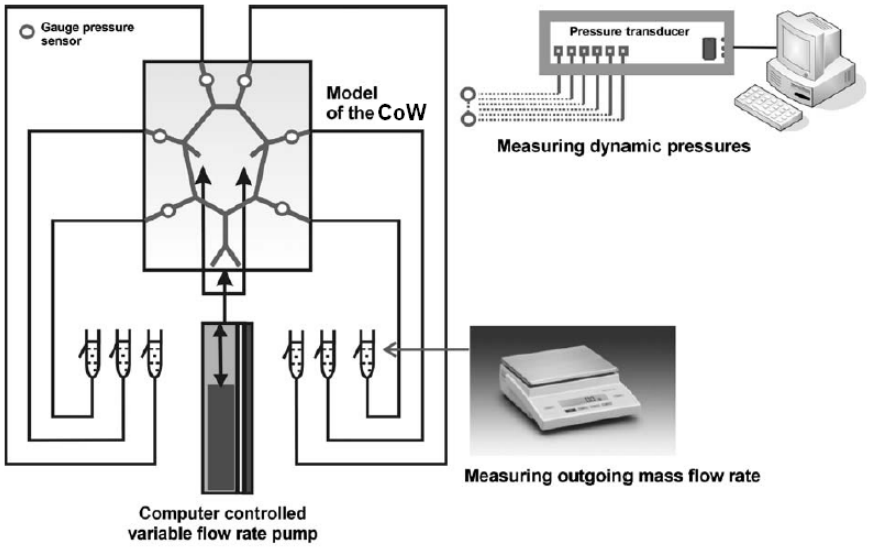

Figure 3.2 The experimental set up for measuring pressure and flowrate in the phantom [26].

and its most frequent anatomic variations under normal or occluded afferent artery conditions. This model is similar to the 1D model by Kufahl et al. [74], where the efferent vascular tree is also terminated by an impedance of two resistances and a compliance.

Fewer researchers have developed 2D and 3D models of the CoW because of the computational cost and complexity. Ferrandez et al. [30, 38] created a 2D time-dependent model of the CoW with an autoregulation function. The model shows the important relationship between the geometrical variations of the CoW and the peripheral resistances. Equations of conservation of flow and conservation of momentum in cartesian coordinates are used. These equations are solved using the commercial computational fluid dynamics (CFD), Fluent. Peripheral resistances of the CoW are implemented using porous blocks. The porous block permeability defines how easily the flow travels through the porous block for a specific pressure gradient across the block. Autoregulation is represented using feedback mechanisms where a standard proportional integral (PI) controller is used. A relation between the mass flux through the artery outlet and permeability is defined to dynamically alter the effective peripheral resistance. This resistance is limited by upper and lower bounds using a sigmoidal function. The 2D model is used to simulate different common abnormalities in the CoW under the condition of ICA stenosis.

Three dimensional models provide better definition of the geometry and might be able to account for deformations of the arterial wall. However, they are computationally very expensive. Cebral et al. created patient-specific 3D numerical models of cerebral hemodynamics [21, 22]. The models are used to predict blood flow distribution in CoW during temporary occlusion of an ACA after a stent implementation in the common

carotid artery. The models neglect the effect of autoregulation by having no change in the distal flow resistances. For computation, realistic arterial geometrical models are reconstructed from contrast-enhanced MR angiography images. Unconstructed grids based on tetrahedral elements are then generated. Physiologic boundary conditions are derived from phase-contrast MR measurements of blood flow velocities and the Navier-Stokes equations are then solved numerically. Owing to the difficulty of measuring flowrates in all CoW efferent vessels, outflow boundary conditions are derived using models of the distal vascular bed. The vascular bed is based on the assumption of self-similarity of arterial bifurcations. This representation implies that the ratio of areas and lengths of each daughter branch to the parent branch is constant over all bifurcations. This was later replaced by coupling the 3D finite element model to 1D flow models along arterial trees generated for each outflow boundary [23]. These arterial trees are generated using an image-based constrained constructive optimization method introduced by Karch et al. [63]. This arterial tree is described in detail in Section 3.2.2. The 3D models by Cebral et al. were also used for intra-cranial aneurysm simulations [24].

Moore et al. developed a 3D model that captures the cerebral hemodynamic autoregulation [88]. MR angiography scans are used to create a CAD model, which is then used to form a mesh of the CoW geometry. The porous block developed by Ferrandez et al. is adopted to model the vascular bed for all efferent arteries. Autoregulation is described by a simple feedback mechanism using a PI controller. The same autoregulation mechanism was adopted in this thesis research for the basic CoW model described in Chapter 4.

3.2.2 Arterial Tree Models

The branching pattern of the arterial system in the cerebral mass and its blood flow is of interest to the research carried out for this thesis. The aim was to reproduce the autoregulation behaviour that takes place at different levels and sizes of the vasculature. All of the autoregulation models reviewed consider a lumped parameter for the vascular bed downstream of the peripheral arteries of the CoW. Therefore, the myogenic and metabolic mechanism that take place in the vascular tree at different diameters of the vasculature are not considered.

General models of vasculature branching patterns are reviewed here. There are no specific models of the cerebrovascular tree in the literature. This might be due to having no major difference in the principles of branching vessels in all organs, or due to the difficulty of obtaining physiological data to support a model of cerebrovascular network. However, it must be taken into consideration that the density of the vasculature in the

cerebral mass is higher than other organs as a result of higher metabolic demand [47].

One of the earliest mathematical fractal models of the human arterial system based on realistic dimensions of the arterial tree was created by Avolio [9]. This was based on the anatomical branching structure of the arterial tree down to and including vessels of the order of 1 mm radius. The model was created due to the practical difficulties of obtaining a whole range of physical measurements in vivo. The systemic vasculature is divided into a multi-segment branching structure consisting of 128 arterial segments accounting for all the central vessels and major peripheral arteries. Peripheral branches are terminated with a specific resistance. Vessels are assumed as thin-walled uniform cylindrical tubes having internal viscous, elastic and inertial properties. Vascular impedance, and pressure and flow waveforms are determined at various locations in the system. The model exhibits the essential features of the physical system with respect to vascular impedance and spatial distribution of pressure and flow waveforms. However, circulation to the brain is considered up to the ICA only, which is terminated by a peripheral resistance. In a later work [7, 8], the role of input impedance spectrum of distributed vascular models is used to investigate hemodynamics concepts related to the branching nature of the arterial tree. The vascular models have random branching and fractal properties. The impedance spectrum for these models was found to be similar to that of anatomical systems even though the branching configuration is different. The research discussed in this thesis did not take wave propagation into consideration. This is due to the assumption that the autoregulation response is much slower than the cardiac cycle.

Zamir et al. analysed in depth the fractal properties of arterial trees over three decades. Only part of their studies are discussed here. In 1988, the arterial tree of a rat was casted and mapped [142]. A total of 1313 vessel segments in the arterial tree was divided into levels. The length and diameter of each segment is measured, and the distribution and averages of different levels are examined to determine the underlaying pattern of the branching process. It is established that the most common mode of branching is the dichotomous mode, where a parent vessel is divided into only two daughter vessels. A more in depth study was later carried on by Zamir, which was based on the tree structure of the right coronary artery of the human heart [141]. The study focuses on the geometrical aspects of the fractal properties, rather than the statistical aspects. Three main properties of the arterial bifurcations are established. These are the bifurcation index, the area ratio, and the power law index. The bifurcation index or asymmetry index γ is a measure of the relative relationship between the two daughter segments. A large number of arterial bifurcations have a mixed degree of asymmetry at all levels of the tree, including the depth of the tree which has been assumed to be symmetrical. The area ratio η is a measure of change in cross sectional area available to the flow as it progresses from the parent segment to

the two daughter segments. The η value is found to be highly mixed at all levels. The power law index k governs the fluid dynamic efficiency of the bifurcation and provides a relation between the vessel diameters. It is based on the requirement that the flowrate though the bifurcation junction satisfies the conservation law. If the value of k is 2, the square law is satisfied. This corresponds to a condition of zero expansion in cross sectional area. If the value of k is 3, the cube law is satisfied, which corresponds to minimum rate of energy expenditure. This is called Murray's law, which states that the cube of the radius of a parent vessel equals the sum of the cubes of the radii of the daughters [111]. The k value is found to range between the two values associated with the cube and square laws. It is clear that η and k are related to each other as they are both measures of expansion or contraction of the cross sectional area. Zamir suggest a distinction between a vascular tree that serves a metabolic function such as the heart and the brain, and one that serves a processing function such as the lung or the kidney.

Olufsen et al. developed a fractal structured tree [94] using the properties of smaller arteries analysed by Zamir. The fractal tree is used as a physiologically based boundary condition so that the arterial tree of the human body is truncated after few generations and the peripheral vasculature is replaced by this fractal tree. The non-linear model is able to predict blood flow and pressure at any position along the larger systemic arteries. The fractal tree is assumed as an asymmetric binary tree where the radius of the two daughter vessels is scaled by factors α and β. These are defined as functions of γ, η and k as defined by Zamir. In the whole of the fractal tree used, these properties are set to constant values. The model then uses a system of equations that calculates the root impedance of the fractal tree. In later work of Olufsen et al. [112], the concept of radius sub-ranges of vessels introduced by Zamir was adopted. Each sub-range has a different value of γ, η and k. This method of modelling the peripheral arterial tree was implemented in the present work, described further in Section 7.1.

Brown [15] created complex fractal branching networks similar to mammalian arterial systems, which terminate at the arteriolar level. The model examines systematically the effects of branching geometry on the input impedance spectrum in fractal-like networks of compliant tubes and focuses on effects of branch asymmetry. The input impedance represents dissipative properties of the system for the time-averaged components of pressure and flow. The networks are constructed from a discretized set of compliant circular vessels. The vessels' radii are dependent on the specified input and terminal vessels radii of 1 and 5×10^{-3} cm respectively. The model allows specification of branching geometry with the parent-daughter area ratio, and daughter-daughter asymmetry ratio. The created trees are modelled with different degrees of asymmetry.

Dokoumetzidis et al. developed a vascular fractal tree model for the transport and dispersion in the circulatory system [34]. The model describes the disposition of a

substance inside a tree-like fractal network using solute kinetics in the fluid as it flows through the system. The vessels in the network are assumed to be non-elastic tubes. As the total flow across a section of the entire network is constant, the vascular tree is reduced to a single 1D tube model based on scaling laws of the fractal structure (Figure 3.3). The total cross sectional area at subsequent levels increases because the tree is not area preserving (Figure 3.3 C). This results in a non-cylindrical tube which is simplified to a cylindrical tube using a geometrical transformation. The fluid velocity through the branching is kept constant by calculating a suitable length (Figure 3.3 D). This model simplifies the general structure of a vascular tree into a single 1D tube, which is suitable for modelling substance dispersion in the circulatory system, but not suitable for modelling autoregulation characteristics.

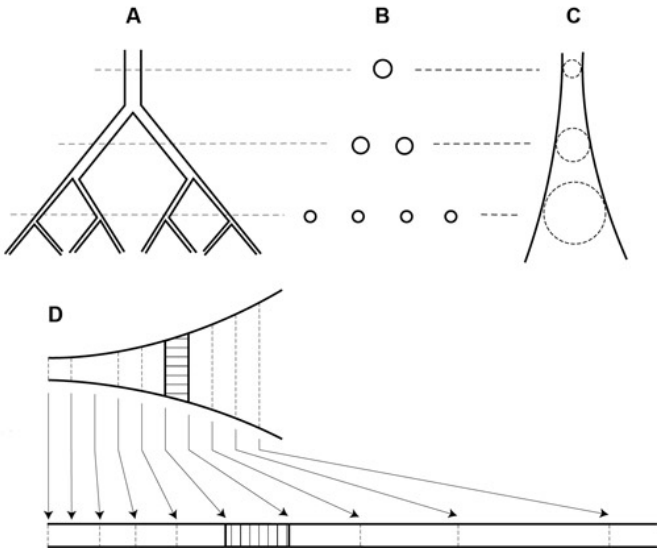

Figure 3.3 Dokoumetzidis et al. fractal simplification model [34]. A)Branching network. B)Cross sections at each level. C)Tree is replaced by a single non-cylindrical tube. The area of the cross section of the tube is equal to the total area of the cross sections of each level of the tree. D)Volume preserving transformation of non-cylindrical tube to a cylindrical one.

Karch et al. used a constrained constructive optimisation (CCO) method to generate a 3D arterial tree model of the human heart, taking into consideration the spatial organization of the tree [63, 109]. The tree is a dichotomous branching network of straight rigid cylindrical tubes with flow conditions controlled by Poiseuille's law. Growing the tree by CCO consists of two main steps: growth, and constrained optimisation. Growth is established by successively adding new terminal segments. Each segment connects a random point within a specific perfusion volume to an existing segment in the tree. This creates a new bifurcation along the existing segment. Constrained optimisation is carried out on the geometric location and topological site using a target function that is calculated from the tree generated so far. A set of boundary conditions is maintained during each step of tree generation. The perfusion sites are randomly selected within a specific perfusion volume and supplied by terminal vessels. Each terminal segment

drains an individual amount of blood flow into the microcirculation. The tree hydrodynamic resistance is calculated so that either the prescribed pressure difference or radius produces a given total perfusion flow. At each bifurcation, the parent and daughter segments radii obey the power law. Three main parameters control the generation of this arterial tree: the target function, the seed of the random number sequence used, and the asymmetry ratio, γ.

3.3 Autoregulation Models

Autoregulation behaviour can be modelled using either a physiological or phenomenological model. Physiological models attempt to simulate the exact interactions that occur in cerebral hemodynamics while phenomenological models attempt to represent the same physiological response in a simplified way but still utilising mathematical expressions. Most of the autoregulation models discussed below do not consider the cerebral vasculature of the CoW.

Research by Ursino et al. on cerebral circulation has extended over two decades. In 1985, the circulation in the rat brain was modelled using an electrical analogy [12]. This represents the extracranial and intra-cranial arteries and veins as a network of compliances and resistances. The model emphasizes the interaction among different control mechanisms in response to perturbation of both jugular veins in the rat. The overall controller considers simple metabolic mechanisms, autoregulation, and cerebral blood volume (Figure 3.4). The metabolic control ensures sufficient blood supply to the cerebral mass. It is based on the hypothesis that the cellular mechanism remains unchanged and equal to its basal normal value. The metabolic control is activated when the blood flowrate through the perfusion resistance differs from its basal value. Autoregulation maintains a relatively constant CBF despite changes in CPP within certain limits. Control of cerebral blood volume (CBV) is dependent on the venous volume change.

This work was further developed to simulate the intra-cranial pressure pulse wave [122]. The developed model explains the intra-cranial pressure pulse wave affected by the pulsating changes in cerebral blood volume. It mimics the behaviour of the cerebral arterial vascular bed, the cerebral venous vascular bed, cerebrospinal fluid absorbtion and production processes, the intra-cranial pressure-volume relationship, and cerebral autoregulation (Figure 3.6). The cerebral vascular bed is represented using a modified electrical analogy (Figure 3.5). The work includes simulation of clinical tests [123]. In subsequent work, they took CO_2 reactivity into account [78]. The time pattern of ICP and MCA blood velocity response was simulated for systemic arterial pressure and CO_2 concentration change.

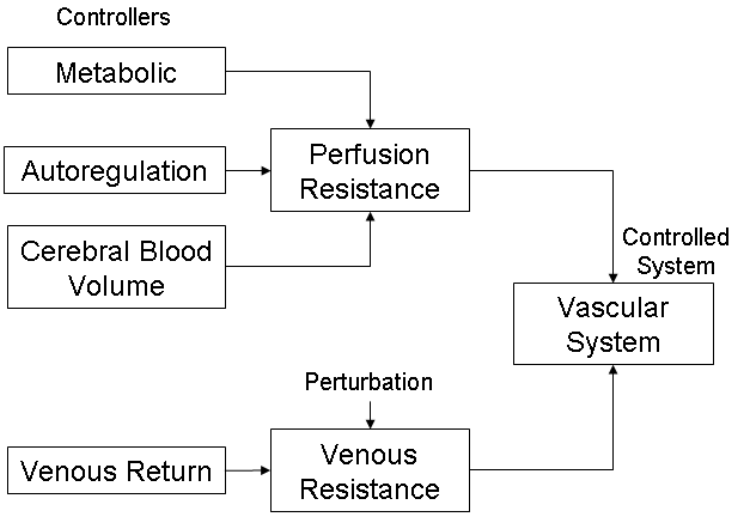

Figure 3.4 Block diagram of the 1985 model by Belardinelli, Gnudi and Ursino [12].

Analysis of real clinical cases suggested that certain physiological phenomena might be described in a much simpler algorithm for the interaction between the ICP and cerebral hemodynamics without significant effect on model performance. A simplified model of ICP dynamics for the study of patients with severe brain damage was created [128]. In this model only one segment representing the arteries and arterioles was used. The segment extends from the large cerebral arteries down to the cerebral arteries. The main results agreed very closely with more complex models developed previously and had the advantage of having less mathematical complexity. The relationship between Doppler velocity pulsatility and autoregulation was investigated based on the previous work of intra-cranial dynamics and cerebrovascular regulation [127].

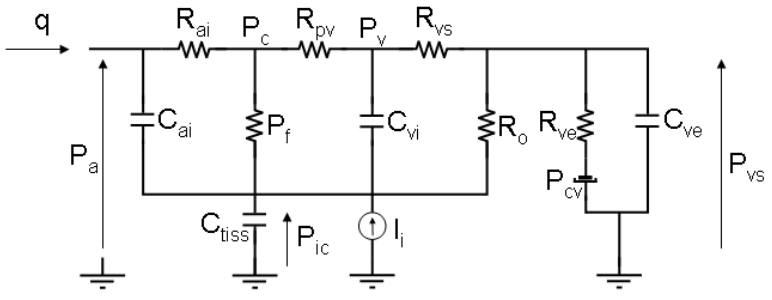

Figure 3.5 The electrical analogy of overall human hydrodynamics by Ursino et al. [122]. q: cerebral blood flow, P_a: arterial pressure, P_c: capillary pressure, P_v: venous pressure, P_{ic}: intra-cranial pressure, P_{vs}: venous sinus pressure, C_{ai}: intra-cranial arterial compliance, R_{ai}: intra-cranial arterial. R_{pv}: proximal venous vascular bed resistance, R_{vs}: distal venous vascular bed resistance,C_{vi}: intra-cranial venous compliance, R_f: resistance to CSF formation, R_o: resistance to CSF outflow, C_{tiss}: cerebral tissue compliance, I_i: rate of saline infusion, R_{ve}: extracranial venous resistance, C_{ve}: extracranial venous compliance, P_{cv}: central venous pressure.

In 2000, Ursino et al. created a mathematical model for acute cardiovascular re-

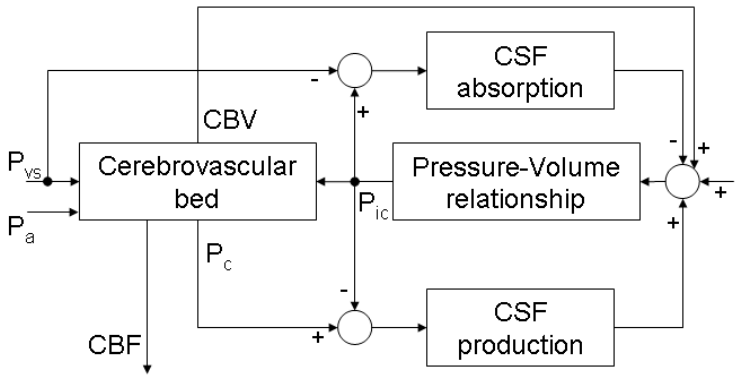

Figure 3.6 Block diagram of the main relationships between the intra-cranial quantities used in Ursino's model [122].

sponse to severe hypoxia. The model includes a pulsating heart, systematic and pulmonary circulation, and the local effect of O_2 on organs with high metabolic needs [129, 130]. The model also includes analysis of the local effect of hypoxia on the vascular beds of such organs. The vascular system is again represented using a hydraulic system with fourteen different vascular compartments for pulmonary and systemic circulations. O_2 concentration in the venous blood leaving each compartment is computed using a mass balance equation between the O_2 extraction and the O_2 consumption rate, where the O_2 consumption rate in the brain and skeletal muscle is kept constant. The model also includes reflex regulatory mechanisms for peripheral chemoreceptors[3], arterial baroreceptors[3], and the hypoxia response of the central nervous system. The peripheral chemoreceptors and arterial baroreceptors are described using a first-order dynamic block, which exhibits a static and rate-dependent gain, in series with a sigmoidal static characteristic. The work was extended further to include the O_2-CO_2 interactions and their effects on the peripheral resistances [81]. The model shown in Figure 3.7 simulates the response to blood gas content in a variety of conditions. The chemoreceptors in this model include a static non-linear characteristic to account for the non-linear O_2-CO_2 interactions. The activity of the chemoreceptors is modelled using a sigmoidal function of PO_2 at constant carbon dioxide partial pressure (PCO_2). The static response to PCO_2 for normal PO_2 is reproduced through a logarithmic curve with a lower threshold, below which the activity approaches zero.

The work of Banaji involved modelling three main physiological sites: the vascular system, metabolic biochemistry of the brain and the properties of VSM [10]. The vascular system is based on the existing Ursino model [131]. Banaji's model is a development of the work of Ursino with the addition of basic brain metabolism biochemistry and VSM mechanisms. The vascular system is divided into compartments: large arteries, arterioles, capillaries, veins, and venules. The brain tissue is divided into sub-regions:

[3]See Section 2

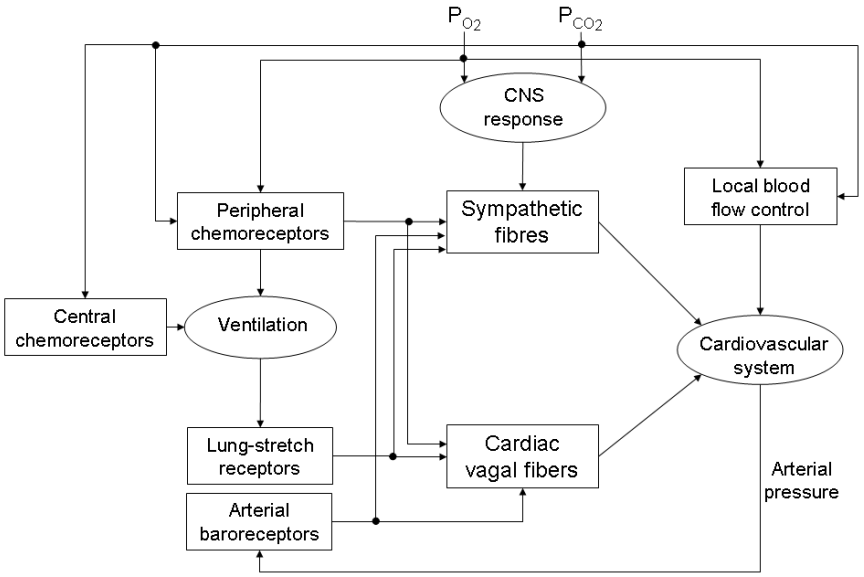

Figure 3.7 Ursino et al. model describing the interactions between regulatory mechanisms [81].

the extracellular and the intra-cellular compartment, and the mitochondrial compartment. Finally, the VSM consists of two regions: VSM cells of the large arteries, and VSM cells of arterioles. Changes in O_2 and CO_2 concentrations in the blood flow result in changes in smooth muscle tension. For chemical reactions modelling, the different compartments consist of conservation equations or phenomenological equations. In addition, the different compartments in the model communicate with each other through blood flow carrying chemicals between the vascular system compartments; exchange of glucose and O_2 between the capillary and extracellular compartments; chemical exchange between the extracellular and cytoplasmic compartments; chemical exchange between the cytoplasmic and mitochondrial compartments; and chemical communication between the extracellular and muscle compartments. The complex model produces the autoregulation curves of CBF in response to blood changes. The results match the expected physiological curves. Figure 3.8 shows some feedback pathways of work during blood flowrate regulations. Sometimes a single event results in several stimuli which can have opposing effects on circulation.

Thoman et al. created an autoregulation model to test the combined effects of physiological variables [117]. The model is intended to be an educational tool, incorporating many simplifying assumptions; it is not a highly accurate physiological model for precisely predicting patient response. Fitted equations are formulated using experimental data from the literature to generate a dynamic response of CBF as it is affected by physiological quantities, which include PO_2, PCO_2, $CMRO_2$ and MAP. This is a simple model where the CBF is calculated by adding or subtracting the changes in CBF

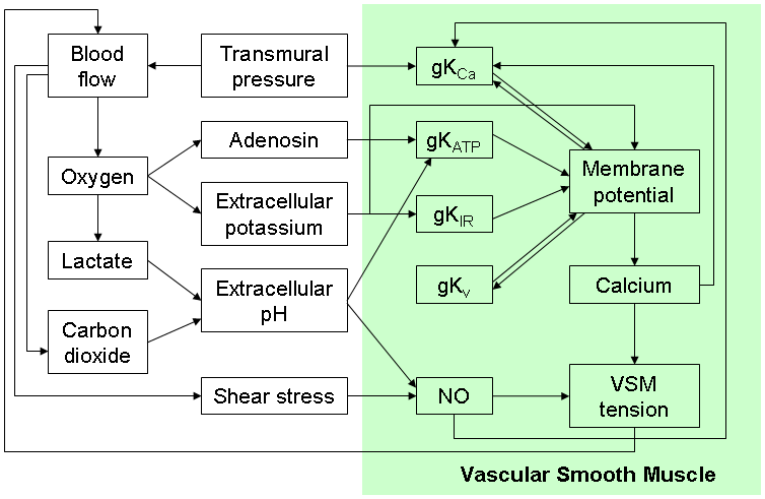

Figure 3.8 Feedback loops in Banaji et al. model [10] where various stimuli cause changes in blood flow. *NO*: nitric oxide. gK_{Ca}, gK_{ATP}, gK_{IR} and gK_V are conductivities of calcium sensitive, ATP sensitive, inward rectifier and voltage dependent potassium channels respectively. Vascular smooth muscle acts to control vessel diameter and hence cerebral blood flow.

caused by changes in physiological quantities.

The model was later developed [118] by adding a dynamic CVR feedback loop (Figure 3.9). The CVR is calculated based on the CVR in the previous time step and the error in CBF (the difference between CBF set point and new CBF, which is a function of physiological quantities). The CBF is defined using Poiseuille's law using CVR and CPP. It is maintained within a range of CPP through CVR to achieve autoregulation. The CPP range of the autoregulation zone is set by lower and upper limits of CVR. The principle mechanism for satisfying oxygen demand is also achieved through CVR.

This model takes into account the oxygen extraction factor (OEF), which is 30% in normal autoregulation range. However, this OEF increases up to 70% if the CPP drops below the lower limit of autoregulation. The arterial oxygen concentration (CaO_2) is defined as a function of blood hemoglobin concentration [Hb], oxygen saturation factor (SaO_2), and PO_2. The same equation was used in the model discussed in this thesis to define the CaO_2.

Research on autoregulation and its modelling usually investigates the steady state response of CBF as a result of change in CPP using physiological processes as discussed above. However, the dynamic response of autoregulation has also been investigated. Most of the models interpret the dynamic autoregulation as a frequency-dependent mechanism. These models do not take into account physiological processes.

Panerai et al. and Mitsis et al. analysed the dynamics of autoregulation [87, 100]. Panerai et al. looked into the different methods used by other authors to model

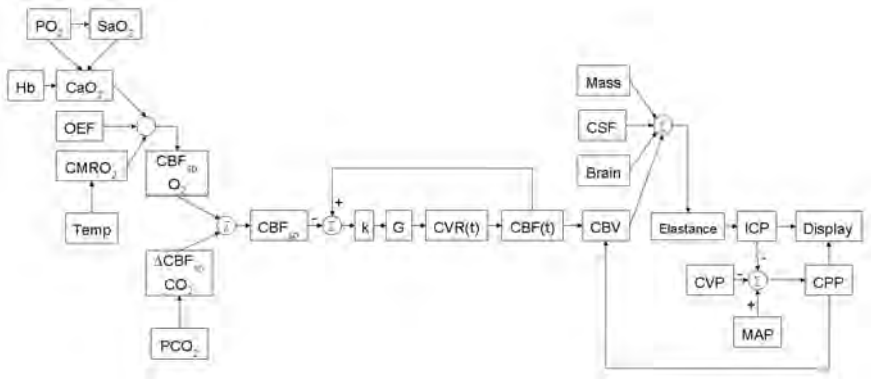

Figure 3.9 Flowchart of the autoregulation model by Thoman et al. [118].

dynamic response. Time-domain and frequency-domain analysis methods were carried out where the relationship between beat-to-beat changes in MAP are quantified using a transfer function. Dynamic response was analysed in neonates[4] with intact and impaired autoregulation [101]. In later work, Panerai et al. investigated a new approach adopted by Mitsis et al. and compared it with the transfer function approach [99]. The artificial neural networks (ANN) approach, which consists of processing elements with filters, and fast and slow dynamics. The slow dynamics indicate that cerebral autoregulation has a longer memory than was previously thought. The CBF is affected by changes in MAP occurring up to a couple of minutes into the past, not only the last few seconds.

Olufsen et al. investigated the circulatory autoregulation and the baroreceptor regulation in the cerebral mass [95, 96]. Measurements of subjects were carried out using the TCD method by performing a postural change from sitting to standing. Instead of trying to explain the biophysics of metabolic, myogenic or neuronic mechanisms that result in regulation, Olufsen et al. modelled the dynamics and control of blood flow. The dynamic changes in pulsatile blood flowrate of the MCA during transient changes in arterial pressure were reproduced using a lumped parameter model. The model consists of two parts. First, the flowrate in the MCA is computed as a passive response to pressure. The MCA is modelled as an electric circuit with two resistors and a capacitor. The relationship between the flowrate and pressure is described using an ordinary differential equation. Second, how the parameters of the lumped parameter model change during the postural change is investigated. The lumped parameter model demonstrates a biphasic cerebrovascular response to acute posture change, which is characterised by initial peripheral vasoconstriction followed by an autoregulatory vasodilation.

Jung et al. developed a mathematical model of cerebral circulation, including the autoregulation mechanism and oxygen supply to the tissue [62]. The model was designed to analyse the slow dynamical variations of long term neurophysiological parameters,

[4]See Glossary

such as PO_2 and CBF, recorded on a neurosurgical intensive care unit. The hydrodynamical model follows closely Ursino et al. model. The circulatory part of the model consists of seven compartments including arteries, capillaries, veins, brain tissue, CSF, sagittal sinus, and an extra compartment for simulation of brain swelling. To account for the properties of the individual compartments, a system of five coupled non-linear differential equations plus a constraint is applied. For autoregulation, the microvascular bed consists of a parallel arrangement of several microvessels with equal inner radius (r). The compliance of a vessel, which represents volume changes as a result of vasoconstriction and vasodilation, is described by a differential equation and is enclosed by upper and lower bounds. This equation is incorporated into coupled non-linear equations. The oxygen supply is based on the Krogh cylinder model where oxygen diffusion occurs only in the capillary compartment.

Gao et al. investigated autoregulation curves reproduced by other researchers and classified them into three types [43]. The first type is based on the concept that once maximal vasoconstriction or vasodilation is reached, the CBF becomes MAP passive. The slopes of lines below the lower limit of autoregulation (LLA) and above the upper limit of autoregulation (ULA) are different. The second type is similar to the first except that the slopes below LLA and above ULA are the same. The third type is a third order polynomial fit. The investigation also introduced an autoregulation model which consists of four compartments for the resistive arterial and arteriolar network. The modelling of CBF is done for normal circulation with the assumption that cerebral venous pressure and ICP are zero. The contribution of different hierarchical levels of vessel sizes is considered in this model. Each of the four compartments consists of vessels of various numbers, diameters, and lengths. The number of vessels in each compartment is based on Murray's law[5]. The diameters of vessels in each compartment are modelled using fitted empirical formulae. To reproduce the autoregulation curve, the equivalent resistance of the four compartments is used as a function of pressure. This model has several limitations. It is not based on physiological properties of the cerebral vascular network, but it is rather a simple model to predict the general behaviour of autoregulation. The dynamic aspects of the autoregulation are not considered. The produced curve does not fit experimental data above the ULA. Finally, absolute CBF values are not used and the amount of cerebral mass is not specified in the model. The number of vessels in each compartment is based on having one vessel in the first compartment. This is not physiologic and does not take into account the part of the vascular bed which contain vessels with diameters less than 50 μm or capillaries.

[5]See Glossary

3.3.1 Metabolic Models

There are many mathematical models of the metabolites in the cerebral arterial blood, venous blood or tissue. Some of these models are concerned with the autoregulatory mechanism of CBF while other are focused only on the metabolites exchange. The most important metabolites are O_2, CO_2, and H^+ concentrations. CO_2 is believed to increase CBF almost entirely by first combining with water in the body fluids to form carbonic acid, with subsequent dissociation of the acid to form H^+. Then, H^+ causes vasodilation of the cerebral vessels. Any other substance that increases the acidity of the brain tissue, and therefore also increase H+ concentration, will likewise increase blood flow. Only a small number of metabolic models that are related to this thesis research are reviewed here.

In 1989, Ursino et al. developed an O_2-dependent CBF regulation model in the rat [125]. The model uses partial differential equations to describe the O_2 production and diffusion processes. It examines two basic parts. First, it analyses O_2 diffusion from blood in capillaries to the cerebral tissue. This relates the change in PO_2 to CBF and change in arterial O_2 concentration. Second, it describes the production and diffusion dynamics of vasoactive metabolites, such as adenosine and H^+, associated with lack of O_2 delivery to the tissue.

In the second part of the studies published in the same year [126], Ursino et al. developed a cerebral vascular model which acts indirectly to the O_2 present in the blood through the release of adenosine and H^+. The cerebral vascular bed is modelled as a series of five resistances where each resistance represents a range of cerebral vessels from large proximal arteries and arterioles to capillary and venous beds. The regulatory metabolic mechanism acts only in the segments representing arterioles. Poiseuille's law is used for the relationship between pressure, resistance and flowrate while Laplace's law is used for the pressure and arterial radius (Figure 3.10). Some of the shortcomings of this model is that the amount of CBF restored by the action of autoregulatory mechanism is not adequate to achieve autoregulation. The time period of the response is also significantly slower than what is expected physiologically.

Keener and Sneyd [65] created a simple autoregulation model based on the oxygen metabolic consumption rate ($CMRO_2$). The $CMRO_2$ is a function of oxygen concentration difference between the arterial blood and venous blood, CaO_2 and CvO_2 respectively. CaO_2 is treated as a given constant while CvO_2 is treated as a variable. The resistance of arterioles is linearly dependent on CvO_2. This is possible, since arteries and veins tend to run side by side, and venous concentrations may regulate arterial resistance by release and diffusion of regulatory substances. This model is described more in detail in Section 5.3 as it is adopted as one of the first models created in this

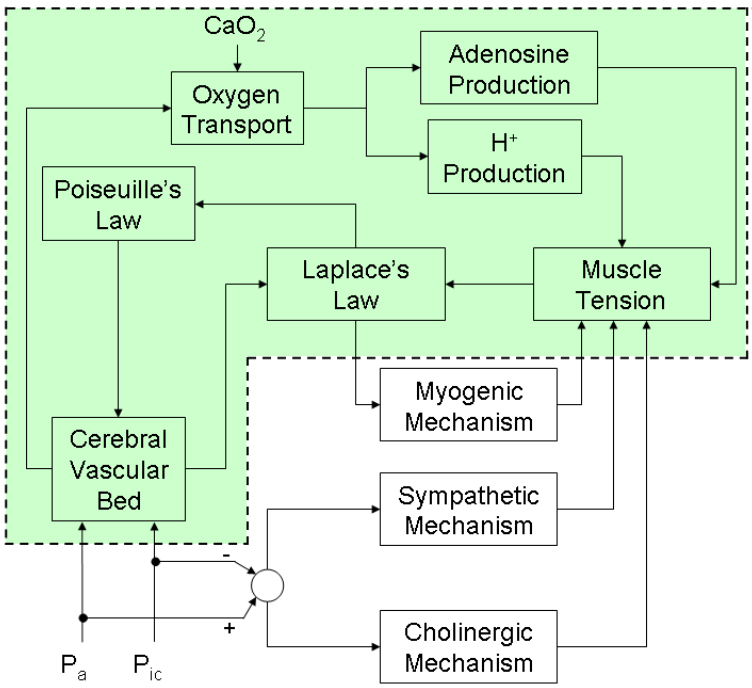

Figure 3.10 Block diagram of Ursino et al. model showing the main relationships between regulatory actions and hemodynamics quantities in the model [124]. The part highlighted in green is the initial model created in 1989 [126].

research.

Gutierrez developed a mathematical model of the CO_2 exchange between blood and tissue during hypoxia [46]. This is a two compartment mass transport model to examine the effect of blood flow and hypoxia on tissue and vascular CO_2 concentration. The model does not take the autoregulation mechanism into account. CO_2 transport from tissue to blood involves several complex, time dependent mass transport processes. Two differential equations for the CO_2 concentration in the tissue and the vasculature are formulated and solved. The equations depend on the CO_2 production in the tissue, the rate of transport between the two compartments, and blood flowrate. Figure 3.11 shows a block diagram of the model.

3.3.2 Myogenic Models

In the literature, most of the studies of the myogenic response are based on an isolated segment or vessel of the cerebral vasculature. The diameter of this vessel in many cases is in the micrometer range. Vessels with this size in the cerebral vasculature do not experience pressure values high enough to result in a myogenic response. Some of these myogenic mechanism models are reviewed here.

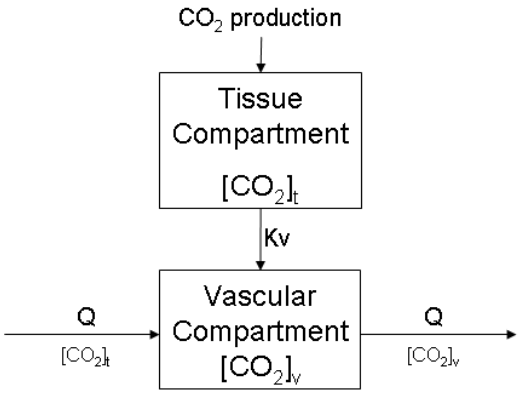

Figure 3.11 The tissue CO_2 exchange model by Gutierrez [46]. $[CO_2]_t$: tissue CO_2 concentration, $[CO_2]_v$: vascular CO_2 concentration, K_v: diffusion constant.

The model in [125, 126] was modified further by Ursino to add the myogenic and neurogenic reactivity of the cerebrovascular bed [124] (Figure 3.10). The myogenic response is active in the proximal segment of the cerebrovascular bed. It is represented using a first order differential equation. The effects of nerves is maximum on proximal segments and declines with the size of vessels. The model represents the sympathetic and parasympathetic mechanisms based on the stimulation frequency. This model is capable of producing only 60-70% of the regulatory capacity of the cerebrovascular bed experienced physiologically. Micro vessels in vivo exhibit stronger vasodilation capacity than this model.

The model by Ermentrout and Gonzalez-Fernandez consists of a system of differential equations that describes the vasomotion mechanism and predicts the myogenic response in cerebral vasculature [44]. The model includes the ionic transports, cell-membrane potential, and muscle contraction of the vessel smooth muscle cells (SMC). The transmural pressure controls the hoop stress of the vessel wall resulting in the changes in calcium (Ca^{2+}) and potassium (K^{+}) fluxes across SMC membrane, which are mediated by voltage-gated and voltage-calcium-gated channels. The hoop stresses result in a change of the vessel radius. This is described more in detail in Section 7.3 as these differential equations defining the myogenic mechanism are used in the model described in this thesis.

The model of Yang et al was focussed on the interaction between the electrical, chemical, and mechanical components of the SMC during the development of active tension [139]. The model consists of two major parts: electro-chemical, and chemo-mechanical (Figure 3.12). The electro-chemical part can analyse the transient intracellular Ca^{2+} production in response to membrane voltage clamp pulses. It consists of the cell membrane electro-physiological behaviour, fluid compartments, Ca^{2+} release

and uptake by the Sarcoplasmic reticulum[6], and cytosolic Ca^{2+} buffering. The chemo-mechanical part consists of the chemical kinetics of myosin phosphorylation; and a model of force generation and mechanical coupling to the contractile filaments.

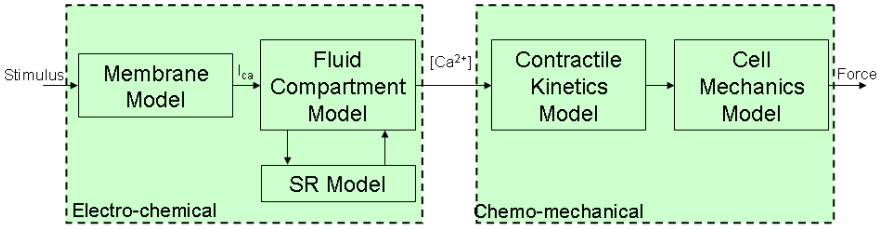

Figure 3.12 Functional block diagram of the Yang et al. model [139].

A study by Koenigsberger et al. examined the role of endothelium on vasomotion of SMCs [68]. A model is created to simulate the Ca^{2+} dynamics of a population of SMCs coupled to a population of endothelial cells. The model analyses the effects of an SMC vasoconstrictor simulation on endothelial cells as well as the feedback of endothelium derived factors. The results of the model show that the endothelium decreases the level of Ca^{2+}, which may results in the SMCs moving from a steady state to an oscillatory state.

3.4 Oxygen Diffusion

Krogh's investigations of the microcirculation concluded that the small arteries run in parallel to muscle fibres [71, 72, 73]. The arterioles branch off the small arteries at consistent intervals. The arterioles run deeper in the fibres and divide into bundles of capillaries which run down the muscle fibres. Using transverse slices, Krogh observed that capillaries are distributed regularly in the fibres. Based on that, an assumption is made stating that each capillary supplies a cylinder of tissue around it independently, making it the only oxygen provider to the tissue cylinder. He formulated equations of the oxygen pressure distributed radially in the tissue. The model has several assumptions: the oxygen pressure at capillary wall is the same as in blood; the oxygen pressure decline along the capillary is neglected; oxygen diffusion in tissue is radial; and the oxygen consumption in the tissue is uniform. The diffusion into tissue was assumed under steady state conditions, and the metabolic rate of oxygen consumption is independent of the oxygen concentration. Krogh also observed that the capillary networks in muscle tissue are more regular than in other tissues, no reference to the capillary network in the cerebral mass was made. From his experiments, Krogh deduced that capillaries are

[6]See Glossary

passive, not active. The flowrate through the capillaries is based on the constriction and dilation of the arterioles.

Middleman investigated in depth the oxygen transport from the capillary to the surrounding tissue using the Krogh cylinder [85]. The equations consider the rate of change of oxygen concentration in the tissue. It also accounts for the diffusion within the capillary in the red blood cells and plasma of the blood. Many other authors investigated the oxygen diffusion in the tissue. Bloch and Blum also considered a steady state situation with well-mixed blood in the capillary [13, 14]. Bloch used a constant metabolic rate while Blum considered linear kinetics as a function of the oxygen concentration. Both models offer an analytical solution; however, Blum considered more realistic boundary conditions.

The Krogh cylinder was used by McGuire et al. to model the oxygen transport in muscle tissue [83]. The method evaluates the oxygen transport at the microvascular level numerically. The diffusion of oxygen from the capillaries into the tissue is considered as a passive process. The higher the oxygen consumption, the shorter the distance is traveled by oxygen to the surrounding tissue. Fick's law is used for the radial oxygen diffusion from the capillary blood into the tissue cylinder, where the $CMRO_2$ is represented using Michaelis-Menton kinetics. The capillary is discretised to 100 units along its length, where the oxygen diffusion equation is solved at each unit. Some of the assumptions in Krogh's model were modified in this model. The capillary wall resistance to oxygen diffusion to the tissue surrounding it is included as a boundary condition. The drop in PO_2 along the capillary is also taken into account. This model by McGuire et al. is used in the present model for oxygen transport to the cerebral tissue. This is explained further in Section 7.4. The goal is to determine the oxygen consumption and then predict if any parts of the cerebral mass experiences lack of oxygen delivery under common pathological conditions.

As mentioned in Section 3.3, the Jung et al. model of cerebral circulation autoregulation includes the oxygen supply to the brain tissue [62]. This is also based on the Krogh cylinder model. Again, Fick's law for diffusion is used. Boundary conditions in this model do not take into account the capillary wall resistance to oxygen diffusion. In addition, the $CMRO_2$ is assumed constant in this model. The PO_2 is solved by integrating over the volume of the tissue cylinder, which is then feed back to the autoregulation model.

3.5 Conclusion

It can be concluded that there is a significant body of literature on the field of cerebrovascular hemodynamics. Many of the models are concerned with investigating one particular aspect of the hemodynamics, such as the cerebral vasculature or the autoregulation mechanism. The few that combine both these aspects include a rather simple phenomenological representation of the myogenic and/or metabolic mechanisms.

For the vascular networks downstream of the CoW peripheral arteries, most autoregulation models use vascular beds that are relatively simple to what they actually are physiologically. In the past, it was considered unreasonable to model the arterial tree because of computational expense. In the present model, the simple fractal tree by Olufsen et al. [94] was adopted. This is a realistic model, yet not as expensive computationally as, for example, the vascular tree created by Karch et al. [63]. The use of fractal tree networks to represent vascular beds allows us to model the metabolic and myogenic mechanisms where they occur at the different levels of the vasculature, making the model presented in this thesis more physiological rather than phenomenological.

The task of modelling the brain metabolism is large and complicated. In this research, reproducing only the features that will affect the circulation is important. For the metabolic mechanisms, modelling of all the processes involved was not attempted. The modelling was restricted to only a collection of the mechanisms which appear to be most important for the purpose of the present research.

A successful model should replicate the way the cerebral circulation behaves under failure and changes of stimuli. The model of cerebral hemodynamics has the capacity and flexibility to represent medical situations, without being expensive computationally. The model is able to simulate any configuration of the cerebral vasculature under most common pathological conditions, where input data is patient specific.

Chapter 4

Basic Model

4.1 Original Model

The basic model of cerebral hemodynamics used in this thesis was based on the autoregulation model by Katherine Moorhead [90]. This basic model was developed further at several stages of the present research. The CoW was modelled as a structure with laminar, viscous and incompressible flow. This basic model is similar to the work by Hillen et al. [58], where the segments of the CoW were represented using Poiseuille and conservation of flow equations. This chapter presents the basic model which shares the same fundamentals as Moorhead's model but with important additional aspects. Further developments were incorporated throughout this research, which are described in subsequent chapters.

4.1.1 Fluid Dynamics

Human blood is composed of blood cells suspended in liquid matrix called plasma. Blood plasma accounts for 55% of blood volume and is 90% water. The blood cells present in blood are mainly red blood cells, which occupy about 45% of the blood volume. A fluid is considered Newtonian if the relationship between the shear stress (τ) and velocity gradient ($\frac{du}{dr}$) is linear such as in Equation 4.1, where μ is the constant viscosity.

$$\tau = \mu \frac{du}{dy} \tag{4.1}$$

In a non-Newtonian fluid, the relation between the shear stress and the velocity gradient is non-linear, and can even be time-dependent. It is generally accepted that blood is a non-Newtonian fluid, and this is due to the existence of red blood cells. When blood plasma alone is tested in a viscometer, it behaves like a Newtonian viscous fluid

[42]. The non-Newtonian behaviour of blood can be represented using Carreau-Yasuda and Casson models. The relationship between blood viscosity and shear rate is shown in Figure 4.1. The plots show that blood viscosity reaches an infinite shear viscosity at shear rates higher than 100 s^{-1}. This means that blood can be assumed to be Newtonian for shear rates higher than this value.

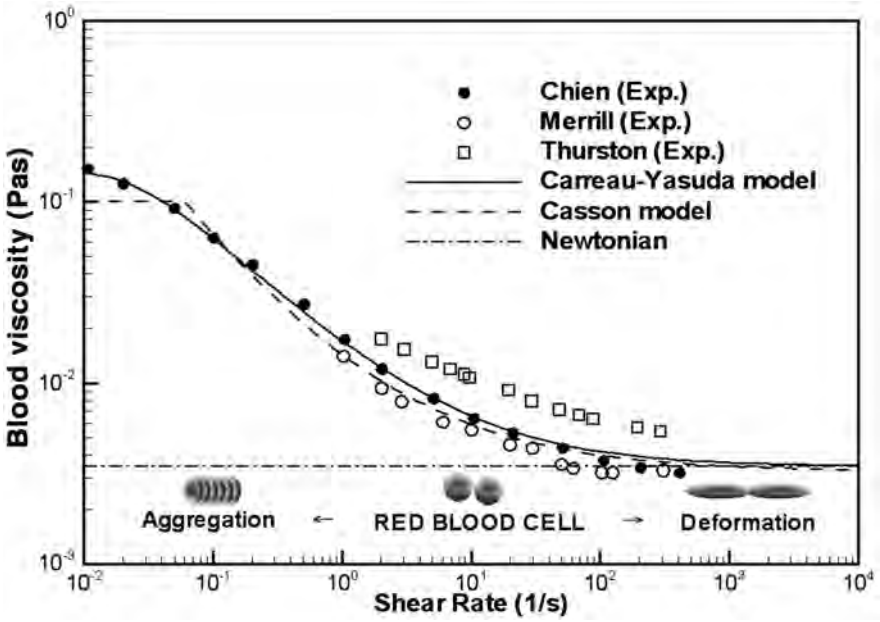

Figure 4.1 Variation of blood viscosity due to shear rate [66].

Initial simulations by Moorhead indicated that shear rates throughout the CoW are well above 100 s^{-1}. Because the forces of high shear stress act parallel to the wall of vessels, arterial flow is assumed to be Newtonian in all developments of the model in this research.

The CoW is modelled as a structure with laminar flow. The arterial segments are modelled as uniform circular tubes. The flow is considered zero-dimensional (0D) because the velocity and pressure are averaged over the cross-section everywhere in the arterial segments. It is not one-dimensional (1D) because there is no discretization along the length of the arteries. The flow is assumed to be laminar because of the relatively small vessels of the CoW, which result in Reynolds numbers of approximately 200. Figure 4.2 (a) shows a cylindrical volume of blood with radius (r) inside a vessel segment. To model this cylindrical body of blood, polar coordinates are used. The flow obeys Navier-Stokes equations of motion of an incompressible fluid. A no-slip boundary condition is assumed, meaning that the blood velocity at all blood-wall boundaries is equal to that of the wall, which is zero.

As the velocity profile, shown in Figure 4.2 (b), is not changing in the x-direction, the inlet momentum flux is equal to the outlet momentum flux and the result is equal

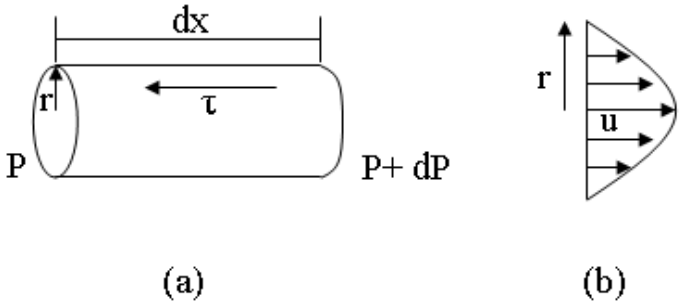

Figure 4.2 (a) Volume inside vessel segment. (b) Velocity profile.

to zero[106]. As the flow in the cylindrical body of blood is axisymmetric, all velocity components cancel out except for u(r). The cylindrical body is subjected to a pressure (P) on left and pressure(P + dP) on the right, acting on area of (πr^2). The shear stress (τ) acts parallel to the wall of vessels on area of ($2\pi r \cdot dx$). The force balance in the x-direction is given in Equation 4.2.

$$P\pi r^2 - (P + dP)\pi r^2 - \tau(2\pi r)dx = 0 \tag{4.2}$$

In this equation, no radial or circumferential flow is considered. The shear stress is related to the velocity gradient as given in Equation 4.3.

$$\tau = -\mu\frac{du}{dr} \tag{4.3}$$

The Poiseuille equation (Equation 4.4) is derived using Equations 4.2 and 4.3, where r_v is the vessel radius and l_v is its length. See Appendix A for detailed derivations of this equation.

$$Q = \frac{\pi r_v^4}{8\mu l_v}\Delta P \tag{4.4}$$

This Poiseuille equation can be re-written in the format of Equations 4.5 and 4.6, where R is the resistance of the vessel. The flowrate Q is a function of pressure gradient along the vessel and resistance R. Resistance of a vessel segment is inversely proportional to the fourth power of the vessel radius. The derived equations describe general blood dynamics in vessels. Throughout this thesis, the terms cerebral blood flow (CBF) and cerebrovascular resistance (CVR) are used instead Q and R, respectively, to describe the hemodynamics inside the cerebral mass.

$$Q = \frac{\Delta P}{R} \tag{4.5}$$

$$R = \frac{8\mu l_v}{\pi r_v^4} \tag{4.6}$$

4.1.2 CoW Vasculature Model

The CoW is modelled as a network of resistances representing all the main vessels in cerebral vasculature. Figure 4.3 (b) shows a schematic representation of the CoW used in this research where each of the boxes represents the resistance of an artery. There is some compliance in the major arteries of the CoW. However, the compliance was not considered in this model because the arteries are located within an incased volume (the brain tissue). In addition, no pulsatile signal was taken into account as only the autoregulation response, which occurs over many cardiac cycles, was considered of importance for the current research. Arteries were assumed to be rigid vessels, and therefore, were modelled with constant resistances using Equation 4.6. The implementation of the CoW arteries' compliance should be examined in future work to determine its effects on the model.

Each of the efferent arteries of the CoW that supply the cerebral tissue (ACA2s, MCAs, PCA2s, AChAs and SCbAs) have two resistances: one resistance represents the vessel from its origin to its first bifurcation; the second resistance represents the vasculature downstream of that vessel from the same bifurcation down to and including the capillaries in the vascular beds. The first resistance is modelled as a constant resistance using Equation 4.6 based on the artery's dimensions, while the second (with an arrow across the resistance box in the schematic diagram) is a variable resistance. The variable resistance is used to represent the vasoconstriction and vasodilation behaviour of the smaller arteries, which results in the autoregulation mechanism. The computation of the variable resistances initial condition is illustrated in Section 4.2.2.

The efferent arteries in the CoW representation by Moorhead was reduced to the main six arteries of LACA2, RACA2, LMCA, RMCA, LPCA2 and RPCA2 as shown in Figure 4.3 (a). These were represented by only single segments of variable resistances. In this research, the LAChA, RAChA, LSCbA, and RSCbA vessels are taken into consideration in addition to the main six efferent arteries as shown in Figure 4.3 (b), where each of the six main efferent arteries consist of two resistances as mentioned above. The BA is also divided into two segments to account for the SCbAs.

An inlet pressure representing the arterial pressure (P_a) is introduced to the CoW at

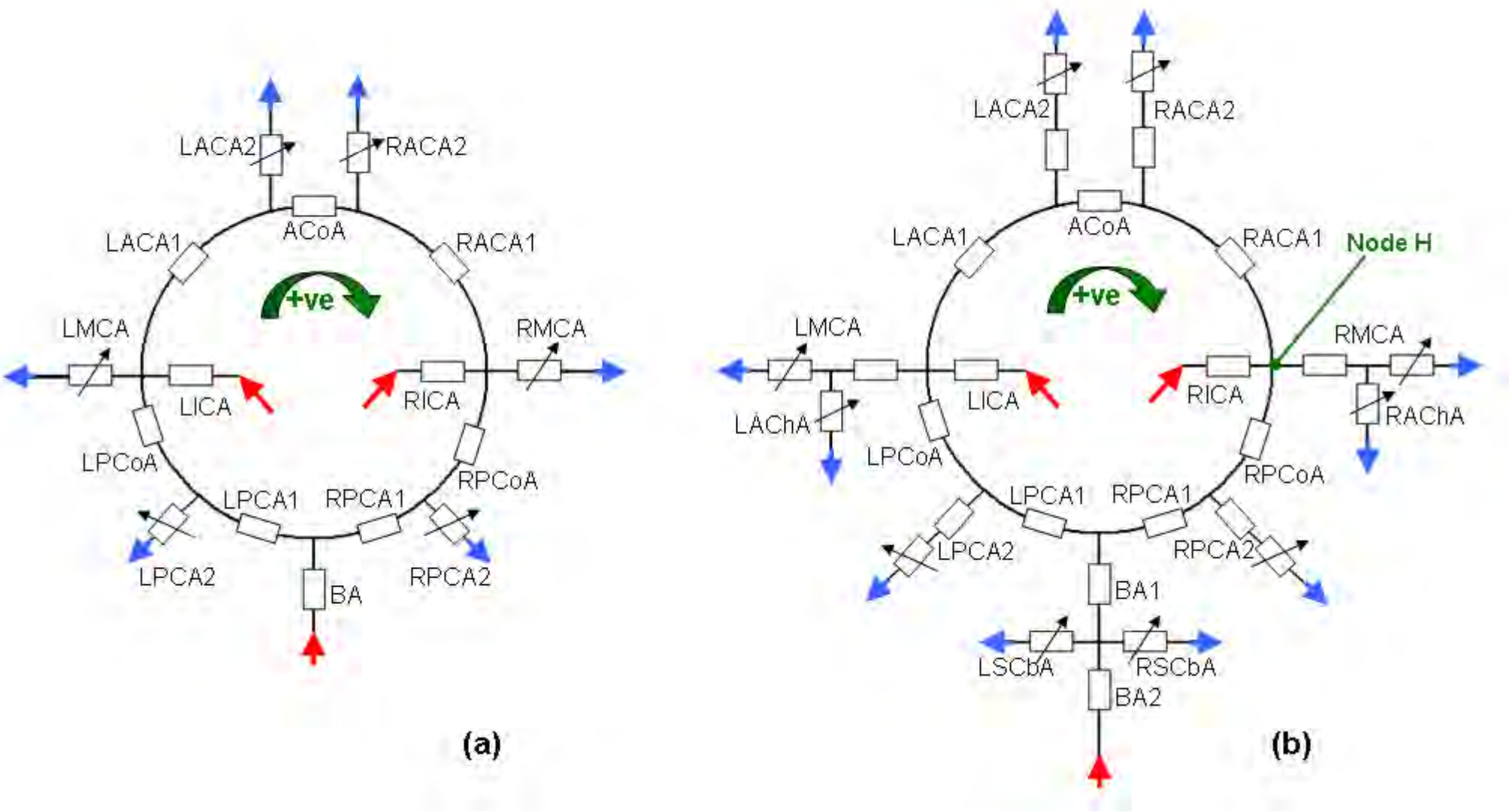

Figure 4.3 Schematic diagram of the CoW (a) by Moorhead. (b) in this research. Red arrows indicate inflowing (afferent) arteries with inlet pressure P_a. Blue arrows indicate outflowing (efferent) arteries with outlet pressure P_v.

the origins of the afferent arteries. An outlet pressure representing the venous pressure (P_v) is defined at the end of the vascular beds of the efferent arteries. Using the sign convection of flow in Figure 4.3, Poiseuille and conservation of flow equations are used to build a set of equations representing the hemodynamics that take place inside the CoW. The Poiseuille equations are formulated for the 17 constant-resistance segments (3 efferent and 14 internal connecting vessels of the CoW) and the 10 variable-resistance segments in the CoW. The conservation of flow equations are formulated for the 14 nodes (the points of bifurcation) in the CoW. These equations are represented in matrix form (Equation 4.7) in order to be solved. This results in a 41×41 matrix A, which contains the CoW vessel resistances. The vector $\tilde{x}$ (to be solved) consists of the flowrates throughout all the CoW vessel segments, and pressures at all the CoW nodes. The vector b contains the input and output pressure of P_a and P_v, respectively.

$$A\tilde{x} = \tilde{b} \tag{4.7}$$

An example of the use of Poiseuille and conservation of flow equations is shown in Figure 4.4. The Poiseuille equation for the RACA1 segment is written as $CBF_{RICA} = \frac{P_a - P_H}{CVR_{RICA}}$. This is rearranged to be in matrix form $CVR_{RICA}\ CBF_{RICA} + P_H = P_a$. Conservation of flow equation at node A is $CBF_{RACA1} + CBF_{RICA} - CBF_{RPCoA} - CBF_{RMCA} = 0$. The complete set of equations is provided in Appendix B.

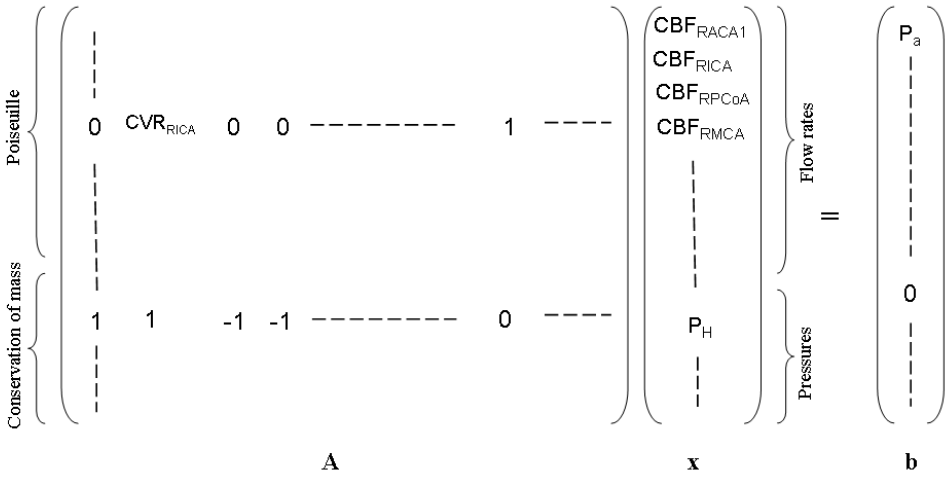

Figure 4.4 Matrix representation of the CoW hemodynamics.

4.1.3 Controller

The flow of blood through the CoW is determined principally by the downstream vascular resistance. Autoregulation is achieved through changing the variable resistance

segments of the CoW efferent arteries representing the vasoconstriction and vasodilation of the vessels downstream of that efferent artery. The vasoconstriction and vasodilation phenomena are modelled using a PI controller shown in Figure 4.5 and represented in Equation 4.8. The PI controller is a well known control loop feedback mechanism, which attempts to correct the error between the current flowrate and a desired set point flowrate by calculating and then outputting a corrective action U(t). In this case the desired set points are set to the reference average values presented in Section 4.2.2. These reference conditions do not change with time. The proportional term has physiological significance as it represents the response when the vessel experiences fluctuations from the normal CBF condition. The integral term acts as a low pass filter so that the controller will not respond to high frequency changes in the CBF encountered as a result of the cardiac cycle. K_i and K_p are the integral and proportional gains, respectively, and err is the error representing the difference between the current flow and reference *set point* flow. The integral term of the controller equation forces the error to zero.

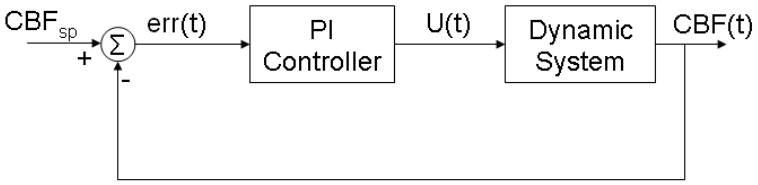

Figure 4.5 PI controller for the basic model.

$$U(t) = K_p\ err(t) + K_i \int_0^T err(t)\ dt \tag{4.8}$$

The variable resistance response is defined by a simple first order dynamic response equation. The controller input ($U(t)$) drives changes in the dynamic behaviour as defined in Equation 4.9, where λ is the time constant associated with response and CVR_{sp} is the *set point* resistance of the artery at optimal reference perfusion. These resistances have upper and lower bounds to model the lower and upper limits of autoregulation (LLA and ULA respectively).

$$\lambda\ C\dot{V}R(t) + (CVR(t) - CVR_{sp}) = U(t) \tag{4.9}$$

4.1.4 Autoregulation Limits

The lower and upper limits of autoregulation (LLA and ULA) are used to model the arteries' utmost ability to vasodilate and vasoconstrict to a maximum or minimum radius. Moorhead set the values of LLA and ULA to 5% and 195% of the normal resistance values, respectively. These assumptions were considered to be too relaxed and to allow for more dilation than is observed physiologically. Therefore, the limits were modified later by Moorhead to match the autoregulation curve by Guyton [47], which shows that autoregulation is active between 75 and 175 mmHg. The LLA and ULA values were therefore modified to 55% and 170% of the normal resistance values. These percentages of the autoregulation limits were found by trial and error.

In this research, the ULA and LLA were modified further to match the Guyton autoregulation plot more closely. They were changed to 65% and 190% of the normal resistance values. Gao et al. [43] reviewed autoregulation studies focusing on the lower and upper limits. The summarised data give 50 to 145 mmHg as the values for the LLA and ULA, respectively. Thoman et al. used the range of 50-150 mmHg [118]. This range was later adopted in this research, which results in LLA and ULA of 40% and 160% of the normal resistance values. The use of this new range of autoregulation is applied in Chapter 6.

4.1.5 Modelling CoW Geometry and Pathological Conditions

As illustrated in Section 1.2.3, 42-52% of the population have an incomplete CoW. The basic model was developed to consider the most common variations in CoW. To model a missing vessel, the radius of that particular vessel is reduced to almost zero value, which results in a very large resistance that represents a non-existing vessel. Other CoW geometry configurations are represented by appropriate modifications in vessels' radii. Pathological conditions, such as an ICA stenosis or occlusion, are also modelled. The total resistance of a stenosed artery consists of two resistances modelled in series: one representing the healthy section of the vessel, the second representing the stenosed section of the vessel. Equation 4.10 represents the total resistance of a stenosed vessel where CVR_h and CVR_s are the resistance of the healthy and stenosed sections, respectively.

$$CVR = CVR_h + CVR_s \tag{4.10}$$

$$CVR_h = \frac{8\mu(l_v - l_s)}{\pi r_v^4} \tag{4.11}$$

$$CVR_s = \frac{8\mu l_s}{\pi(r_v(1 - DoS))^4} \tag{4.12}$$

The lengths, l_v and l_s, and diameters, d_v and d_s are defined as in Figure 4.6. The degree of stenosis (DoS) is ratio of the stenosed opening inside the vessel to the actual vessel diameter. For the modelling of a vessel occlusion, the resistance is set again to very large resistance.

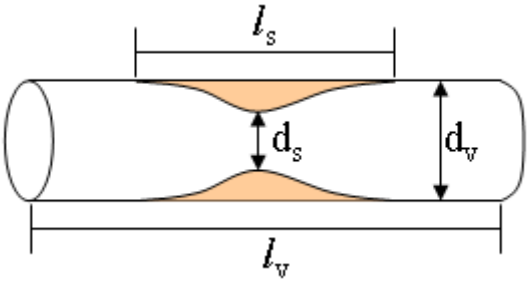

Figure 4.6 Modelling a stenosed vessel.

$$DoS = \frac{d_v - d_s}{d_v} \tag{4.13}$$

4.2 Numerical Procedure

The numerical computing environment and programming language, MATLAB, was used to write the code of all the models created for this thesis, as well as run the models' simulations. For efficiency of the matrix calculations written in MATLAB, the pressure units were changed from $mmHg$ to Ncm^{-2}, using the factor of 0.01332. In this thesis, all pressure values are given in $mmHg$ for simplicity.

4.2.1 Model Parameters

The inlet pressure P_a introduced at the afferent arteries is defined as the difference between the mean arterial pressure (MAP) and the intra-cranial pressure (ICP).

$$P_a = MAP - ICP \tag{4.14}$$

The outlet pressure P_v located at the end of the efferent variable resistances is equal to the central venous pressure (CVP). Note that there are slight differences in some of the physiological data found in the literature. This is because of the different

techniques used, or owing to the fact that these experimental data are obtained from different groups. This has small consequences for the model as these can be easily modified. The values of the physiological parameters used in the model are shown in Table 4.1. The MAP set point value (MAP_{sp}) is the normal average value of the mean arterial pressure.

Table 4.1 *Basic model parameters.*

Parameter	Value	Units
MAP_{sp}	100	$mmHg$
ICP	10	$mmHg$
CVP	4	$mmHg$
μ	$3.48 \times 10{-}7$	$Nscm^{-2}$
λ	3	s

The values of the controller parameters, K_i and K_p, used in the controller were chosen to replicate the experimental results of Newell et al. [91]. The experimental data shows the dynamic response of the flow through an MCA as a result of MAP drop from 100 mmHg to 80 mmHg in humans using TCD (Figure 4.7). The response takes approximately 20 seconds to go back to the normal initial value. Because the flowrates delivered to the brain tissue through the different efferent arteries are different, the values of K_i and K_p for each are different. These were obtained through trial and error to imitate the same response obtained by Newell et al. and are listed in Table 4.2. The value of the time constant λ used in the resistance dynamic response equation is adopted from the models of Ferrandez et al. [30, 38] and is shown in Table 4.1.

Table 4.2 *Controller equation parameters.*

Artery segment	K_p	K_i
ACA2	-0.1	-0.53
MCA	-0.1	-0.13
PCA2	-0.1	-0.23
AChA	-0.1	-80
SCbA	-0.1	-80

In this research the radii and lengths of the various arterial segments of a normal/classical complete CoW were obtained from a population study of MRA scans that was carried out by Arnold et al. [6, 88]. The mean values of the vessel's radii and length are shown in Table 4.3. Arnold et al. was not able to obtain the lengths of the ACA2 segments, therefore, the lengths of the ACA2s were adopted from data provided by Cieslicki et al. [26]. Moorhead has used similar averaged CoW data of the human population provided by Ferrandez et al. [38].

The parameters in this model are designed so they can be easily adjusted to account

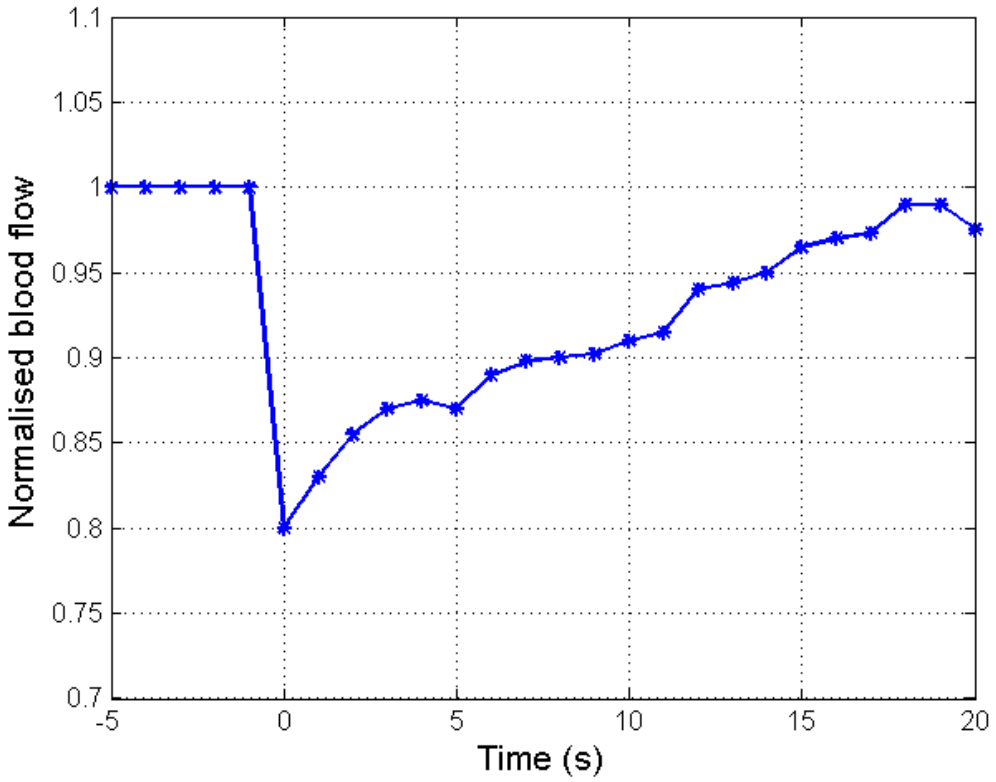

Figure 4.7 MCA flowrate change as a result of 20 mmHg drop in MAP [91].

for patient-specific data. This includes physiological parameters, such as the MAP, or CoW vessels' dimensions and geometry.

4.2.2 Initial Conditions

The average flowrate supplied to the human cerebral mass is $12.5cm^3s^{-1}$ [58]. The flowrates of the efferent arteries are taken to be inversely proportional to the mass of the brain territory which they supply. The normal values of the efferent arteries' variable resistances (calculated in $Nscm^{-5}$) were estimated based on the normal flowrates ratios through these efferent arteries. Moorhead, following Hillen et al., used the ratio of 6:3:4 for the arteries ACA2:MCA:PCA2 [58]. In this research, this ratio was modified slightly to 6:3:4:75:75 for the arteries ACA2:MCA:PCA2:AChA:SCbA to take into account the extra efferent arteries added. The initial values of variable resistance were established by solving the matrix Equation 4.7 using the normal MAP of 100 mmHg and the normal flowrates through the efferent arteries. The vector $\tilde{x}$ solves the values of the following: the *flowrates* through the constant-resistance segments of the CoW model, *resistance* of the variable-resistance segments, and *pressures* at all the CoW nodes.

Table 4.3 *Measured radii and lengths of the CoW vessels using MRA scans.*

Artery segment	**Radius (cm)**		**Length (cm)**	
	Mean	S.D.	Mean	S.D.
Afferent arteries				
BA1	0.1482	0.0236	0.1820	0.1019
BA2	0.1574	0.0249	2.8507	0.4517
Left ICA	0.2287	0.0261	17.0001	1.6487
Right ICA	0.2276	0.0264	17.1590	1.5879
CoW internal arteries				
ACoA	0.0750	0.0211	0.4332	0.1708
Left ACA1	0.1096	0.0287	1.7703	0.2362
Right ACA1	0.0919	0.0384	1.8283	0.3216
Left PCoA	0.0767	0.0211	1.5193	
Right PCoA	0.0812	0.0223	1.4800	0.2905
Left PCA1	0.1019	0.0217	0.9962	0.3033
Right PCA1	0.0961	0.0214	1.1040	0.4030
Efferent arteries				
Left ACA2	0.1136	0.0203	4.5	-
Right ACA2	0.1134	0.0231	4.5	-
Left MCA	0.1357	0.0170	1.7722	0.5665
Right MCA	0.1381	0.0213	1.7199	0.6863
Left PCA2	0.1032	0.0135	2.3799	0.6380
Right PCA2	0.0991	0.0144	2.5100	0.7179

4.2.3 Simulations

The simulation of the CoW hemodynamics is run as a function of time. For instance, for a MAP drop at time t, the matrix equation becomes a function of t as in Equation 4.15.

$$A(\tilde{x}(t))\ \tilde{x}(t) = \tilde{b}(t) \tag{4.15}$$

The pressure drop results in a flowrate drop at time (t=0). The error between the current flowrate and the reference flowrate is fed to the controller equation, which in turn activates the dynamic response of the variable resistances of the CoW efferent arteries (Equation 4.9). The variable resistances are therefore considered to be functions of the x vector, and they alter over time until the flowrates through the efferent arteries are restored to their original values, or until they reach their limit of vasoconstriction or vasodilation. At each time step, a stable solution of the variable resistances is found by iterating between Equations 4.15 and 4.9, where the latter equation is solved

numerically. The solution is then checked to make sure it is within the resistance limits set by the model. Figure 4.8 shows a schematic diagram of the numerical procedure of the basic CoW model. A dead-band was also implemented in this model, where the controller representing the arteries' vasomotion stops acting if the solution reaches a value within 7% of the optimal conditions. This was implemented in an attempt to achieve the slope observed in the autoregulation curve by Guyton et al. [47].

Results of the CoW hemodynamics simulations, including dynamic and static responses, are run for normal and abnormal configurations of the CoW under normal and various pathological conditions. These are shown in Section 8.1.

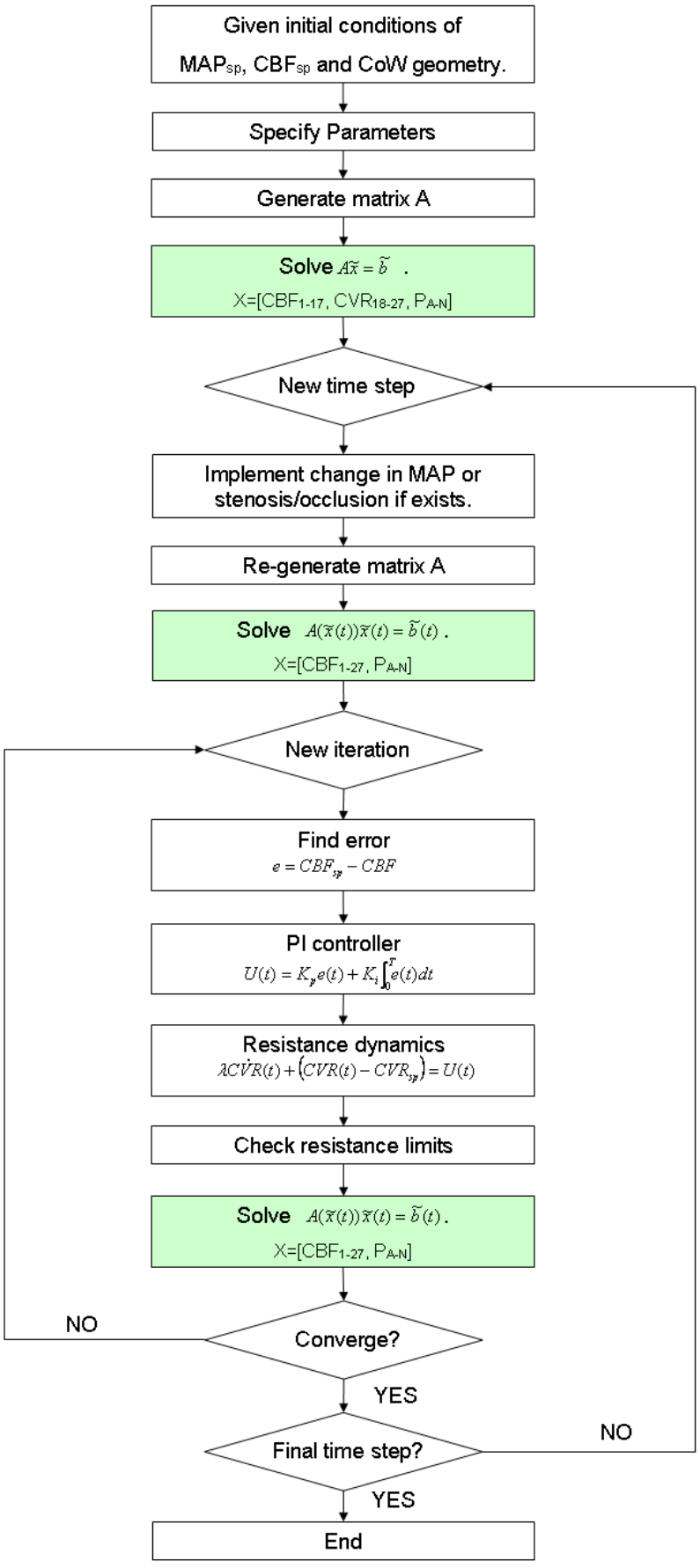

Figure 4.8 Numerical procedure of the CoW basic model.

Chapter 5

Linear Models

Using the fixed dead-band algorithm in the basic CoW model, described in Chapter 4, did not precisely attain the slope observed in the Guyton plot. Results of the fixed dead-band algorithm are provided in Chapter 8. The current chapter describes how different algorithms were applied as an attempt to reproduce this particular slope. The memory algorithm has a phenomenological basis while the metabolic rate algorithm has a more physiological basis. The CoW autoregulation model was also examined in terms of how the response may alter as some parameters are varied. These variations in parameters represent the differences between individuals in terms of speed of response as well as CoW geometry.

5.1 Variable Dead-band

The use of a 7% dead-band was implemented initially by Moorhead [90] in an attempt to replicate the slope observed in autoregulation curves. This dead-band algorithm did not achieve the autoregulation slope desired (autoregulation plots are provided in Section 8.1). In this research, the dead-band was modified by having a *variable* dead-band algorithm, which was carried out aiming to reproduce the autoregulation curve presented by Guyton et al. [47]. It was implemented using simple equations to achieve a dead-band of 7% at the LLA and ULA points; this dead-band decreases linearly until it reaches 0% at the optimal MAP of 100 mmHg. This is based on the assumption that different vessels in the cerebrovasculature have different ranges of dead-bands. This produces a reasonable slope in the autoregulation range (see results in Section 8.2). However, this algorithm is not justified physiologically.

5.2 Memory Algorithm

Although autoregulation holds flow almost constant in the steady state, the underlying change in the arteriolar radius takes 30-60 seconds to develop fully [76]. The development of the memory algorithm discussed here was performed to achieve the autoregulation slope on a phenomenological basis. The assumption that the autoregulation response in CoW takes into account the recent blood flux errors and disregards previous variations in flux was used in this memory algorithm. Originally, the integral part of Equation 4.8 was estimated numerically using Equation 5.1. The integral is estimated at time T+h as the numerical integration is evaluated at the end of each time step of the simulation, where h is the time step.

$$\int_0^{T+h} err(t)dt \;=\; err(T) \times h \;+\; \int_0^{T} err(t)dt \tag{5.1}$$

The term $exp(-\zeta h)$ was added to the integral estimation as in Equation 5.2 to represent the short memory adaptation where more recent fluctuations in the flowrate error correspond to greater influence on the controller input. The term ζ in the exponential term controls the duration of the short term memory in the algorithm.

$$\int_0^{T+h} err(t)dt \;=\; err(T) \times h \;+\; exp(-\zeta h) \int_0^{T} err(t)dt \tag{5.2}$$

The memory algorithm for short term adaptation to blood flow fluctuations in the model was implemented using Equation 5.3. This was derived from Equation 5.2 where it is simplified to a single integral term. The derivation is supplied in Appendix C.

$$\int_0^{T} err(t)dt = \int_0^{T} \; exp(-\zeta(T-\gamma)) \; err(\gamma)d\gamma \tag{5.3}$$

As a result of this memory algorithm adaptation, the controller gains, K_p and K_i, were modified to maintain the same blood flow dynamic response observed by Newell et al. [91]. These new values are given in Table 5.1.

5.3 Simple Metabolic Rate

The simple model of autoregulation was modified further to take into account the brain metabolism. The model of Keener et al. [65] (which is based on replicating the autoregulation slope of Guyton et al.) was implemented. It was assumed that the

Table 5.1 *Controller equation parameters for the memory algorithm.*

Artery segment	K_p	$K_i(\times 10^{-5})$
ACA2	-0.009	-0.53
MCA	-0.0023	-0.13
PCA2	-0.0041	-0.23
AChA	-0.01	-900
SCbA	-0.01	-900

resistance of arterioles is a function of the oxygen concentration in the venous blood. This assumption is based on the fact that arteries and veins tend to run side by side in the body, and therefore, the venous oxygen concentration may regulate the arterial resistance by the release and diffusion of regulatory substances.

The autoregulation was based on the basic Poiseuille equation defined by Equation 5.4 (similar to Equation 4.5) coupled with the cerebral oxygen consumption defined by Equation 5.5.

$$P_a - P_v = CVR \cdot CBF \tag{5.4}$$

$$(C_aO_2 - C_vO_2)CBF = CMRO_2 \tag{5.5}$$

Where C_aO_2 and C_vO_2 are the arterial and venous oxygen concentration, $CMRO_2$ is the metabolic rate of the oxygen consumption by the brain. $CMRO_2$ is defined as the rate of oxygen consumption per unit time. A linear relationship between arterial resistance (CVR) and venous oxygen content (C_vO_2) is defined in Equation 5.6. Keener et al. [65] considered the linearity assumption between CVR and C_vO_2 is reasonable in restricted ranges of oxygen content. S_R is the sensitivity of resistance to oxygen constant, which could represent physiologically the transfer of information from the venous to arterial beds.

$$CVR = CVR_{sp}(1 + S_R \cdot C_vO_2) \tag{5.6}$$

Equations 5.4, 5.5 and 5.6 are rearranged to define the CBF as a function of metabolic rate oxygen concentration and arterial oxygen concentration as given in Equation 5.7. See Appendix D for Equation 5.7 derivation.

$$CBF = \frac{1}{1 + S_R \cdot C_aO_2}\left(CMRO_2 \cdot S_R + \frac{P_a - P_v}{CVR_{sp}}\right) \tag{5.7}$$

The parameters S_R and CVR_{sp} were estimated using the autoregulation slope by Guyton et al., where the autoregulation range can be represented by Equation 5.8. Here the autoregulation is defined as a linear function of arterial pressure P_a. The CBF and P_a variables are normalised by their set point values CBF_{sp} and $P_{a_{sp}}$. The venous pressure P_v is a constant while P_a is a function of MAP as defined above in Equation 4.14. The values of set points are presented in Chapter 4.

$$\frac{CBF}{CBF_{sp}} = \frac{2}{3} + \frac{1}{3}\frac{P_a - P_v}{P_{a_{sp}} - P_v} \tag{5.8}$$

Equation 5.8 is equated with the normalised Equation 5.7 to evaluate the S_R and CVR_{sp} parameters defined in Equations 5.9 and 5.10. The derivations are provided in Appendix D.

$$S_R = \frac{2CBF_{sp}}{3CMRO_2 - 2C_aO_2 \cdot CBF_{sp}} \tag{5.9}$$

$$CVR_{sp} = \frac{3(P_{a_{sp}} - P_v)}{CBF_{sp}(1 + S_R \cdot C_aO_2)} \tag{5.10}$$

The equations by Keener et al. were designed for the total flowrate in the cerebral mass. In the model discussed in this thesis, these were modified so they can be implemented separately for each of the efferent arteries of the CoW. The $CMRO_2$, as well as the S_R and CVR_{sp} parameters were defined individually for the efferent CoW arteries as these arteries supply different amounts of brain tissue, and therefore, have different values of oxygen consumption. During the running of the model simulation the CBF, expressed as a function of pressure (defined in Equation 5.7), was calculated at each time step. This was set as the new reference CBF value used to calculate the error in the controller equation defined in Equation 4.8.

5.4 Leptomeningeal Arteries (LMA) Modelling

The leptomeningeal arteries (LMA) were previously described in Section 1.2.4.2. The 2003 study by Van der Zwan and Hillen [16] summarises the research done by different groups on LMAs. The LMAs are described as varying greatly between individuals. A number of authors also indicate the presence of intra-individual variability in number and size. This intra-individual variability influences the functional significance of LMA in, for example, stroke mechanisms. From the physical and physiological points of view, a LMA is an artery in which the blood can flow in both directions as a

function of hemodynamic and metabolic needs of the two territories that are connected by it. The most important factor influencing flow direction is the pressure drop between the ends of the artery. The compensatory capacity of one LMA is then inversely proportional to its hydraulic resistance. Therefore, size and number determine the total capacity of the LMA.

As mentioned above, several LMAs may be present to connect the distal sections of the main CoW efferent arteries (ACA2s, MCAs, and PCA2s). Owing to their number and size variability, all LMAs that connect two CoW efferent arteries were lumped together in one resistance. The LMA vessels were added to the CoW configuration as shown in Figure 5.1.

The Poiseuille and conservation of flow equations were rewritten to construct a new set of equations that represent the hemodynamics inside the CoW, taking into account the LMA vessels represented by 4 extra resistances. The size of matrix A in Equation 4.7 becomes 45×45. The additional number of Poiseuille equations and the modification of some of the conservation of flow equations are provided in Appendix B. The flowrates through LMAs were estimated to be 5% of the flow through the MCA at normal conditions. The literature lacks data on the blood flow through the smaller vessels in the CoW, especially on the LMA vessels. The estimates were guesses chosen to be sufficiently small not to have great effects on the general CoW hemodynamics as reported in the literature. Even though the LMAs are small in terms of size and the amount of flow that travels through them in normal conditions, physiologically these may have great compensatory capacity in some occlusion cases. Running the model with the LMA configuration shows almost exactly the same results as the original model without implementing the LMAs. The results are supplied in Chapter 8.

5.5 Model sensitivity

The current model consists of few assumed parameters. These parameters are the proportional gain K_p, the integral gain Ki, and the time constant of the autoregulation response λ. The proportional and integral gains are different for each efferent artery and were chosen so the response of the flowrate matches the response observed by Newell et al. [91] as described in Section 4.2.1.

The λ parameter has a physiological dependence. The walls of all arteries undergo changes as they age. Degenerative changes in arteries due to, for example, arteriosclerosis result in changes in the smooth muscle contraction time. These changes occur in many individuals and become more severe with advancing age [76]. This can be modelled by increasing the value of λ which will cause a slower response in CoW hemo-

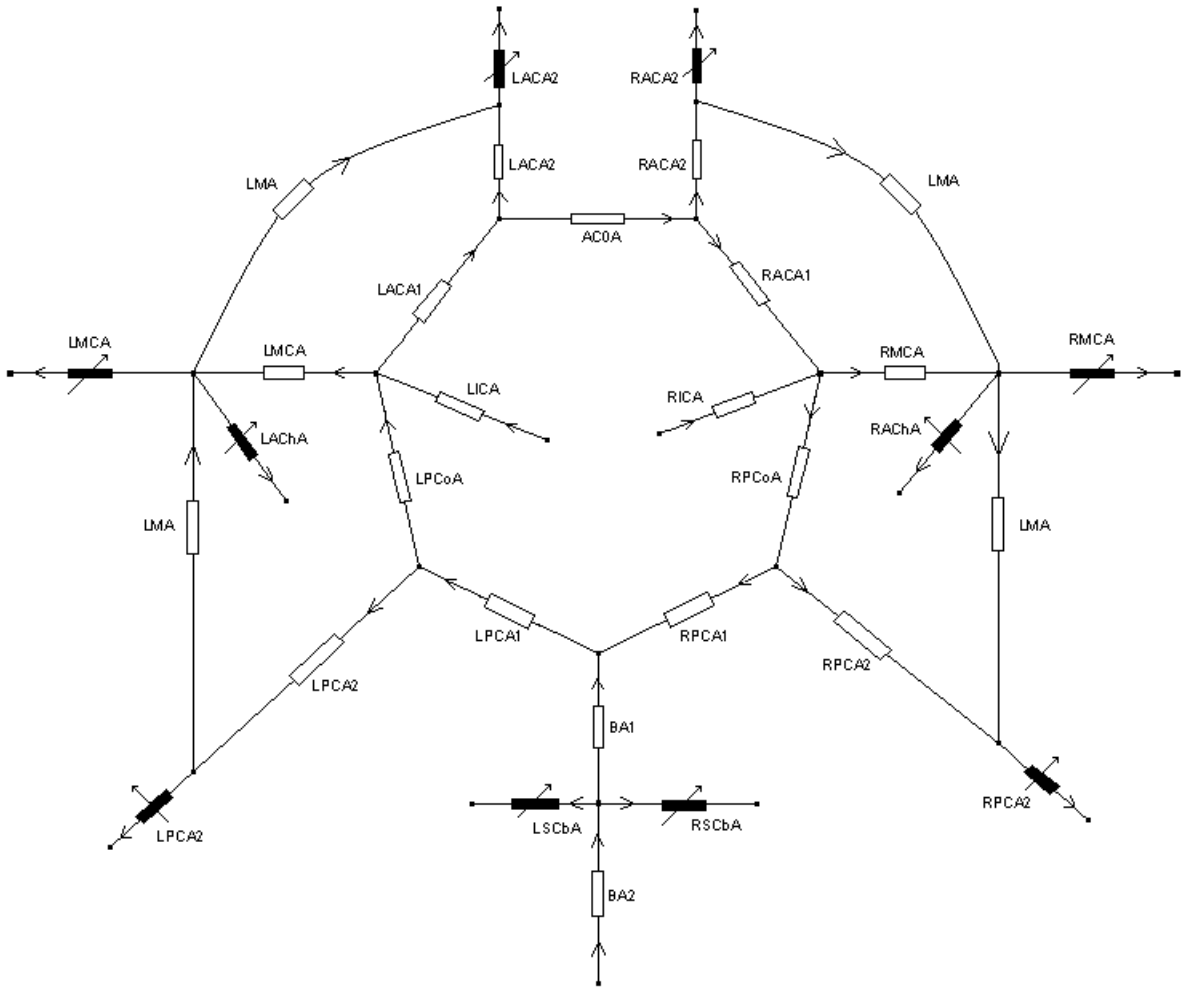

Figure 5.1 CoW configuration with LMA.

dynamics, and therefore, shift the upper and lower limits of autoregulation to higher pressure values.

In order to test how varying λ influences the response, in other words to test the sensitivity of the model to that specific parameter, λ was increased from the value of 3 to 10, 30 and 100. This was tested under the condition of having a 20 mmHg pressure drop in MAP. It was expected that any efferent artery that had a higher λ value would affect the flow response in that particular artery. It was also expected that the flow response in other efferent arteries of the ipsilateral side would change by having a small increase in response as a result of reduced flow in the efferent artery with the higher value of λ. Tables and plots of the response as a consequence to changing the time constant parameter are provided in Chapter 8.

Another aspect that should be considered in modelling the CoW is the fact that the dimensions of the CoW arteries are averaged values from the population study

by Arnold et al. [6, 88]. These dimensions vary slightly from one person to another and an important issue is to examine how varying the dimensions might influence the hemodynamics of the current model and how sensitive the model is to these variations.

The CoW configuration has 17 afferent and internal arteries, and 10 efferent arteries. Varying the radius of one of these internal arteries has an effect on the flow response in other arteries. Here, the radius variability was tested for specific arteries of the CoW, which are the ACoA, PCoA, and MCA. These were chosen because the ACoA and PCoA play a very vital role in terms of collateral cerebral circulation in the case of an afferent artery stenosis or occlusion. The MCA was also chosen for testing because it represents the biggest efferent artery that supplies the cerebral mass. The relationship between varying the radius of one of the selected arteries and the change in response in the CoW was examined to see if it was negligible or if it resulted in, for example, a linear relationship.

As indicated in Section 4.1.2, the matrix A contains the CoW vessel resistances. Varying the radius of any vessel of the CoW changes its resistance. The change in resistances was represented by the matrix ∂A. This is implemented in the matrix equation as in Equation 5.11.

$$x = (A + \partial A)^{-1} b \tag{5.11}$$

To be calculated numerically, Equation 5.11 is rewritten as given in Equation 5.12. See Appendix E for matrix transformations of this equation.

$$x = (A^{-1} - A^{-1} \partial A A^{-1}) b \tag{5.12}$$

The resistance of the artery with a change in its radius is represented by Equation 5.13.

$$R = \frac{8 \mu l_v}{\pi (r_v + dr_v)^4} \tag{5.13}$$

This resistance includes both the resistance encountered in matrix A and the difference of resistance encountered in matrix ∂A. The radius equation provided in Equation 5.13 is rewritten in a different format, provided in Equation 5.14, in order to distinguish between the two parts of the resistance.

$$R = C_R \, r_v^{-4} - 4 C_R \, r_v^{-4} \frac{dr_v}{r_v} + C_R \, r_v^{-4} \frac{20}{2!} \left(\frac{dr_v}{r_v} \right)^2 - C_R \, r_v^{-4} \frac{120}{3!} \left(\frac{dr_v}{r_v} \right)^3 + \ldots \tag{5.14}$$

The first term on the RHS is the normal resistance of a particular vessel in the matrix A, while the the rest of the terms on the RHS contribute to the change in resistance for the same vessel, which is implemented in the ∂A matrix. See Appendix E for the derivation of the resistance provided in Equation 5.14. To test the linearity, the radius of a specific artery was reduced by 1 standard deviation at a time, while measuring the difference in the flowrate response as a result of 20 mmHg pressure drop in MAP. The results are supplied in Chapter 8.

Chapter 6

Non-Linear Models

Up to this point, the CoW autoregulation model used had resulted in a linear system. No losses of energy were considered as a result of the shape of the CoW geometry. In this chapter, the pressure losses encountered at the CoW bifurcations were first considered while still keeping the model as a linear system. This was modified further by adopting the resistance equations proposed by Cieslicki et al. [26], resulting in a non-linear model. Using the new non-linear system of equations, the metabolic model was further modified.

6.1 Pressure Losses in CoW Nodes

The CoW configuration can be considered as a very small and fine network of pipes where the flow of fluid (in this case blood) might combine or divide at the junctions. Pipe networks have head losses at junctions. These losses are pressure drops which resemble the energy lost in order to change the direction of fluid flow and as a result of recirculation eddies. An algorithm for implementing the pressure losses was added to the model to account for any losses at the CoW nodes. In terms of hydrodynamics, the CoW is an extremely complicated flow system.

The vessels of the CoW system encounter laminar flow within its vessels because of the low Reynolds numbers. Only viscous forces are important at low Reynolds numbers, making shear, and therefore, energy dissipation directly proportional to velocity. The pressure losses in CoW junctions (nodes), also called minor losses, are expressed in terms of the coefficient K_L as given in Equation 6.1, where V is the average velocity and ρ is blood density [86, 106].

$$P_{Loss} = K_L \frac{\rho V^2}{2} \tag{6.1}$$

For a laminar flow, the loss coefficient K_L for a particular junction is inversely

proportional to the Reynolds number as shown in Equation 6.2, where C_L is defined as a constant [86].

$$K_L = \frac{C_L}{Re} \tag{6.2}$$

In the literature, the loss coefficients are well investigated for turbulent flows. Researchers have provided loss coefficient data with respect to bifurcating and combining vessels' angles. Since the Reynolds number for blood is small, the same loss coefficients used in the normal pipe networks could not be used. There were no data available to evaluate the constant C_L; therefore, an estimation of C_L was made defining it as a function of the bifurcating or combining angle as in Equation 6.3.

$$C_L = C\frac{\theta}{180} \tag{6.3}$$

The parameter C was varied between 0.5-1000 to examine the effects it has on the CoW hemodynamics. The parameter θ is the angle between the vessels' bifurcation or combination as in Figure 6.1. The Reynolds number is defined in Equation 6.4, where V is the average blood velocity, d_v is the vessel diameter, and ν is the blood kinematic viscosity.

$$Re = \frac{Vd_v}{\nu} \tag{6.4}$$

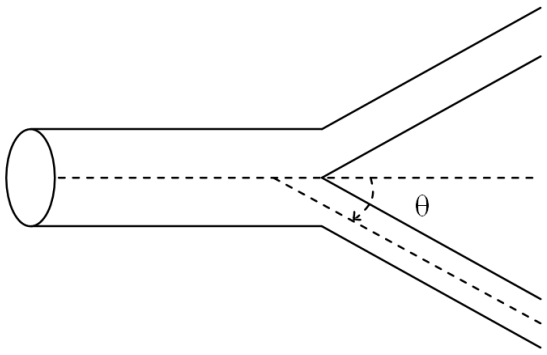

Figure 6.1 Angle between the vessels' bifurcation or combination.

The average blood velocity can be defined in terms of flowrate and cross sectional area A_{cs} as in Equation 6.5, where CBF stands for the cerebral blood flow. The blood kinematic viscosity is a function of absolute viscosity (μ) and blood density (ρ) as in Equation 6.6. Equations 6.2, 6.4, 6.5, and 6.6 are inserted in Equation 6.1, which is rearranged as given in Equation 6.7.

$$V = \frac{CBF}{A_{cs}} \tag{6.5}$$

$$\nu = \frac{\mu}{\rho} \tag{6.6}$$

$$P_{Loss} = \frac{C_L \mu}{4\pi r^3} CBF \tag{6.7}$$

Equation 6.7 was introduced to the CoW system by inserting the pressure loss term in the Poiseuille equation defined in Equation 4.5. An example is given in Figure 6.2.

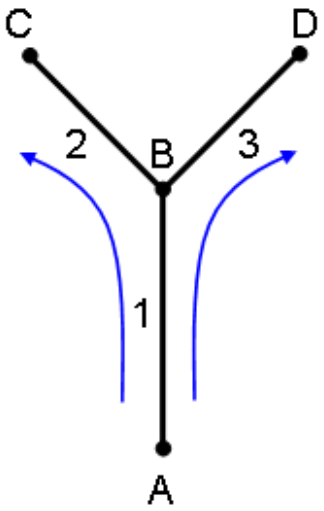

Figure 6.2 Simple example to demonstrate pressure losses implementation.

The original Poiseuille equation for segment 2 in the example is given by Equation 6.8.

$$CVR_2 \; CBF_2 = P_B - P_C \tag{6.8}$$

To take into account the pressure loss at node B as a result of flowrate in segment 1 dividing into segments 2 and 3, the equation is rewritten as in Equation 6.9.

$$CVR_2 \; CBF_2 = P_B - P_C - \frac{C_L \mu}{4\pi r_1^3} CBF_1 \tag{6.9}$$

This is rearranged to be in a matrix form as in Equation 6.10.

$$CVR_2 \; CBF_2 + \frac{C_L \mu}{4\pi r_1^3} CBF_1 - P_B + P_C = 0 \tag{6.10}$$

The matrix A is rearranged so that the extra flowrate term in the equation is

accounted for. This does not increase the number of unknowns in the system. The CoW system is still linear with the addition of the pressure losses at the CoW nodes; therefore, there is no significant increase in the amount of computation required to solve the system.

6.2 Tortuosity of CoW Vessels

The CoW nodes cause flow disturbances that result in velocity profile development along the outgoing branches of the nodes. On the other hand, tortuosity of the CoW segments gives rise to centripetal forces which are developed through the appearance of secondary flows in the plane perpendicular to the main stream. Because of these two effects, pressure-flow relations in all arterial segments are assumed to be non-linear. These effects were investigated by Cieslicki et al. [26]: a vascular phantom of the CoW was created by a group of neurosurgeons and anatomists based on the microsurgical anatomy of a large number of specimens. As described in the Literature Review (Chapter 3), this phantom was used to run tests on the pressure and flowrates in the CoW phantom.

The experimental investigations by Cieslicki et al. lead to the conclusion that the CoW vessels' resistance cannot simply be represented by Equation 4.6. A straight vessel segment in the CoW experiences an increase of energy dissipation because of velocity profile development and the non-zero net kinetic energy flowing in the the segment. The new resistance of a straight vessel (R_s) is represented by Equation 6.11, where R is the original hydraulic resistance defined in Equation 4.6. The new equation shows that the resistance of a segment increases linearly as the Reynolds number increases and that the greater the diameter to length ratio, the faster the increase.

$$R_s = R\left(1 + 0.044\frac{d_v}{l_v}Re\right) \tag{6.11}$$

The resistance of a tortuous CoW vessel (R_t) is defined as a function of its radius and bend curvature radius (a_k). Two equations are introduced to calculate the resistance of a tortuous CoW vessel: the first is for a segment experiencing a Reynolds number smaller than 100 (Equation 6.12) and the second is for a segment with a Reynolds number higher than 100 (Equation 6.13). The equations were based on experimental work by Cieslicki et al. on the resistance of multiple bent segments.

$$R_t = R\left(0.526 + \sqrt{0.225 + 0.022\sqrt{\frac{r_v}{a_k}}Re}\right) \tag{6.12}$$

$$R_t = R\left(0.626 + 0.1455\sqrt[4]{\frac{r_v}{a_k}}\sqrt{Re}\right) \tag{6.13}$$

Figure 6.3 displays the plots for the different equations used to calculate the resistance of a CoW vessel for a Reynolds number range typical in physiology. The three different equations represent the original hydraulic resistance, the straight vessel resistance and the tortuous vessel resistance, all normalised by the original hydraulic resistance. The tortuous resistance plot is for d/l ratio of 0.1 and r/a_k ratio of 0.36. The figure shows that the non-linear resistances are 1.5 to 3 times larger than the linear resistance calculated by the original hydraulic resistance equation.

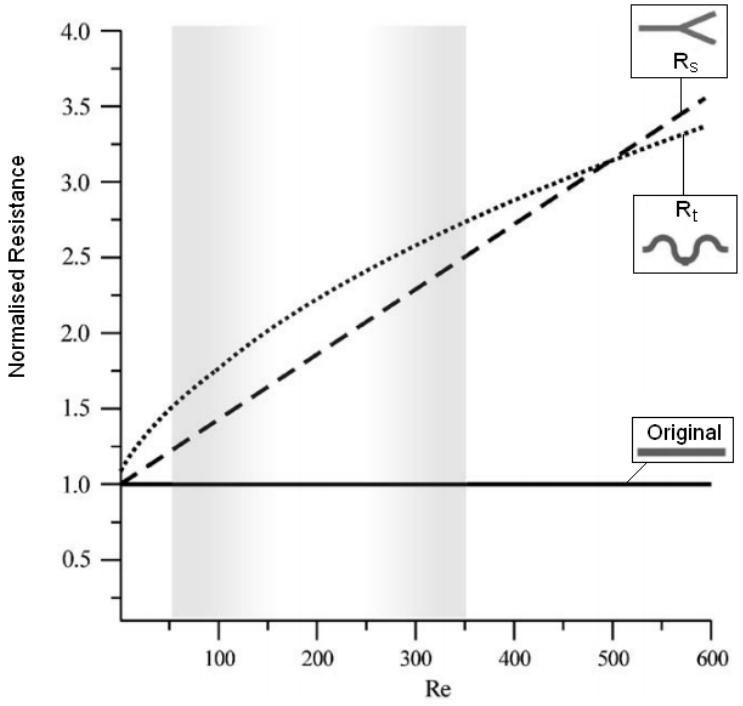

Figure 6.3 Plots for using original resistance, straight vessel resistance, and tortuous resistance equations within a physiological range of Reynolds number [26].

The straight vessel resistance equation (Equation 6.11) is implemented for the BA and PCoA while the tortuous vessel resistance equation (Equation 6.11 or 6.13) is used for the rest of the CoW segments. When these new resistance equations are implemented into the CoW model, the set of Poiseuille equations become non-linear; therefore, Newton's method was used in solving these equations. The non-linear system of equation is written in the form:

$$\begin{aligned}\mathbf{F}(\mathbf{x}) &= 0 \\ &= \mathbf{F}(x_1, x_2, \cdots, x_{41}) \\ &= (\ f_1(x_1, x_2, \cdots, x_{41}), f_2(x_1, x_2, \cdots, x_{41}), \cdots, \\ &\quad f_{41}(x_1, x_2, \cdots, x_{41})\ )\end{aligned} \tag{6.14}$$

The Jacobian matrix used in Newton's method for numerically solving a system of non-linear equations is defined by:

$$\mathbf{J}(\mathbf{x}) = \begin{bmatrix} \frac{\partial f_1(\mathbf{x})}{\partial x_1} & \frac{\partial f_1(\mathbf{x})}{\partial x_2} & \cdots & \frac{\partial f_1(\mathbf{x})}{\partial x_{41}} \\ \frac{\partial f_2(\mathbf{x})}{\partial x_1} & \frac{\partial f_2(\mathbf{x})}{\partial x_2} & \cdots & \frac{\partial f_2(\mathbf{x})}{\partial x_{41}} \\ \vdots & \vdots & & \vdots \\ \frac{\partial f_{41}(\mathbf{x})}{\partial x_1} & \frac{\partial f_{41}(\mathbf{x})}{\partial x_2} & \cdots & \frac{\partial f_{41}(\mathbf{x})}{\partial x_{41}} \end{bmatrix} \tag{6.15}$$

Figure 6.4 shows a schematic diagram of the numerical procedure to solve the non-linear set of equations. This algorithm is inserted every time the linear set of equations was solved in the basic model, replacing the green shaded boxes in the initial schematic diagram (Figure 4.8). Results of running this non-linear model are presented in Section 8.3, where they are compared with the linear CoW model.

6.3 The Metabolic Model

The simple metabolic model represented in Section 5.3 was further modified in collaberation with Steve Moore [89]. As mentioned above, the cerebral blood flow (CBF) is closely related to the metabolism of the cerebral tissue. Three main metabolic factors have great effects on controlling cerebral blood flow. These are oxygen (O_2) concentration, carbon dioxide (CO_2) concentration and hydrogen ion (H^+) concentration.

The O_2 and CO_2 exchange dynamics equations were based on the models by Thoman et al. and Gutierrez et al. [46, 118]. The cerebral metabolic rate of oxygen consumption is defined as a function of temperature (T) as in Equation 6.16.

$$CMRO_2 = exp(-2.7579 + 0.1089T) \tag{6.16}$$

The amount of oxygen delivered to the brain is determined by arterial oxygen content CaO_2 defined by

$$CaO_2 = (SaO_2 \times [Hb] \times 1.39) + (PO_2) \tag{6.17}$$

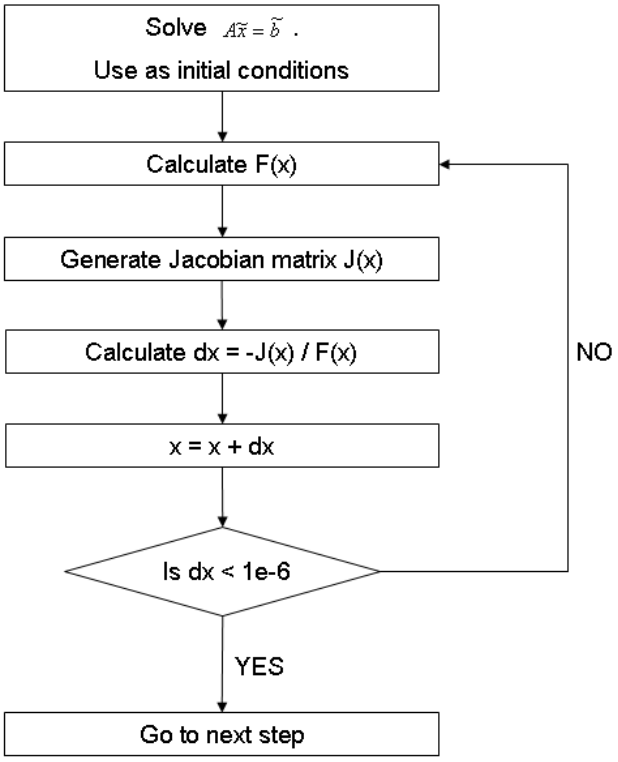

Figure 6.4 Numerical procedure for evaluating the non-linear equations using Newton's method.

Where [Hb] is the haemoglobin concentration and SaO_2 is the oxygen saturation factor, which is a function of oxygen partial pressure (PO_2) as follows:

For $0 \leq PO_2 < 40$

$$SaO_2 = -0.9175607 + (1.0438527 \times PO_2) - (0.021241344 \times PO_2^2)$$

For $40 \leq PO_2 < 140$

$$SaO_2 = -34.991452 + (4.766072 \times PO_2) - (0.067696104 \times PO_2^2) + (0.0004358606 \times PO_2^3) - (1.045397 \times 10^{-6} \times PO_2^4)$$

For $PO_2 \geq 140$

$$SaO_2 = 100$$

The arterial carbon dioxide content is defined in Equation 6.18 using Douglas et al.'s model [35].

$$\begin{aligned} CaCO_2 = & 2.26 \times 0.0307 \times PCO_2 \times \left(1 + 10^{pH-6.0907}\right) \\ & \times \left(\frac{1 - 0.0289[Hb]}{(3.352 - 0.00456SaO_2)(8.142 - pH)}\right) \end{aligned} \tag{6.18}$$

Where PCO_2 is the carbon dioxide partial pressure and pH is a measure of concentration of hydrogen ions in the blood.

Under normal conditions, the amount of oxygen delivered to the brain far exceeds the demand. When CBF decreases below the lower limit of autoregulation but the oxygen demand remains high, extraction of oxygen (OEF) from blood can be increased to 70%. For this model, the default oxygen extraction was 30%.

$$O_2Delivery = CBF \times OEF \times CaO_2 \tag{6.19}$$

The following equations were derived from Gutierrez's two compartments model. The rate of change of carbon dioxide in the tissue is a function of metabolic rate and the net difference of CO_2 in tissue and artery, which are removed by the blood.

$$\frac{dCtCO_2}{dt} = CMRO_2 + CBF \times (CaCO_2 - CtCO_2) \tag{6.20}$$

The ideal or set-point of carbon dioxide concentration in tissue is determined by setting the $CtCO_2$ differential equation to zero ($\frac{dCtCO_2}{dt} = 0$), where the resultant is defined as

$$CtCO_{2,sp} = CaCO_2 + \frac{CMRO_2}{CBF} \tag{6.21}$$

The cerebrovascular resistance (CVR) is bound by two limits: the lower limit where the artery is at its maximum dilation radius, and the upper limit where the artery is at its maximum constriction radius. The CVR is assumed to have a sigmoidal function

$$CVR = \frac{CVR_{ll} \ + \ CVR_{ul} \times exp(AUT_{CVR} - c)}{1 + exp(AUT_{CVR} - c)} \tag{6.22}$$

The AUT_{CVR}, defined by Equation 6.23, is the actuator as a function of how far the CO_2 concentration in the tissue is from its set point, where K2 is a proportional gain. Equation 6.24 defines the variable c in the sigmoidal function, which is inserted to ensure non-activation when the resistance is at the ideal set point value. It is essential to use c in the sigmoidal equation because the upper and lower limits are not equally distant from the ideal resistance.

$$\frac{dAUT_{CVR}}{dt} = K2(CtCO_{2,sp} - CtCO_2) \tag{6.23}$$

$$c = -ln\left(\frac{CVR_{sp} - CVR_{ll}}{CVR_{ul} - CVR_{sp}}\right) \tag{6.24}$$

Similarly, the oxygen extraction factor (OEF) is bound by two limits: the lower limit of zero extraction, and the upper limit of 70%. The OEF is a sigmoidal function, as defined in Equation 6.25, where the rate of change in the actuator AUT_{OEF} (Equation 6.26) is a function of oxygen demand and oxygen delivery. K3 is a proportional gain and o is the sigmoidal function where it has no activation at the OEF set point of 30% as defined in Equation 6.27.

$$OEF = \frac{OEF_{ll} \ + \ OEF_{ul} \times exp(AUT_{OEF} - o)}{1 + exp(AUT_{OEF} - o)} \tag{6.25}$$

$$\frac{dAUT_{OEF}}{dt} = K3(CMRO_2 \ - \ CBF \times OEF \times CaO_2) \tag{6.26}$$

$$o = -ln\left(\frac{OEF_{sp} - OEF_{ll}}{OEF_{sul} - OEF_{sp}}\right) \tag{6.27}$$

The equations presented above replace the autoregulation model equations discussed in the basic model section, where the three differential equations for C_tCO_2, AUT_{CVR} and AUT_{OEF} autoregulate the system. The actuator equations replace the function of the PI controller equation described in Chapter 4. The reference conditions are now based on the CO_2 concentration in the tissue rather than the CBF, which is

more realistic physiologically. This is because the tissue is not affected by the amount of blood flowrate but rather by the metabolites that are delivered to or removed from the tissue. Figure 6.5 shows a schematic diagram of the new numerical procedure of the model. Results of running this modified metabolic model are presented in Section 8.3, where they are compared with the basic CoW model results.

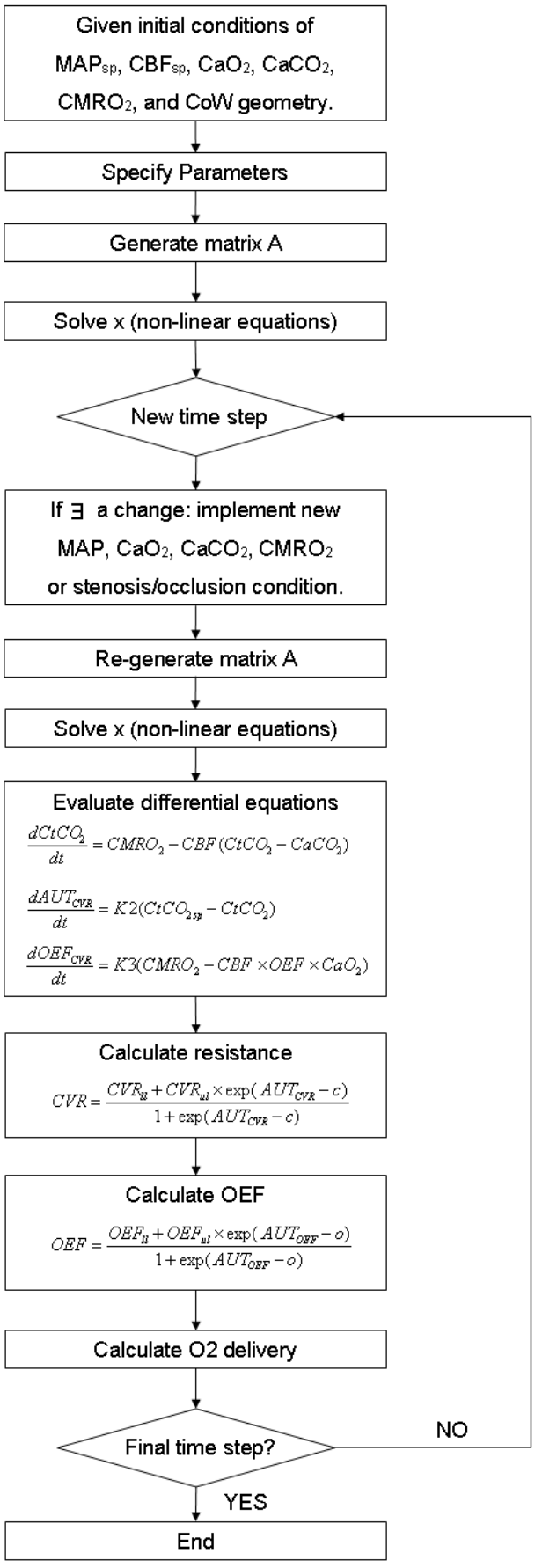

Figure 6.5 Numerical procedure of the metabolic model.

Chapter 7

Arterial Tree Model

The blood delivered through the vascular system carries oxygen and important nutrients to all parts of the body as well as removing metabolic wastes. As mentioned in Chapter 1, the brain consumes 20% of the total oxygen supplied to the body even though it is, on average, only 2% of the total body weight. This makes the study of the vasculature in the cerebral mass crucial in understanding how the oxygen delivery is maintained through the sufficient supply of oxygen-rich blood to different parts of the brain.

Up to this stage in the research, the CoW peripheral arteries were modelled as lumped parameters, which represent the resistance encountered by the vascular system from a specific CoW efferent artery to the venous bed. This chapter presents a model of the arterial tree that represents the cerebral vasculature from the CoW efferent arteries down to the capillaries. This arterial tree implements blood autoregulation at different levels of the tree, which is maintained using myogenic and metabolic mechanisms. These two mechanisms are assumed to be active at different levels of the tree depending on the size of the vessels.

7.1 Binary Arterial Tree

In the literature, many models exist for coronal arterial trees but almost none are available for the arterial tree in the cerebral mass. The principles of branching algorithms are the same for all organs. However, branching patterns may differ in the cerebral mass as a result of higher vasculature density to meet the high metabolic demand. Zamir suggests a distinction between a vascular tree that serves a metabolic function, such as the heart and the brain, and one that serves a processing function, such as the lung or the kidney [141].

The model created here is simple, fractal, non-spatial and has no branching angles. It is based on structural and functional parameters that affect vessels' radii and blood

flowrate delivered to a specific cerebral mass. The arterial tree branching mechanism was based on the fractal vascular network by Steele et al. [112], which utilises Zamir's tree structure examination of the right coronary artery of a human heart. It is able to predict blood flow and pressure at any position of the tree and is mainly based on two variables: power exponent k and asymmetry ratio γ.

The power exponent describes the bifurcation relationship between the parent vessel radius, r_p, and the daughter vessels radii, r_{d1} and r_{d2}. There are two ways to describe this relationship. First, the area ratio principle defined in Equation 7.1, which is a measure of the change in cross sectional area available to the flow as it progresses from the parent segment to the two daughter segments. Second, the power law principle defined in Equation 7.2.

$$\eta = \frac{r_{d1}^2 + r_{d2}^2}{r_p^2} \tag{7.1}$$

$$r_p^k = r_{d1}^k + r_{d2}^k \tag{7.2}$$

The area will be conserved if the k value was chosen to be 2, resulting in a η value of 1. This corresponds to a condition of zero expansion in the cross sectional area. The cube law is satisfied if the k value was chosen to be 3, which corresponds to maximum efficiency for blood flow (Murray's law[1]).It is clear that η and k are related to each other as they are both measures of expansion or contraction of the cross sectional area. Studies by different researchers suggest that the k value is not constant or organ specific, but rather varies between the two values associated with the square and cube laws based on size of the parent vessel radius.

The asymmetry ratio (also called bifurcation index) describes the relative relationship between the two daughter vessels. Again, the asymmetry ratio does not appear to be organ specific. A large number of arterial bifurcations have a mixed degree of asymmetry at all levels of the tree. The γ value was set to vary based on the parent vessel radius.

The radii of the daughter vessels r_{d1} and r_{d2} were defined as a function of the parent vessel radius r_p as given in Equations 7.3 and 7.4, where they were scaled by the factors α and β.

$$r_{d1} = \alpha r_p \tag{7.3}$$

$$r_{d2} = \beta r_p \tag{7.4}$$

[1]See Glossary

The parameters α and β were defined by Zamir [141] as functions of k and γ as in Equations 7.5 and 7.6.

$$\alpha = \left(1 + \gamma^{(k/2)}\right)^{-(1/k)} \tag{7.5}$$

$$\beta = \alpha\sqrt{\gamma} \tag{7.6}$$

The concept of radius sub-ranges of vessels introduced by Zamir was adopted in this research. Each sub-range has a different value of the power exponent and the asymmetry ratio. The k and γ values are given in Table 7.1 as a function of the parent vessel's radius.

Table 7.1 *Values of the power exponent and asymmetry ratio at different ranges of the arterial tree.*

	Radius r (cm)	Power Exponent k	Asymmetry Ratio γ
Arteries	$250\times10^{-4} <$ r	2.50	0.4
Arterioles	$250\times10^{-4} <$ r $< 50\times10^{-4}$	2.76	0.6
Capillaries	r $< 50\times10^{-4}$	2.9	0.9

Using the radius of a specific vessel, called the *root* vessel, the arterial tree was created using the algorithm described above. Initially, the root vessel was defined as the parent vessel producing two daughter vessels as defined by Equations 7.3 and 7.4. Then, every new daughter vessel becomes a parent vessel in turn, where the scaling parameters α and β were used again as shown in Figure 7.1. This was repeated for all new vessels created in the arterial tree until the vessels reach an assumed arteriole radius of $10\mu m$. These are called *terminal vessels* or *leaves*. Figure 7.2 shows a schematic diagram of the process of creating an arterial binary tree. Each of the terminal vessels were set to supply a capillary bed which have a large number of capillaries with radius size of $2.5\mu m$. Each one of the capillaries supply a certain cylindric volume of tissue which surrounds it. This is described more in detail in Section 7.4.

Another important aspect that defines the arterial tree is the length of the vessels. This was set as a function of the radius of that particular vessel. The length to radius ratio l_{rr} was introduced to describe this relationship. Studies by different researches (Brown [15], Iberall [61], Zamir [141]) give different values for l_{rr} ranging from a mean of 20 to a maximum value of 70. In this model, the l_{rr} value was chosen to be 20.

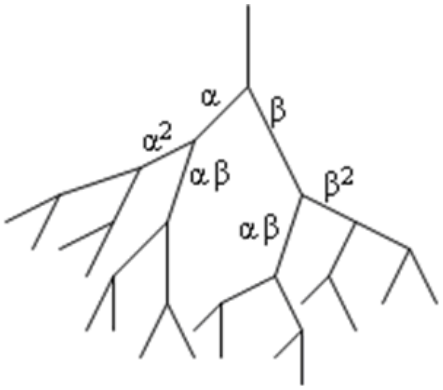

Figure 7.1 Asymmetric arterial tree using scaling parameters α and β.

7.1.1 Microcirculation Morphometry

There are not many human or animal studies on the morphometry of the cerebrovascular system in the literature, especially down to the microcirculation level. The latest study by Lauwers et al. [75] has shed light on the statistical and quantitative data of the arterial tree in the cortex. The study was done by scanning a specific volume (35.5 mm^3) of the cerebral cortex (Figure 7.3). As a result, more than 350,000 vessels were digitized and identified as part of either a tree-like or a net-like network. The topological structure of the cerebral arterioles and venules is tree-like, while that of the capillaries is net-like. The statistical data of the length and diameter of the vessels in the examined volume were presented. The 3D images of the network were of an India ink-injected part of the brain located next to the collateral sulcus in the right temporal lobe.

The statistical data of Lauwers et al. were used in the generation of vessels in the arterial binary tree model. The main statistical data obtained from the study were the complete network and capillary network population distributions. These were used to provide a normal distribution to the vessel radii of the arterial tree model as found in that research. The distributions are shown in Figure 7.4 and Table 7.2. The distributions of the length and diameter of the vessels across the complete network were asymmetric. However, a mapping using the transformation function of the natural logarithm for length, and the inverse square root for the diameter, resulted in normal distributions. Other authors have noted these distribution features (Hudetz et al. [60] and Pawlik et al. [103]). The capillary network diameter by itself has a normal distribution. The distributions properties from the Lauwers et al. study were utilized in the current arterial tree model in order to have probability density functions that reflect the same data. Each time a new daughter vessel is created, the distributions properties were applied. First, the inverse square root transformation function was applied to the diameter of the daughter vessel. The resulting value was used as the mean for a

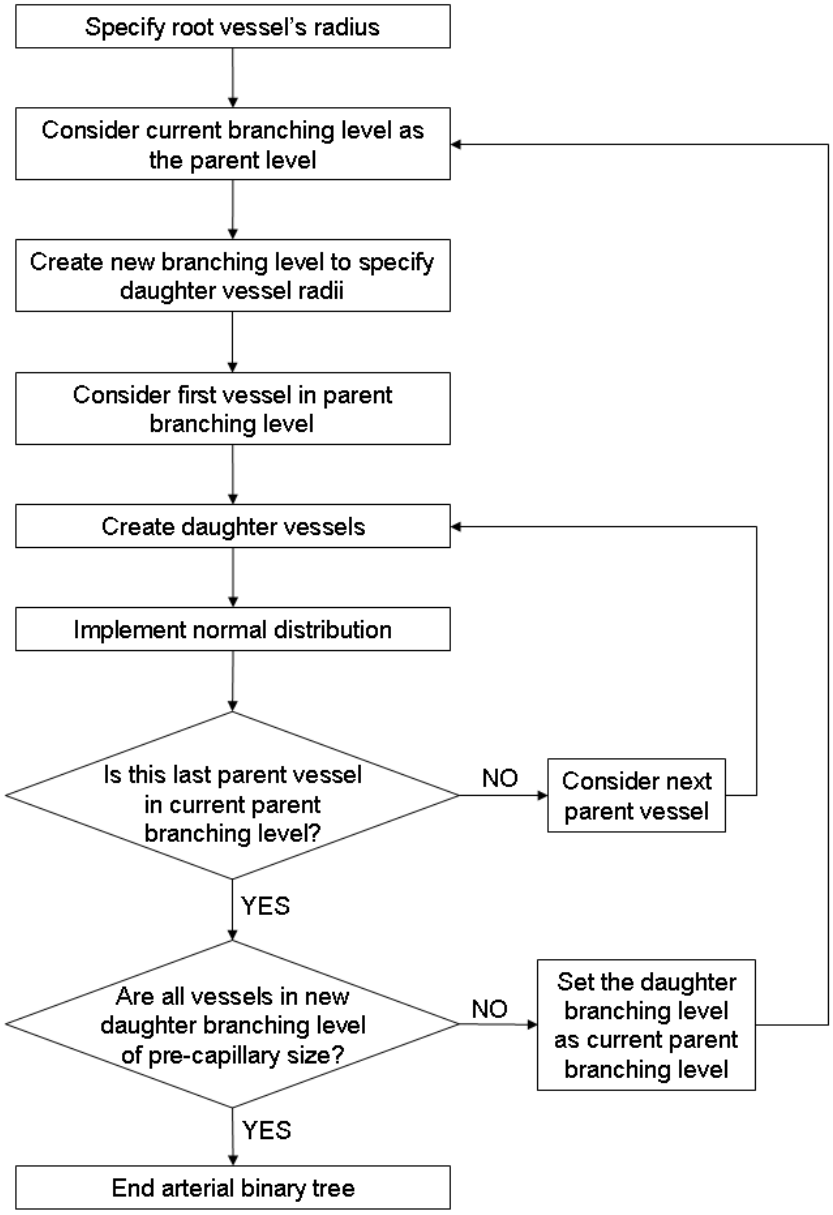

Figure 7.2 Schematic diagram of the process of creating an arterial binary tree.

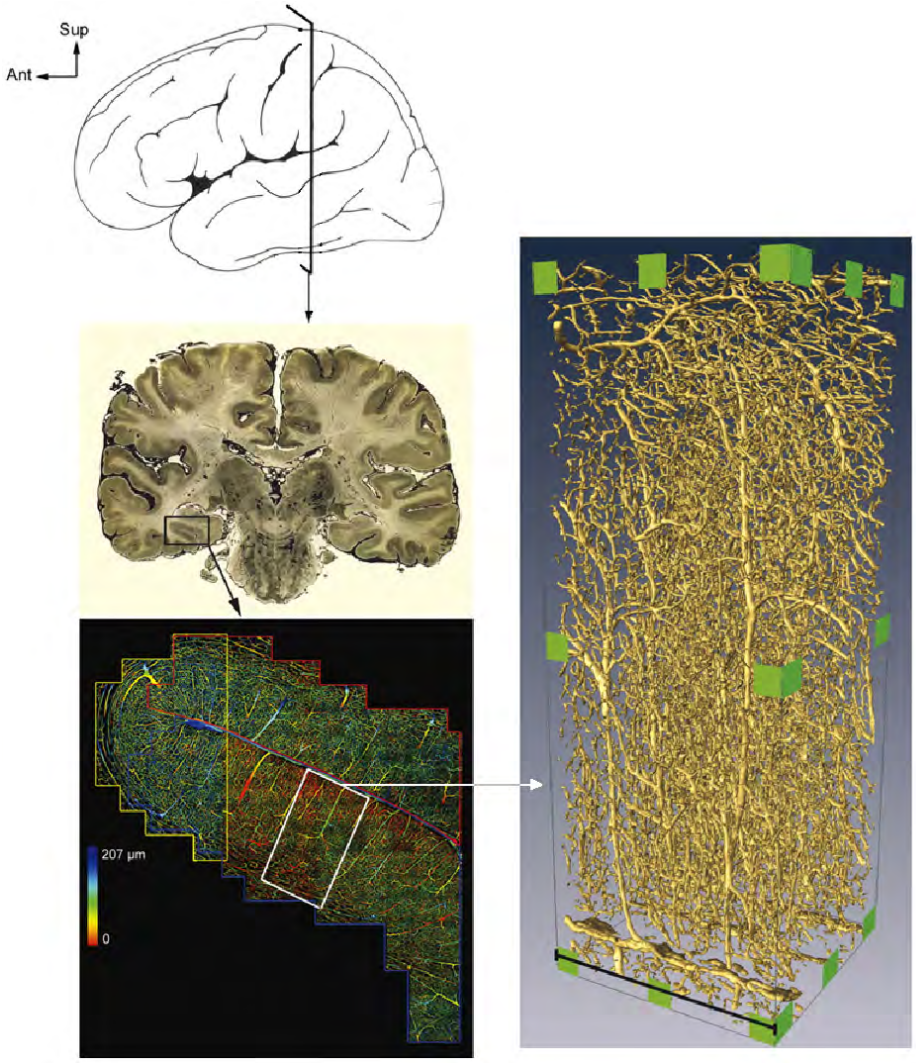

Figure 7.3 Lauwers et al.'s method of scanning and mapping cerebral vasculature [75].

normal distribution where the standard deviation value was adopted from the Lauwers at al. study. A random value from the normal distribution is selected and the reverse-transformation function was applied to find the new diameter of the daughter vessel. The same process is implemented for the length of the same vessel but using the natural logarithm transformation function instead. This is repeated for each daughter vessel created in the binary arterial tree.

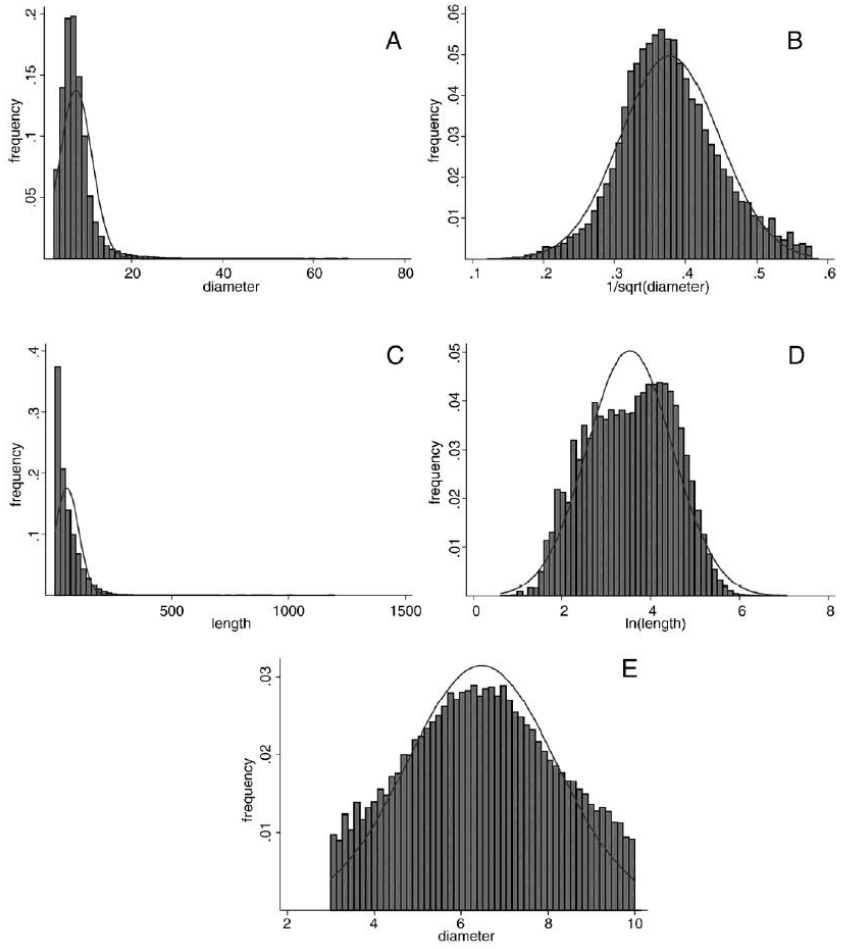

Figure 7.4 A,B) Distributions of all vessels radii. C,D) Distributions of all vessels lengths. E) Distribution of capillary radii. Taken from Lauwers et al. [75].

7.1.2 Arterial Tree Resistances, Pressures and Flowrates

Once the arterial tree is created using the algorithm described above, calculations are carried out to find the properties of this arterial tree. The most important are: the resistance of the tree, pressures at the nodes, and flowrates through the vessels of the tree. The resistance was calculated by regarding the tree as an electrical circuit with each vessel's individual resistances arranged in-series or in-parallel compared to other

Table 7.2 *Mean and standard deviation for vessels distributions [75].*

	All vessels (μm)		Capillaries (μm)	
	$1/\sqrt{Diameter}$	$\ln(Length)$	$Diameter$	$Length$
Mean	0.38	3.54	6.47	52.95
S.D.	0.07	0.96	1.70	49.75

vessels' resistances. Figure 7.5 shows an example of a small arterial tree with three branching levels.

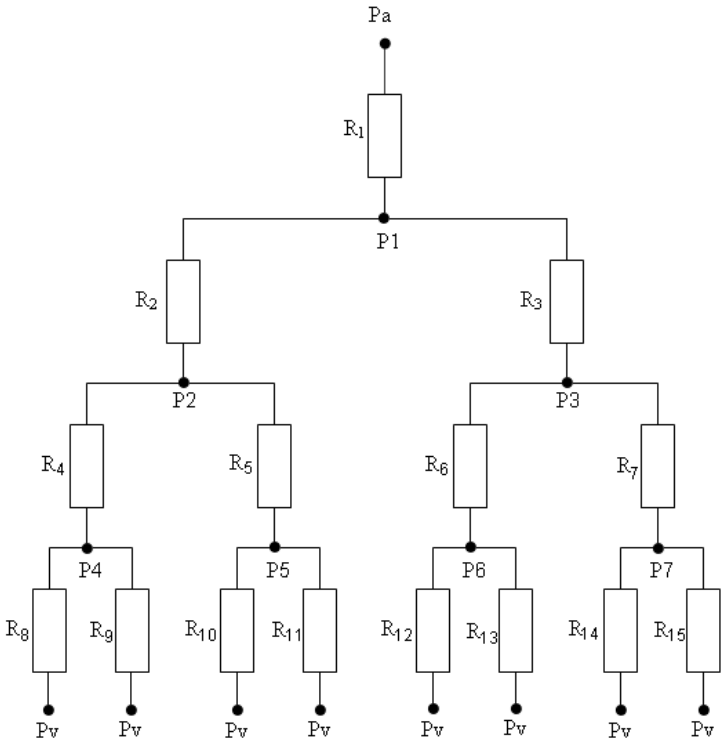

Figure 7.5 An example of a small arterial tree.

First, the individual resistances of all vessels are calculated using Equation 4.6. However, since the length of the vessel was defined as a function of its radius, the length to radius ratio term l_{rr} was used resulting in Equation 7.7. These resistances are different in value because the radii values are different for each vessel.

$$R_i = \frac{8\mu l_{rr_i}}{\pi r_i^3} \tag{7.7}$$

The viscosity (μ) was calculated using Equation 7.8 derived by Pries et al. [107], where μ_{45} is as defined in Equation 7.9 and d_v is the vessel's diameter. The experi-

mental work by Pries et al. examined the resistance of blood flow in microvessels. The hematocrit[2] was assumed to be at the normal value of 45%.

$$\mu = \left[1 + (\mu_{45} - 1)\left(\frac{d_v}{d_v - 1.1}\right)^2\right]\left(\frac{d_v}{d_v - 1.1}\right)^2 \tag{7.8}$$

$$\mu_{45} = 6\ exp(-0.085 d_v) + 3.2 - exp(-0.06 d_v^{0.645}) \tag{7.9}$$

The total resistance of the whole tree was calculated by using both the resistance in-series and in-parallel rules defined in Equations 7.10 and 7.11 respectively. R_{series} is the total resistance of R_a and R_b aligned in series, while $R_{paralell}$ is the total resistance of R_c and R_d aligned in parallel.

$$R_{series} = R_a + R_b \tag{7.10}$$

$$R_{paralell} = \frac{R_c \times R_d}{R_c + R_d} \tag{7.11}$$

The total resistance was calculated starting from the smallest vessels (terminal vessels including the capillary bed resistance) up to the root vessel ending up with the resistance of the whole tree represented by Figure 7.6 (a). R_v and R_{Tv} were used to distinguish between the individual resistance of a specific vessel and the total resistance from the end of the arterial tree up to the same vessel. For example, Figure 7.5 shows R_1 as the individual resistance of the root vessel while Figure 7.6 (a) shows R_{T1} as the total resistance from the end of the tree up to, and including, the root vessel. Figure 7.7 shows a schematic diagram of the process of calculating the resistances of the arterial binary tree.

Once the resistance of the whole arterial tree was calculated from the smallest vessels *upwards*, the pressure values at the tree nodes and the flowrates through the vessels were calculated *downwards* from the root vessel. Based on the inlet pressure P_a and outlet pressure P_v, the flowrate through the whole tree (Q1) was calculated using Poiseuille expression given by Equation 4.5, where the total resistance of the arterial tree (R_{T1}) was used and $\Delta P = P_a - P_v$. The pressure at the node P1 could then be calculated using Equation 4.5 again, where $\Delta P = P_a - P_1$ and the root individual resistance (R1) was used as given in Equation 7.12.

$$P1 = Pa - (Q1R1) \tag{7.12}$$

[2]See Glossary

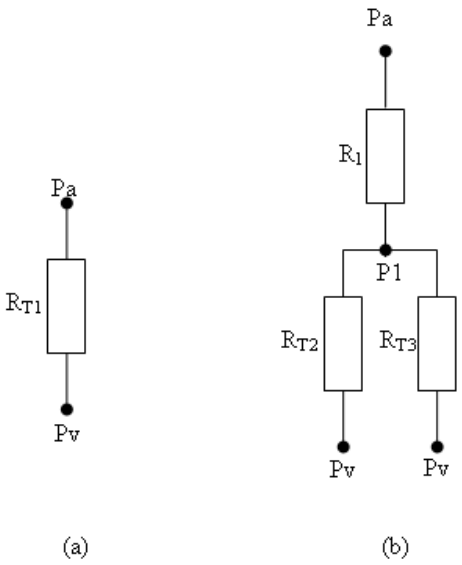

Figure 7.6 The total resistance of the arterial tree is simplified down to (a) a single resistance (b) two branching levels tree.

Then, to calculate the pressures and flowrates throughout the rest of the arterial tree, the vessels in the next branch level as in Figure 7.6 (b) were considered. Instead of the total resistance at the root vessel, the tree with only one branching was considered. R1 became the individual resistance of the root vessel, while RT2 and RT3 were each the total resistance of the two vessels off the root plus the remainder of the tree that was branching off them, as given in Equations 7.13 and 7.14.

$$RT2 = R2 + total\ resistance\ of\ vessel\ 2\ subtree \tag{7.13}$$

$$RT3 = R3 + total\ resistance\ of\ vessel\ 3\ subtree \tag{7.14}$$

The flowrates Q2 and Q3 traveling through vessels 2 and 3 were calculated similarly to vessel 1 (root vessel) by using Equation 4.5, where $\Delta P = P_1 - P_v$. RT2 and RT3 account for the total resistances from the bottom to the tree up to and including vessels 2 and 3.

The process described above was repeated for the remainder of the arterial tree until the pressure at each node and flowrate through each vessel has been calculated. Figure 7.8 shows a schematic diagram of the process of calculating the pressures and flowrates of the arterial binary tree.

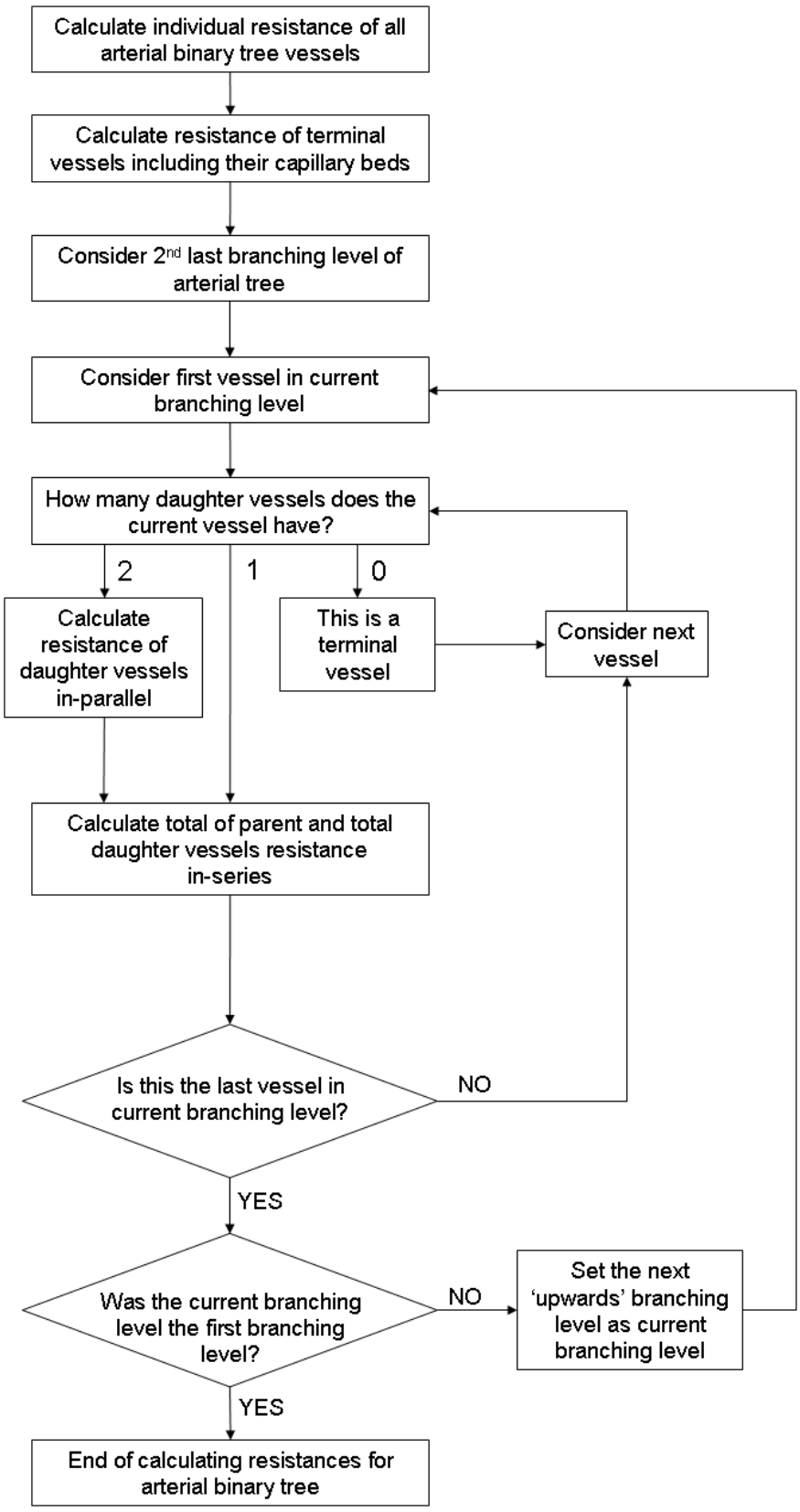

Figure 7.7 Schematic diagram of the process of calculating the resistances of the arterial binary tree.

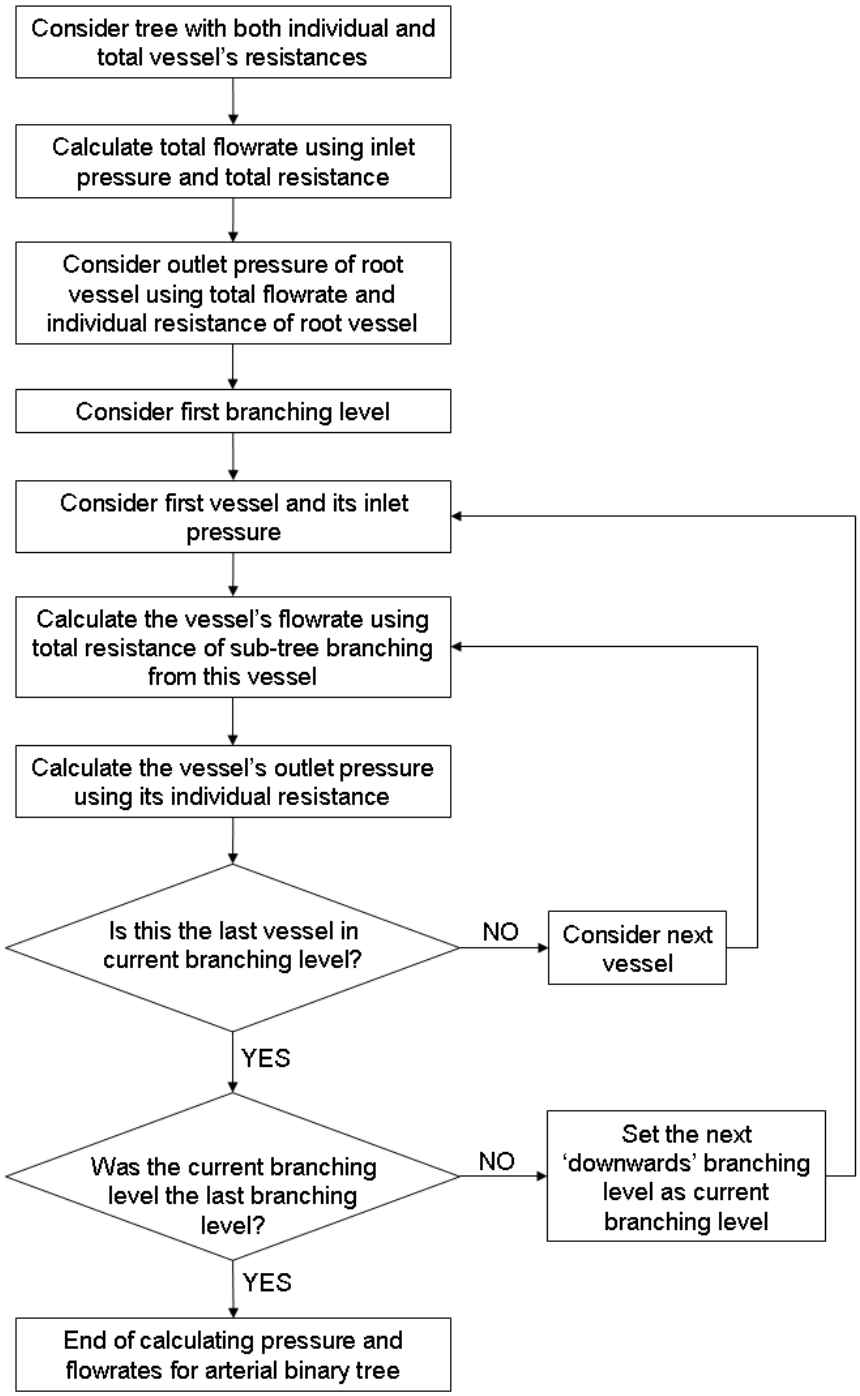

Figure 7.8 Schematic diagram of the process of calculating the pressures and flowrates of the arterial binary tree.

7.2 Metabolic Model

The metabolic model presented in Chapter 6 describes the metabolic autoregulatory mechanism for the CoW model where the main efferent arteries were implemented as lumped parameters. The efferent resistances represented the vasculature from the efferent arteries down to and including the capillary bed. The metabolic induced autoregulation was a phenomenological algorithm, which directly regulated the efferent arteries' resistance based on the carbon dioxide (CO_2) concentration in the arteries and cerebral tissue. In reality, the CO_2 influences the radius size of the different numerous vessels in the arterial tree, which consequently results in the change of overall resistance of the whole arterial tree.

The arterial binary tree was developed to replace the lumped parameter resistance representing the cerebral vasculature downstream from the main efferent arteries. As a result, it was necessary to modify the autoregulation mechanism so that it would be dependent on the condition of each vessel in the arterial tree rather than the overall resistance of the whole tree. The selective ion channel in the smooth muscle cells (SMC) respond to CO_2 and pH alternations [36]. However, in this metabolic model, the simple assumption of having the arterioles and venules running side by side was used. Therefore, the radii of arterioles feeding the capillaries were regulated by release and diffusion of excess CO_2 from the venules [65]. This results in induced vasoconstriction or vasodilation of the arterioles, which consequently leads to increased or decreased resistance of the overall arterial tree, and therefore, decrease or increase of blood flow to the cerebral tissue to maintain the constant concentration of CO_2.

The CO_2 rate of change in the tissue is balanced by the CO_2 production (equal to the O_2 consumption rate due to metabolism) and the net difference of CO_2 in tissue and artery, which is removed by the blood, is as given by Equation 7.15. This is the same differential equation (Equation 6.20) used in Section 6.3.

$$\frac{dCtCO_2}{dt} = CMRO_2 + CBF \times (CaCO_2 - CtCO_2) \tag{7.15}$$

The rate of change of a vessel's radius is given by Equation 7.16, where G_{CO_2} is the gain which results in the smooth muscle cells to react in approximately 10 seconds. The reaction time of 10 seconds was based on experimental work of Halsey et al. [48]. The value and unit of G_{CO_2} is provided in Table 7.3. The unit for $CtCO_2$ is $ml\ O_2$ per $ml\ tissue$, so it is basically a ratio.

$$\frac{dr}{dt} = G_{CO_2}(CtCO_2 - CtCO_{2,sp}) \tag{7.16}$$

For simpler implementation in the arterial binary tree, the two equations were non-dimensionalised using the set of definitions given in Equation 7.17, where r_0 is a constant characteristic value assigned to the terminal vessel radius of 10 $\times 10^{-4}$. The CBF_0, which is the blood flowrate per unit volume of cerebral tissue at normal physiological conditions, was estimated using the blood flowrate traveling through an MCA at normal conditions divided by the cerebral tissue volume supplied by that MCA. The cerebral volume supplied by the MCA was estimated by using Hillen's ratio [58] on the average brain volume of 1400 cm^3. This ratio was presented in Chapter 4, which was used to estimate the flowrates through the efferent arteries of the CoW. The values of r_0 and CBF_0 are provided in Table 7.3.

$$C' = \frac{CtCO_2}{CaCO_2},\ r' = \frac{r}{r_0},\ CBF' = \frac{CBF}{CBF_0},\ t' = \frac{t}{CBF_0} \tag{7.17}$$

The non-dimensional differential equations of the tissue carbon dioxide and radius of an arterial vessel are defined by Equations 7.18 and 7.19 respectively.

$$\frac{dC'}{dt'} = (\Gamma - 1) + CBF'(1 - C') \tag{7.18}$$

$$\frac{dr'}{dt'} = \Pi(C' - \Gamma) \tag{7.19}$$

where the terms Γ and Π are defined by Equations 7.20 and 7.21 respectively.

$$\Gamma = 1 + \frac{CMRO_2}{CaCO_2 CBF_0} \tag{7.20}$$

$$\Pi = \frac{G_{CO_2} CaCO_2}{r_0 CBF_0} \tag{7.21}$$

Consequently, the non-dimensional blood flow (CBF') through a vessel in the arterial tree becomes a function of the radius of that vessel as in Equation 7.22.

$$CBF' = \Delta P\ (r')^3 \tag{7.22}$$

Table 7.3 *Parameters for metabolic model.*

Symbol	Definition	Value	Units
G_{CO_2}	Metabolic gain	3×10^{-5}	$s\ cm^{-1}$
r_0	Terminal vessel radius	10×10^{-4}	cm
CBF_0	Flowrate per unit volume	9.5×10^{-3}	$mL\ blood/mL\ tissue\ s^{-1}$

The experimental results by Kontos et al. [69] on the responses of the cerebral pre-capillary vessels to changes in arterial blood pressure in cats show that the autoregulation mechanism is carried out by various degrees depending on the radius size of the vessels. The smaller the arterial vessel, the greater it is affected by the changes in arterial blood pressure. Therefore, when implementing the metabolic model described above in the arterial binary tree, the metabolic mechanisms were restricted to arterioles with radius size of $50\mu m$ and below. The method of implementation in the arterial binary tree is described further in detail in Section 7.5 below.

7.3 Myogenic Model

The cyclic variation in the arterioles' and terminal vessels' vasomotion plays a major role in the physiology and pathology involved in cerebral microcirculation.

Harder et al.'s experiments [49, 50] show that the MCA of cats decreases in diameter as a result of increased transmural pressure. This is called the *myogenic* response, which is achieved by the contraction and relaxation of smooth muscle cells (SMC). The transmural pressure of a vessel determines a hoop stress, resulting in calcium flux change across the SMC membrane. The wall elastic and SMC stresses result in a rate of change of the vessel's radius. Changes in the vessel's radius, or vasomotion, is facilitated by electromechanical coupling within smooth muscle cells. The complex nature of the small arteries' vasomotion was implemented in the current cerebral hemodynamics model.

A system of differential equations describing the vasomotion mechanism in small arteries was implemented based on the model by Gonzalez-Fernandez and Ermentrout [44]. This model predicts the myogenic response by the SMCs, reducing or increasing the radius of a cerebral vessel as a result of changes in arterial pressure. The model includes the ionic transports, cell-membrane potential, and muscle contraction of the vessel's smooth muscle cells. The interaction of calcium (Ca^{2+}) and potassium (K^{+}) fluxes, mediated by voltage-gated and voltage-calcium-gated channels respectively, brings about periodicity of those transports. The myogenic model consists of six differential equations. These are described below.

7.3.1 Ion Channel Open States

The Ca^{2+} variations in smooth muscle was simulated using Ca^{2+} and Ca^{2+}-dependent K^{+} ion channel open probabilities. The variations of the time-dependent Ca^{2+} concentration were used to establish the variation in cross bridge links to the

myosin light chain (MLC[3]) kinase[3], which results in the vasomotion of the arterial wall. The Ca^{2+} channel was assumed to be in equilibrium beacuse it has a very fast reaction time compared to the Ca^{2+}-dependent K^+ channel. Its distribution of open states was represented by the sigmoidal function in Equation 7.23 where v is the membrane voltage, v_1 is the voltage associated with the opening of half the population and v_2 is a measure of the spread of the distribution. To model the stretch activation of the Ca^{2+} channel, v_1 was varied by defining it as a function of the transmural pressure (Δp) as in Equation 7.24. This function is similar to the function presented by Gonzalez-Fernandez and Ermentrout [44].

$$m_\infty = \frac{1}{2}\left(1 + tanh\left(\frac{v - v_1}{v_2}\right)\right) \tag{7.23}$$

$$v_1 = -19\ - \frac{10\ \Delta p}{190} \tag{7.24}$$

Similarly, the equilibrium distribution of open states for the Ca^{2+}-dependent K^+ ion channel was represented by Equation 7.25 where v_3 implements a Ca_i-dependent shift in the Ca^{2+}-dependent K^+ open states distribution with respect to membrane voltage (v) as given in Equation 7.26.

$$n_\infty = \frac{1}{2}\left(1 + tanh\left(\frac{v - v_3}{v_4}\right)\right) \tag{7.25}$$

$$v_3 = -\frac{v_5}{2}\ tanh\left(\frac{Ca_i - Ca_3}{Ca_4}\right) + v_6 \tag{7.26}$$

The time course of the fraction of Ca^{2+}-dependent K^+ open channel states (n) has a slower reaction time; therefore, it was described by the first order kinetics as in Equation 7.27 where λ_n was based on statistical considerations as defined by Equation 7.28.

$$\frac{dn}{dt} = \lambda_n(n_\infty - n) \tag{7.27}$$

$$\lambda_n = \phi_n\ cosh\left(\frac{v - v_3}{2v_4}\right) \tag{7.28}$$

The values of $v_2, v_4, v_5, v_6, Ca_3, Ca_4$, and ϕ_n are all known constants as given in Table 7.4.

[3]See Glossary

7.3.2 Membrane Voltage

The time rate of change of the membrane potential (v) was defined as the sum of currents across the membrane as given in Equation 7.29 where C is the cell membrane capacitance. The parameters g_L, g_K and g_{Ca} are maximum whole-cell membrane conductance for the leak, potassium and calcium currents. v_L, v_K, and v_{Ca} correspond to the Nernst reversal potentials.

$$C\frac{dv}{dt} = -g_L(v - v_L) \ - g_K \ n(v - v_K) \ - g_{Ca} \ m_\infty(v - v_{Ca}) \tag{7.29}$$

All of the constants mentioned above are listed in Table 7.4.

7.3.3 Free Cytosolic Calcium Concentration

The time rate of change of cytosolic[4] calcium ion concentration was defined as in Equation 7.30.

$$\frac{dCa_i}{dt} = (-\alpha_{Ca} \ g_{Ca} \ m_\infty(v - v_{Ca}) - k_{Ca} \ Ca_i)\rho_{Ca} \tag{7.30}$$

Where the calcium equilibrium distribution of open channel states m_∞ was defined by Equation 7.23 above and ρ_{Ca} is given by Equation 7.31. The constant values of k_{Ca}, α_{Ca}, K_d and B_T are listed in Table 7.4.

$$\rho_{Ca} = \frac{(K_d + Ca_i)^2}{(K_d + Ca_i)^2 + K_d \ B_T} \tag{7.31}$$

The increase in the cytosolic calcium concentration results in smooth muscle cell contraction, which is affected by the crossbridges formation between overlapping myosin[4] and actin[4] filaments. The calcium first combines with calmodulin[4]. The combination then activates the MLC kinase, which as a result phosphorylates the myosin. Actin interacts with the phosphorylated myosin to form crossbridges and develop stress. The formation of crossbridges are formulated in the next section.

The decrease in the cytosolic calcium concentration results in dissociation of calcium and calmodulin from the MLC kinase, which becomes inactive. As a result, the myosin dephosphorylates causing muscle relaxation. The process of how the cytosolic calcium results in SMCs contraction or relaxation is provided in more detail by Gonzalez-Fernandez and Ermentrout's work [44].

[4]See Glossary

7.3.4 The Fraction of Crossbridges

The resulting stress depends on the number of crossbridges formed between myosin and action filaments. For a given myosin-action overlapping segment, there is a maximum possible number of crossbridges. ω stands for the fraction of actual crossbridges. The rate of change of ω is given by Equation 7.32.

$$\frac{d\omega}{dt} = k_\psi \left(\frac{\psi}{\psi_m + \psi} - \omega \right) \tag{7.32}$$

It was assumed that the dependence of phosphorylation on calcium is a sigmoidal one. Thus, ψ was defined as in Equation 7.33, where the number q is the power to which the association quantity is raised. The variables k_ψ and ψ_m are constants.

$$\psi = \frac{Ca_i^q}{Ca_{im}^q + Ca_i^q} \tag{7.33}$$

7.3.5 Contractile Component Length

In a cylindrical element inside the vessel wall with $0 \leq \theta \leq 2\pi$, thickness Δr and unit length along z, a longitudinal slit of constant θ and surface ΔS was considered as shown in Figure 7.9, where x is the average circumference of the element.

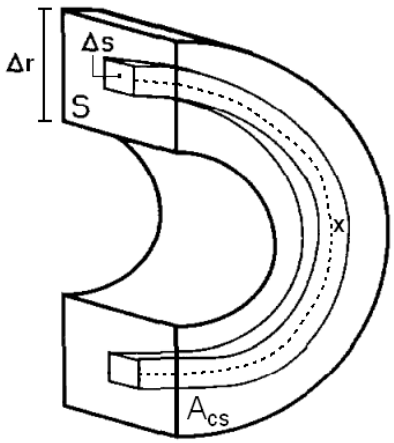

Figure 7.9 A longitudinal (S) and transversal/cross-sectional (A_{cs}) sections of a cylindrical element of the wall. Taken from Gonzalez-Fernandez and Ermentrout [44].

For the analysis of the stresses on S, a Maxwell model (as shown in Figure 7.10) was adopted along x, consisting of a contractile component (CC) of length y, a series elastic component (SEC) of length u, a parallel elastic component (PEC) of length $x = u + y$. The x and u units are purely elastic, while y is contractile and depends on

the amount of crossbridges. The hoop stresses σ_x, σ_u, and σ_y are associated with PEC, SEC and CC respectively. The normalized stresses in terms of normalized lengths are given by Equations 7.34 - 7.36. The coefficients used in these equations were chosen by Gonzalez-Fernandez and Ermentrout [44] to make the expressions fit the experimental data.

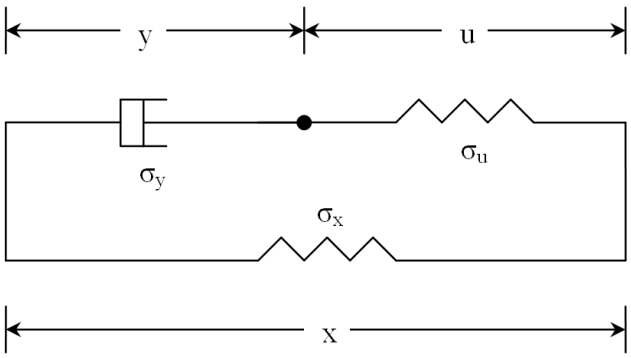

Figure 7.10 Maxwell Model.

$$\sigma'_x = x'_3 \left(1 + tanh\left(\frac{x' - x'_1}{x'_2}\right)\right) + x'_4 \left(x' - x'_5\right) - x'_8 \left(\frac{x'_6}{x' - x'7}\right) - x'_9 \tag{7.34}$$

$$\sigma'_u = u'_2 exp(u'_1 u') - u'_3 \tag{7.35}$$

$$\sigma'_y = \frac{\sigma_{y0}}{\sigma_0^{\#}} \frac{exp\left(\frac{-(y'-y'_0)^2}{2s^2}\right) - y'_3}{1 - y'_3} \tag{7.36}$$

The four terms on the RHS of Equation 7.34 represent the different components of circumferential wall extensions. These terms represent the stiffer collagen fibres activated at large expansions, the compliant elastin fibres influence at small deformations, the larger stiffness for significant vessel's radius reductions, and an additional term to closer fit σ'_x to experimental data. Equation 7.36 represents the muscle's isometric stress-length relationship, where the function s was used to reproduce the relationship asymmetry about its maximum as defined in Equation 7.37 and $\sigma_0^{\#}$ is the hoop stress at the maximum muscle activation.

$$s = \left(\frac{y'_1}{y' + y'_2}\right)^{y'_4} \tag{7.37}$$

The parameter σ_{y0} is the hoop stress σ_y associated with CC at optimum length

of $y0$ and defined by Equation 7.38, where the reference fraction of crossbridges (ω_{ref}) is as given by Equation 7.39. The ψ value is calculated with equation 7.33 using the reference cytosolic calcium ion concentration value.

$$\sigma_{y0} = \frac{\sigma_{y0}^{\#}}{\omega_{ref}}\ \omega \tag{7.38}$$

$$\omega_{ref} = \frac{\psi(Ca_{i,ref})}{\psi_m + \psi(Ca_{i,ref})} \tag{7.39}$$

The force-velocity relationship was based on Hill's hyperbolic force-velocity principle, which states that as the velocity of muscle contraction increases, there is a decrease in the maximal tension that a muscle may produce. In an arterial muscle, the steady-state contraction velocity at zero load is linearly related to the crossbridge phosphorylation. As a result, the velocity-load relationships were scaled by the corresponding phosphorylation levels. The rate of change of the normalized contractile (CC) component length was described by Equation 7.40. These equations were defined based on experimental data [44].

$$\frac{dy'}{dt} = \begin{cases} -a'v'_{ref}\frac{\psi}{\psi_{ref}}\frac{1-\frac{\sigma'_u}{\sigma'_y}}{a'+\frac{\sigma'_u}{\sigma'_y}} & \text{for } 0 \leq \frac{\sigma'_u}{\sigma'_y} \leq 1 \\ c'\left[exp\left(b'\left(\frac{\sigma'_u}{\sigma'_y} - d'\right)\right) - exp\left(b'\left(1-d'\right)\right)\right] & \text{for } 1 \leq \frac{\sigma'_u}{\sigma'_y} \end{cases} \tag{7.40}$$

Where v'_{ref} is the normalised zero load velocity of the contractile component at reference muscle activation level. For an activation level, the velocity was based on the ratio of muscle load to muscle isometric force $\frac{f_u}{f_y}$, which is equivalent to $\frac{\sigma'_u}{\sigma'_y}$ as used in Equation 7.40 above. For the range $0 \leq \frac{\sigma'_u}{\sigma'_y} \leq 1$, the load is smaller than the muscle-stress activation and $\frac{dy'}{dt}$ is a function of the $\frac{\sigma'_u}{\sigma'_y}$ ratio as well as the phosphorylation level. For the range $1 \leq \frac{\sigma'_u}{\sigma'_y}$, loads exceeds the muscle-stress, which is a condition for lengthening during contraction.

7.3.6 Circumferential Distance of Artery Wall

The following expressions (Equations 7.41 - 7.43) define the forces on the wall of the vessel, where $f_{\Delta p}$ is the systemic blood pressure force normal to S, and f_x and f_u are the loads experienced by the parallel elastic and series elastic components. w_e and w_m are weights representing the contribution by the muscular and elastic parts to the hoop forces. These coefficients permit to incorporate the proportions of elastic fibers and smooth muscle for different vessel wall types in the system dynamics.

$$f_{\Delta p} = \frac{1}{2}\Delta p \left(\frac{x}{\pi} - \frac{A_{cs}}{x} \right) \tag{7.41}$$

$$f_x = w_e S \sigma'_x \sigma_0^{\#} \tag{7.42}$$

$$f_u = w_m S \sigma'_u \sigma_0^{\#} \tag{7.43}$$

The rate of change of the arterial circumferential distance x was defined by the resultant of the forces on S (or acting on the Maxwell model) as given in Equation 7.44 where ξ is a characteristic time for smooth muscle relaxation.

$$\frac{dx}{dt} = \frac{1}{\xi} \left(f_{\Delta p} - f_x - f_u \right) \tag{7.44}$$

All constants used in the definitions above are given in Table 7.4. The six differential equations defined by Equations 7.27, 7.29, 7.30, 7.32, 7.40, and 7.44 form a closed system that represents the myogenic mechanism with the corresponding vessel radius. However, the model by Gonzalez-Fernandez and Ermentrout, described above, represents the myogenic response for a specific radius vessel, which was in the range of $250\mu m$. In the current cerebral hemodynamics model, this was modified to adapt for vessels with various radii sizes. Hannah Farr in the brain group at the University of Canterbury worked on non-dimensionalising the Gonzalez-Fernandez and Ermentrout model [29]. The new systemic blood pressure force was defined by Equation 7.45 where R_r is the ratio of inner to outer radius of the vessel adopted from the work of Burton [17]. The value of R_r varies between 0.5 for smaller arterioles and 0.7 for larger arteries. It is relatively higher for large arteries because of larger amounts of elastic tissue and smooth muscles. In this model, the R_r was assumed to be the same for all arteries in the binary tree. This was necessary as a simplification to ensure that the non-dimensional myogenic mechanism can be applied to all vessels in the arterial tree.

$$f_{\Delta p} = \frac{1}{2}\Delta p \frac{(1+R_r)}{1-R_r} \left[\frac{x}{0.8} - \frac{0.8}{x} \frac{(1-R_r)}{1+R_r} \right] \tag{7.45}$$

The non-dimensional equation of the rate of change of x is given by Equation 7.46 where t' and ξ' were defined as in Equations 7.47 and 7.48 respectively.

$$\frac{dx}{dt'} = \frac{1}{\xi'} \left(f_{\Delta p} - f_x - f_u \right) \tag{7.46}$$

$$t' = \frac{t g_{Ca}}{C} \tag{7.47}$$

$$\xi' = \frac{0.8\sigma_0^{\#} C}{\xi g_{Ca} \pi} \frac{(1 - R_r)}{1 + R_r} \tag{7.48}$$

7.3.7 Endothelial Nitric Oxide (eNOS) Dynamics

Farr [37] also implemented the autoregulatory response of arterial wall shear stress on arteries to produce a coupled fluid dynamics/ myogenic regulation. Arterial regions that experience low wall shear stress correspond to regions with impaired eNOS signalling in the endothelial cells. This results in reduced amounts of nitric oxide (NO), which is a potent vasodilator. It is believed that an increase in the arterial blood pressure causes smooth muscle cells to contract, while an increase in wall shear stress causes the arterial walls to dilate [27, 105]. The dynamics of eNOS as a function of wall shear stress was adopted from the work of Comerford et al. [27]; the non-dimensional differential equation of the conservation of eNOS is given by Equation 7.49.

$$\frac{d\ eNOS}{dt'} = \frac{k_{dis} Ca_i}{Ca_i + k_e} - \mu_e eNOS + (1 - \varphi) g_{max} F(\tau) \tag{7.49}$$

The terms on the RHS of the above equation accounts for eNOS production through a calcium production pathway, a simple decay rate, and through a calcium independent Akt pathway, which is described more in detail by Dimmeler et al [33]. The parameter φ was used to find the ratio of influx between the direct Ca^{2+} channel and that mediated by the Akt pathway. The dimensionless parameters k_e, k_{dis}, μ_e, and g_{max} are listed in Table 7.6. $F(\tau)$ is a function of wall shear stress acting on the endothelial cell membrane adopted from the work by Wiesner et al. [138] as defined by Equation 7.50, where ϱ is the no-load channel constant.

$$F(\tau) = \frac{1}{1 + \varrho exp(-W(\tau))} \tag{7.50}$$

The shear-dependent influx was assumed to be proportional to the fraction of open Ca^{2+} channels. The function $W(\tau)$ defined by Equation 7.51 implements a Boltzmann dependence on the strain energy density in the membrane, where δ and W_0 are non-dimensional and are listed in Table 7.6.

$$W(\tau) = W_0 \frac{\left(\tau + \sqrt{16\delta^2 + \tau^2} - 4\delta\right)^2}{\tau + \sqrt{16\delta^2 + \tau^2}} \tag{7.51}$$

Table 7.4 *Parameters for myogenic model.*

Symbol	Definition	Value	Units
$v2$	Measure of the Ca^{2+} open states distribution	25.0	mV
$v4$	Measure of the K^{+} open states distribution	14.5	mV
$v5$	Parameter in Equation 7.26	8	mV
$v6$	Parameter in Equation 7.26	-15	mV
Ca_3	Parameter in Equation 7.26	400	nM
Ca_4	Parameter in Equation 7.26	150	nM
$Ca_i m$	Parameter in Equation 7.33	3.5×10^{2}	nM
ϕ_n	Parameter in Equation 7.28	2.664	s^{-1}
C	Cell capacity	1.9635×10^{-14}	$C\ mV^{-1}$
g_L	Maximum membrane conductance for leak current	7.854×10^{-14}	$C\ s^{-1}\ mV^{-1}$
g_K	Maximum membrane conductance for potassium current	3.1416×10^{-13}	$C\ s^{-1}\ mV^{-1}$
g_{Ca}	Maximum membrane conductance for calcium current	1.57×10^{-13}	$C\ s^{-1}\ mV^{-1}$
v_L	Nernst reversal leak potential	-70	mV
v_K	Nernst reversal potassium potential	-90	mV
v_{Ca}	Nernst reversal calcium potential	80	mV
α_{Ca}	Parameter in Equation 7.30	7.9976×10^{15}	$nM\ C^{-1}$
k_{Ca}	Ratio of calcium outflux to cytosolic calcium	1.3567537×10^{2}	s^{-1}
K_d	Parameter in Equation 7.31	1×10^{3}	nM
k_ψ	Parameter in Equation 7.32	3.3	s^{-1}
B_T	Constant for cell calcium-buffer systems	1×10^{5}	nM
ψ_m	Parameter in Equation 7.32	0.3	
q	Power index for phosphorylation dependence on calcium	3	
x_1'	Parameter in Equation 7.34	1.2	
x_2'	Parameter in Equation 7.34	0.13	
x_3'	Parameter in Equation 7.34	2.224425	
x_4'	Parameter in Equation 7.34	0.711816	
x_5'	Parameter in Equation 7.34	0.8	
x_6'	Parameter in Equation 7.34	0.01	
x_7'	Parameter in Equation 7.34	0.32133758	
x_8'	Parameter in Equation 7.34	0.88977	
x_9'	Parameter in Equation 7.34	9.0462916×10^{-3}	
u_1'	Parameter in Equation 7.35	41.76	
u_2'	Parameter in Equation 7.35	0.0473958	
u_3'	Parameter in Equation 7.35	0.058399958	
y_0'	Parameter in Equation 7.36	0.928	
y_1'	Parameter in Equation 7.37	0.639	
y_2'	Parameter in Equation 7.37	0.35	
y_3'	Parameter in Equation 7.36	0.78847	
y_4'	Parameter in Equation 7.37	0.8	
$\sigma_0^{\#}$	Hoop stress at the maximum muscle activation	3×10^{6}	$dyne\ cm^{-2}$
$\sigma_{y0}^{\#}$	Parameter in Equation 7.38	2.6×10^{6}	$dyne\ cm^{-2}$
a'	Parameter in Equation 7.40	0.28125	
b'	Parameter in Equation 7.40	5	
c'	Parameter in Equation 7.40	0.03	
d'	Parameter in Equation 7.40	1.3	
v_{ref}'	Normalised zero load velocity of the CC at reference level	0.24	s^{-1}
w_e	Weight representing electrical contribution to hoop forces	0.9	
w_m	Weight representing muscular contribution to hoop forces	0.7	
S	Longitudinal section of vessel wall	9×10^{-3}	cm^2
A_{cs}	Cross sectional area of vessel wall	1.5×10^{-3}	cm^2
ξ	Characteristic time for smooth muscle relaxation	0.2	$dyne\ cm^{-1}\ s$
R_r	Ratio of inner to outer radius	0.6	

The wall shear stress (τ) was calculated using the Hagen-Poiseuille formula [64], as given in Equation 7.52

$$\tau = \frac{4\mu CBF}{\pi r^3} \tag{7.52}$$

The wall shear stress calculated using the equation above resulted in reasonably high values. This might be because of the small size of vessels. Lipowsky et al. [77] carried out experiments to study the distribution of blood rheological[5] parameters in the vasculature of cat mesentery[5]. The study suggests to use different correlations for wall shear stress based on the radius size of vessels in place of the above equation used for vessels of all sizes. The radius-based correlation of wall shear stress is given in Equation 7.53, with parameters listed in Table 7.5.

$$\tau = \left(L_1 + L_2 \sqrt{\frac{CBF}{2\pi r^3}} \right)^2 \tag{7.53}$$

Table 7.5 *Parameters for Lipowsky et al.'s wall shear stress correlations [77].*

Radius (μm)	L_1	L_2
$5 <$ r ≤ 7.5	1.484	0.364
$7.5 <$ r ≤ 10	1.748	0.289
$10 <$ r ≤ 12.5	2.058	0.311
$12.5 <$ r ≤ 15	0.228	0.481
$15 <$ r ≤ 17	0.903	0.505
$17 <$ r ≤ 20	3.091	0.304
$20 <$ r ≤ 22.5	3.337	0.236
$22.5 <$ r ≤ 25	2.194	0.291
$25 <$ r ≤ 27.5	2.383	0.250
$27.5 <$ r	3.641	0.271

The eNOS dynamics were implemented to be part of the myogenic mechanisms in two steps. First, the term ($\varphi F(\tau)$) was added to the non-dimensional cytosolic calcium differential equation defined in Section 7.3.3. Second, the coefficient k_ψ in Subsection 7.3.3 was re-defined as given in Equation 7.54. It is now defined as a function of eNOS to implement a linear decrease in phosphorylation as eNOS concentration increases. This implementation was based on experimental results of van Riper et al. [135], which shows that nitrovasodilators cause significant decreases in phosphorylation without significant changes in the intracellular calcium. This suggests that nitrovasodilators decrease calcium sensitivity of MLC phosphorylation.

$$k_\psi = 1 - \beta_e[eNOS] \tag{7.54}$$

[5]See Glossary

Although the myogenic mechanism accounts for dynamics within smooth muscle cells and eNOS equation accounts for dynamics within the endothelial cells, it was assumed that the concentrations of different components in the endothelial cells are instantaneously propagated to the smooth muscle cells and vise versa, for simplicity. The method of implementing the myogenic model in the arterial binary tree is described in Section 7.5 below.

Table 7.6 *Parameters for eNOS model.*

Symbol	Definition	Value
k_{dis}	eNOS-caveolin disassociation rate	8.95 $\times 10^{-4}$
k_e	Parameter in Equation 7.49	0.0358
μ_e	eNOS-caveolin association rate	0.00209
φ	Relative strength of the Ca2+-dependent	0.1
g_{max}	Maximum WSS-induced eNOS activation	5.973 $\times 10^{-4}$
ϱ	No-load channel constant	2
W_0	Shear gating constant	111
δ	Membrane shear modulus	2.63
β_e	Parameter in Equation 7.49	1 $\times 10^{-4}$

7.4 Tissue-Blood O2 and CO2 Exchange Dynamics

The Krogh cylinder representation has been used by McGuire et al. [83] to model the oxygen transport in muscle tissue. The same method was implemented to represent the oxygen transport to the cerebral tissue in the current arterial tree model. This method evaluates the oxygen transport at the microvascular level between the capillaries and cerebral tissue. The algorithm can be used to determine the normal oxygen consumption mechanisms by cerebral tissue and to predict if any parts of the cerebral mass experience lack of oxygen delivery under common pathological conditions.

The diffusion of oxygen from the capillaries into the tissue is a passive process. The higher the oxygen consumption, the shorter the distance oxygen travels to surrounding tissue. Krogh's initial model assumptions were: setting each capillary as the only oxygen provider to the cylinder of tissue surrounding it, assuming that oxygen pressure at the capillary wall is the same as in blood, neglecting the oxygen pressure decline along the capillary, assuming radial oxygen diffusion, and assuming that consumption of oxygen is uniform in tissue. Some of these assumptions have been modified by McGuire et al.. The capillary-wall resistance to oxygen diffusion to the tissue surrounding it was included. The drop in oxygen partial pressure (PO_2) along the capillary was also taken into account.

Using Fick's law of diffusion and conservation of mass results in Equation 7.55 for

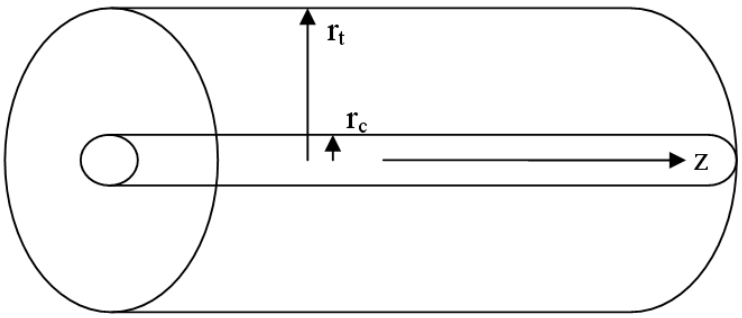

Figure 7.11 Krogh cylinder.

radial oxygen diffusion to the tissue as shown in Figure 7.11. This is a balance equation for diffusion of oxygen and reaction rate with no convection taking place.

$$K_o \left[\frac{d}{r\ dr} \left(r \frac{dP_t}{dr} \right) \right] = M(P_t) \tag{7.55}$$

The axial diffusion was not taken into account here. The oxygen consumption rate per unit volume of the tissue cylinder was defined by Michaelis-Menten kinetics given in Equation 7.56.

$$M(P_t) = \frac{M_o P_t}{(P_o + P_t)} \tag{7.56}$$

The boundary conditions, given in Equations 7.57 and 7.58, define the oxygen diffusion across the capillary wall and at the outer wall of the tissue cylinder. Owing to the capillary wall resistance, the PO_2 in the blood-tissue barrier is lower than the PO_2 in blood. Since it was assumed that the capillary is the only source of oxygen to the tissue cylinder surrounding it, the oxygen diffusion was set to zero across the outer wall of the tissue cylinder.

$$\left. \frac{dP_t}{dr} \right|_{r_c} = -\frac{M_t[P_b - P_t|_{r_c}]}{2\pi r_c K_o} \tag{7.57}$$

$$\left. \frac{dP_t}{dr} \right|_{r_t} = 0 \tag{7.58}$$

Although the axial diffusion was neglected, the drop of oxygen partial pressure in the blood stream along the capillary was taken into account. The capillary was expressed as a function of its radius, using the length to radius ratio l_{rr}. It was divided into i equally spaced sections along its length. At each section, the radial oxygen diffusion was solved numerically using Equations 7.55, 7.57 and 7.58. The total oxygen consumption per unit length was calculated using Equation 7.59 for some specified z value along the

capillary.

$$TC_{O_2}(z) = \int_{r_c}^{r_t} M(P_t)\ 2\pi r\ dr \tag{7.59}$$

The PO_2 of blood flow traveling inside the capillary (P_b) declines as a result of oxygen extraction by the tissue cylinder. The decline of convective oxygen flux must equal to the oxygen diffusion from the capillary. The drop in blood oxygen content, Ω, was calculated using Equation 7.60.

$$\frac{d}{dz}(CBF\ \Omega) = -TC_{O_2}(z) \tag{7.60}$$

At the start of the next capillary section, the P_b was calculated using Hill's equation describing the oxyhemoglobin saturation in the blood (S_{Hb}) as a function of P_b, where P_{50} is P_b at which hemoglobin is 50% saturated and H is a constant.

$$S_{Hb}(P_b) = \frac{(P_b/P_{50})^H}{1 + (P_b/P_{50})^H} \tag{7.61}$$

The S_{Hb} term is defined in terms of oxygen content in blood and carrying capacity of blood at 100% as in Equation 7.62. This was calculated and inserted into Equation 7.61 to find the oxygen partial pressure in the blood traveling through the capillary at the start of the next section of the capillary (P_b). Equations 7.59 to 7.62 were repeated for each section of the capillary along its length. Table 7.7 lists the values and definitions of all constants used.

$$S_{Hb}(P_b) = \frac{\Omega}{\Omega_B} \tag{7.62}$$

Table 7.7 *Parameters for Krogh oxygen diffusion model.*

Symbol	Definition	Value	Units
r_c	Capillary radius	2.5×10^{-4}	cm
r_t	Tissue cylinder radius	2.5×10^{-3}	cm
K_o	Krogh diffusion coefficient	9.4×10^{-10}	$(cm^2\ s^{-1})(\frac{cm^3 O_2}{cm^3 tissue}\ mmHg^{-1})$
M_o	Oxygen demand	2.5×10^{-3}	$\frac{cm^3 O_2}{cm^3 tissue}\ s^{-1}$
P_o	PO_2 at which consumption is half of demand	1	mmHg
P_{50}	PO_2 at which hemoglobin is 50% saturated	26	mmHg
M_t	Mass transfer coefficient	6.25×10^{-9}	$(cm^2\ s^{-1})(\frac{cm^3 O_2}{cm^3 tissue}\ mmHg^{-1})$
Ω_B	Oxygen carrying capacity in blood	0.2	$\frac{cm^3 O_2}{cm^3 blood}$
H	Hill equation exponent	2.7	

7.5 Numerical Procedure

The mathematical programming software, MATLAB, was used to create, solve and produce results for the binary arterial tree with the metabolic and myogenic autoregulation mechanisms as well as implement the oxygen diffusion into the cerebral mass. The fractal arterial tree code uses a *while* loop ending when all vessels branch down to the pre-capillary size. At each iteration of the while loop, a new branching level is created. At each branching level, two daughter vessels are created for each vessel in the previous branching level. This is done until all terminal vessels reach a specific size, which is considered to be the size of the pre-capillary sphincter. The first branching level contains only the root vessel specified. The terminal vessels were set to have a 10 μm radius. The capillary bed perfuses the cerebral tissue with oxygen-rich blood. The capillary beds are modelled as thousands of vessels lined in parallel with a 2.5 μm radius, branching off each terminal vessel. The number of capillaries in a capillary bed was calculated using the known perfused volume supplied by the specified MCA.

The efferent cerebral arteries of the CoW were used as the root arteries from which the vessels branch to create arterial trees. For the purpose of testing, a single arterial binary tree of the MCA, with radius of 1.5 mm, was used. Once an arterial tree is created, the vessels' individual resistances and the tree's total resistance is calculated. Then, the flowrates and pressures for all the vessels and nodes in the network are calculated, as described in Section 7.1.2 above. The total resistance of the arterial tree with the MCA root radius was smaller than the distal MCA resistance experienced physiologically. The power exponent (k) values for the different ranges of vessels' radii recorded in Table 7.1 were slightly modified from 2.5, 2.76 and 2.9 to 2.4. 2.66, and 2.8 respectively. This resulted in the correct resistance value of the MCA expected physiologically. Testing of the power exponent (k) and asymmetry ratio (γ) on the binary tree was carried out by Boudewijn Deurloo in the Brain Group of the University of Canterbury [32]. The k and γ values listed in Table 7.1 were varied for each of the vessels' radii size ranges, then the properties of the tree were recorded for these variations. The properties of the arterial binary tree can be calculated and displayed as required by the user.

The arterial binary tree created using the MCA as a root vessel had more than 800,000 vessels (further details of this binary tree's properties are given in the results chapter in Section 8.4).The inlet pressure at the root of the MCA was determined to be 85 $mmHg$ under normal conditions. This was obtained through running the non-linear CoW model described in Chapter 6.

The autoregulation function is a process which was implemented by using the metabolic and myogenic mechanisms as described in Sections 7.2 and 7.3 respectively.

These were run by using an iterative loop, which involved finding new radii values for all or most vessels in the tree that change as a result of change in the tree's inlet pressure. The differential equations used for the metabolic and myogenic algorithms describe the time rate of change of different entities. The computation of these differential equations for each vessel in the tree at each iterative step was a significant computations effort that can not be carried out with an ordinary PC. Therefore, as presented in more detail below, the use of the *look-up* tables for implementing the metabolic and myogenic mechanisms was necessary due to the high computation cost of running these mechanisms.

To implement the metabolic autoregulation, the two non-dimensional differential equations in Section 7.2 were solved numerically using a fourth order predictor-corrector method for an initial-value ordinary differential equation (ODE). This method is based on the fourth order Adams-Bashforth method as predictor and one iteration of the Adams-Moulton method as corrector, with the starting values obtained from the fourth order Runge-Kutta method. When a pressure disturbance is introduced as a result of a change in the systemic arterial pressure at the root of the binary tree, the new pressures and flowrates for each vessel in the tree are calculated. The metabolic mechanism is activated when the vessels experience a change in the flowrates. At time zero, the change in flowrate that each vessel experiences is modelled using Equation 7.22, where the radius of the vessels is not changed at time zero, and the pressure is defined as a step function that changes by the same ratio as the change in flowrate. The two metabolic non-linear equations are solved numerically as in the schematic diagram in Figure 7.12. The time steady state asymptotic value of each vessel's radius is considered to be the new value in the tree. Once new radii values of vessels are adopted in the arterial tree, the resistance of each of these vessels changes. Consequently, the resistance of the whole arterial tree also changes. Therefore, the process described in Section 7.1.2 was repeated, where the resistance of the arterial tree is calculated from the smallest vessels *upwards*; then, the pressure values and the flowrates were calculated *downwards* from the root vessel. This is considered to be a quasi time iteration step, or an outer iterative loop. At each outer iterative step, the new changes in flowrates are calculated to activate the metabolic mechanism (inner loop defined in Figure 7.12) resulting in new radii; then, the new resistances, pressure and flowrates are calculated. This step is repeated until each metabolically active vessel converges to a new radius that, through a new tree resistance, results in the flowrate delivered to the whole arterial tree to return back to the physiological condition dictated by the myogenic/ metabolic conditions.

However, the metabolic algorithm was not possible to implement as presented in the schematic diagram in Figure 7.12 because of the high computational demand. More than 99% of the vessels in the tree used were metabolically active (arterioles with radius of 50 μm or lower). The calculation of metabolic response of each vessel will require

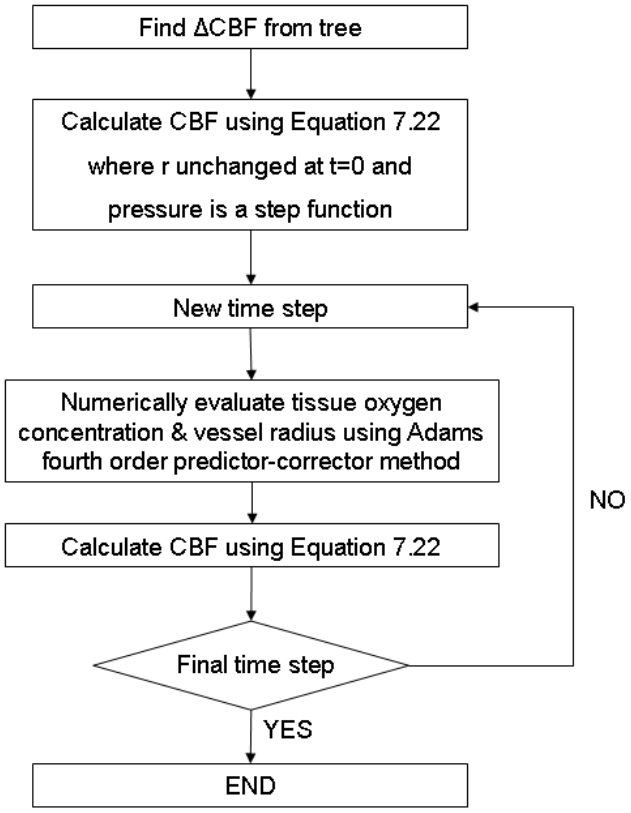

Figure 7.12 Solving the two metabolic differential equations using the Adams fourth order predictor-corrector method.

a huge amount of computations. Instead, the metabolic response was implemented through the use of a look-up table. The two differential equations were solved for a range of non-dimensional change in flowrates. Once the response reached an asymptotic value, the results were stored in a data-set creating a look-up table consisting of the non-dimensional radius response vs non-dimensional change in the flowrate. The change in radius for metabolically active vessels at each quasi time iterative loop was implemented using a linear interpolation so that new radii values are produced for each vessel as a result of the change in flowrates.

For the myogenic mechanism, the seven differential expressions (Equations 7.27, 7.29, 7.30, 7.32, 7.40, 7.46, and 7.49) defined in Section 7.3 were solved using MATLAB's ode23 built-in function. Similarly to the metabolic algorithm, once the response reached an asymptotic value, the results were stored as a 3D look-up table consisting of non-dimensional radius vs non-dimensional pressure and wall shear stress. The myogenic mechanism was set to be active in *all* vessels of the arterial tree. A bilinear interpolation was implemented in order to produce new values of vessels' radii. Then, the same steps to evaluate the resistance, pressure and flowrate for the arterial tree were performed repeatedly until the tree converges to a new peripheral resistance.

The oxygen diffusion into the cerebral mass, supplied by the MCA, was then calculated using the Krogh cylinder model described in Section 7.4. However, because of computational limitations, the model cannot calculate PO_2 profiles for a tissue size equivalent to the volume supplied by the MCA, which was approximated as three billion capillaries with tissue cylinder surrounding them. It would take a significant amount of computational time and memory to run the model and save the PO_2 profile data for such a volume.

The oxygen diffusion calculations can be done faster. All the capillaries are set to have the same radius, which results in the same tissue cylinder, i.e. the same volume supplied by each capillary. This means that the variable that affects the PO_2 profile is simply the flowrate. Since all capillaries in a capillary bed have the same radius, they have the same resistance. Therefore, because the capillaries were assumed to be lined up in parallel, the blood flowrate through each capillary is equal to the flowrate through the terminal (pre-capillary) vessel supplying the capillary bed divided by the number of capillaries. However, the terminal vessels have different values of flowrates. Instead of calculating the oxygen diffusion separately for each capillary to find the PO_2 profile for a large tissue volume, the distribution of the flowrates at the terminal vessels is used instead to find the total oxygen diffusion into that volume. The terminal vessels' flowrate distribution is divided up into χ groups, each group has N number of terminal vessels. For each group, the median flowrate traveling in a representative capillary is calculated and used to obtain the oxygen consumption by the tissue cylinder

surrounding the representative capillary. Then, the total oxygen consumption by the specified tissue volume is added up as given by Equation 7.63, where ς is the oxygen consumption by the tissue cylinder and N_{ccb} is the number of capillaries per capillary bed.

$$Total\ Oxygen\ Consumption = N_{ccb} \sum_{i=1}^{\chi} N(i)\ \varsigma(CBF_i) \tag{7.63}$$

The numerical procedure of creating the arterial binary tree and implementing the metabolic and myogenic autoregulation mechanism is shown in Figure 7.13.

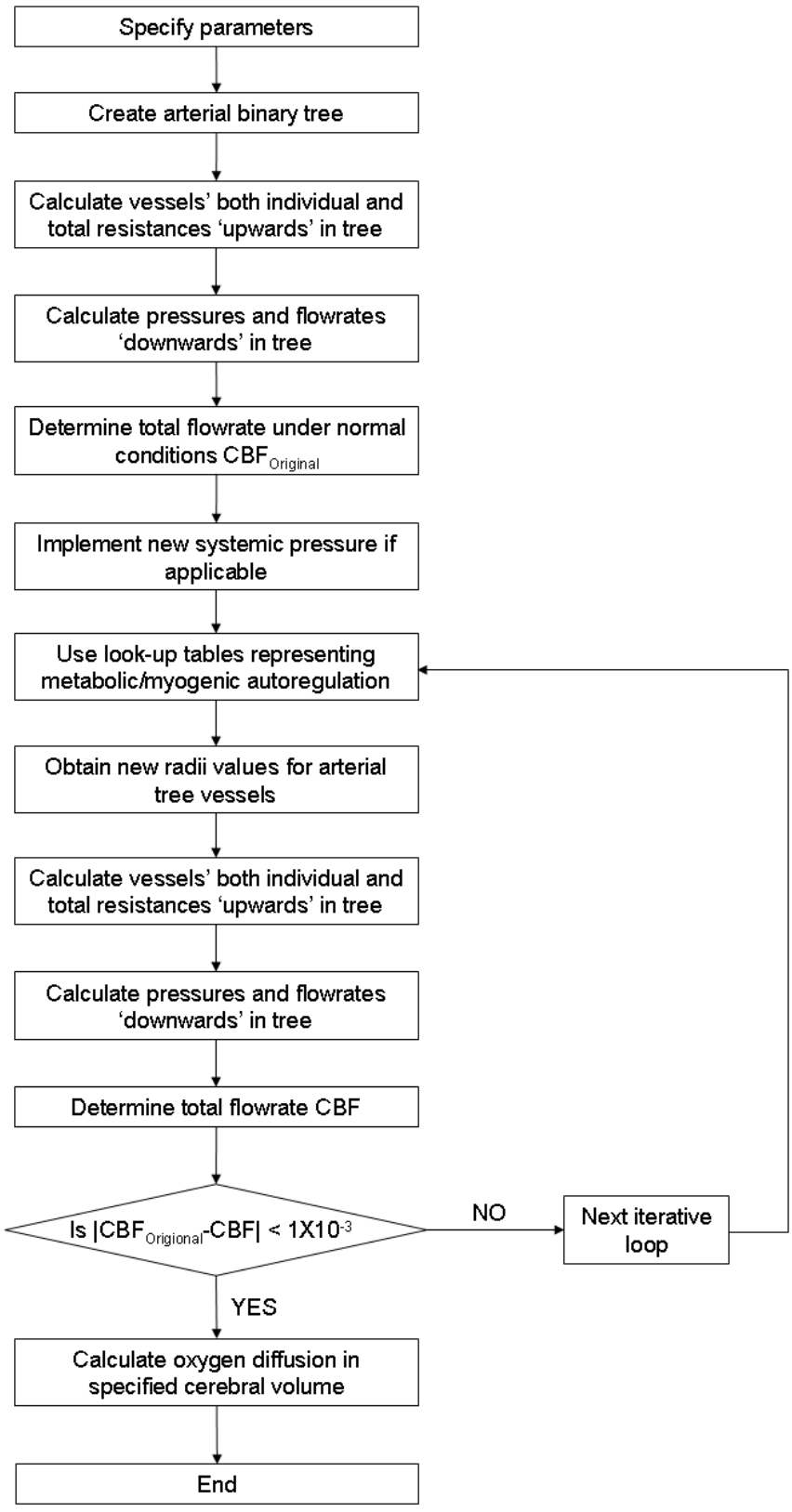

Figure 7.13 Schematic diagram of the numerical procedure of the arterial binary tree.

Chapter 8

Results and Discussions

This chapter provides the results of the several modifications made to the CoW model. It starts with the basic model simulations for the classical complete and incomplete CoW under normal conditions and some pathological conditions.

8.1 Basic Model

The basic model is defined in Chapter 4. The results provided in this section are used as a basis and a point of comparison between the several modifications made to the model that follows. The simulations were run first for the classical complete CoW under MAP of 100 mmHg. Both the dynamic response and the steady state responses were considered.

8.1.1 Classical Complete CoW

8.1.1.1 Dynamic Response

The dynamic response of the model is controlled by the time constant, λ, and the PI controller parameters, K_i and K_p. The PI controller is not activated unless it detects a fluctuation in the reference flowrates through the variable resistances of the efferent arteries. Simulations of the CoW model with normal and abnormal MAP were carried out.

Normal Conditions

The basic CoW model was run for a classical complete CoW with an inlet MAP of 100 mmHg, which is the average pressure experienced under normal circumstances. Since there was no change of the CoW circumstances, the flowrates did not fluctuate.

Therefore, the PI controller was not activated and none of the efferent variable resistances changed. Figures 8.1 and 8.2 show the pressures of the CoW nodes at the start of the efferent variable resistance segments and the flowrates for these segments, respectively. In the literature, the threshold for penumbra was determined to be $20cm^3min^{-1}$ per 100g [11, 54]. As mentioned above, the average total cerebral flowrate used in this research was $12.5cm^3s^{-1}$. This is equivalent to $53.6cm^3min^{-1}$ per 100g for an average cerebral mass of 1400 g. The penumbra threshold is, therefore, 37% of the normal flowrate. This risk threshold is represented by the red line in the flowrates' plot.

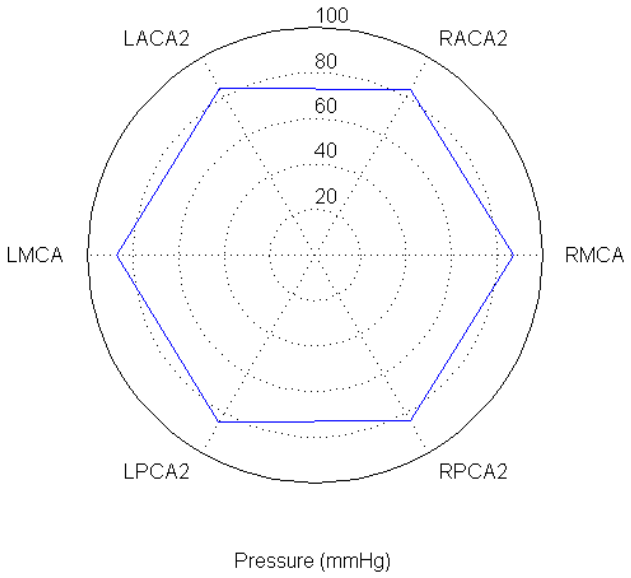

Figure 8.1 Pressures at the efferent arteries' nodes under normal conditions.

The bar graph in Figure 8.3 shows the flowrates in all CoW arteries: the afferent arteries, internal connecting arteries, and efferent arteries. The flowrates in the CoW are asymmetric. This is because of the asymmetry of the CoW geometry based on the data provided in Table 4.3. However, the flowrate through the efferent arteries is symmetric. This is because the variable resistances adjust to give the optimal flowrates to the different territories of the cerebral mass defined by the ratio stated in Chapter 4. The resistances for a normal complete CoW at normal MAP of 100 mmHg are listed in Table 8.1.

Pressure Drop of 20 mmHg

The MAP at the inlet of the CoW network can vary in individuals. Here the classical complete CoW was subjected to a MAP drop of 20 mmHg. The MAP experienced at the inlet of the CoW geometry in this case was 80 mmHg as shown in Figure 8.4.

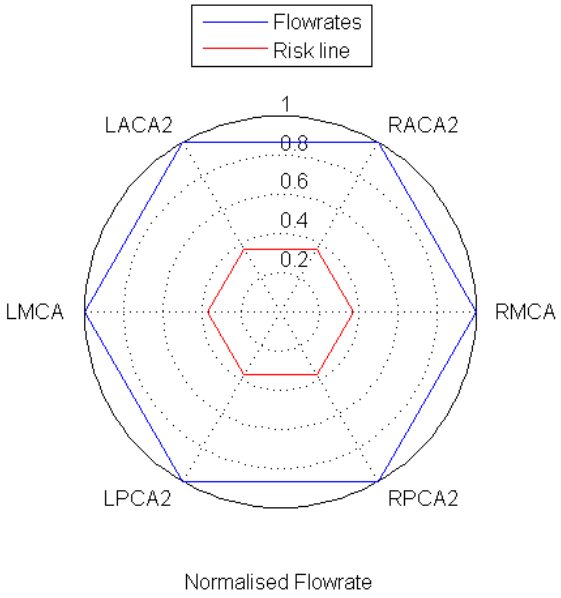

Figure 8.2 Efferent arteries' flowrates under normal conditions.

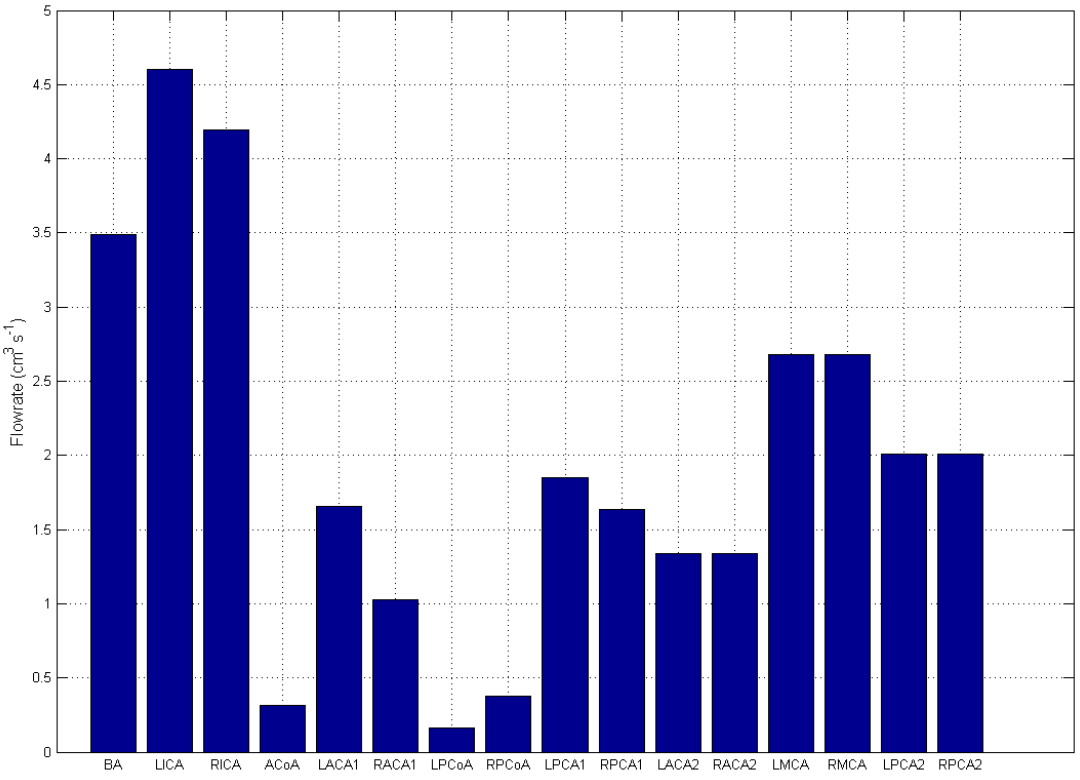

Figure 8.3 Flowrates through all CoW vessels under normal conditions.

Table 8.1 *Efferent arteries' resistances for a normal complete CoW under normal conditions.*

Artery	**Resistance** ($Nscm^{-5}$)	
	Left segment	Right segment
ACA2	0.798	0.795
MCA	0.413	0.414
PCA2	0.535	0.529
AChA	10.320	10.346
SCbA	10.534	10.534

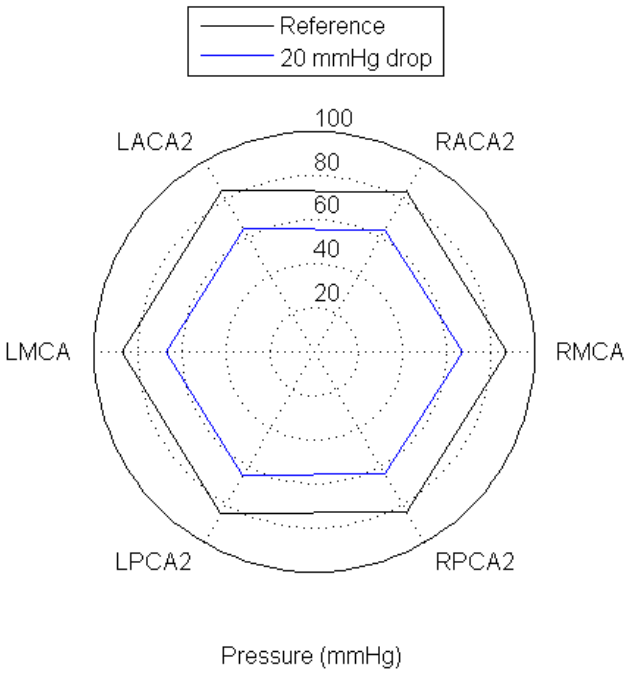

Figure 8.4 Pressures at the efferent arteries' nodes under MAP drop of 20 mmHg.

When the MAP drops, the blood flowrates delivered to the cerebral mass alter, resulting in the activation of the PI controller. As a result, the efferent variable resistances (Figures 8.5 - 8.6) are altered until the flowrates in the efferent vessels are restored to their original normal flowrates. The response in the left and right segments is identical because both segments experience the same drop in pressure, which is identical because of the classical complete CoW condition as well as the absence of any pathological conditions such as the occlusion of a supplying artery.

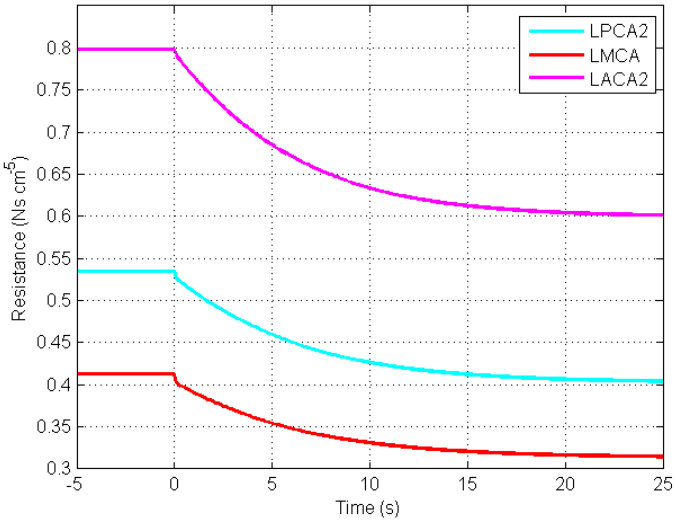

Figure 8.5 Response of the left efferent arteries' variable resistances as a result of MAP drop of 20 mmHg.

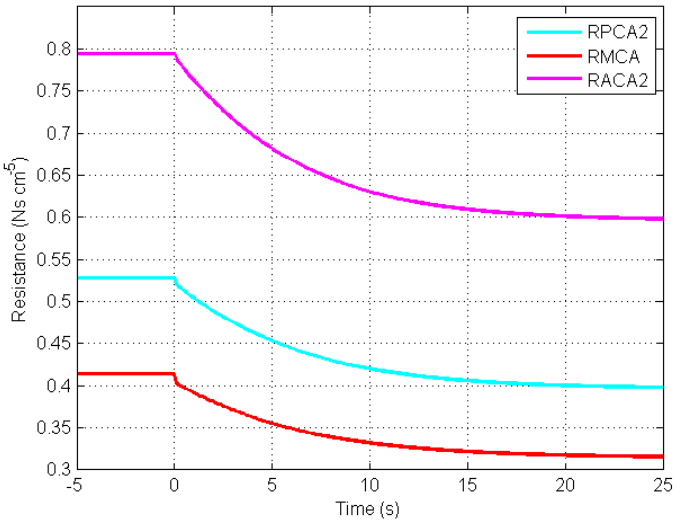

Figure 8.6 Response of the right efferent arteries' variable resistances as a result of MAP drop of 20 mmHg.

The blood flow responses in the variable resistance segments (ACA2s, MCAs, PCA2s, AChAs and SCbAs) are all shown in Figures 8.7 - 8.11. In the figures, the responses of the left segments are not clear because the responses of the right segments overlie them, making them indistinguishable. As mentioned above, the PI controller parameters were chosen so that the blood flow response would follow the response reported by Newell et al. [91]. That is, as a result of the 20 mmHg drop in MAP, the cerebrovascular system requires approximately 20 seconds to return to the optimal conditions observed with the normal MAP of 100 mmHg.

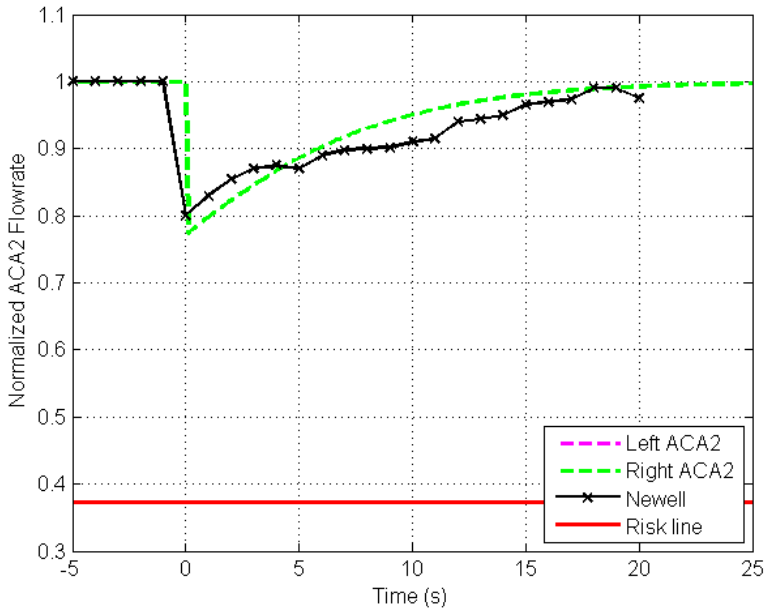

Figure 8.7 Flowrate response of the ACA2 arteries as a result of MAP drop of 20 mmHg.

The values of the flowrates encountered at the end of the dynamic simulations are termed *steady state* in this thesis. The steady state values of the flowrates as a result of a MAP drop of 20 mmHg are shown in Figure 8.12. In this case, the CoW model was able to return to the normal flowrates experienced under normal conditions: this is *autoregulation*. The bar graph in Figure 8.13 shows the original flowrates through all segments of the CoW at normal conditions in blue and the flowrates after the pressure drop in brown. The flowrates for both cases are almost exactly the same for all vessels in the CoW.

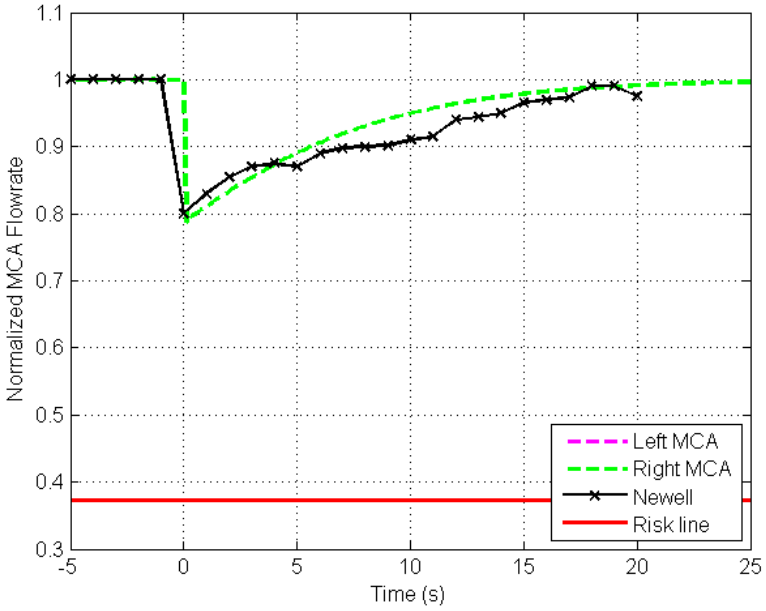

Figure 8.8 Flowrate response of the MCA arteries as a result of MAP drop of 20 mmHg.

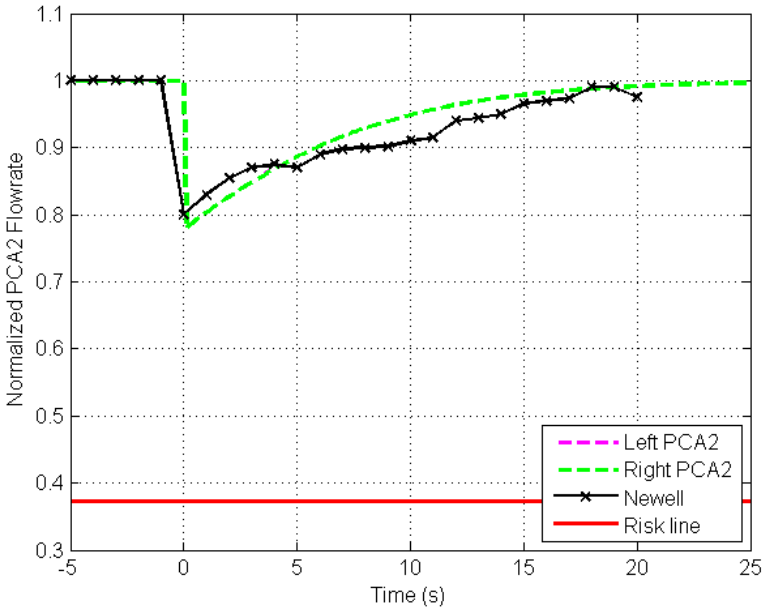

Figure 8.9 Flowrate response of the PCA2 arteries as a result of MAP drop of 20 mmHg.

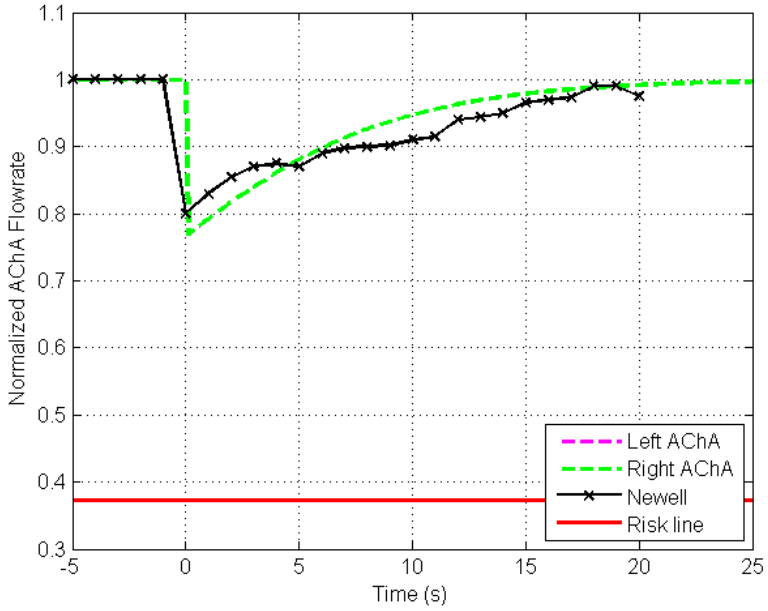

Figure 8.10 Flowrate response of the AChA arteries as a result of MAP drop of 20 mmHg.

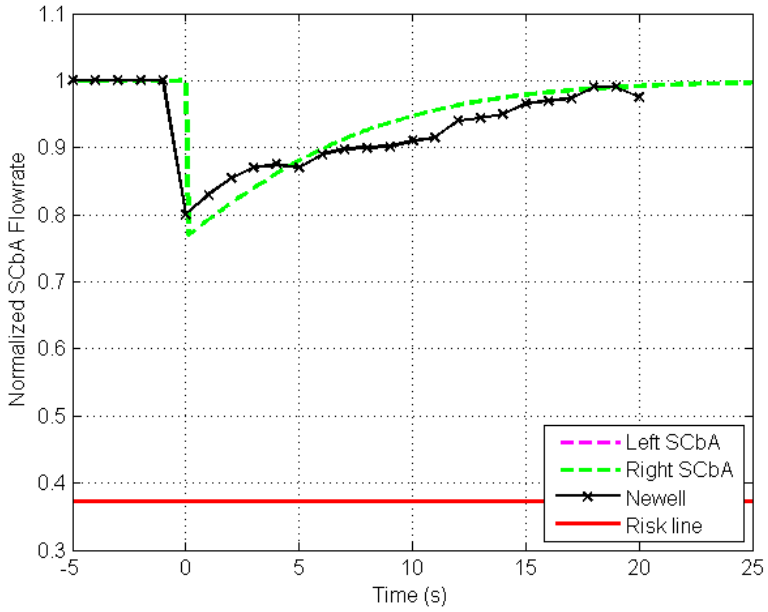

Figure 8.11 Flowrate response of the SCbA arteries as a result of MAP drop of 20 mmHg.

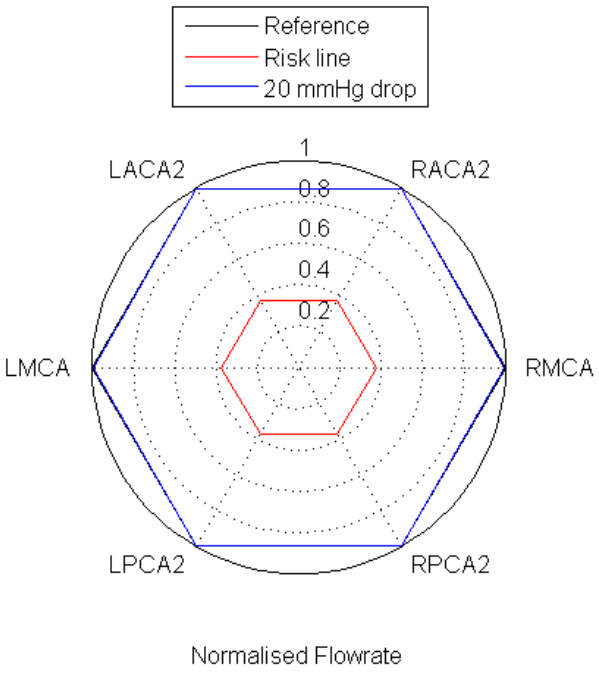

Figure 8.12 Efferent arteries' flowrates under MAP drop of 20 mmHg.

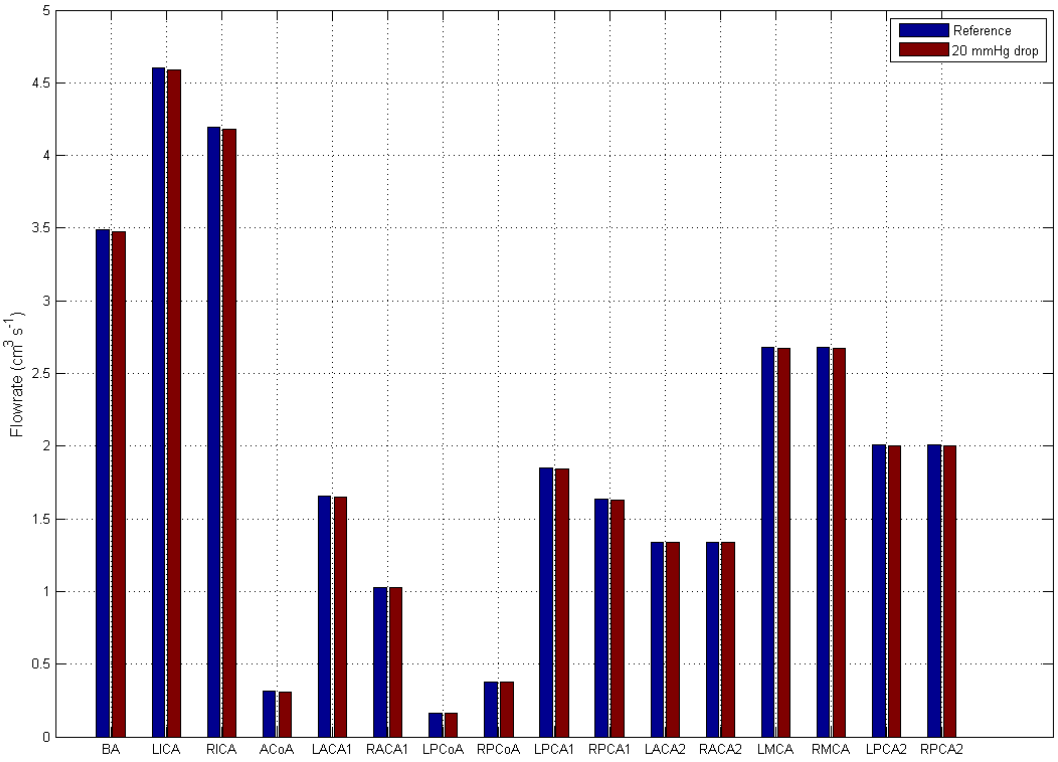

Figure 8.13 Flowrates through all CoW vessels under normal conditions (blue) and under MAP drop of 20 mmHg (brown).

In this Chapter, some simulations were run with only one value of MAP drop (20 mmHg). This is to limit the amount of results and plots presented in this thesis. The value of 20 mmHg was chosen in particular because it was the value used in the experimental work of Newell et al. [91].

8.1.1.2 Steady State Response (Autoregulation)

The autoregulation plot is produced by executing the CoW model for a range of MAP and obtaining the steady state response for each pressure in the range. Figure 8.14 shows the autoregulation plot of the basic CoW model. This plot will be referred to as *original* when compared to other autoregulation plots in subsequent sections. As stated in Section 4.1.4, the upper and lower limits of autoregulation were set using upper and lower bounds of resistance to match the Guyton autoregulation plot limits. Figures 8.15 and 8.16 show the resistances of the efferent arteries for the MAP range. The resistances are constant below the LLA and above the ULA. Between the two limits of autoregulation, the resistance alter in order to achieve the optimal flowrates for the cerebral mass.

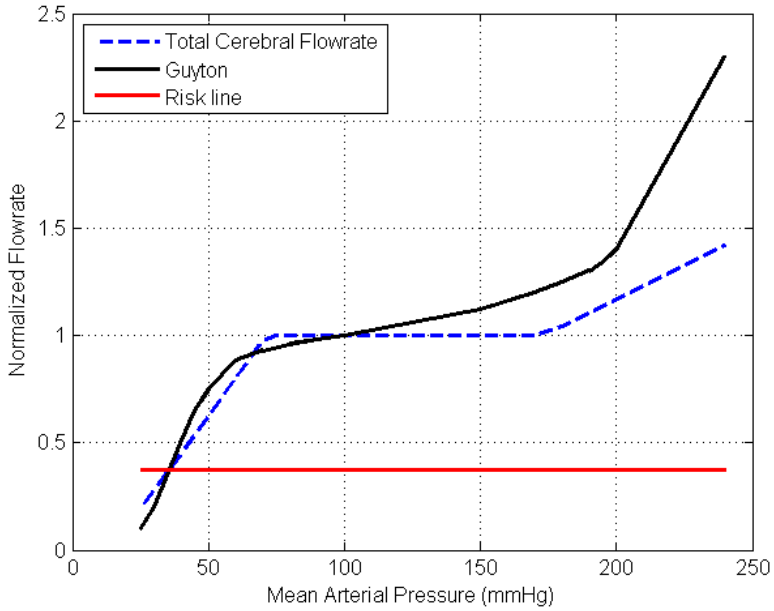

Figure 8.14 Autoregulation plot for the basic model with classical complete CoW. This is referred to as *original* in other plots.

In an attempt to reproduce the Guyton autoregulation slope observed in Figure 8.14, the dead-band was introduced in Moorhead's model as discussed in Section 4.2.3. Figure 8.17 shows the autoregulation plot for a classical complete CoW, with the dead-band algorithm. The plot shows that the dead-band algorithm was not successful in

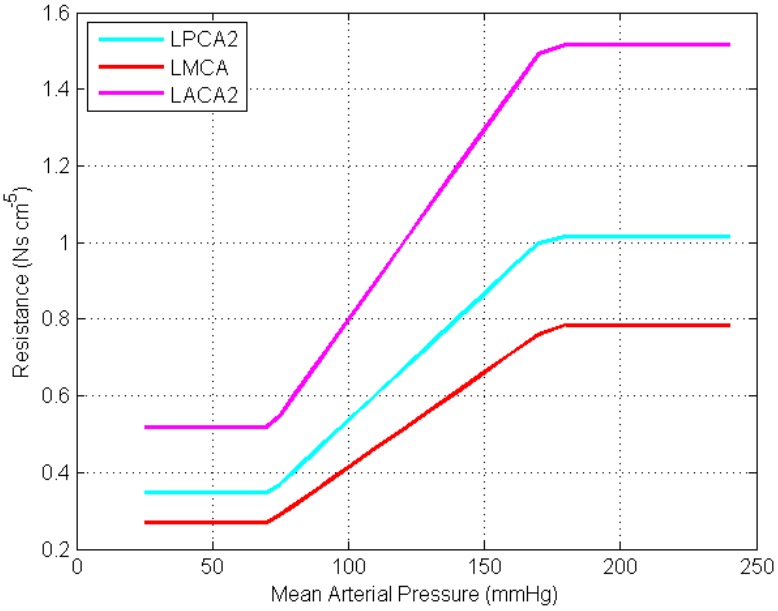

Figure 8.15 Left efferent arteries' variable resistances for the MAP range.

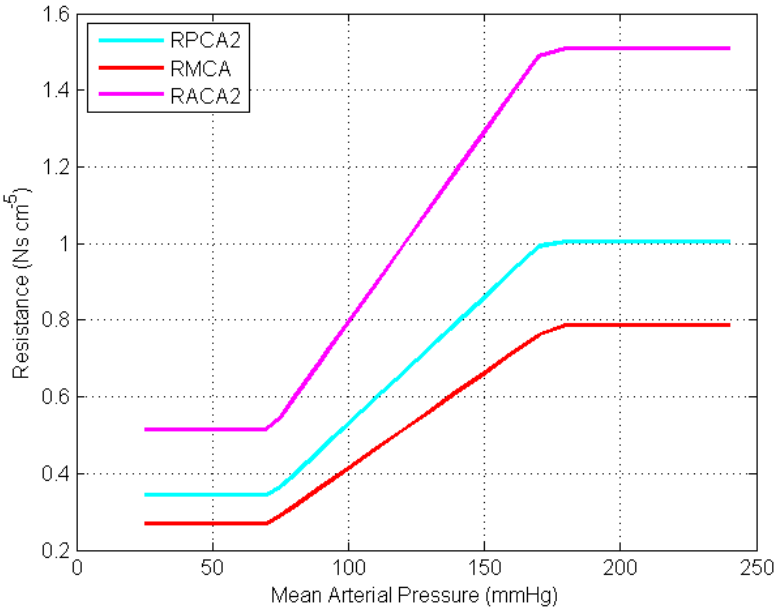

Figure 8.16 Right efferent arteries' variable resistances for the MAP range.

obtaining the autoregulation slope. The steady state solutions reached were always 7% off the normal flowrate experienced at MAP of 100 mmHg. For the autoregulated range of MAP below 100 mmHg, the steady state solution always reached 93% of the normal flowrate. For the autoregulated range of MAP above 100 mmHg, the steady state solution always reached 107% of normal flowrate. Figures 8.18 and 8.19 show the corresponding resistances of the efferent arteries with the dead-band algorithm.

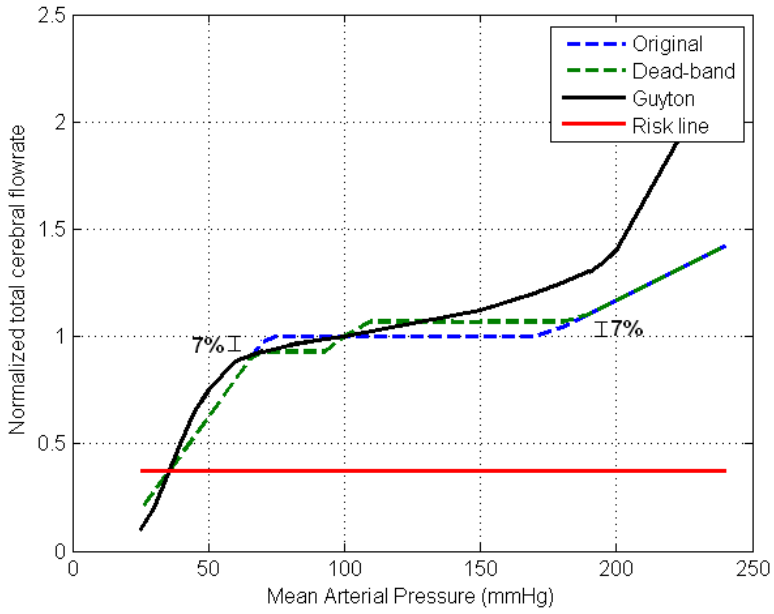

Figure 8.17 Autoregulation plot for the basic model with classical complete CoW using the dead-band algorithm.

8.1.2 Clinical Scenarios

In reality, the cerebral hemodynamics rarely behave in an ideal way. This is because a large percentage of the population have CoW abnormalities as discussed in Section 1.2.3. In addition, the CoW network may be subjected to some pathological conditions such as a stenosis or an occlusion of a supplying artery. In this section, the basic model is run for the most common abnormal CoW configurations: two anterior abnormalities and two posterior abnormalities. The anterior abnormalities are the absence of the ACoA or a unilateral absence of an ACA1. The posterior abnormalities are the unilateral absence of a PCoA or a unilateral fetal case. A left ICA occlusion was implemented for all these cases by having the abnormality on either the ipsilateral or contralateral side of the ICA occlusion. Modelling of a missing vessel of the CoW or an occlusion to a supplying artery was done by setting the resistance of that particular vessel to a very large value, by multiplying the normal resistance of that vessel by 1×10^{10}. When

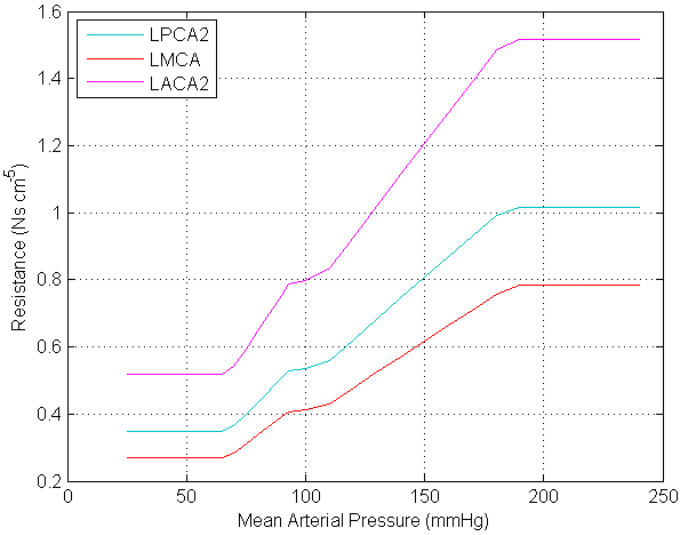

Figure 8.18 Left efferent arteries' variable resistances using the dead-band algorithm.

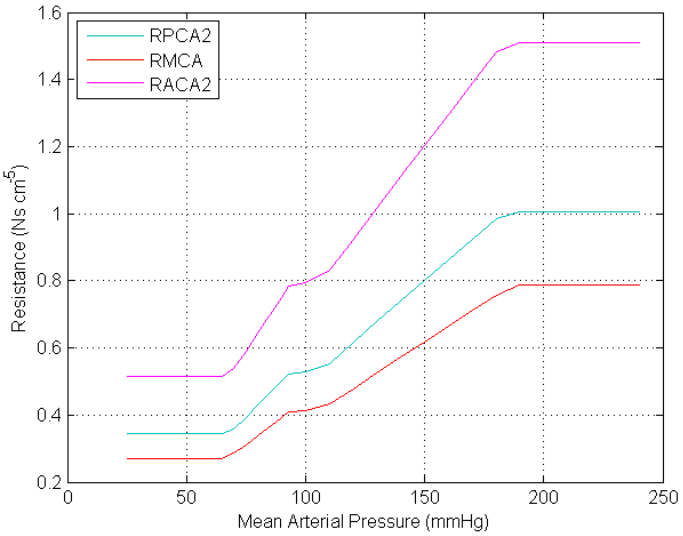

Figure 8.19 Right efferent arteries' variable resistances using the dead-band algorithm.

referring to a vessel in the CoW, the terms *ipsilateral* and *contralateral* are always used in relation to the ICA occlusion.

8.1.2.1 ICA Occlusion for Complete CoW

The classical complete CoW geometry is subjected to a left ICA occlusion at the normal MAP of 100 mmHg. Figure 8.20 shows the pressures and the flowrates for the major efferent CoW arteries. As is clear from the plots, the steady state flowrates through all the efferent arteries are not affected. The CoW compensated for the loss of blood flow from the left ICA, which usually supplies the ipsilateral MCA and ACA2, by delivering a large percentage of the blood flow from the BA to these two effected efferent arteries via the ipsilateral PCA1. The MCA and ACA2 also receive blood supply from the contralateral ICA delivered through the ACoA.

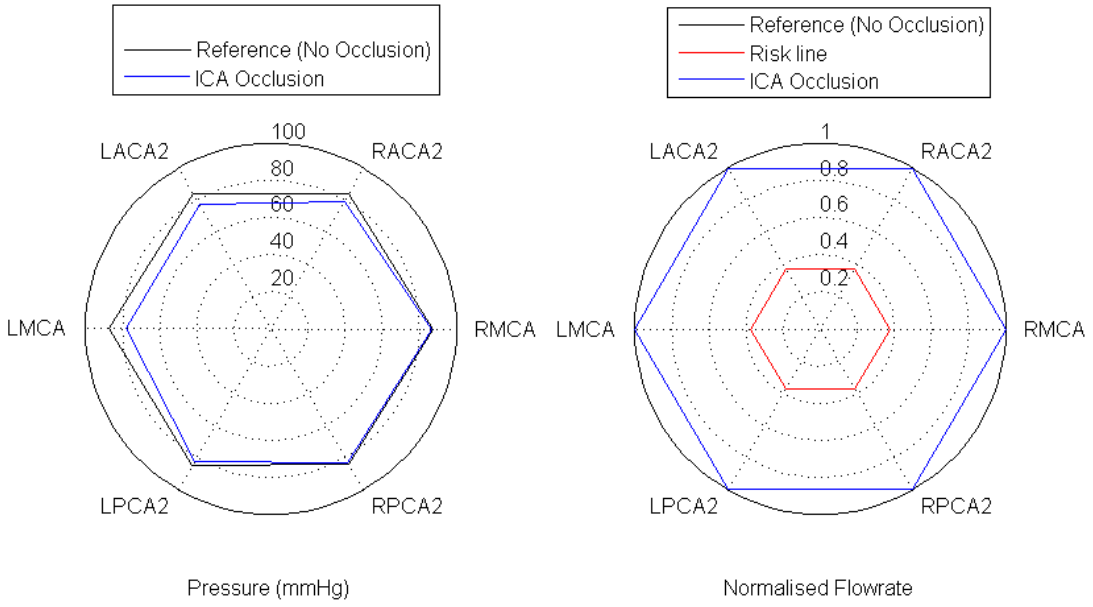

Figure 8.20 Efferent arteries' pressures and flowrates for a classical complete CoW with ICA occlusion.

The bar graph in Figure 8.21 shows the flowrates through all segments of the CoW after the ICA occlusion. The bars that display negative flowrates illustrate that the flowrate direction changed from the original. Owing to the asymmetry of the CoW in terms of averaged lengths and radii of the vessels, there was a low flowrate through the ACoA from the left hemisphere to the right hemisphere under normal conditions. Owing to the ICA occlusion, this changed significantly in terms of flowrates and their directions. The flowrate through the ipsilateral ACA1 significantly changed; before ICA occlusion, the flowrate through the ipsilateral ACA1 segment supplied the ipsilateral efferent artery of ACA2 as well as partially supplying the contralateral ACA2 through

the ACoA; after ICA occlusion, flowrate through the ipsilateral ACA1 only delivered blood flow to the ipsilateral MCA from the contralateral side through the ACoA; hence the change in direction. The flowrate through the contralateral ACA1 also increased because, after the occlusion, not only did it deliver blood flow to the ACA2 in its side, but it also supplied blood flow to the ACA2 and MCA segments of the side affected by the ICA occlusion. In terms of posterior circulation, the PCoAs play an insignificant role in terms of blood delivery under normal conditions; they only supply a small portion of blood from the ICAs to the ipsilateral PCAs. Similar to the ACoA, the role of the PCoAs becomes extremely significant when the CoW experiences abnormalities. In this case, the flowrate through the ipsilateral PCoA rose significantly and changed its direction of travel to supply the ipsilateral MCA from the BA. The flowrate through the supplying arteries also changed. To compensate for the loss of flowrate through the left ICA, the flowrate in the other two supplying arteries, the contralateral ICA and BA, increased significantly.

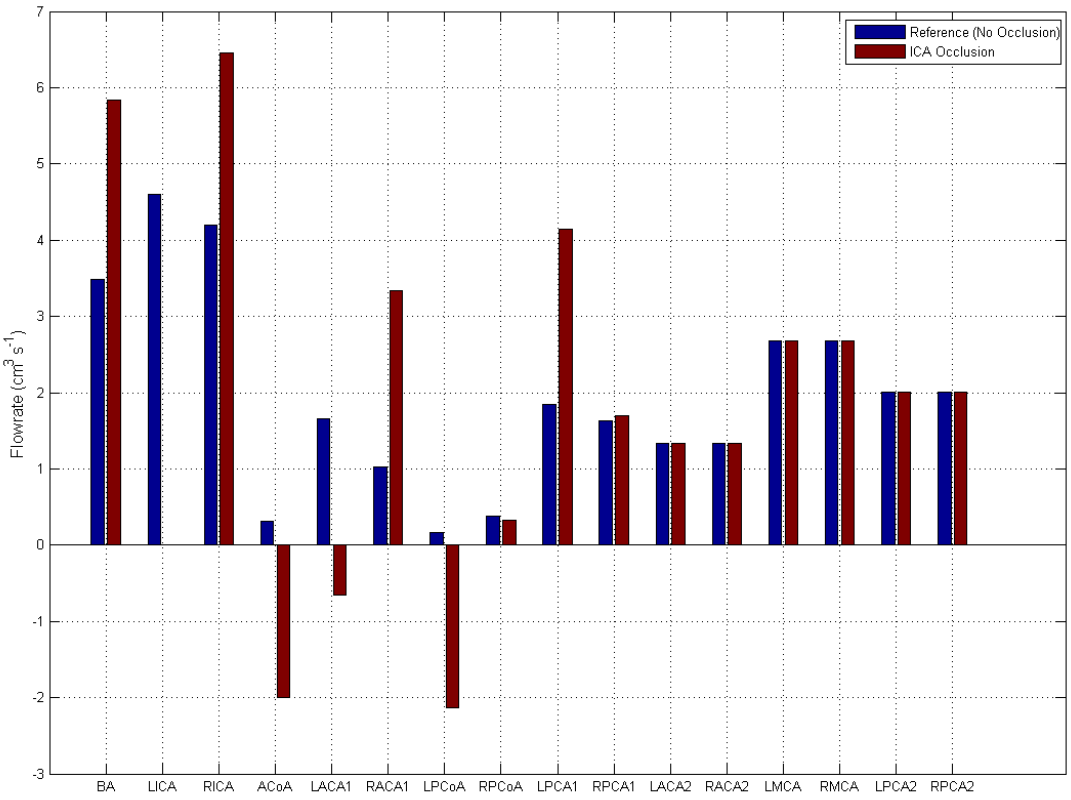

Figure 8.21 Flowrates through all CoW vessels under normal conditions (blue) and under ICA occlusion (brown) for a classical complete CoW.

As discussed above, the flowrates through the efferent arteries experienced few consequences, if any, as a result of a unilateral ICA occlusion when the MAP was 100mmHg (Figure 8.22). This is because, once the PI controller detects a change in

the flowrates, the variable resistances are forced to alter (representing radii dilation) until the flowrates return to the normal values. The variable resistances' response in Figure 8.23 show that both the ACA2 and the MCA segments change their resistances significantly as a result of ICA occlusion in a classical complete CoW. Resistance changes in the contralateral MCA and both PCA2s are insignificant.

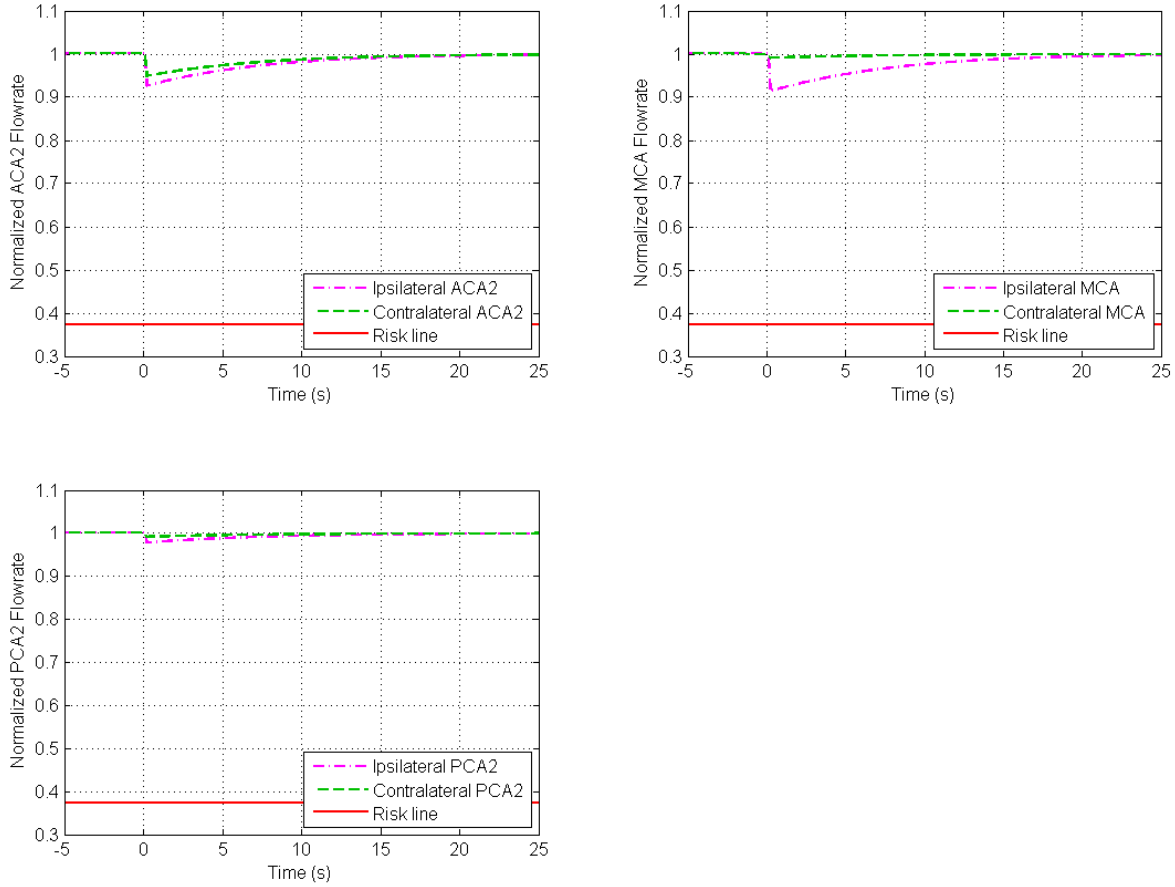

Figure 8.22 Flowrate response of the major efferent arteries as a result of ICA occlusion in a classical complete CoW.

In regards to the autoregulation plot, an ICA occlusion shifts the autoregulation range to the right, that is, towards a higher range of MAP. This is shown in Figure 8.24, where the overall effect on the total cerebral flowrate is small but the effect on the left MCA is more noticeable with the autoregulation range shifted to the right by approximately 10 mmHg.

8.1.2.2 ICA Occlusion with Missing ACoA

The ACoA segment is the most common site of abnormalities in the CoW. The ACoA can be duplicated or triplicated, or less commonly, hypoplastic (missing). The

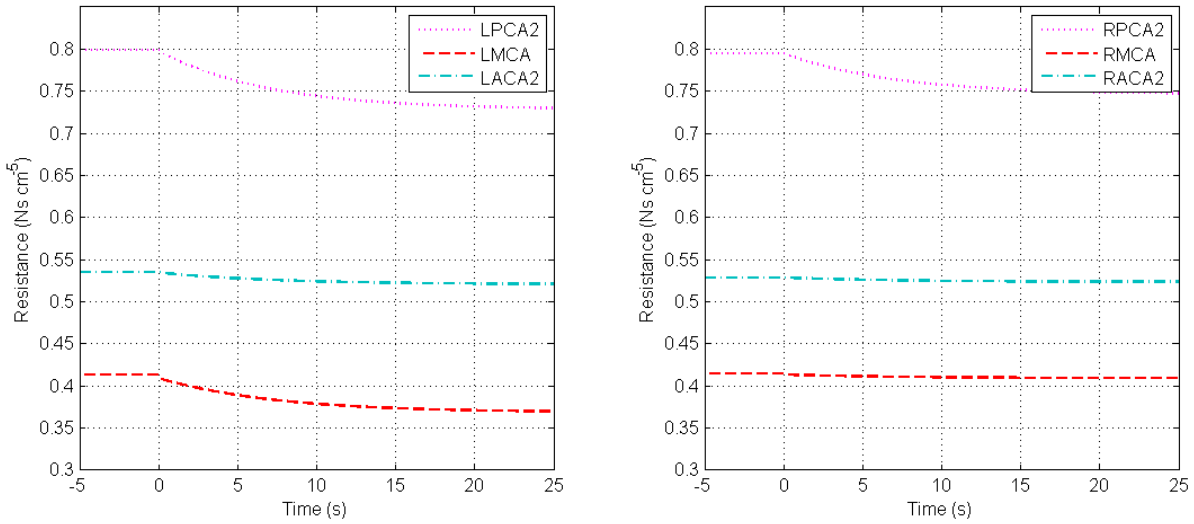

Figure 8.23 Response of the efferent arteries' variable resistances as a result of ICA occlusion in a classical complete CoW.

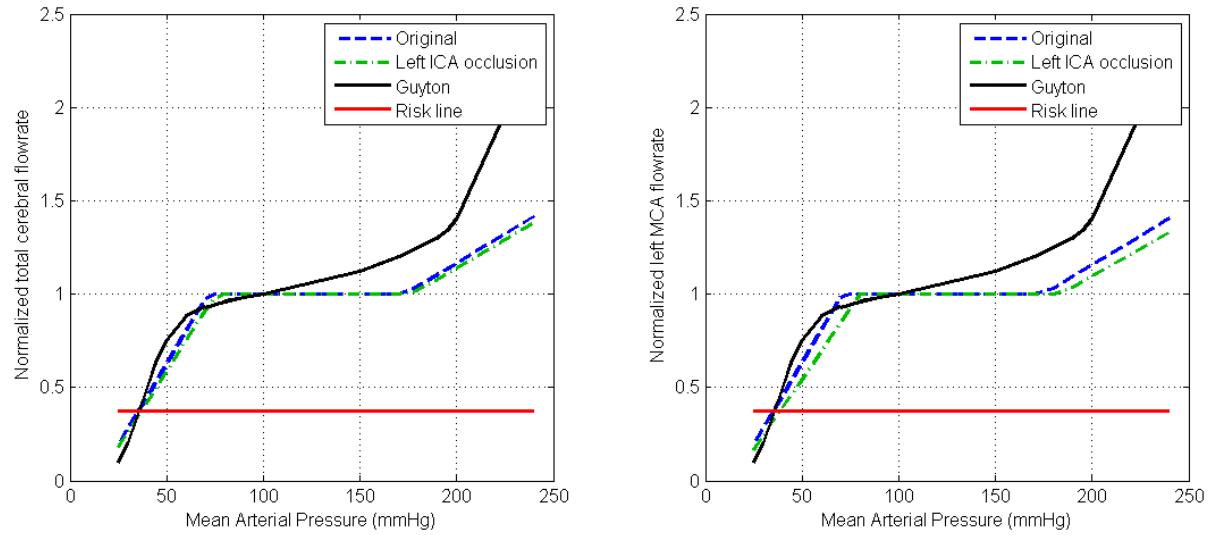

Figure 8.24 The autoregulation plot for a) total cerebral flowrate and b) left MCA flowrate in a classical complete CoW with a left ICA occlusion.

condition of multi-vesseled ACoA does not affect the flowrates in the CoW significantly. More risk is involved when one or more vessels in the CoW are missing, such as the case of a missing ACoA, which contributes to 18% of the population. The model was run with a missing ACoA, assuming a normal MAP of 100 mmHg. Figure 8.25 shows that the steady state values of the flowrates are not affected. However, the pressure at the ipsilateral efferent vessels dropped significantly.

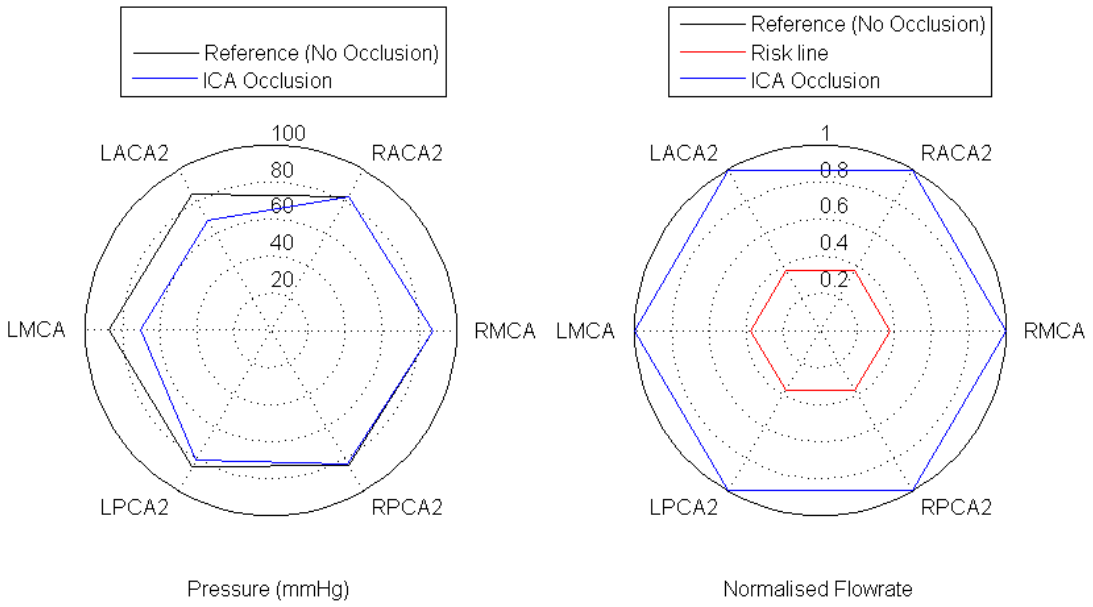

Figure 8.25 Efferent arteries' pressures and flowrates for a CoW with an ICA occlusion and missing ACoA.

The flowrates through all the CoW segments are shown by the bar graph in Figure 8.26. As a result of the missing ACoA, no compensation was available through the anterior of the CoW. Therefore, the flowrates through the ipsilateral PCA1 and PCoA increased tremendously, compared to the ICA occlusion with a classical complete CoW. In the missing ACoA case, the ipsilateral ACA2 and MCA were supplied solely by the BA, which explains the approximately-double increase of flow through it. There was only a small increase of blood flow through the contralateral ICA because it did not take part in supplying the opposite site affected by the occlusion. However, it did contribute more to the supply of the contralateral PCA2 via the contralateral PCoA. The contralateral PCoA flowrate undergoes the same increase experienced by the contralateral ICA. This was because some of the blood flow that usually supplied the contralateral PCA2 by the BA was redirected to supply the efferent arteries affected by the left ICA occlusion, hence the small decrease in flowrate through the contralateral PCA1.

As shown by the response of flowrates in Figure 8.27 and variable resistances in Figure 8.28, the ipsilateral efferent arteries were affected most by the ICA occlusion in the CoW with a missing ACoA. The ipsilateral ACA2 and MCA variable resistances

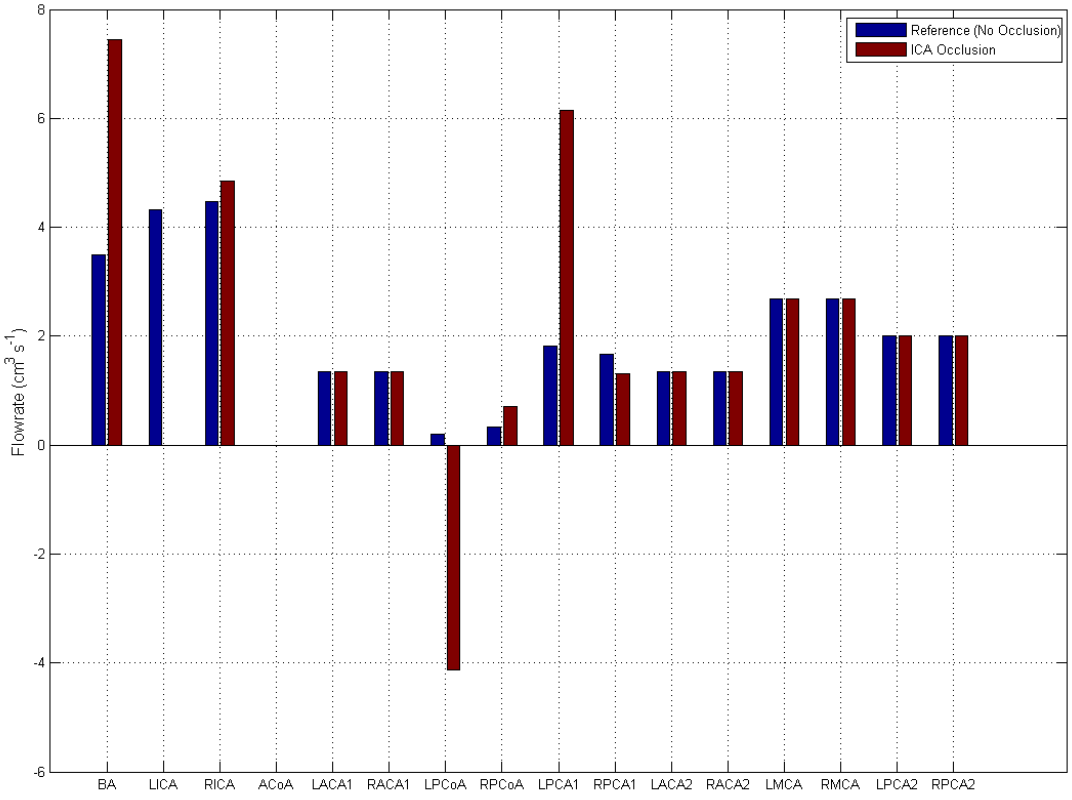

Figure 8.26 Flowrates through all CoW vessels under normal conditions (blue) and under ICA occlusion (brown) for a CoW with missing ACoA.

experienced the most change in order to return flowrates to original values, followed by the ipsilateral PCA2 variable resistance. The contralateral efferent arteries experienced negligible changes as a result of part of the blood flow being redirected towards the side affected most by the left ICA occlusion.

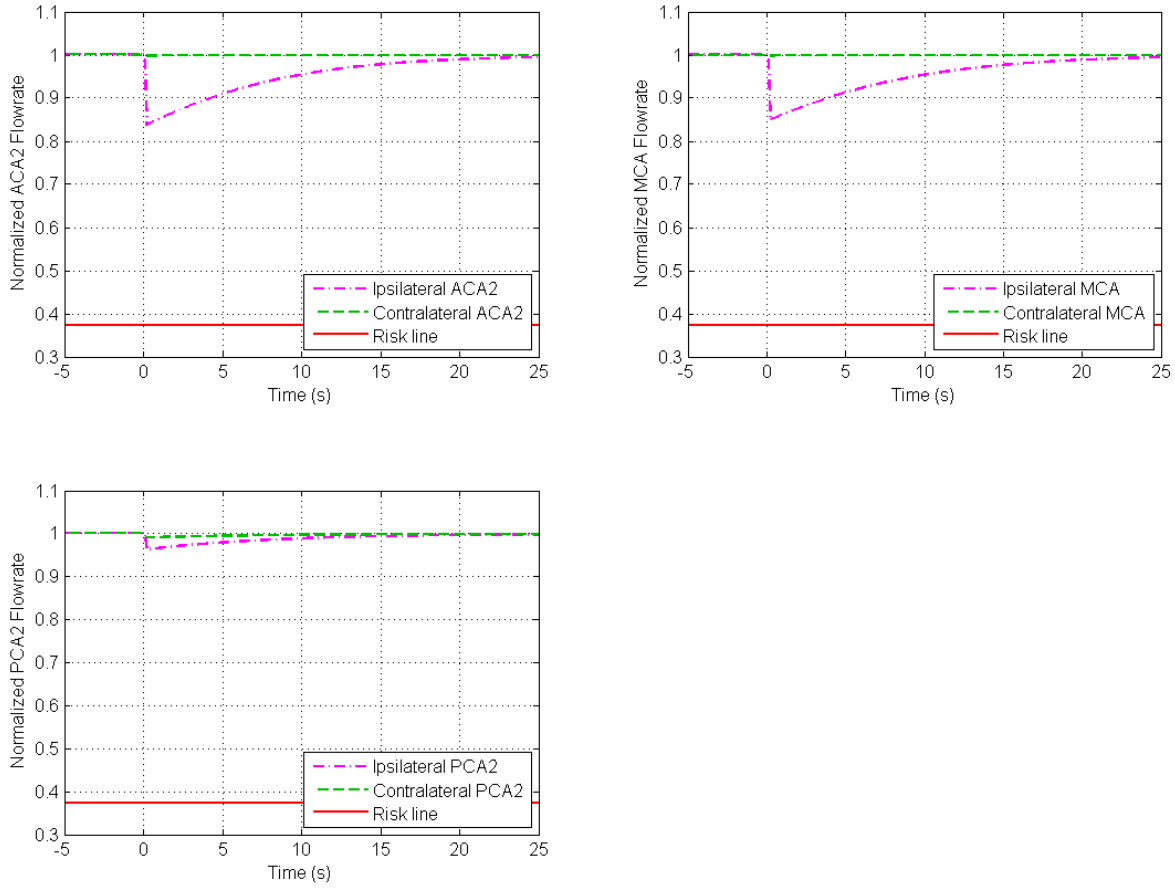

Figure 8.27 Flowrate response of the major efferent arteries as a result of ICA occlusion in a CoW with missing ACoA.

8.1.2.3 ICA Occlusion with Missing Ipsilateral ACA1

The second most common abnormality in CoW's anterior that might disadvantage the cerebral blood circulation is a unilateral missing ACA1, which occurs in 6.7% of the population. The model was run for a left ICA occlusion with an ipsilateral missing ACA1. The steady state response in the efferent arteries was not affected as shown in Figure 8.29. The flowrates through all the CoW vessels for this case are shown in the bar graph in Figure 8.30. The reference bars shown in blue are the flowrates for the CoW with the missing ipsilateral ACA1 before the left ICA occlusion. In all the clinical scenarios discussed in this thesis, the references are assumed to be the flowrates for the abnormal CoW rather than the complete CoW because approximately

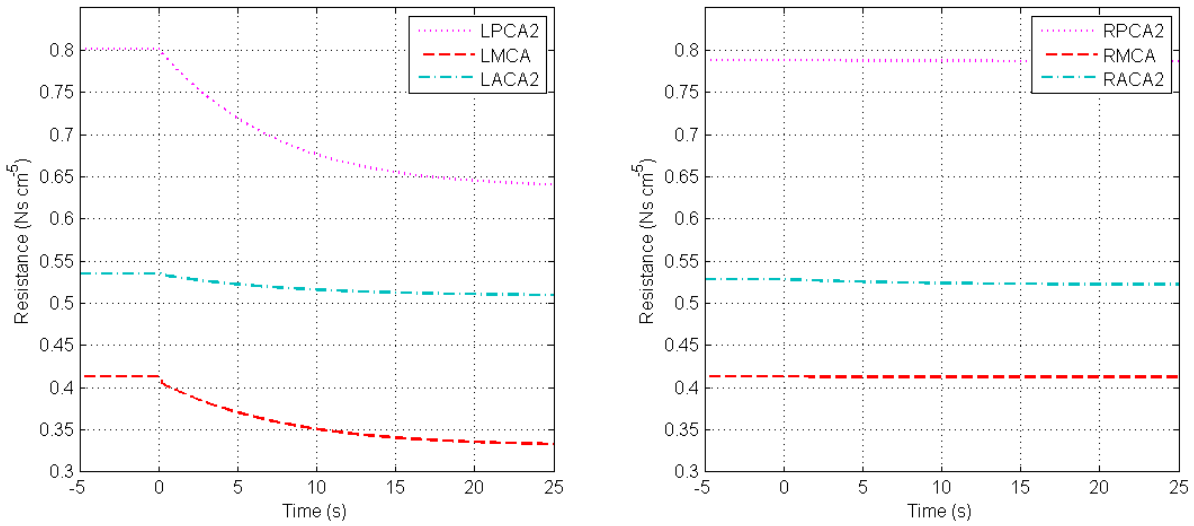

Figure 8.28 Response of the efferent arteries' variable resistances as a result of ICA occlusion in a CoW with missing ACoA.

half of the population have abnormal CoW configurations with no risk of having an insufficient blood supply unless a cerebrovascular pathological condition develops, such as an occlusion of a supplying artery.

As a result of the occlusion, in order to supply the ipsilateral MCA, the BA flowrate increased by almost the amount usually supplied by the left ICA. Therefore, the same increase was experienced by the ipsilateral PCoA and PCA1. The contralateral ICA experienced a slight increase of blood flow, which was delivered to the contralateral PCA2. This was because part of the blood flow usually delivered to the contralateral PCA2 by the BA was redirected to supply the ipsilateral side that suffered the occlusion. As a result of the increase of blood flow from the contralateral ICA to the contralateral PCA2, the same increase of flowrate was experienced by the contralateral PCoA and PCA1.

The response in terms of flowrates and resistances are shown in Figures 8.31 and 8.32 respectively. As both the ACA2s were supplied by the contralateral ICA, they did not experience any disturbances to their response. The resistance of the ipsilateral MCA is the most altered to compensate for the drop in flowrate by the occlusion, followed by the ipsilateral PCA2. The ipsilateral PCA2 is not normally supplied by the ICA; however, it did undergo some changes due to sharing its blood supply with the MCA.

8.1.2.4 ICA Occlusion with Missing Contralateral ACA1

The steady state values of the flowrates were not altered in the case of an ICA occlusion for a CoW with a missing contralateral ACA1 as shown in Figure 8.33. The

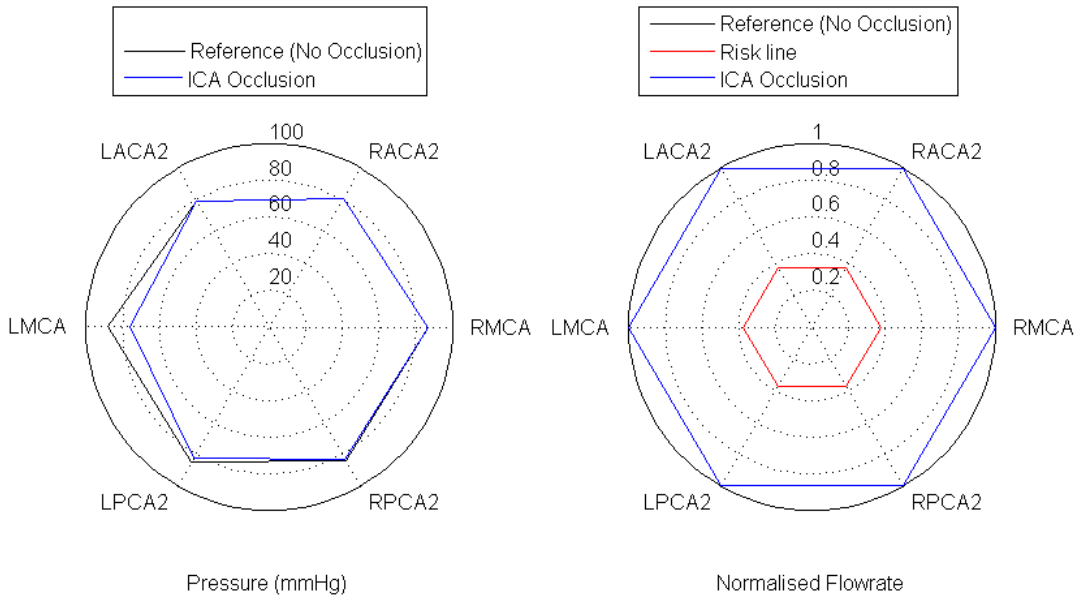

Figure 8.29 Efferent arteries' pressures and flowrates for a CoW with an ICA occlusion and missing ipsilateral ACA1.

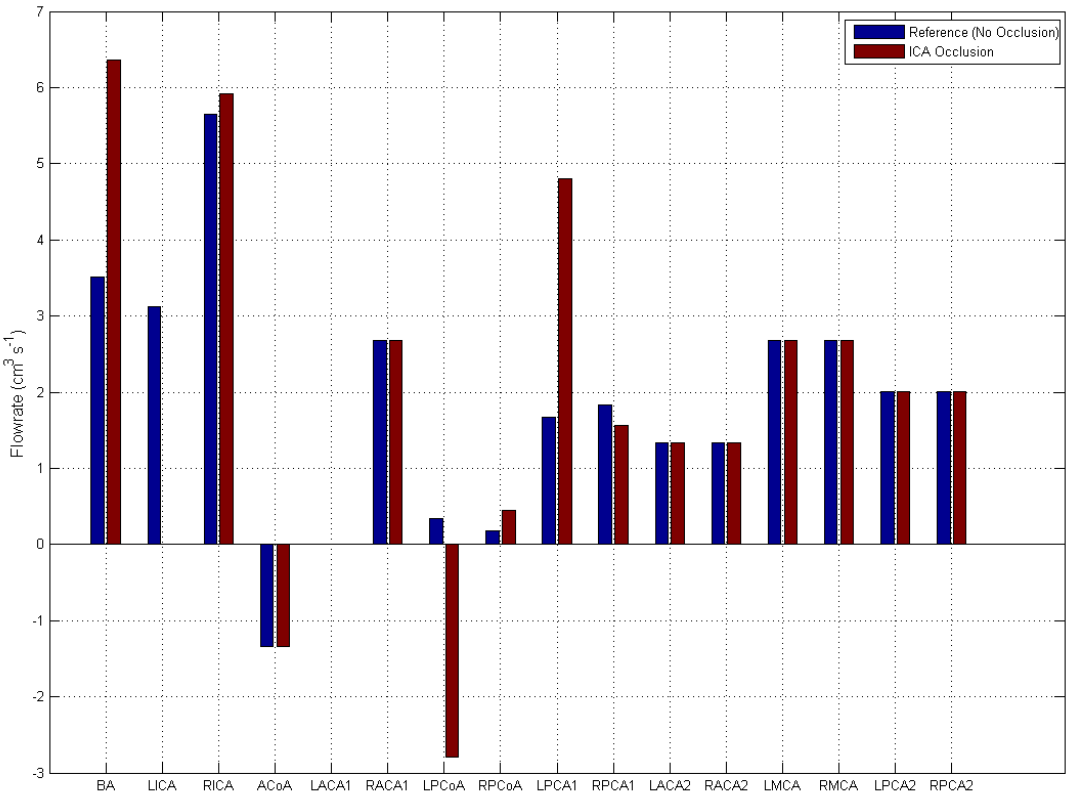

Figure 8.30 Flowrates through all CoW vessels under normal conditions (blue) and under ICA occlusion (brown) for a CoW with missing ipsilateral ACA1.

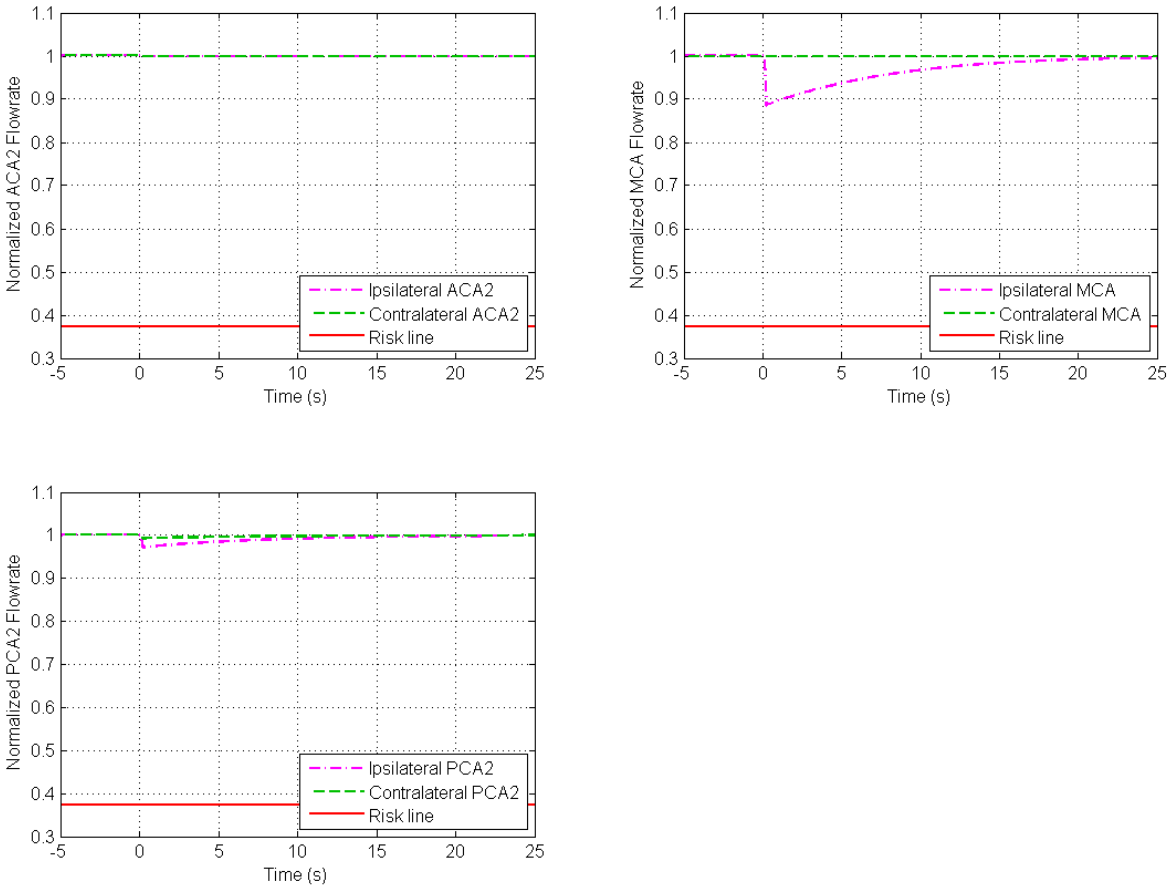

Figure 8.31 Flowrate response of the major efferent arteries as a result of ICA occlusion in a CoW with missing ipsilateral ACA1.

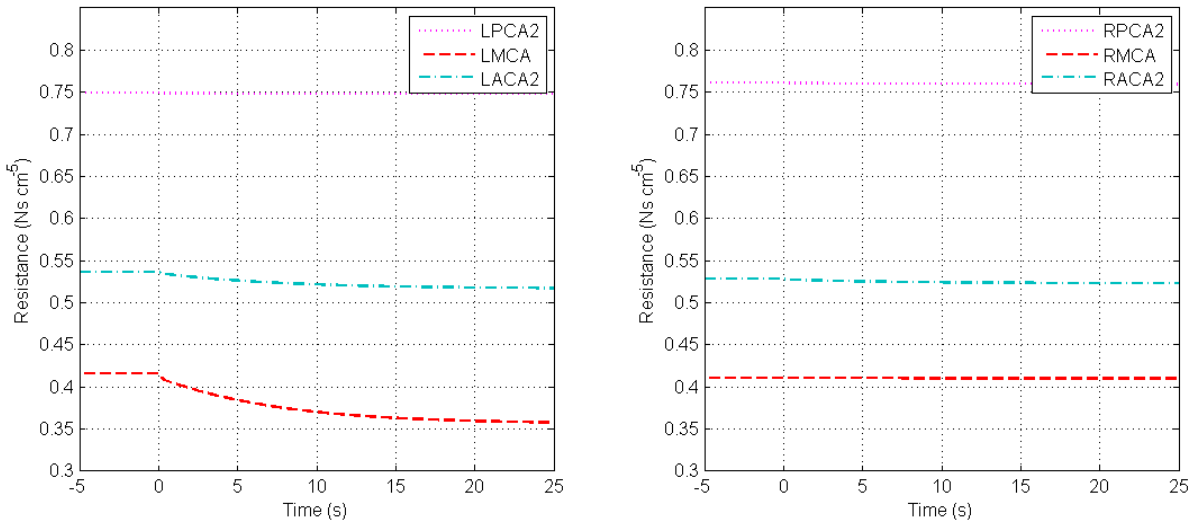

Figure 8.32 Response of the efferent arteries' variable resistances as a result of ICA occlusion in a CoW with missing ipsilateral ACA1.

effects of the occlusion, however, are clear from the pressures plot. The bar graph in Figure 8.34 shows the flowrates in the CoW before and after the left ICA occlusion. Before the occlusion, the left ICA played a more important role than the left ICA in the CoW with a missing ipsilateral ACA1 described in Section 8.1.2.3 above. The left ICA in the current case did not only supply the ipsilateral MCA, but it also supplied (solely) the ipsilateral as well as the contralateral ACA2. Therefore, after its occlusion, the increase in the BA blood flow was even greater than the increase in the missing ipsilateral ACA1 case. Consequently, the flowrates in the ipsilateral PCoA and PCA1 increased by the same amount. However, the blood flow increase in the contralateral ICA and the contralateral PCoA was similar in terms of quantity to the missing ipsilateral ACA1 case. Again, the slight increase occured because of the high demand from the BA, which was not able to deliver the same supply to the contralateral PCA2, hence the drop in the contralateral PCA1.

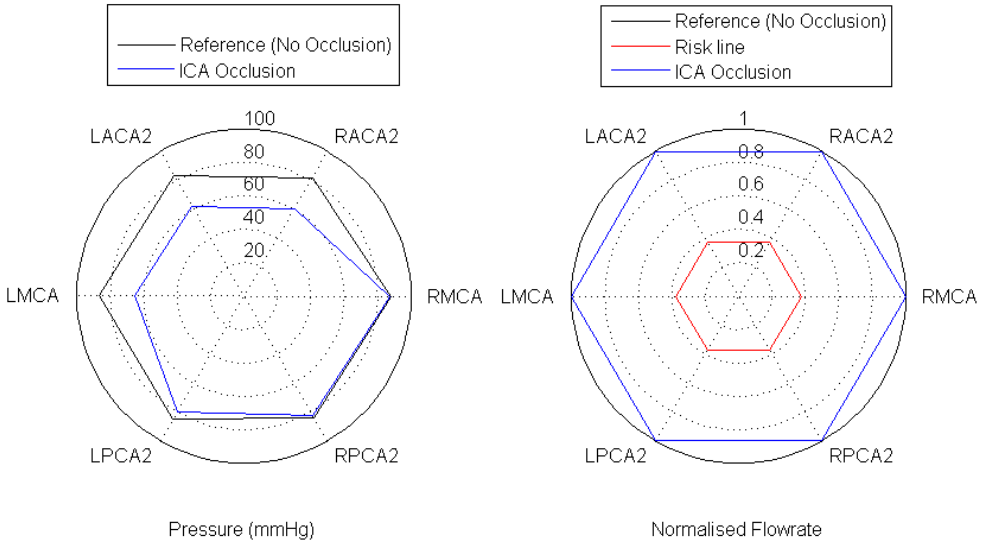

Figure 8.33 Efferent arteries' pressures and flowrates for a CoW with an ICA occlusion and missing contralateral ACA1.

The flowrates and resistances response presented in Figures 8.35 and 8.36 show that the ACA2 arteries responded equally to the occlusion as they were both supplied by the same source. The response was similar in the ipsilateral MCA as it was supplied by the same ICA, while the ipsilateral PCA2 experienced a smaller drop initially as it was mainly supplied by the BA, but the flowrate disturbance was due to suddenly having to share its blood source with three other main efferent arteries.

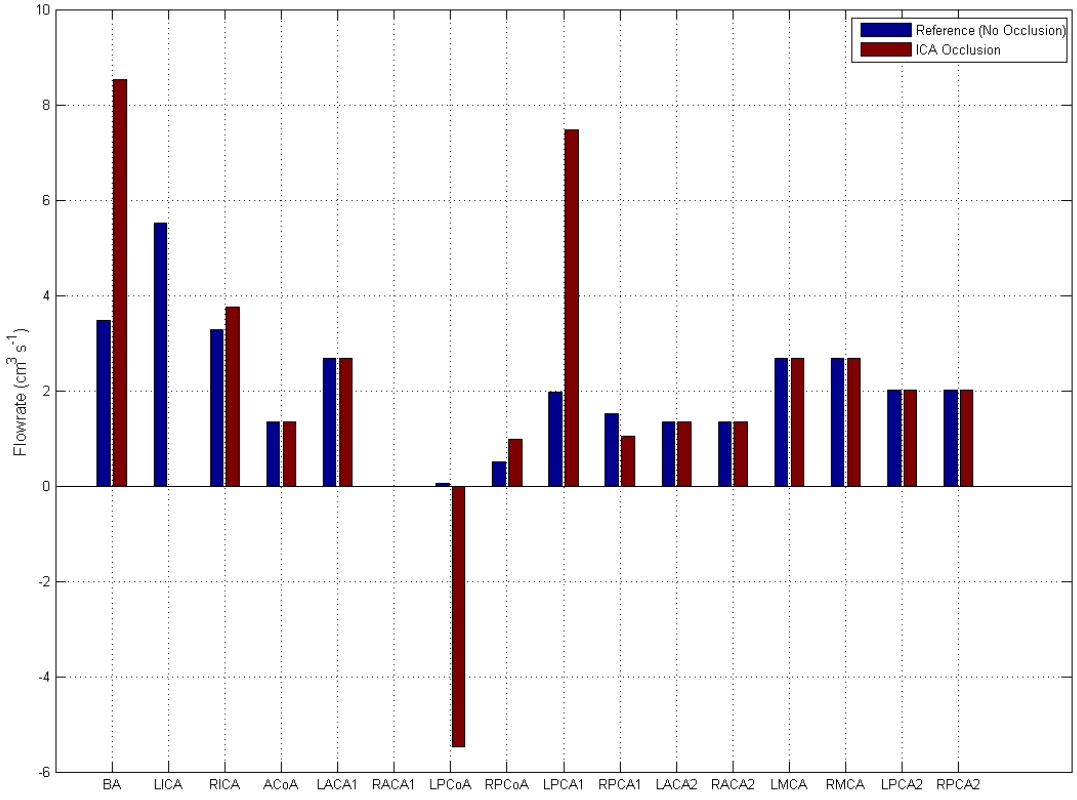

Figure 8.34 Flowrates through all CoW vessels under normal conditions (blue) and under ICA occlusion (brown) for a CoW with missing contralateral ACA1.

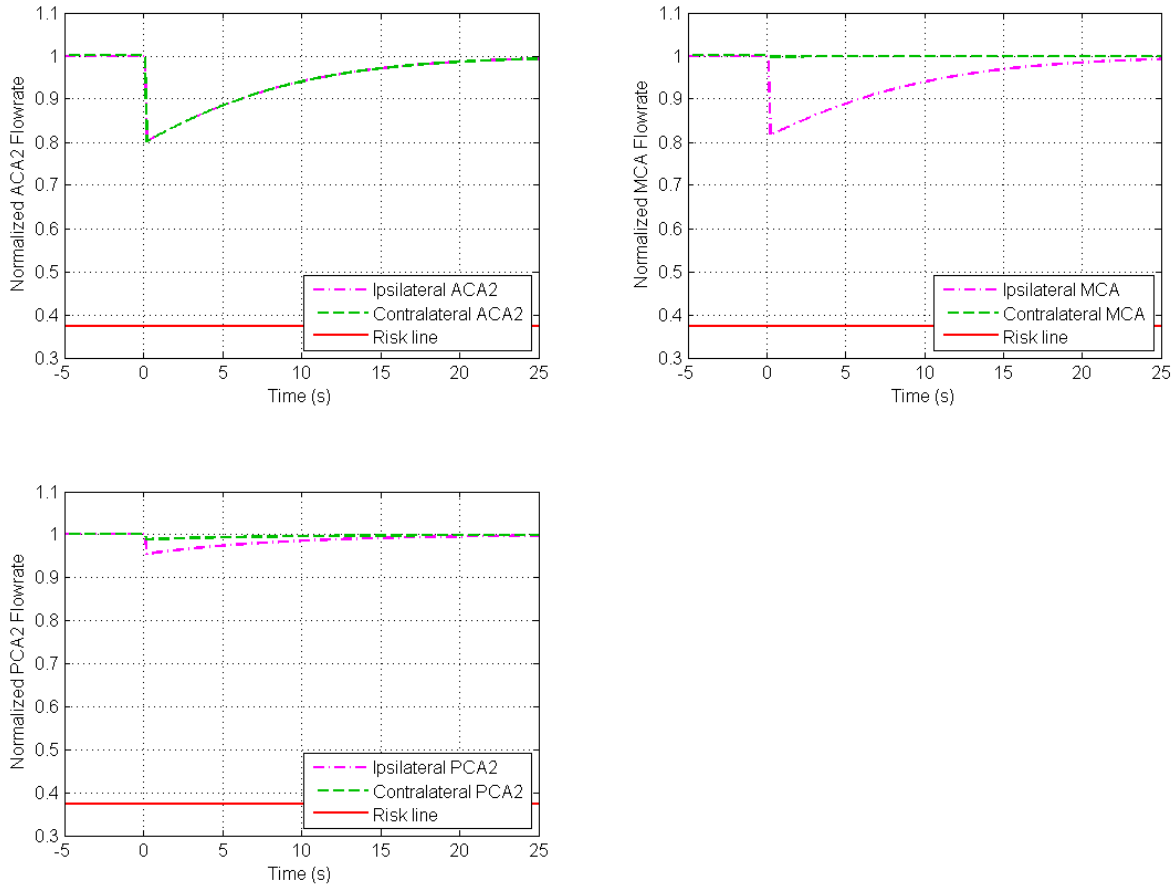

Figure 8.35 Flowrate response of the major efferent arteries as a result of ICA occlusion in a CoW with missing contralateral ACA1.

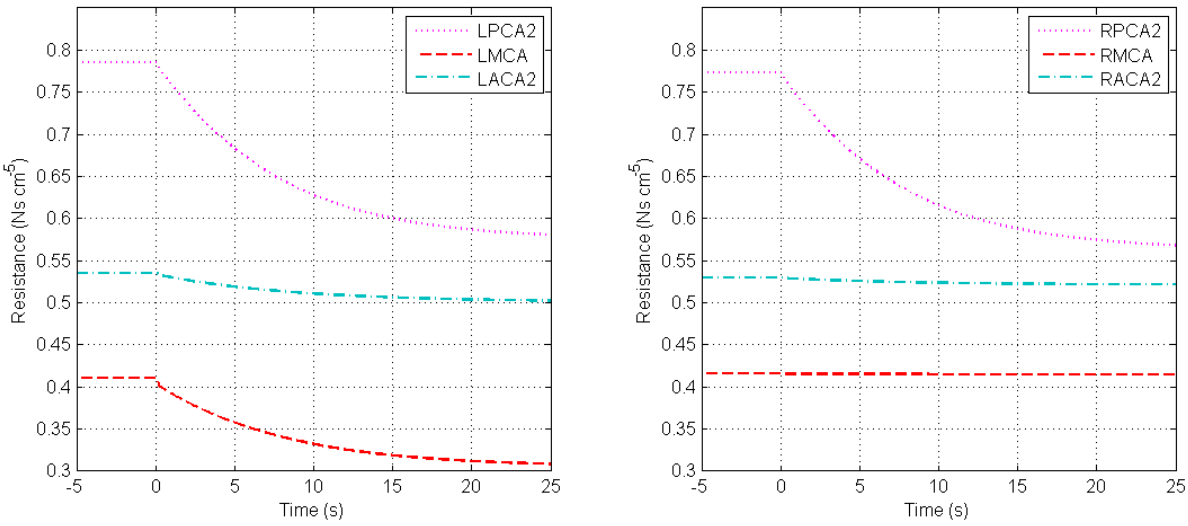

Figure 8.36 Response of the efferent arteries' variable resistances as a result of ICA occlusion in a CoW with missing contralateral ACA1.

8.1.2.5 ICA Occlusion with Missing Ipsilateral PCoA

The posterior of the CoW experiences more abnormalities than the anterior with only 28.7% of the population having a normal complete CoW posterior. The most common posterior abnormality is a unilateral missing PCoA, which contributes to 28.7% of all cases (the same percentage as a normal complete CoW posterior). The basic model was run to simulate the left ICA occlusion with an ipsilateral missing PCoA. The steady state flowrates are shown in Figure 8.37, where none of the efferent arteries experiences loss of blood flow. The bar graph in Figure 8.38 shows that the loss of blood flow from the left ICA is compensated for mostly by the contralateral ICA. The greatest increase in a CoW internal vessel was experienced by the contralateral ACA1, which, as a result of the occlusion, was required to supply the ipsilateral MCA and ACA2 in addition to the contralateral ACA2. This was followed by the change in direction and the increase of flowrate in the ACoA to deliver blood to the ipsilateral MCA and ACA2. Before the occlusion, the ACoA delivered a small amount of blood flow from the left to the right of the CoW, which was due to the asymmetry of the CoW. The ipsilateral ACA1 also changed blood flow direction as it was required to supply blood from the contralateral side to the ipsilateral MCA. The flowrate in the BA increased slightly to contribute more to the blood supply to the ipsilateral PCA2, which was affected by the contralateral ICA redirecting the blood to the side affected by the occlusion through the anterior section of the CoW.

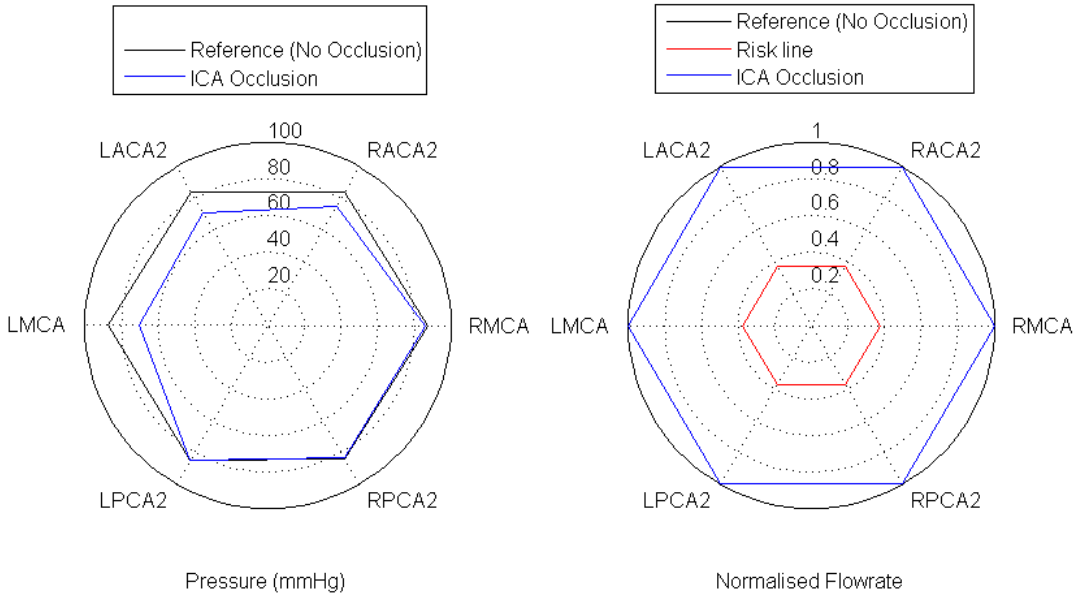

Figure 8.37 Efferent arteries' pressures and flowrates for a CoW with an ICA occlusion and missing ipsilateral PCoA.

From the flowrates and resistances response displayed in Figures 8.39 and 8.40, the most disturbance was experienced by both the ACA2s and the ipsilateral MCA. The responses in the ACA2s were not identical, such as in the case discussed in Section 8.1.2.4 because the ACA2s in this case were supplied by different sources before the occlusion, while in Section 8.1.2.4, both ACA2s were supplied by the same source.

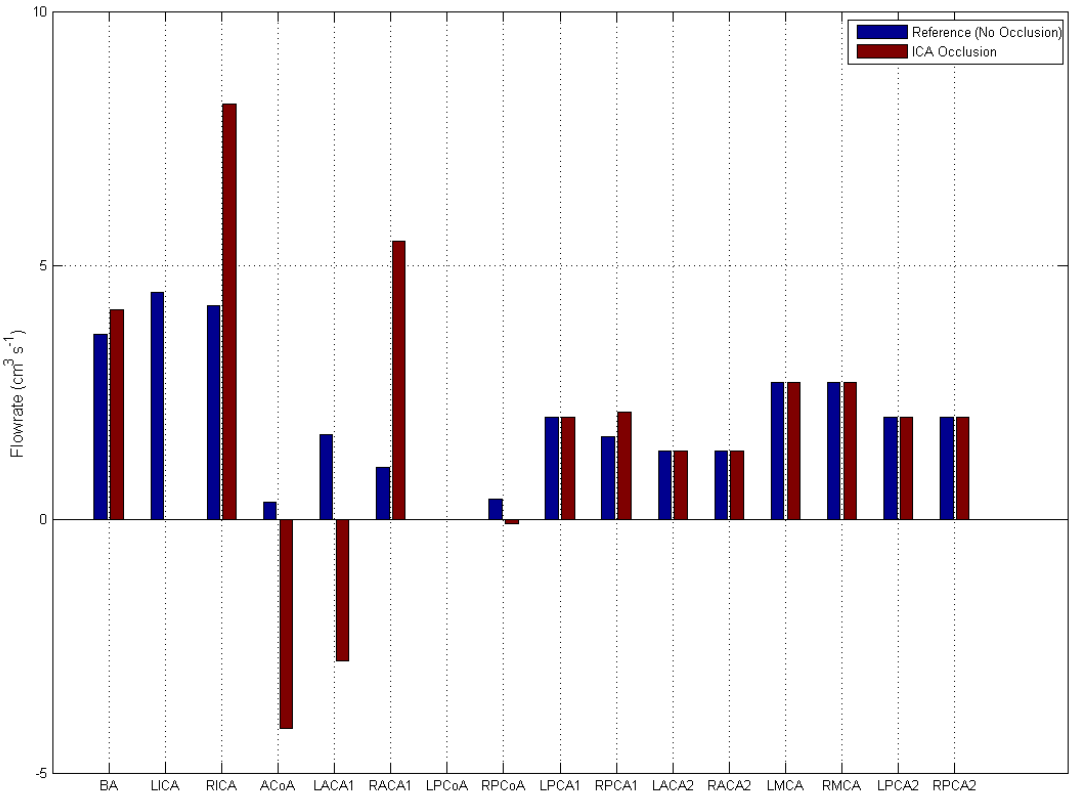

Figure 8.38 Flowrates through all CoW vessels under normal conditions (blue) and under ICA occlusion (brown) for a CoW with missing ipsilateral PCoA.

8.1.2.6 ICA Occlusion with Missing Contralateral PCoA

The pressure and flowrate steady state response in the efferent arteries as a result of an ICA occlusion with a missing contralateral PCoA is shown in Figure 8.41. The bar graph in Figure 8.42 shows that the BA and the contralateral ICA equally contributed to compensate for blood loss as a result of the occlusion. The anterior of the CoW experienced the same effect as in the missing ipsilateral PCoA case (Section 8.1.2.5) but with a lesser extend. Because of the availability of the ipsilateral PCoA, the BA was able to contribute more to the side affected by the occlusion. In this case the contralateral ICA supplied mainly the ipsilateral ACA2 while the BA supplied mainly the ipsilateral MCA.

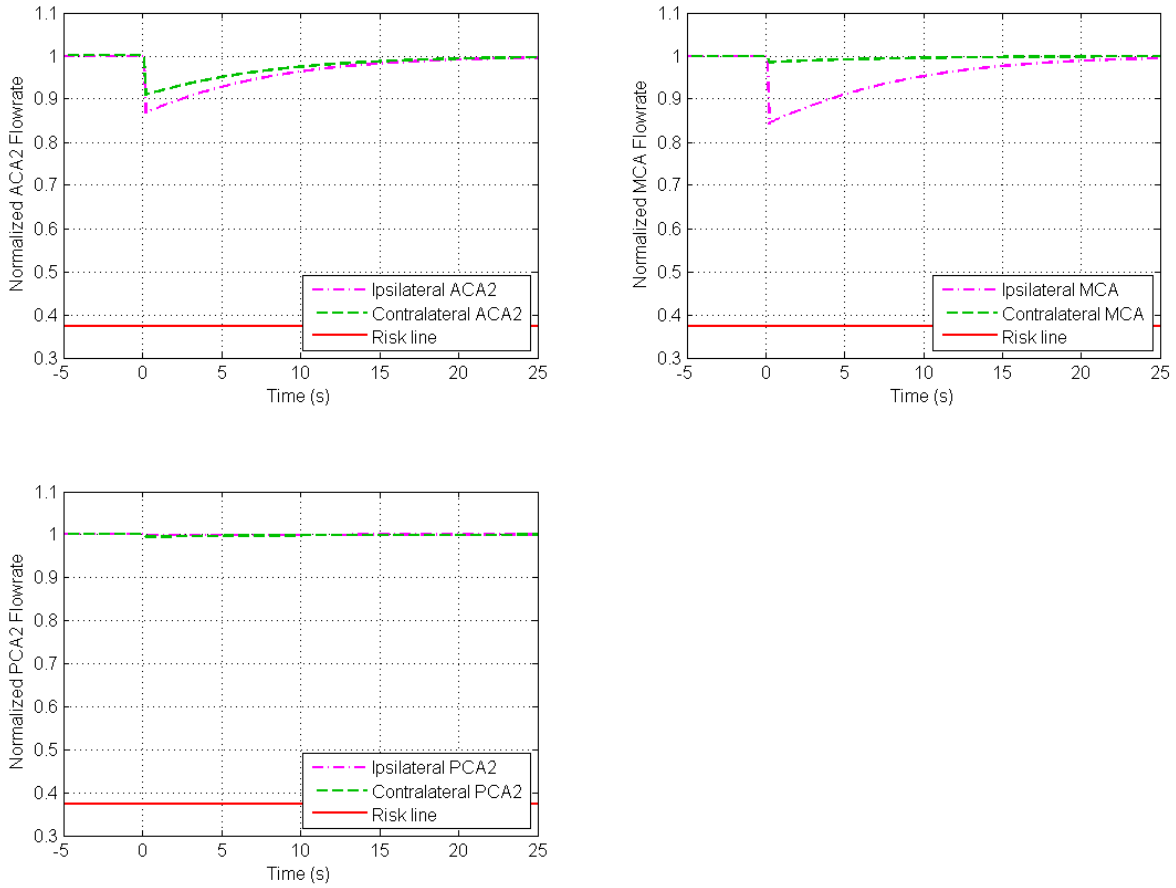

Figure 8.39 Flowrate response of the major efferent arteries as a result of ICA occlusion in a CoW with missing ipsilateral PCoA.

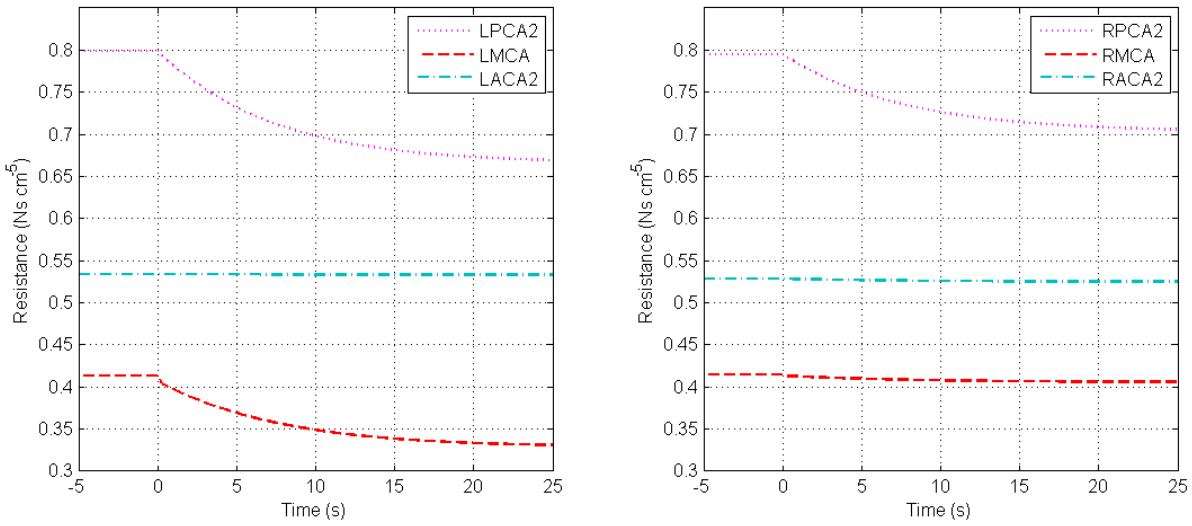

Figure 8.40 Response of the efferent arteries' variable resistances as a result of ICA occlusion in a CoW with missing ipsilateral PCoA.

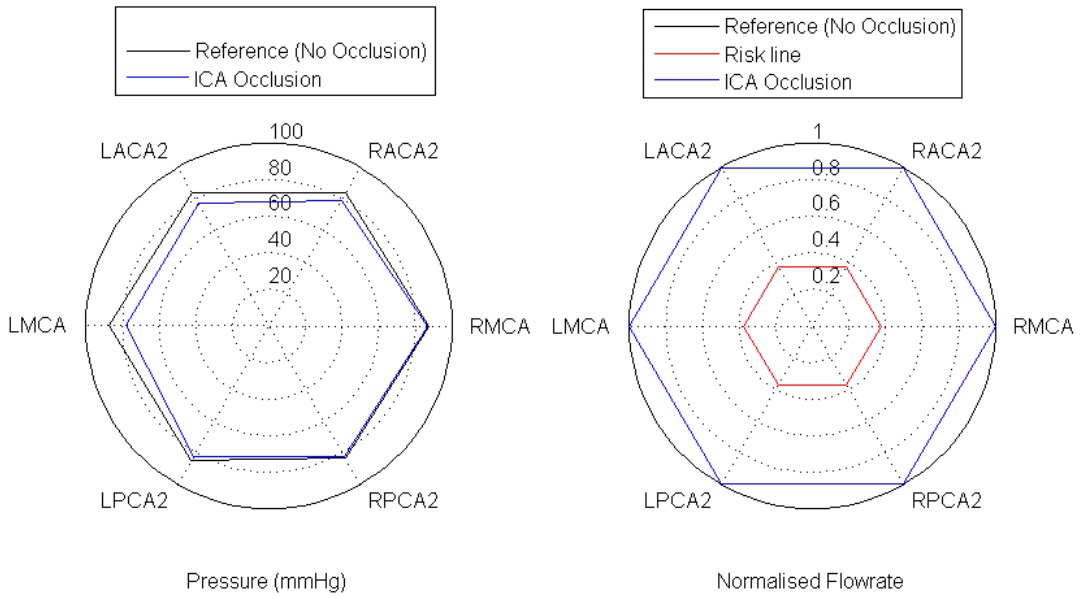

Figure 8.41 Efferent arteries' pressures and flowrates for a CoW with an ICA occlusion and missing contralateral PCoA.

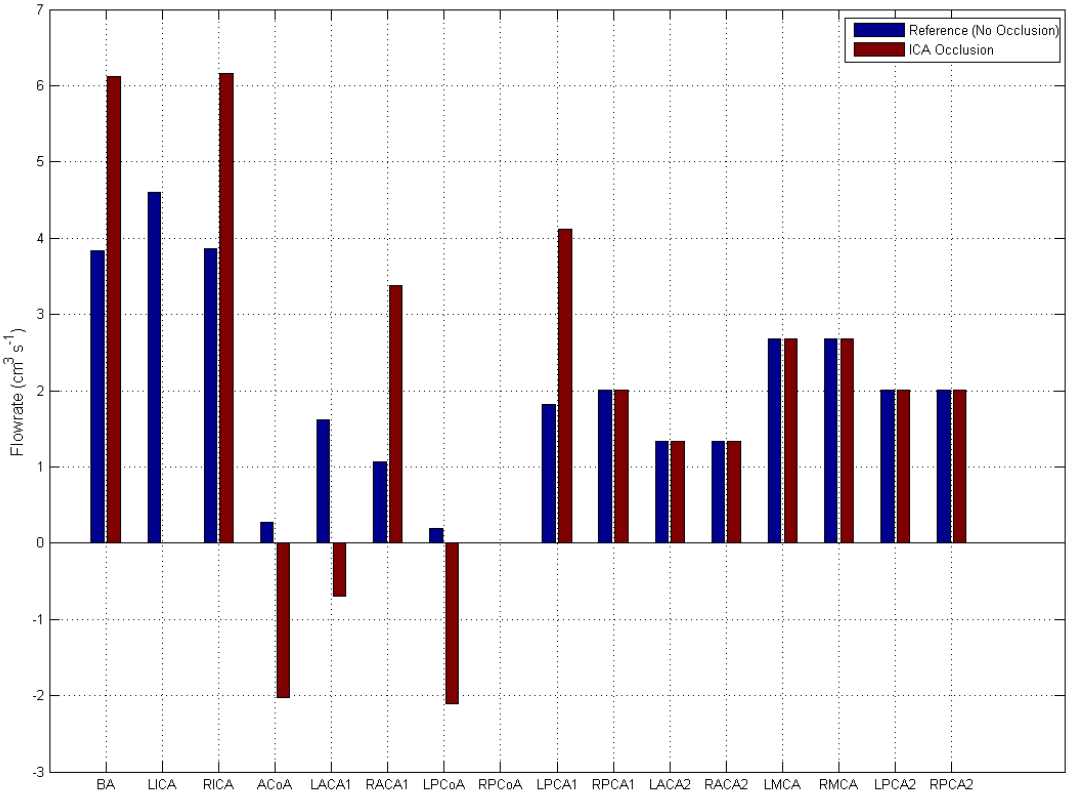

Figure 8.42 Flowrates through all CoW vessels under normal conditions (blue) and under ICA occlusion (brown) for a CoW with missing contralateral PCoA.

The responses in Figure 8.43 and 8.44 show that the efferent arteries most affected by the ICA occlusion in this case are the ipsilateral MCA nd ACA2, followed by the contralateral ACA2. The ipsilateral PCA2 undergoes a small disturbance in flowrate as a result of having part of the blood redirected to the MCA and ACA2s at the first instant of the occlusion.

8.1.2.7 ICA Occlusion with Ipsilateral Fetal Case

The second most common abnormality in the CoW posterior is a unilateral fetal case described in Section 1.2.3. This abnormality contribute to 18% of the population. Based on the MRA population study by Arnold et al. [6, 88], the fetal case was modelled by assigning the PCA1 radius size to the ipsilateral PCoA radius size, and vice versa. The model was run for a left ICA occlusion with an ipsilateral fetal case. The pressures for most of the major efferent arteries were affected significantly. However, the efferent arteries still managed to regain their normal flowrates as shown by the steady state values in Figure 8.45. The bar graph in Figure 8.46 shows that before the occlusion, the left ICA supplied more blood to the CoW than the contralateral ICA and BA. After the left ICA occlusion, the BA increased significantly to compensate for the blood loss by supplying all the blood needed by the ipsilateral PCA2 and the ipsilateral MCA. The ipsilateral PCA1 was increased by the same amount experienced by the BA for the same reasons. Before the occlusion, the ipsilateral PCoA delivered a small part of the blood demand by the ipsilateral PCA2; after the occlusion, this flowrate changed its direction and increased in quantity to deliver a sufficient amount of blood to the ipsilateral MCA. Some of the blood flow from the BA was even delivered to the ipsilateral ACA2. The anterior part of the CoW was in charge of meeting the demand for the ipsilateral ACA2 that suffered blood loss after the occlusion. The blood supply by the contralateral ICA was increased to deliver blood to the ipsilateral ACA2 via the contralateral ACA1s and the ACoA. The flowrate through the ACoA changed its direction and increase in amount for that reason.

After the occlusion, all the main ipsilateral (left) efferent arteries suffered a sudden loss of blood (Figure 8.47), which was compensated for by the increase in the other supplying arteries as well as change in the ipsilateral efferent arteries' resistances shown in Figure 8.48. The contralateral ACA2 also suffered a significant drop initially because of having to share its blood flow with the ipsilateral ACA2.

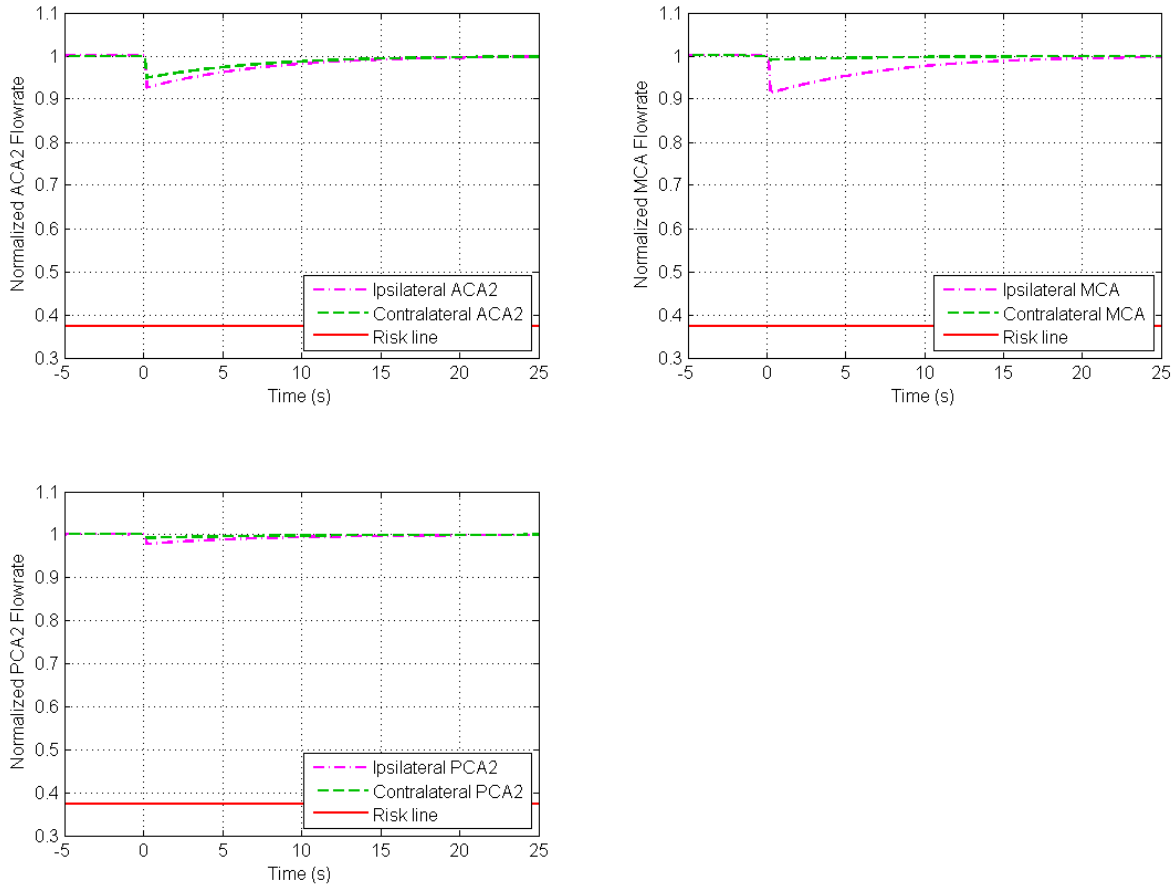

Figure 8.43 Flowrate response of the major efferent arteries as a result of ICA occlusion in a CoW with missing contralateral PCoA.

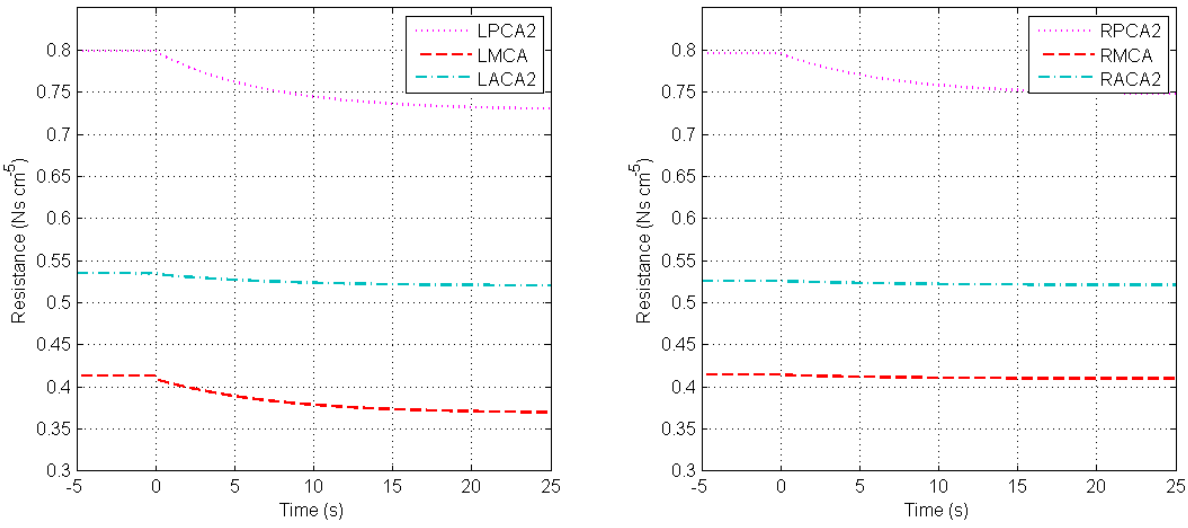

Figure 8.44 Response of the efferent arteries' variable resistances as a result of ICA occlusion in a CoW with missing contralateral PCoA.

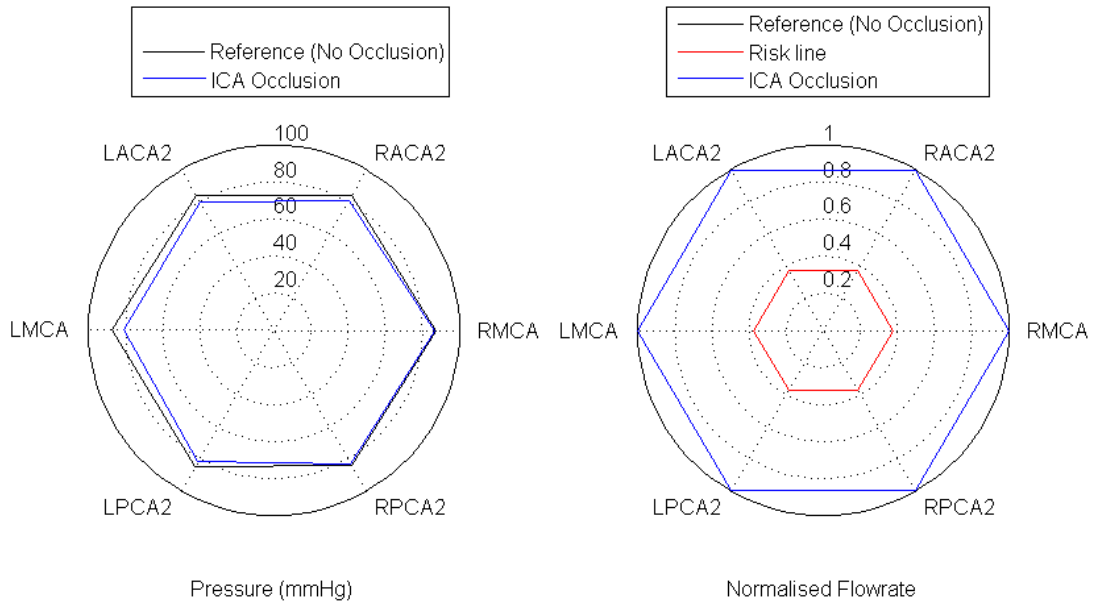

Figure 8.45 Efferent arteries' pressures and flowrates for a CoW with an ICA occlusion and ipsilateral fetal case.

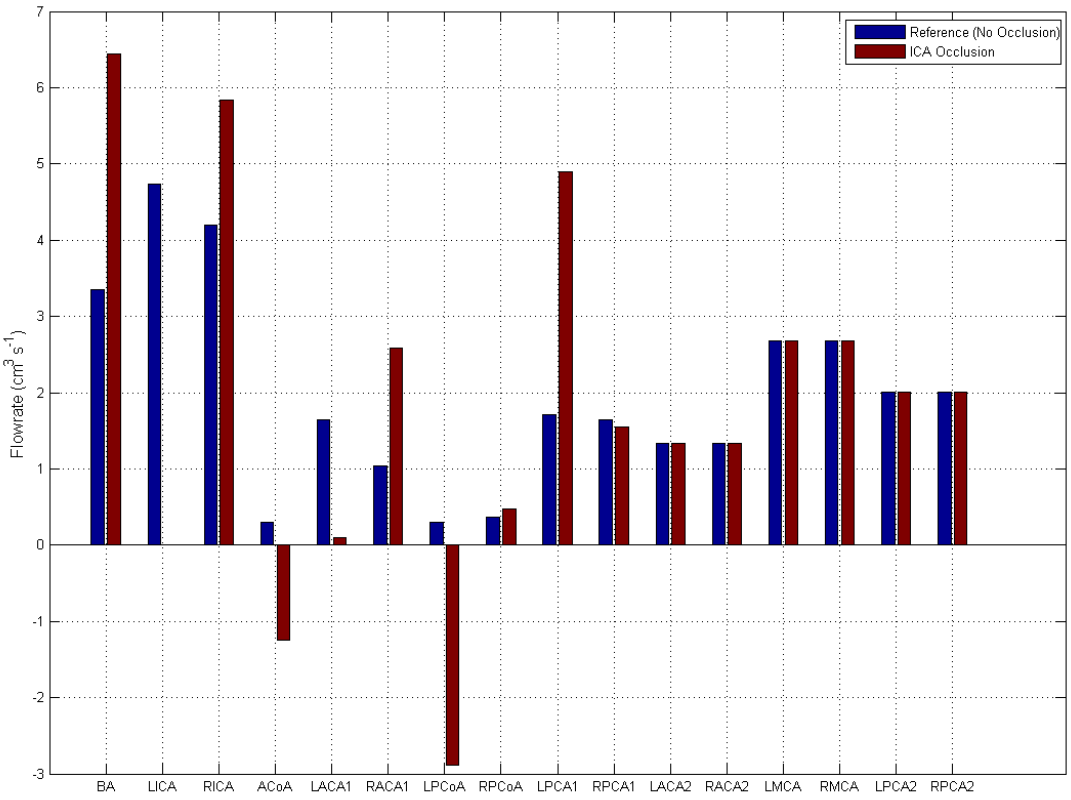

Figure 8.46 Flowrates through all CoW vessels under normal conditions (blue) and under ICA occlusion (brown) for a CoW with ipsilateral fetal case.

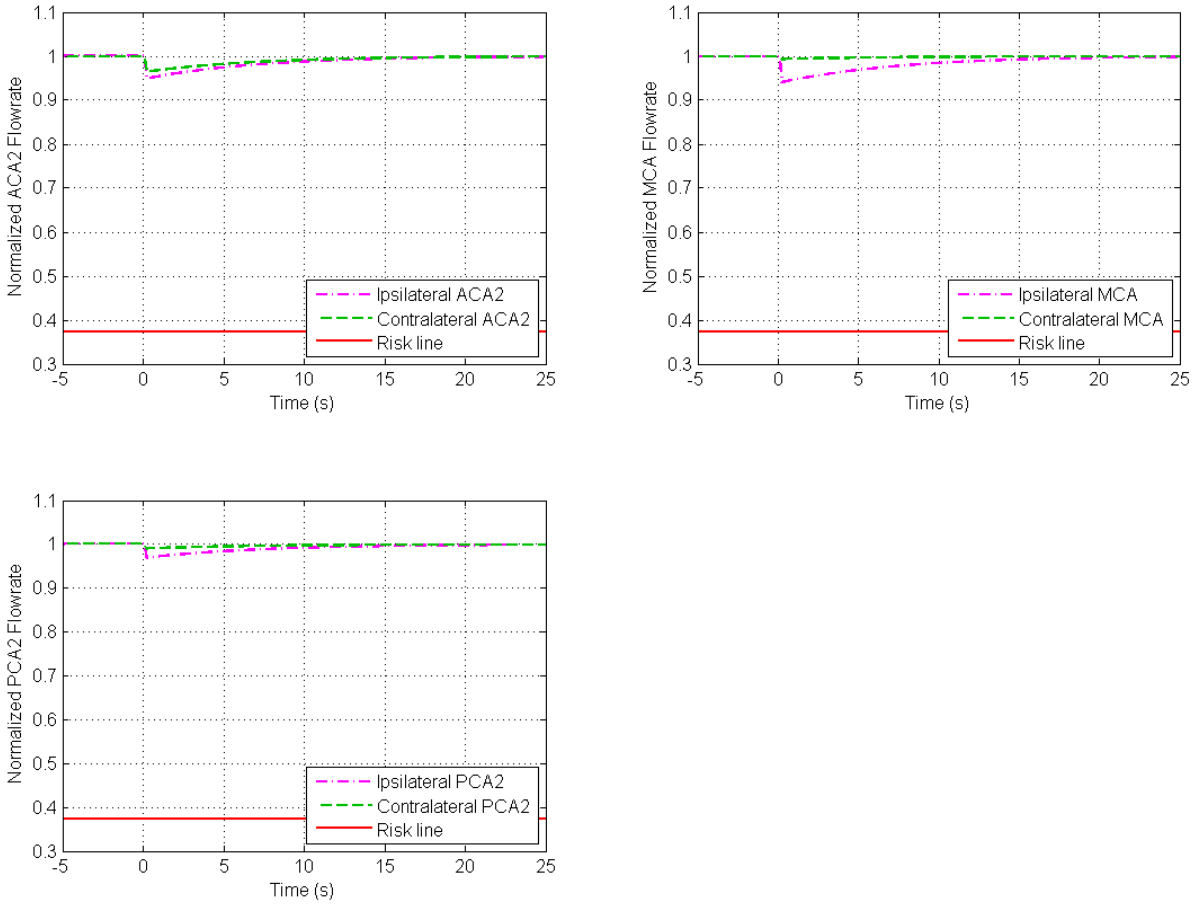

Figure 8.47 Flowrate response of the major efferent arteries as a result of ICA occlusion in a CoW with ipsilateral fetal case.

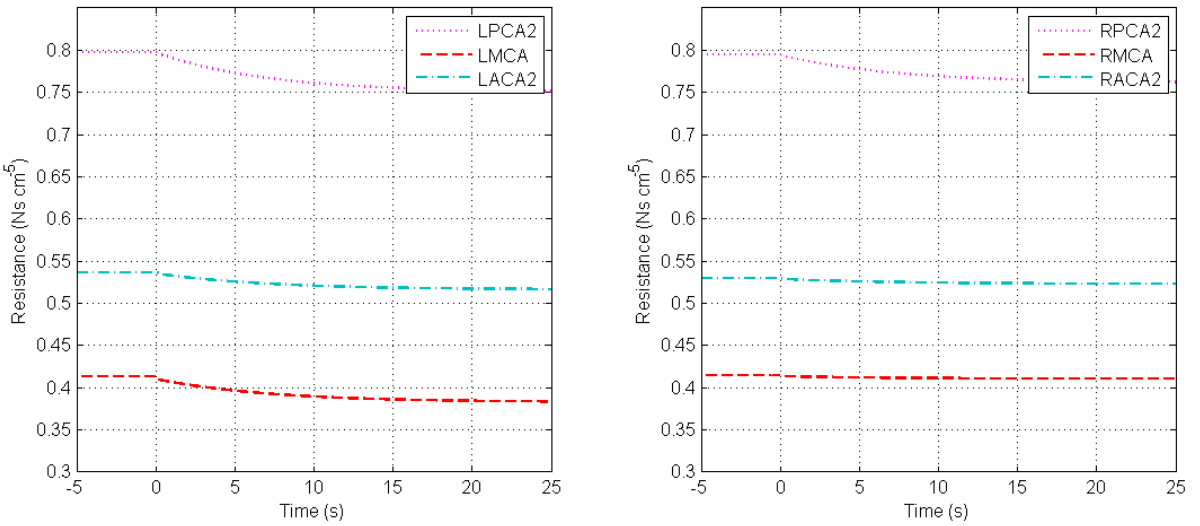

Figure 8.48 Response of the efferent arteries' variable resistances as a result of ICA occlusion in a CoW with ipsilateral fetal case.

8.1.2.8 ICA Occlusion with Contralateral Fetal Case

The pressure and flowrate steady state response for the ICA occlusion with a contralateral fetal case is shown in Figure 8.49. The bar graph in Figure 8.50 shows that the increase of supplying arteries' flowrates after the ICA occlusion is similar to the increase experienced in the ipsilateral fetal case, but with smaller increase by the BA. The flowrates through the CoW internal arteries behaved in a similar manner to the ipsilateral fetal case but with slightly more contribution of blood supply through the anterior part rather than the posterior.

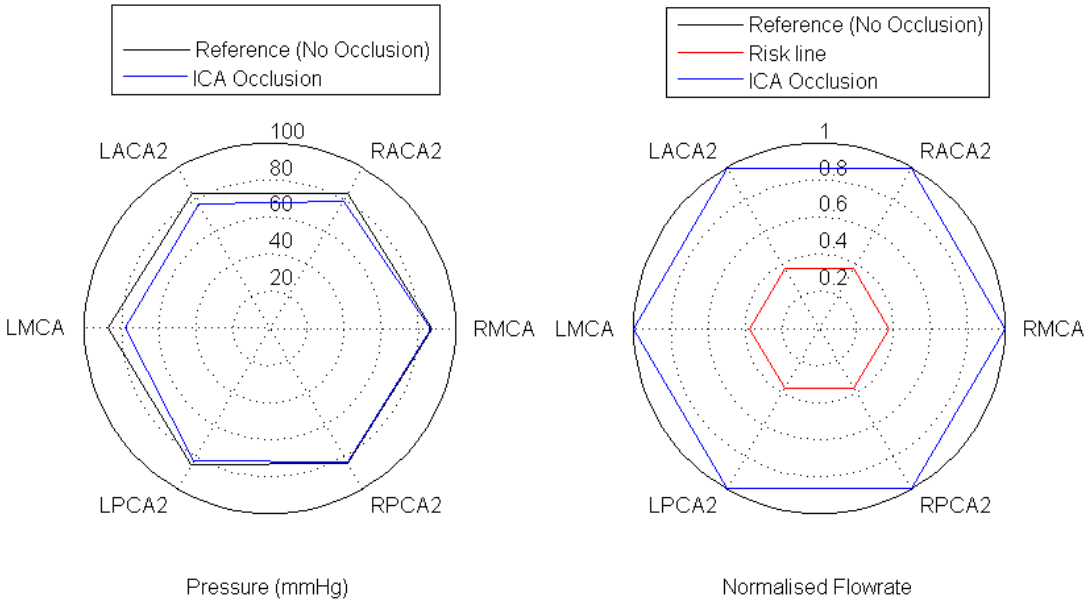

Figure 8.49 Efferent arteries' pressures and flowrates for a CoW with an ICA occlusion and contralateral fetal case.

The flowrates and resistances response, shown in Figures 8.51 and 8.52, was similar to the ipsilateral fetal case response. All the main efferent arteries in the ipsilateral side as well as the contralateral ACA2 experienced a sudden drop in flow as a result of the occlusion, but the flowrates recovered and regained normal values as a result of redirecting blood flow from other supplying arteries and changing the variable resistances by the PI controller.

8.1.2.9 ICA Stenosis in Special Case

The modelling of a stenosis is discussed in Section 4.1.5. To see the effects of different levels of stenosis, a specific clinical scenario was set up where the CoW had two abnormalities, one anterior and one posterior. The model was run for a CoW with a stenosed left ICA, a missing ACoA, and a missing ipsilateral PCoA as in Figure 8.53.

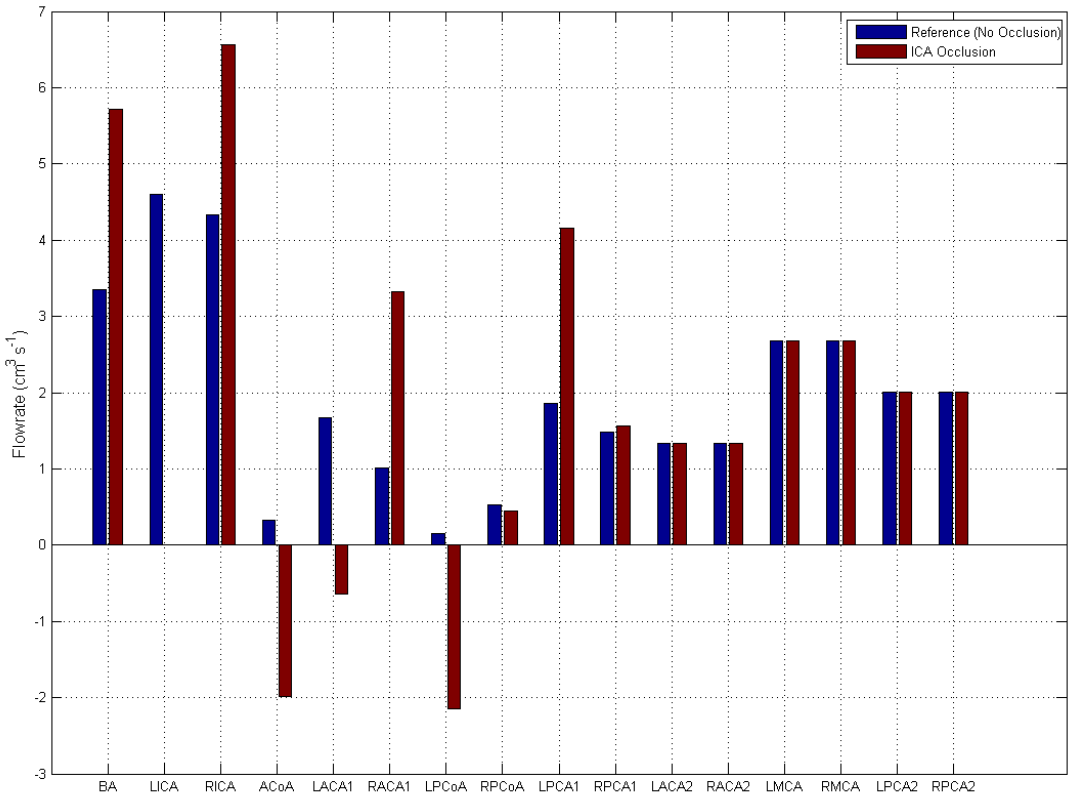

Figure 8.50 Flowrates through all CoW vessels under normal conditions (blue) and under ICA occlusion (brown) for a CoW with contralateral fetal case.

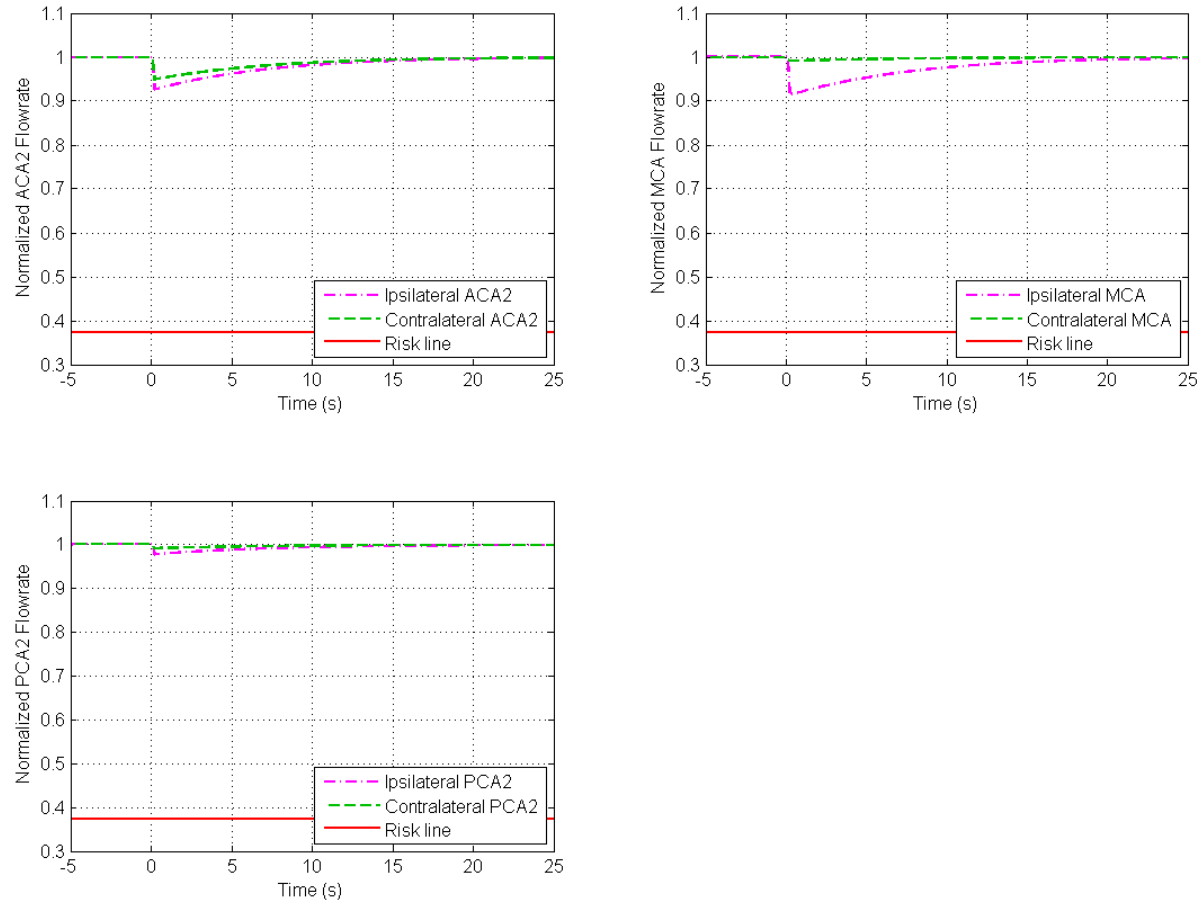

Figure 8.51 Flowrate response of the major efferent arteries as a result of ICA occlusion in a CoW with contralateral fetal case.

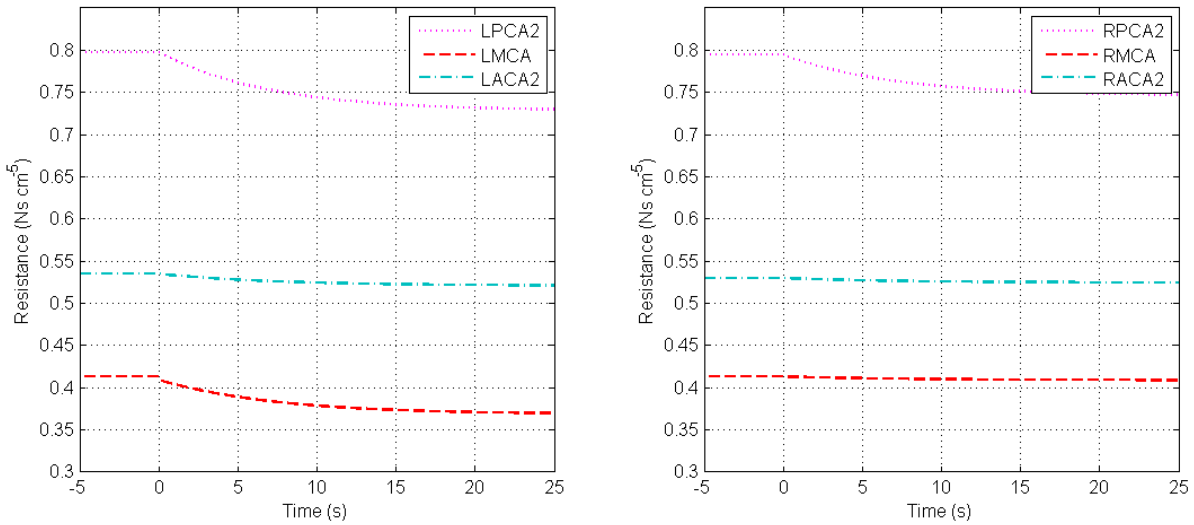

Figure 8.52 Response of the efferent arteries' variable resistances as a result of ICA occlusion in a CoW with contralateral fetal case.

The stenosis was varied from 50% to 100% (occlusion). Figure 8.54 shows the steady state flowrates for the main efferent arteries before the left ICA stenosis and after the stenosis. It can be seen that there is a risk of having insufficient blood when the stenosis percentage increases above 75% for this particular case.

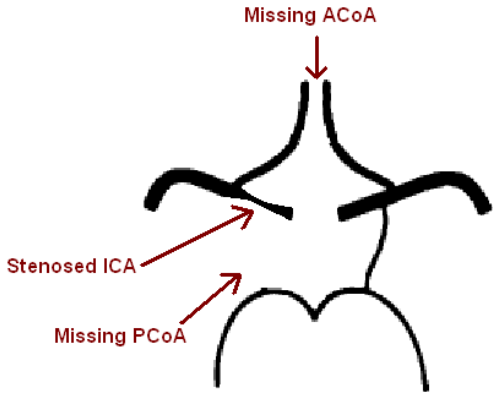

Figure 8.53 The special case CoW.

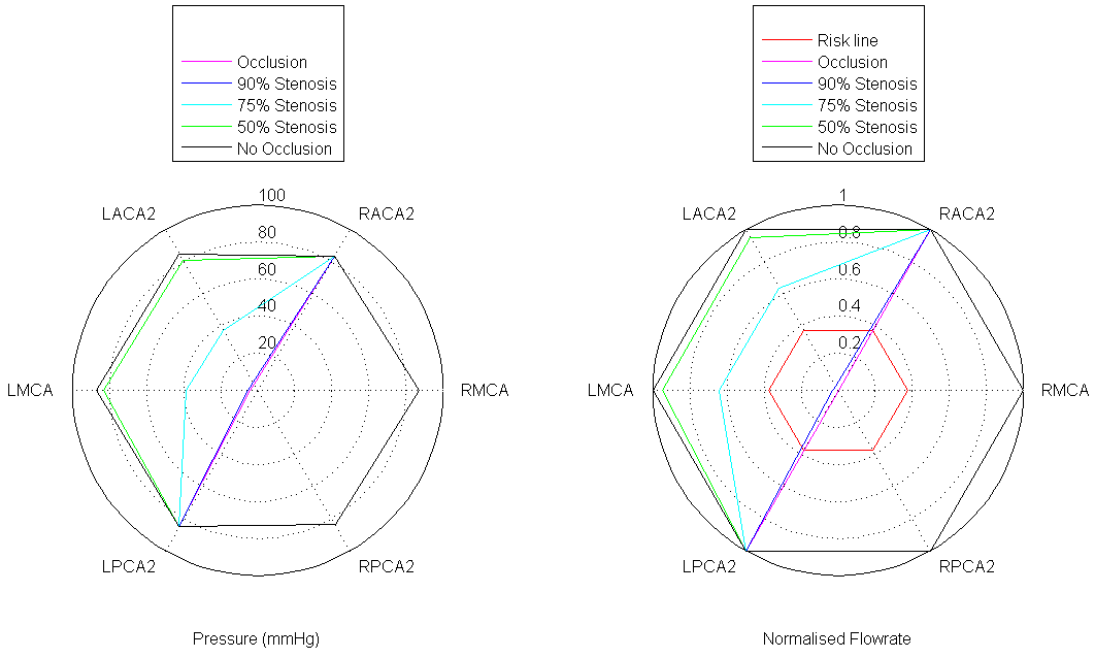

Figure 8.54 Efferent arteries' pressures and flowrates for a CoW exposed to several levels of ICA stenosis, missing ACoA, and ipsilateral missing PCoA.

8.2 Linear Models

As discussed in Chapter 5, several attempts were made to develop the model so that it would produce an autoregulation plot with a slope in the autoregulation range similar

to Guyton et al.'s autoregulation plot. Initial results of the basic CoW model presented in this thesis produced an autoregulation slope with a flat autoregulation range as shown in Figure 8.14. A fixed dead-band algorithm was created by Moorhead, as shown in Figure 8.17, which did not produce a desirable autoregulation result. This is because the PI controller stopped functioning when the flowrate reached 7% of the normal flowrate experienced at a MAP of 100 mmHg, which resulted in the autoregulation range having two flat sections: one at 93% of the normal flowrate for MAP lower than 100 mmHg and higher than lower limit of autoregulation; the other at 107% of the normal flowrate for MAP higher than 100 mmHg and lower than the upper limit of autoregulation. The following are further modifications to the model to achieve the autoregulation slope.

8.2.0.10 Variable Dead-band

The variable dead-band algorithm was explained in Section 5.1. The model with the variable dead-band was run for a classical complete CoW with a MAP drop of 20 mmHg. The flowrates response shown in Figure 8.55 is initially similar to the response in the basic model with no dead-band. However, when the response reached a certain value that was at the percentage defined by the variable dead-band, the PI controller was deactivated. This resulted in the autoregulation plot shown in Figure 8.56 where a small slope in the autoregulation range had formed. The slope at the MAP under 100 mmHg is overlied by the Guyton line and has a different gradient to the slope at the MAP above 100 mmHg.

8.2.1 Memory Algorithm

The memory algorithm was introduced to replace the variable dead-band algorithm. Even though the variable dead-band algorithm succeeded in producing a slope for the autoregulation range, the slope was not consistent for the whole autoregulated range and was not as steep as the Guyton autoregulation plot. It also did not have a physiological basis. Simulations for the memory algorithm model (described in Section 5.2) were run to examine the dynamic and steady state response. Figure 8.57 shows the flowrates response of the major efferent arteries as a result of a 20 mmHg drop in MAP. The steady state reponse is shown in the autoregulation plot in Figure 8.58. The ULA was changed from 190% to 160% of the normal resistance values to achieve the same upper limit as Guyton's plot. As shown in Figure 8.58, the memory algorithm achieved the desired autoregulation slope that is similar to Guyton's plot.

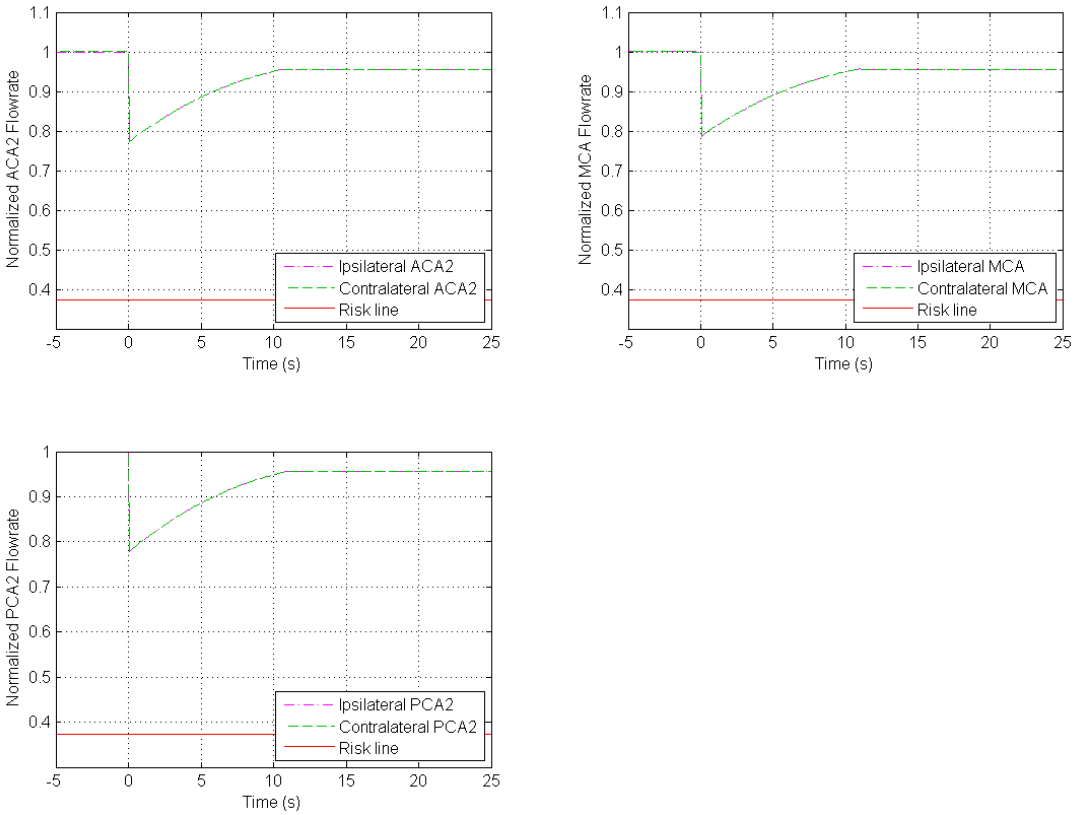

Figure 8.55 Flowrate response of the major efferent arteries as a result of 20 mmHg MAP drop using the variable dead-band model.

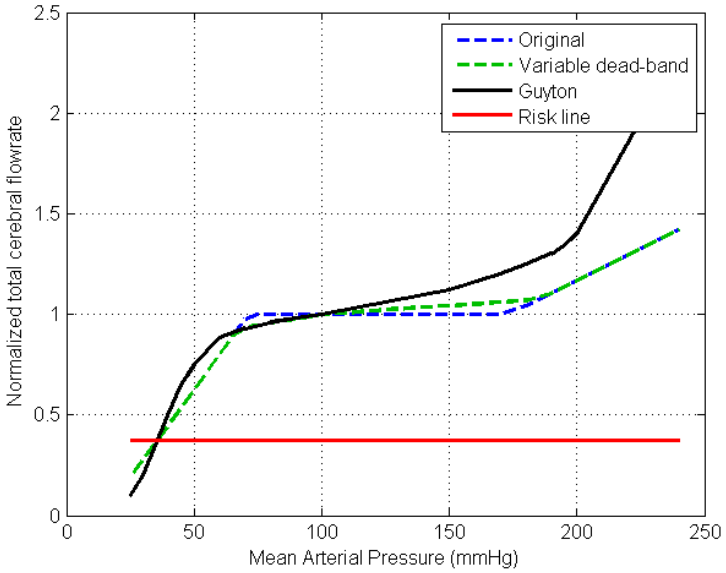

Figure 8.56 Autoregulation plot for the basic model with classical complete CoW using the dead-band algorithm.

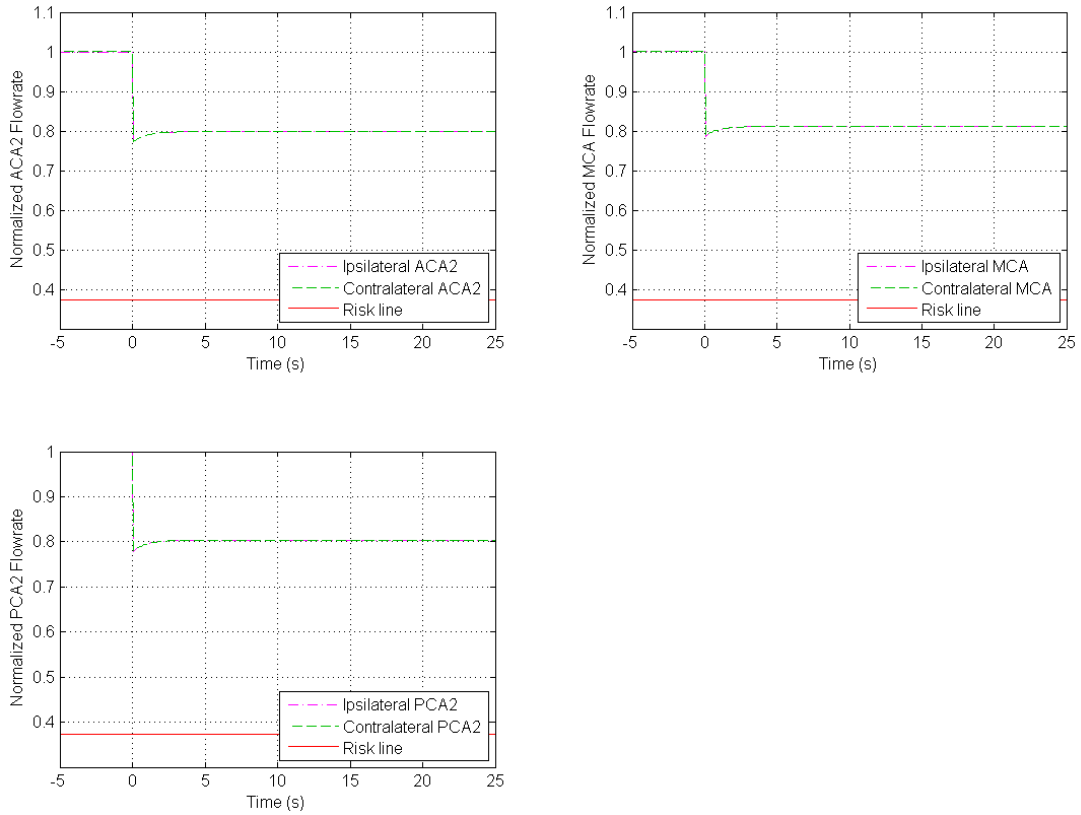

Figure 8.57 Flowrate response of the major efferent arteries as a result of 20 mmHg MAP drop using the CoW model with memory algorithm.

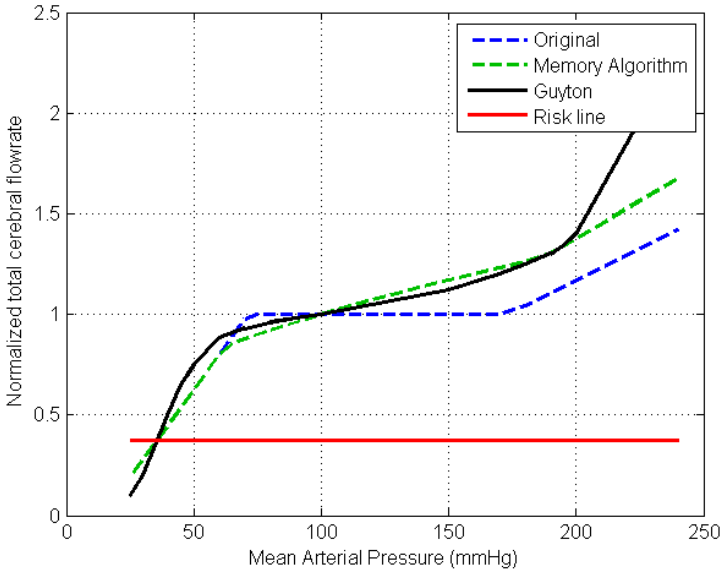

Figure 8.58 Autoregulation plot for the basic model with classical complete CoW using the memory algorithm.

8.2.2 Simple Metabolic Rate

The model was developed further to include brain metabolism as discussed in Section 5.3. The metabolic rate model is dependent on the arterial and venous oxygen concentrations. Figure 8.59 shows the dynamic response of this model as a result of MAP drop of 20 mmHg. The flowrates response show that instead of returning to the original flowrate experienced at normal condition, a new steady state value was reached, which was defined by Equation 5.7. The ULA was modified from 190% to 150% of the normal resistance values to achieve the same upper limit as Guyton's plot. The autoregulation plot shown in Figure 8.60 shows that the autoregulation slope by Guyton was reproduced closely by the metabolic rate algorithm. Both the memory and metabolic rate algorithm succeeded in reproducing the autoregulation plot by Guyton et al.; however, the metabolic rate was chosen to be used in subsequent development of the model because it has more physiological importance.

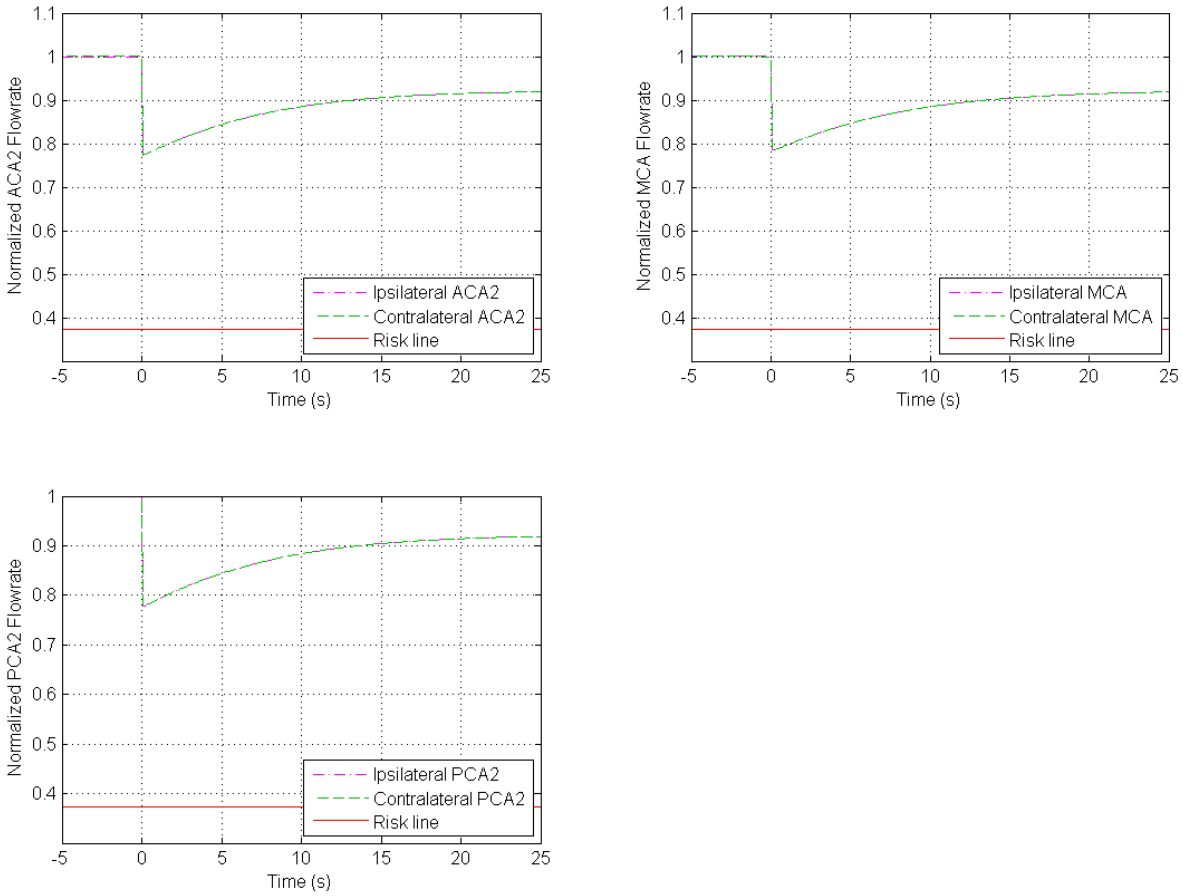

Figure 8.59 Flowrate response of the major efferent arteries as a result of 20 mmHg MAP drop using the metabolic rate model.

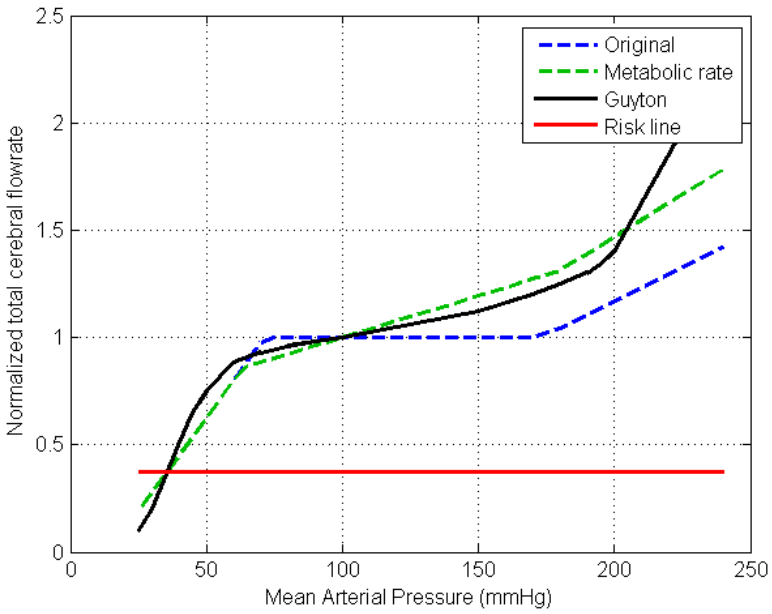

Figure 8.60 Autoregulation plot for the basic model with classical complete CoW using the metabolic rate model.

8.2.3 Leptomeningeal Arteries (LMA)

The LMA arteries were added to the basic CoW model as described in Section 5.4. To examine the effect of adding the LMA arteries to the model, the same clinical scenario described in Section 8.1.2.9 was used here where the left ICA was subjected to an 80% stenosis. Figure 8.61 shows the steady state response of the major efferent arteries with and without the LMAs.

The plot shows that the difference between the two responses is insignificant. This does not necessary mean that the LMA do not play an essential role in delivering blood to where it is needed in stroke cases. Owing to the lack of data in the literature, all LMAs that connect two CoW efferent arteries were lumped together in one resistance, which was evaluated using a guessed estimation of the flowrates that might travel through them under normal conditions. If the estimation in Section 5.4 was set to a higher value than 5% of the flow through the MCA, the difference would have been more significant. This should be modified once more data is available in the literature.

8.2.4 Model Sensitivity

As discussed in Section 5.5, the linear CoW model was tested for sensitivity. This is very important owing to the fact that the model is based on averaged data of the cerbrovasculature. As each individual's CoW is unique, the parameters chosen in this

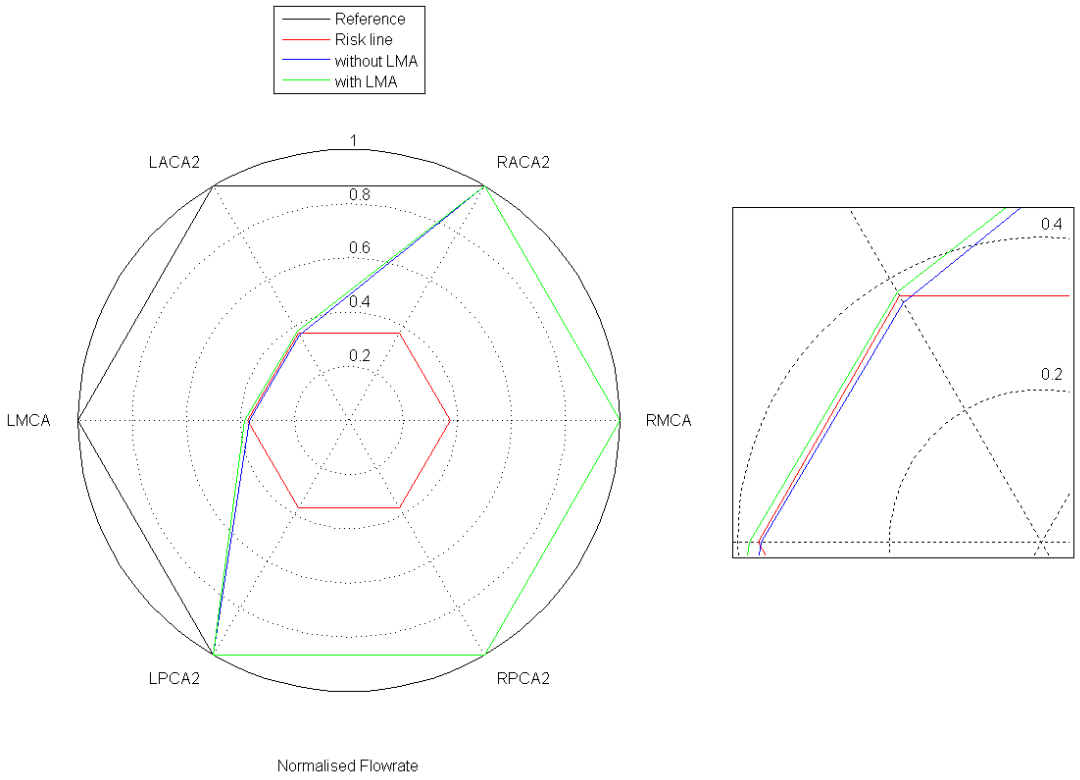

Figure 8.61 Steady state flowrates for major efferent arteries with and without LMA vessels in the CoW.

model should be resilient to suit small variations in the CoW and its hemodynamics. Examining the CoW sensitivity was done by testing two different aspects of the model: the time constant used for efferent arteries and the CoW radii.

8.2.4.1 λ Sensitivity

The three major efferent arteries in each side of CoW are the ACA2, MCA and PCA2. The time constant λ used in the resistance dynamics equation for the variable resistance of the efferent arteries were varied from the original value of 3 to 0.5, 1, 5, 10, 30 and 50 in one efferent artery at a time. This was executed for the major efferent arteries in one side only of the CoW (the left side) because the response will be similar wether the left or the right vessel was chosen. In order to examine the effects of λ on the response, a MAP drop of 20 mmHg was introduced. The dynamic response as a result of a change in λ for a specific efferent artery was observed in all major efferent arteries on both the ipsilateral and contralateral sides. The percentages of maximum change from the original response (errors) in all the efferent arteries were measured and tabulated (Table 8.2).

An example of the flowrates response for changing the λ in an efferent artery is

Table 8.2 *Errors in the steady state flowrate values for all major efferent arteries as a result of changing the time constant λ.*

Artery	λ	LACA2	RACA2	LMCA	RMCA	LPCA2	RPCA2
Left ACA2	0.5	18.73	-0.12	-0.18	-0.05	-0.01	-0.00
	1	11.84	-0.07	-0.10	-0.03	-0.00	-0.00
	5	-5.46	0.02	0.04	0.01	0.00	0.00
	10	-11.79	0.05	0.07	0.02	0.00	0.00
	30	-18.41	0.06	0.09	0.02	0.00	0.00
	50	-20.26	0.07	0.10	0.03	0.00	0.00
Left MCA	0.5	-0.37	-0.09	17.60	-0.03	-0.02	-0.01
	1	-0.20	-0.05	10.94	-0.02	-0.01	-0.00
	5	0.07	0.02	-5.20	0.01	0.00	0.00
	10	0.13	0.03	-11.35	0.01	0.01	0.00
	30	0.18	0.05	-17.92	0.02	0.01	0.00
	50	0.19	0.05	-19.78	0.02	0.01	0.00
Left PCA2	0.5	-0.01	-0.01	-0.01	-0.00	17.74	-0.06
	1	-0.01	-0.00	-0.01	-0.00	11.33	-0.04
	5	0.00	0.00	0.00	0.00	-5.27	0.01
	10	0.00	0.00	0.01	0.00	-11.39	0.02
	30	0.01	0.00	0.01	0.00	-17.84	0.03
	50	0.01	0.00	0.01	0.00	-19.64	0.03

shown in Figures 8.62 - 8.67. Figures 8.62, 8.63 and 8.64 show the response and the difference in response in the ACA2s, MCAs and PCA2s as a result of setting the λ parameter of the left MCA to the *smaller* value of 0.5, respectively. Figures 8.65, 8.66 and 8.67 show the response as a result of setting λ to the *larger* value of 50.

The results of simulations show that the error in the efferent artery that has its λ changed is large, i.e. it takes more time to reach its normal response, which is what was expected. However, the error in the other efferent arteries is very small (negligible), therefore we can assume that there is no effect on the response of other efferent arteries. The relationship between the percentage errors and the λ value in the left MCA is shown in Figure 8.68.

8.2.4.2 CoW Radii Sensitivity

As mentioned in Section 5.5, the ACoA, left MCA and left PCOA were chosen to test the CoW radii sensitivity. Each one of these vessels had its radius increased or decreased by several standard deviations (S.D.) reported in Table 4.3. In order to examine the effects of changing the radii on the response, an ipsilateral ICA occlusion was introduced. The dynamic response as a result of a radius change for a specific CoW artery was observed in all major efferent arteries on both the ipsilateral and contralateral sides. The percentages of maximum change from the original response (errors) in all

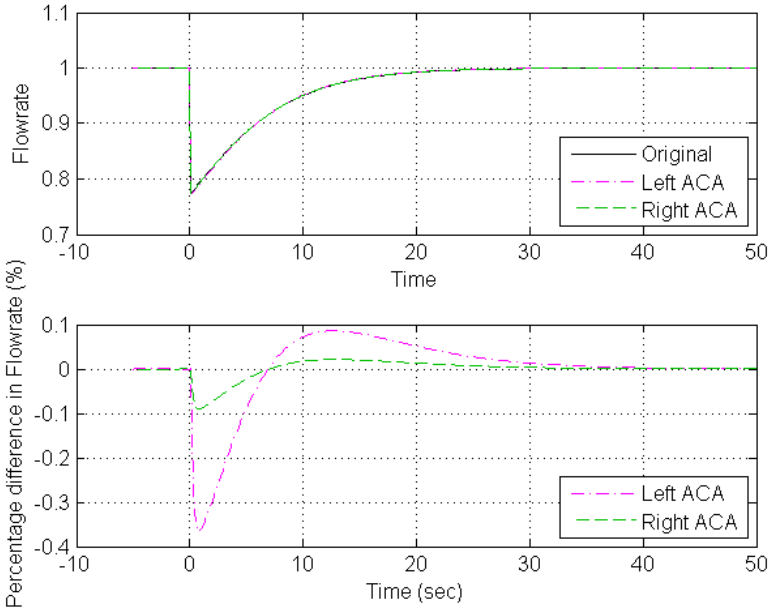

Figure 8.62 Flowrates response in the ACA2s as a result of the left MCA λ change from 3 to 0.5.

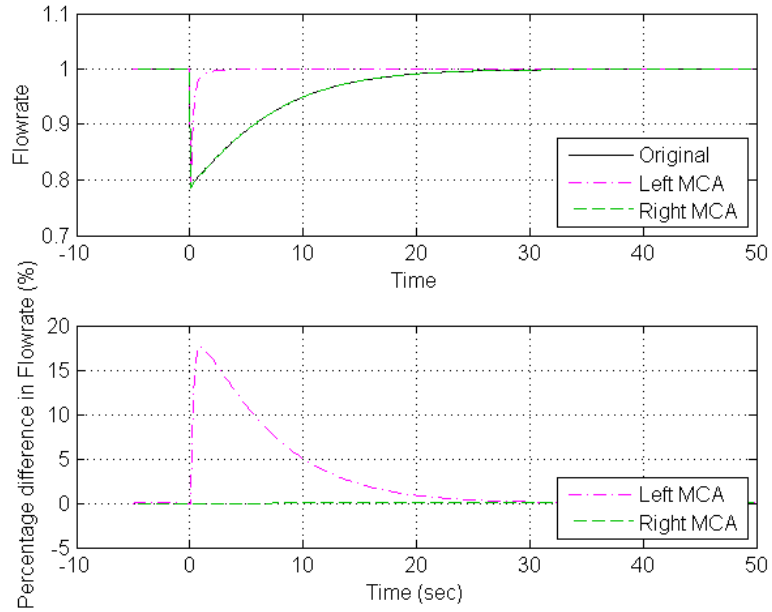

Figure 8.63 Flowrates response in the MCAs as a result of the left MCA λ change from 3 to 0.5.

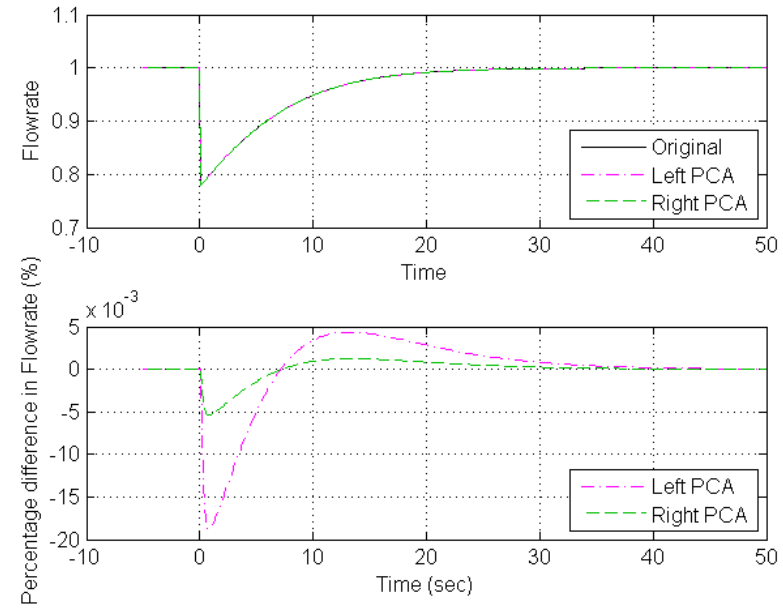

Figure 8.64 Flowrates response in the PCA2s as a result of the left MCA λ change from 3 to 0.5.

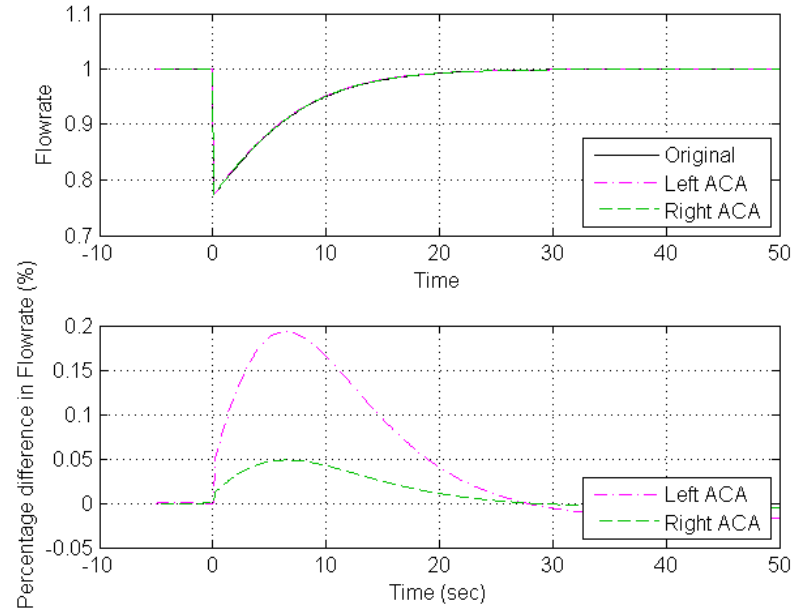

Figure 8.65 Flowrates response in the ACA2s as a result of the left MCA λ change from 3 to 50.

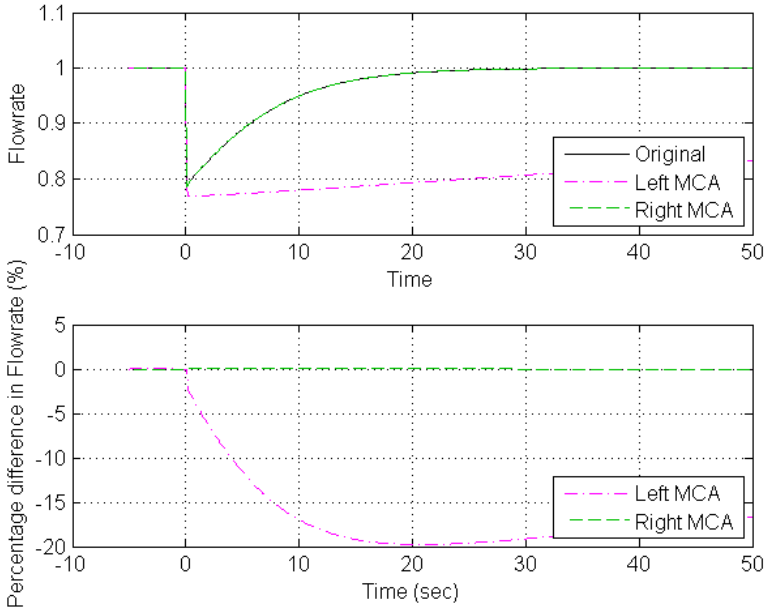

Figure 8.66 Flowrates response in the MCAs as a result of the left MCA λ change from 3 to 50.

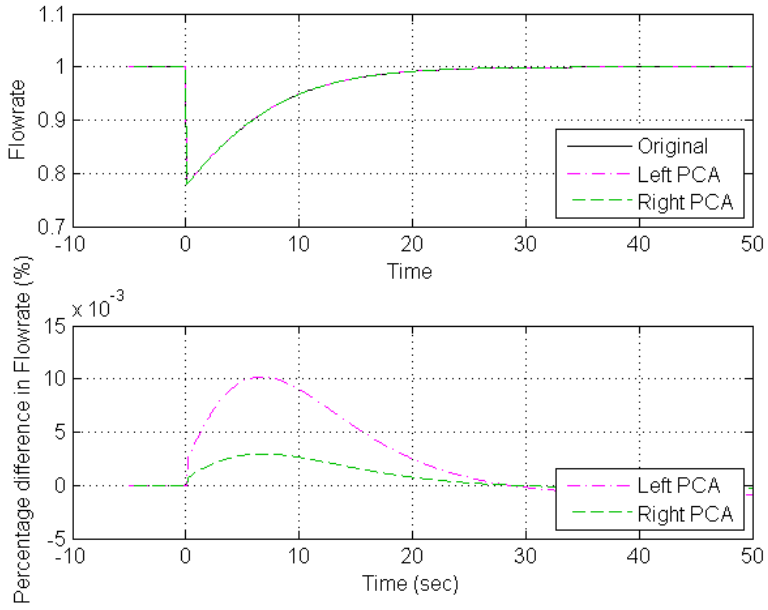

Figure 8.67 Flowrates response in the PCA2s as a result of the left MCA λ change from 3 to 50.

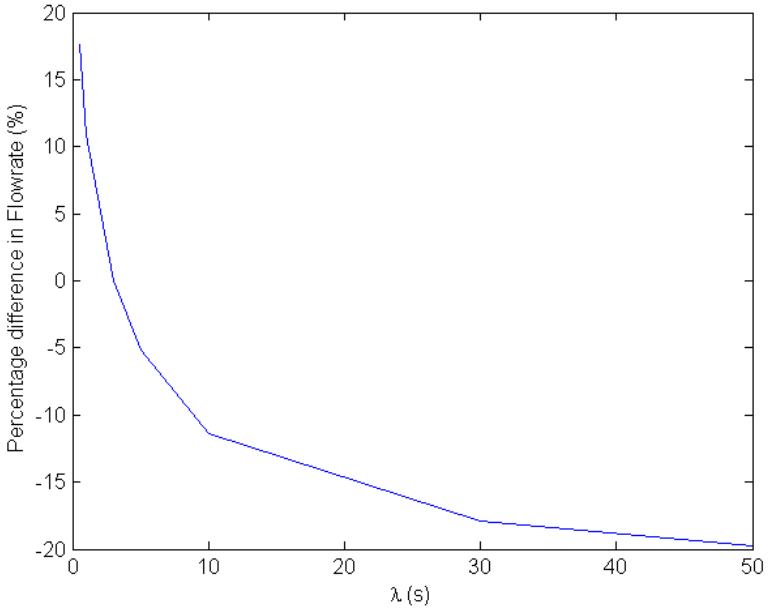

Figure 8.68 Flowrates percentage errors versus λ in the left MCA.

the efferent arteries were measured and tabulated (Table 8.3). The second column in the table shows how many S.D. where added to a particular vessel where a negative sign indicates a decrease in the radius.

The drop in the left PCoA's radius by 4 S.D. with an ipsilateral ICA occlusion was chosen as an example to show the flowrates response for changing the radii in the CoW. Figures 8.69, 8.70 and 8.71 show the response and the difference in response in the ACA2s, MCAs and PCA2s as a result of changing the radius.

The results of simulations show that the error in the efferent arteries that are directly dependent on the CoW for its supply in case of an occlusion is sensitive, which is what was expected. This is clear by observing the left MCA response in all the cases tested, and the left ACA2 in the ACoA and left PCoA cases. In the ACoA and left PCoA cases, both the left ACA2 and MCA are dependent on the connecting vessels for their blood supply as a result of left ICA occlusion. In the left MCA case, it was expected that the blood supply through it was the only one to be affected. The relationship between the percentage errors in the left ACA2 and the S.D. in the ACoA is shown in Figure 8.72. The relationship between the percentage errors in the left MCA and the S.D. in the left MCA and left PCoA are shown in Figures 8.73 and 8.74 respectively. The error in the other efferent arteries is very small (negligible), therefore we can assume that there is no effect on the response of other efferent arteries.

Table 8.3 *Errors in the steady state flowrate values for all major efferent arteries as a result of changing some of the CoW vessels' radii.*

Artery	S.D. (cm)	S.D. #	LACA2	RACA2	LMCA	RMCA	LPCA2	RPCA2
ACoA	0.0211	-1	-0.64	0.32	-0.48	0.05	-0.11	-0.01
		-2	-1.80	0.91	-1.35	0.14	-0.32	-0.03
		-3	-4.11	2.06	-3.07	0.31	-0.72	-0.06
		-4	-9.17	4.59	-6.87	0.70	-1.61	-0.14
		1	0.37	-0.19	0.28	-0.03	0.07	0.01
		2	0.61	-0.30	0.45	-0.05	0.11	0.01
		3	0.75	-0.38	0.56	-0.06	0.13	0.01
		4	0.83	-0.42	0.62	-0.06	0.15	0.01
Right MCA	0.0213	-1	0.04	0.03	-0.89	0.01	0.01	0.00
		-2	0.15	0.11	-3.21	0.02	0.05	0.02
		-3	0.51	0.35	-10.71	0.06	0.15	0.06
		-4	1.98	1.37	-56.76	0.24	0.59	0.22
		1	-0.02	-0.01	0.40	-0.00	-0.01	-0.00
		2	-0.03	-0.02	0.60	-0.00	-0.01	-0.00
		3	-0.03	-0.02	0.66	-0.00	-0.01	-0.00
		4	-0.04	-0.03	0.80	-0.00	-0.01	-0.00
Left PCoA	0.0211	-1	-0.70	-0.48	-0.84	-0.07	0.24	0.03
		-2	-1.68	-1.15	-2.03	-0.17	0.56	0.08
		-3	-3.10	-2.12	-3.73	-0.31	1.04	0.14
		-4	-5.18	-3.55	-6.25	-0.53	1.73	0.23
		1	0.51	0.35	0.61	0.05	-0.17	-0.02
		2	0.89	0.61	1.07	0.09	-0.30	-0.04
		3	1.18	0.81	1.42	0.12	-0.40	-0.05
		4	1.40	0.96	1.68	0.14	-0.47	-0.06

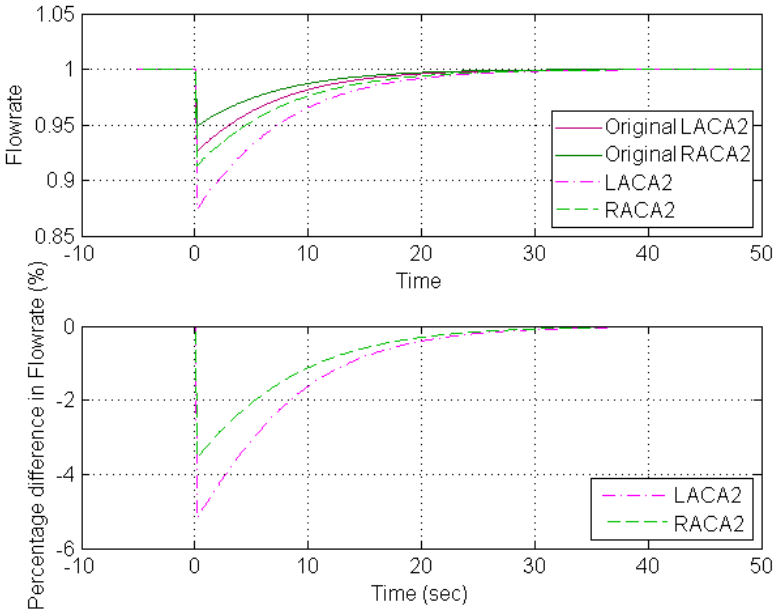

Figure 8.69 Flowrates response in the ACA2s as a result of the left PCoA radii decrease by 4 S.D..

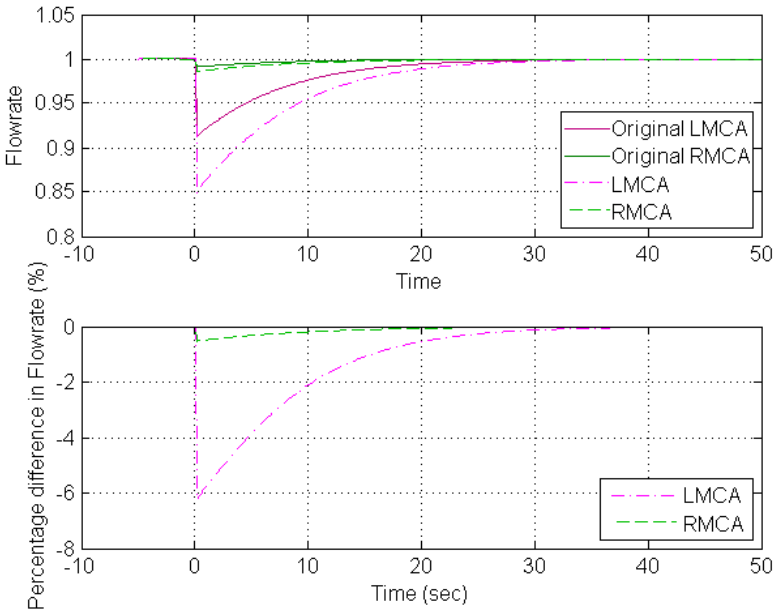

Figure 8.70 Flowrates response in the MCAs as a result of of the left PCoA radii decrease by 4 S.D..

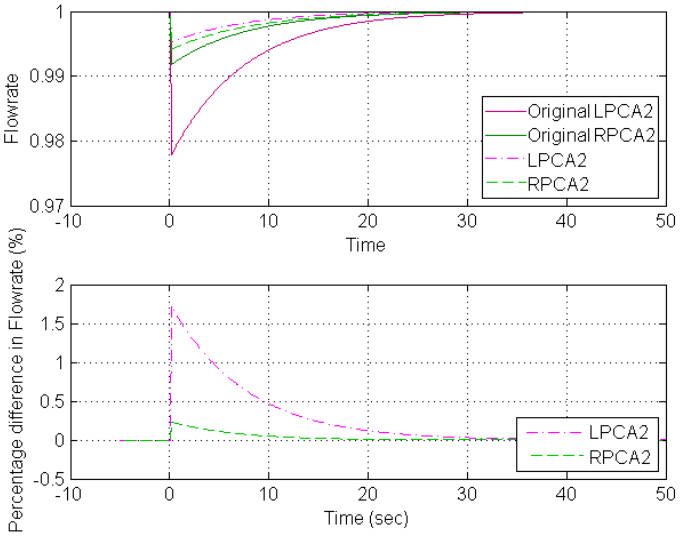

Figure 8.71 Flowrates response in the PCA2s as a result of the left PCoA radii decrease by 4 S.D..

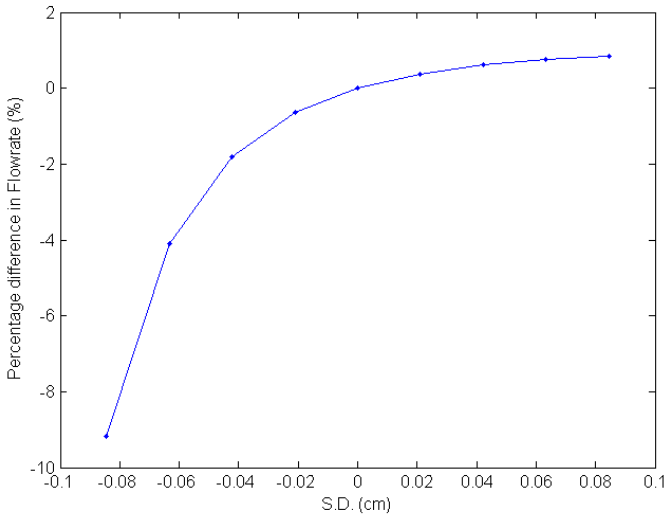

Figure 8.72 Flowrates percentage errors in the left ACA2 versus ACoA S.D..

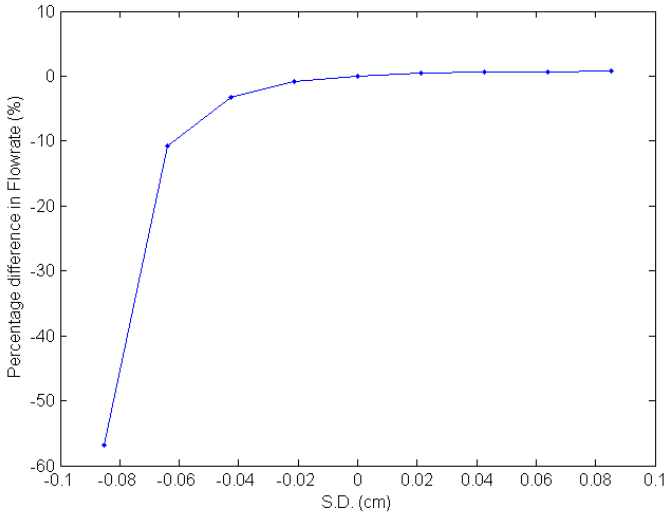

Figure 8.73 Flowrates percentage errors in the left MCA versus S.D. in the left MCA.

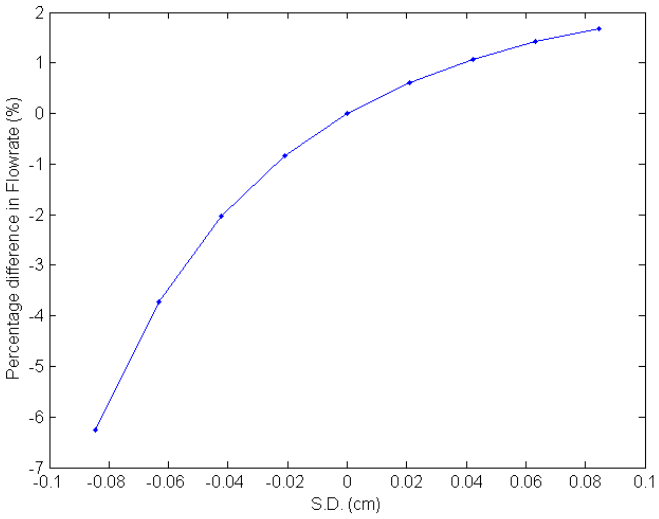

Figure 8.74 Flowrates percentage errors in the left MCA versus PCoA S.D..

From the results above for testing the λ and CoW radii sensitivity, we can state that the CoW autoregulation model has very low sensitivity. This was very clear while testing the λ sensitivity. For testing the CoW vessels' radii sensitivity, a dependence by the efferent arteries affected by the ICA occlusion on the connecting vessels was observed. However, this dependence is small unless the radii decrease by several standard deviations. An increase in the radii had negligible effects.

8.3 Non-Linear Models

At this stage of the research, the simple metabolic model presented in Sections 5.3 and 8.2.2 was being used as the latest developed version of the CoW model. Although the addition of the LMA arteries using assumed values for flowrates showed some differences in the efferent arteries' response, these differences were not significant enough to be included in the latest developed version of the model. The lack of data in the literature to support the size of these arteries and flowrates through them, resulted in the elimination of the LMA vessels in the CoW model with the aim of including them when more data becomes available.

Two modifications were added to the simple metabolic model to take into account the extra losses encountered in the CoW nodes. These losses are encountered as a result of velocity profile development along the vessel, as well as centripetal forces experienced because of the tortuosity of some of the vessels. First, a simple head loss term was added to the set of Poiseuille equations where the loss coefficients were based on the angle of the CoW bifurcations (nodes). Then, as presented in Section 6.2, new non-linear equations

were implemented based on Cieslicki et al.'s work [26]. The metabolic model was also further developed where the CO_2 concentration in the brain tissue was the main driver for the response in the efferent arteries. The results of the two losses models and the new metabolic model are presented below.

8.3.1 Angle Pressure Losses in CoW Nodes

Simulations of the CoW model with the angle-based pressure losses were run at different values of C, defined in Equation 6.3. The angles of the bifurcations were estimated based on MRA images. The results were compared to the same model without the pressure losses in a classical complete CoW with no pathological conditions. Table 8.4 shows the percentages of change experienced by the CoW arteries (afferent and internal connecting arteries) for different values of C. The most arteries affected by the addition of the angle pressure losses were the communicating arteries (anterior and both posterior arteries). This is because, under normal conditions in a classical complete CoW, these arteries do not have high values of flowrates through them. Once the losses are added, the pressure values at the CoW nodes decrease accordingly. In the case of the anterior communicating artery, if C is increased beyond the value of 600, the losses become high enough to reverse the direction of the flow. Negative change percentages that are below -100 mean that the flowrate has changed its direction. Figures 8.75, 8.76 and 8.77 show the flowrates in the CoW arteries for C values of 100, 500 and 1000 respectively.

Table 8.4 *Percentage changes in flowrate of the CoW afferent and internal connecting vessels as a result of adding the angle pressure losses.*

C	BA	LICA	RICA	ACoA	LACA1	RACA1	LPCoA	RPCoA	LPCA1	RPCA1
0.5	-0.00	-0.00	0.00	-0.11	-0.02	0.03	0.20	-0.05	-0.02	0.01
5	-0.04	-0.00	0.03	-1.06	-0.20	0.32	1.96	-0.49	-0.17	0.11
50	-0.35	-0.04	0.34	-10.35	-1.95	3.14	18.95	-4.82	-1.64	1.11
60	-0.42	-0.05	0.40	-12.35	-2.33	3.75	22.58	-5.76	-1.96	1.33
70	-0.48	-0.06	0.47	-14.33	-2.71	4.35	26.15	-6.69	-2.27	1.54
80	-0.54	-0.07	0.53	-16.29	-3.08	4.94	29.68	-7.62	-2.57	1.75
90	-0.60	-0.08	0.59	-18.23	-3.44	5.53	33.15	-8.54	-2.87	1.97
100	-0.66	-0.09	0.65	-20.15	-3.80	6.11	36.57	-9.45	-3.17	2.18
200	-1.18	-0.21	1.21	-38.27	-7.22	11.61	68.33	-18.21	-5.93	4.19
300	-1.58	-0.35	1.70	-54.68	-10.32	16.58	96.15	-26.36	-8.34	6.07
400	-1.89	-0.51	2.13	-69.60	-13.14	21.10	120.72	-33.97	-10.47	7.82
500	-2.13	-0.67	2.50	-83.24	-15.71	25.24	142.58	-41.09	-12.37	9.46
600	-2.31	-0.84	2.83	-95.76	-18.07	29.03	162.15	-47.78	-14.06	11.00
700	-2.44	-1.00	3.13	-107.29	-20.25	32.53	179.77	-54.08	-15.59	12.45
800	-2.53	-1.17	3.39	-117.94	-22.26	35.76	195.71	-60.03	-16.97	13.82
900	-2.59	-1.33	3.62	-127.83	-24.13	38.76	210.21	-65.65	-18.23	15.11
1000	-2.63	-1.49	3.82	-137.01	-25.86	41.54	223.44	-70.97	-19.38	16.34

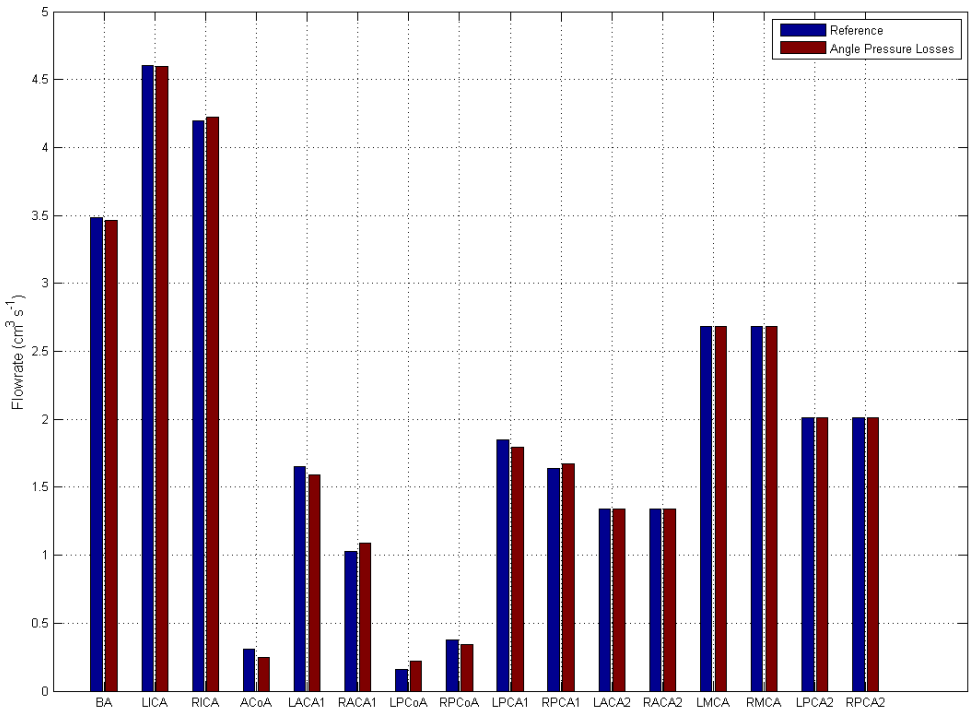

Figure 8.75 Flowrates through all CoW vessels without (blue) and with (brown) angle pressure losses where C = 100.

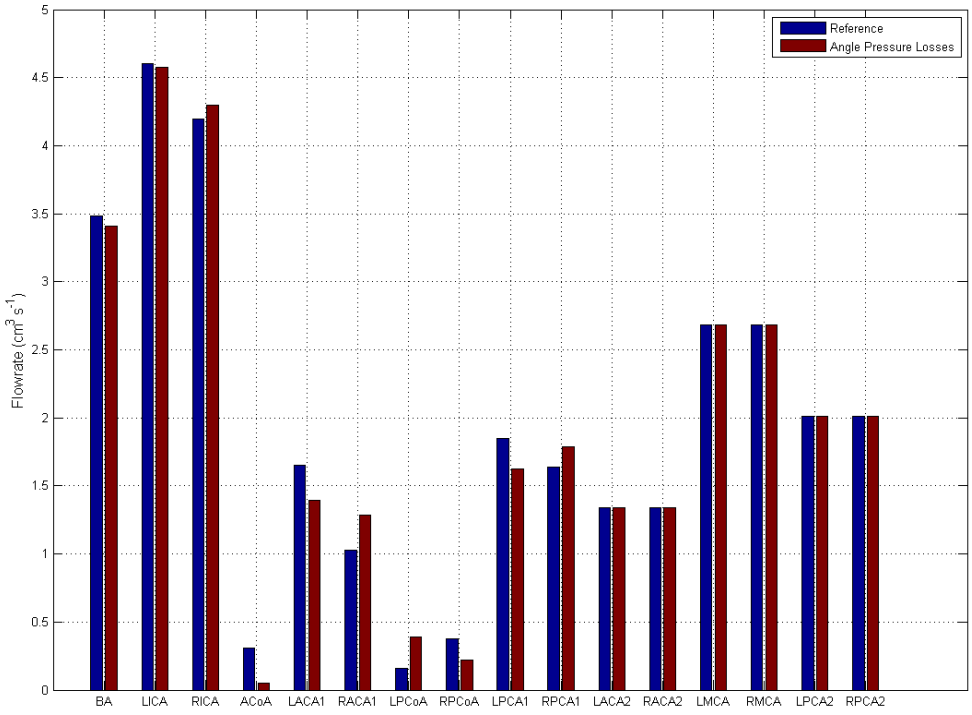

Figure 8.76 Flowrates through all CoW vessels without (blue) and with (brown) angle pressure losses where C = 500.

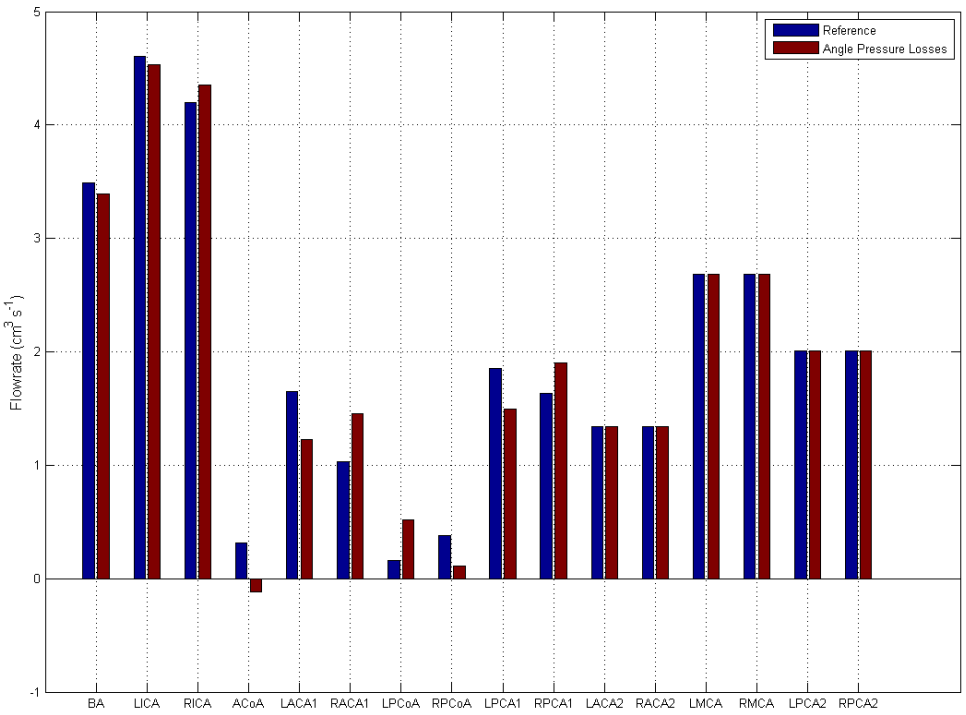

Figure 8.77 Flowrates through all CoW vessels without (blue) and with (brown) angle pressure losses where C = 1000.

Testing the model under a pathological condition gives a better indication of the effects of modifying it. The CoW was subjected to a unilateral ICA occlusion in addition to the angle pressure losses. Table 8.5 shows the percentages of change experienced by the CoW arteries for different values of C. All the internal connecting vessels of the CoW are affected greatly as a result of the addition of angle pressure losses in a CoW with a left ICA occlusion except for the right PCA, which experiences the least change of flowrate. Figures 8.78, 8.79 and 8.80 show the flowrates in the CoW arteries for C values of 100, 500 and 1000 respectively.

Table 8.6 shows the percentages of maximum change experienced by the main efferent arteries' response. Positive values indicate an increase in the immediate response after the occlusion while negative values indicate a decrease in the immediate response. The table shows that, once the C value increases above 200, the difference in response between the model with the angle pressure losses and without the losses takes the opposite sign for some of the efferent arteries. For example, the percentage of maximum change encountered by the left ACA2 is 1.17% when C is 100, but it is −5.39% when C is increased to 300. This could be as a result of the blood flow steal phenomenon[1] which may occur once the pressure losses at some of the nodes become too high.

[1]See Chapter 2

Table 8.5 *Percentage changes in the CoW afferent and internal connecting vessels as a result of adding the angle pressure losses under the condition of a unilateral occlusion ICA.*

C	BA	LICA	RICA	ACoA	LACA1	RACA1	LPCoA	RPCoA	LPCA1	RPCA1
0.5	-0.01	0.01	0.01	0.04	0.13	0.03	-0.04	-0.06	-0.02	0.01
5	-0.12	0.10	0.11	0.44	1.34	0.26	-0.41	-0.59	-0.21	0.11
50	-1.18	0.95	1.07	4.39	13.35	2.63	-4.12	-5.89	-2.12	1.12
60	-1.41	1.12	1.28	5.26	15.99	3.15	-4.93	-7.06	-2.54	1.34
70	-1.65	1.27	1.49	6.13	18.63	3.67	-5.75	-8.22	-2.96	1.56
80	-1.88	1.42	1.70	7.00	21.26	4.19	-6.56	-9.38	-3.38	1.78
90	-2.11	1.57	1.91	7.86	23.89	4.70	-7.37	-10.53	-3.79	2.00
100	-2.35	1.70	2.12	8.72	26.50	5.22	-8.18	-11.68	-4.21	2.21
200	-4.63	2.63	4.19	17.21	52.28	10.30	-16.13	-22.96	-8.30	4.35
300	-4.55	10.11	4.09	16.99	51.78	10.16	-16.01	-23.70	-8.24	4.49
400	-5.87	12.88	5.31	22.05	67.00	13.19	-20.67	-30.63	-10.64	5.81
500	-7.13	15.35	6.45	26.76	81.33	16.01	-25.10	-37.14	-12.91	7.04
600	-8.32	17.57	7.52	31.21	94.85	18.68	-29.27	-43.26	-15.06	8.20
700	-9.44	19.56	8.54	35.42	107.64	21.20	-33.21	-49.04	-17.09	9.30
800	-10.51	21.33	9.50	39.40	119.75	23.58	-36.95	-54.49	-19.01	10.33
900	-11.52	22.91	10.41	43.18	131.23	25.84	-40.49	-59.65	-20.83	11.31
1000	-12.48	24.31	11.28	46.77	142.13	27.99	-43.86	-64.54	-22.56	12.24

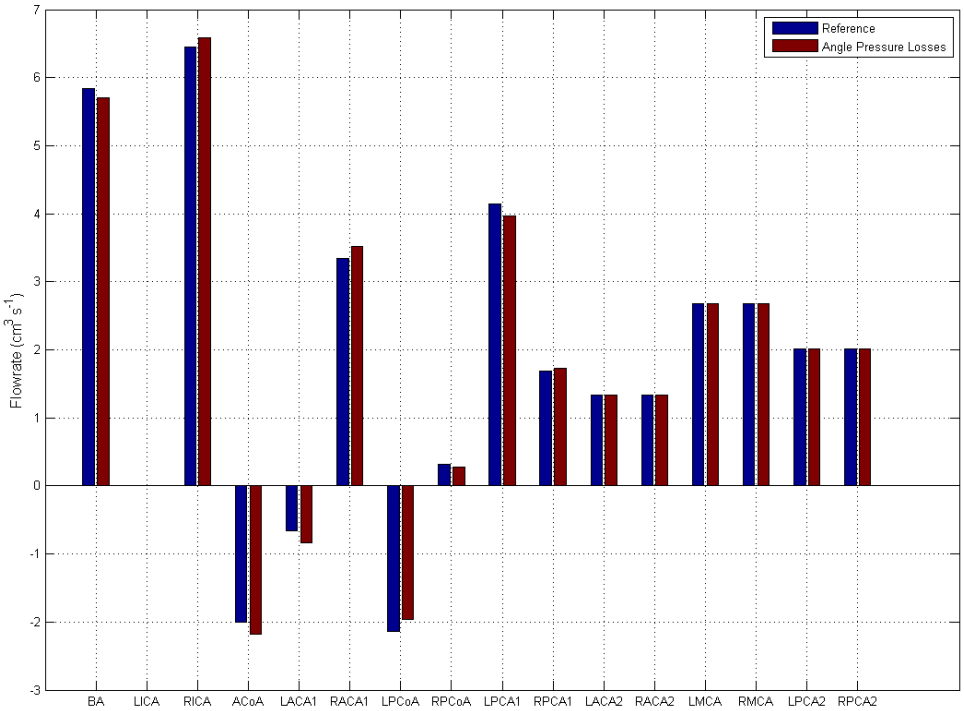

Figure 8.78 Flowrates through all CoW vessels without (blue) and with (brown) angle pressure losses where C = 100 under an ipsilateral ICA occlusion condition.

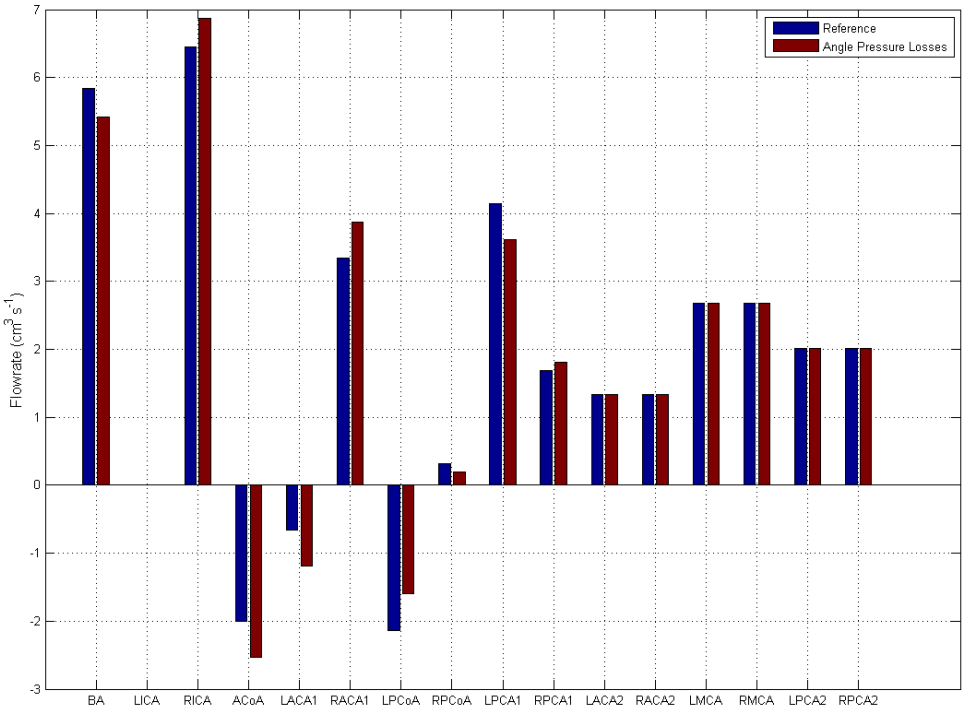

Figure 8.79 Flowrates through all CoW vessels without (blue) and with (brown) angle pressure losses where C = 500 under an ipsilateral ICA occlusion condition.

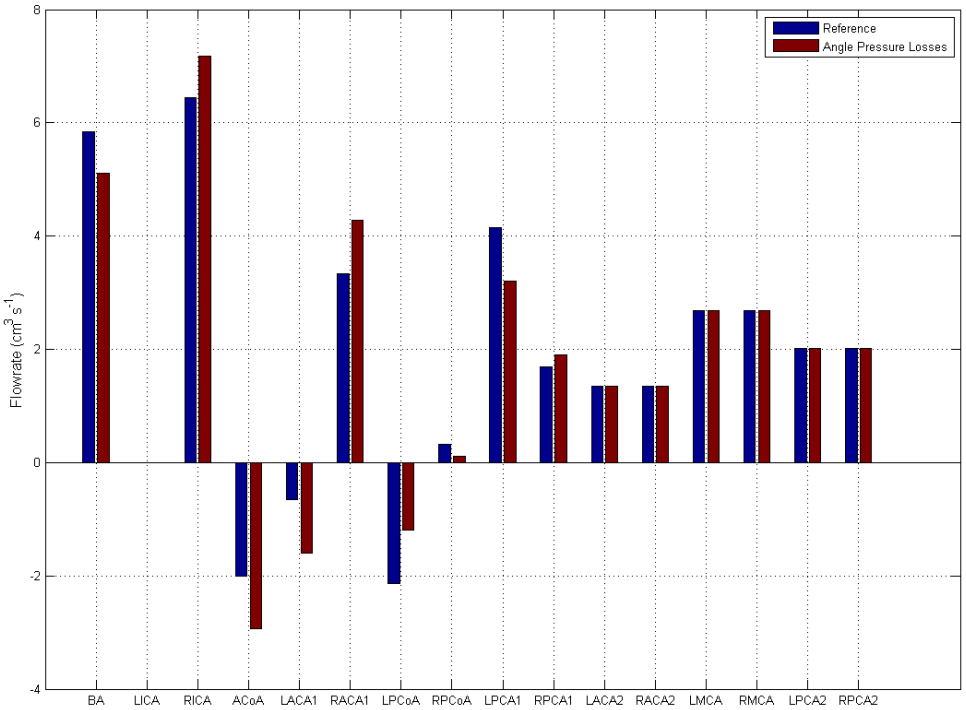

Figure 8.80 Flowrates through all CoW vessels without (blue) and with (brown) angle pressure losses where C = 1000 under an ipsilateral ICA occlusion condition.

Table 8.6 *Percentage of maximum changes in the CoW efferent arteries' response as a result of adding the angle pressure losses under the condition of a unilateral occlusion ICA.*

C	**LACA2**	**RACA2**	**LMCA**	**RMCA**	**LPCA2**	**RPCA2**
0.5	0.01	-0.00	-0.00	-0.00	-0.00	-0.00
5	0.05	-0.05	-0.01	-0.00	-0.00	-0.00
50	0.55	-0.49	-0.12	-0.04	0.00	-0.00
60	0.66	-0.59	-0.14	-0.05	0.00	-0.00
70	0.78	-0.69	-0.16	-0.06	0.00	-0.01
80	0.91	-0.79	-0.18	-0.06	0.00	-0.01
90	1.04	-0.89	-0.20	-0.07	0.00	-0.01
100	1.17	-1.00	-0.22	-0.08	0.00	-0.01
200	2.64	-2.09	-0.35	-0.17	0.02	-0.01
300	-5.39	-3.29	-0.88	-0.26	-0.16	-0.04
400	-6.67	-4.58	-1.39	-0.37	-0.14	-0.06
500	-0.58	-4.60	-1.65	-0.27	-0.14	-0.07
600	-0.58	-5.62	-1.87	-0.33	-0.15	-0.09
700	-0.55	-6.68	-2.11	-0.38	-0.16	-0.10
800	-0.36	-7.78	-2.18	-0.45	-0.17	-0.12
900	-0.26	-8.88	-2.31	-0.50	-0.17	-0.13
1000	-0.20	-10.00	-2.42	-0.56	-0.17	-0.15

Figures 8.81, 8.82 and 8.83 show the response and the percentage differences in the response in the main efferent arteries of ACA2s, MCAs and PCA2s respectively, where C is set to 100. The table and figures show that the ACA2s are the efferent arteries most affected by the addition of the angle pressure losses. This is because the blood flow, especially in the CoW anterior, has to travel through several nodes, which results in more encountered losses.

8.3.2 Non-Linear Equations

The implementation of the non-linear equations adopted from Cieslicki et al.'s work is presented in Chapter 6. Results of implementing the non-linear equations for straight and tortuous vessels are presented here. Figure 8.84 shows the total cerebral flowrate autoregulation plots of using the linear and non-linear models. The linear and non-linear plots have almost the same outline; however, the non-linear plot has a slightly narrower autoregulation range.

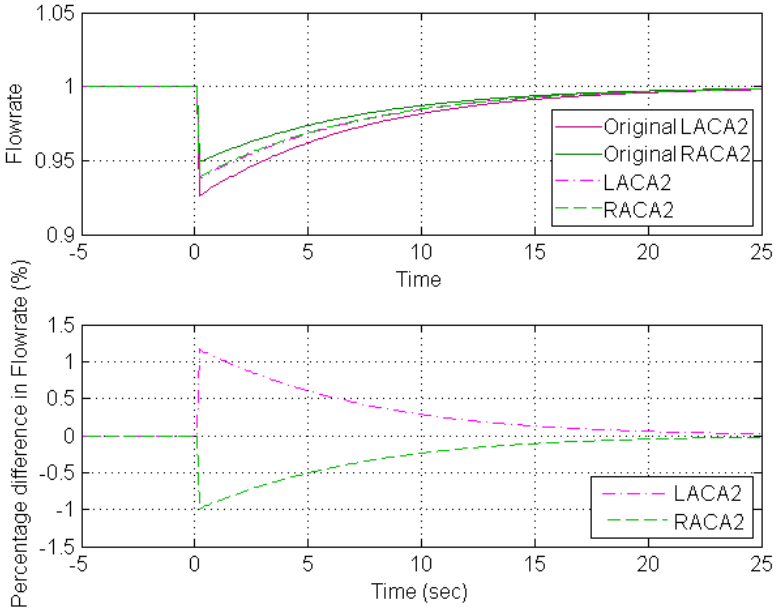

Figure 8.81 Flowrates response in the ACA2s using pressure losses model with C=100.

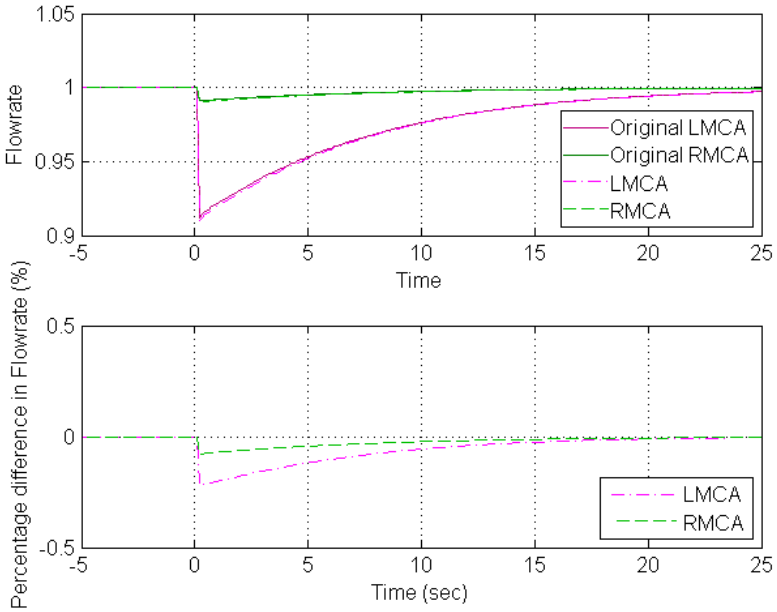

Figure 8.82 Flowrates response in the MCAs using pressure losses model with C=100.

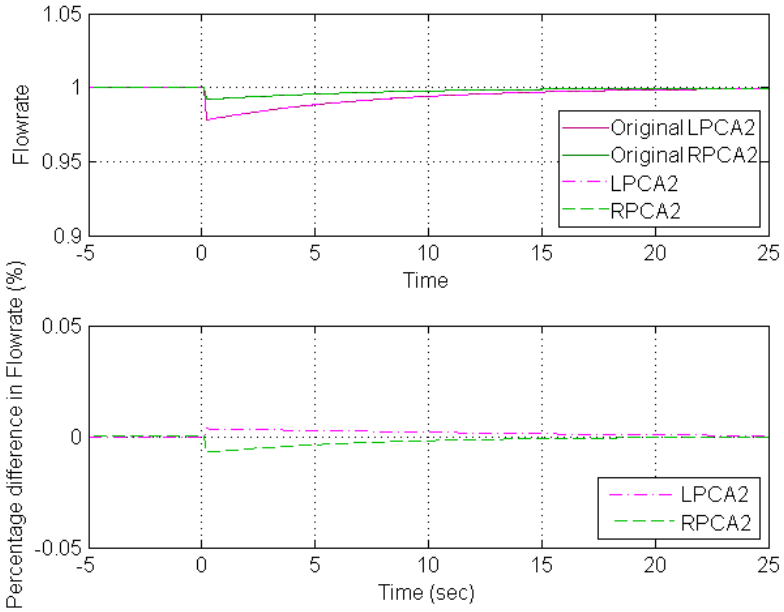

Figure 8.83 Flowrates response in the PCA2s using pressure losses model with C=100.

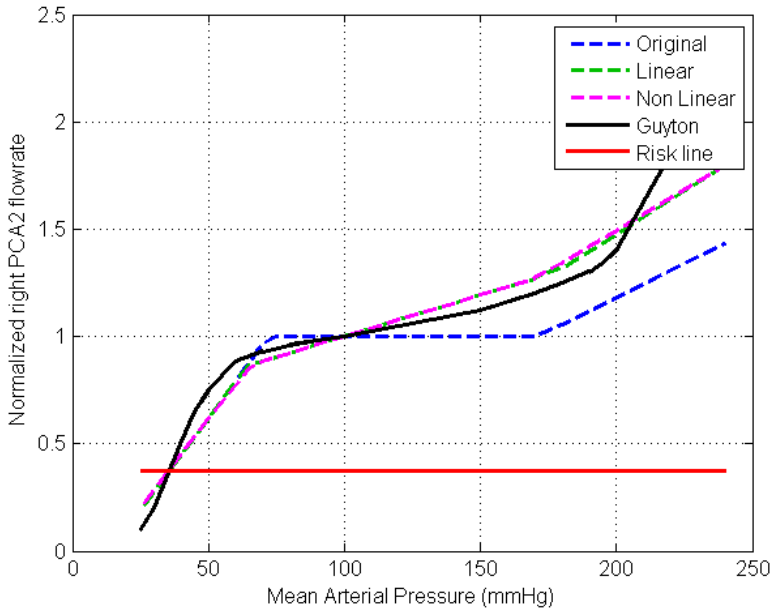

Figure 8.84 The total cerebral flowrate autoregulation plots of the simple metabolic model using linear and non-linear equations for a classical complete CoW under no pathological conditions.

The CoW was also subjected to different pathological conditions. First, the simulation for classical complete CoW with a unilateral ICA occlusion was run using the non-linear equations. Figure 8.85 shows the total cerebral flowrate autoregulation plots where the non-linear plot has a narrower autoregulation range and is shifted upwards to a higher MAP range as a result of the left ICA occlusion. The efferent arteries affected most by the occlusion are the left ACA2 and MCA, where they have almost identical responses. Figure 8.86 shows the autoregulation plots for the left MCA efferent artery. The right ACA2 is affected less by the occlusion than the left ACA2 and MCA, while the right MCA and both PCA2s experience almost no disturbance.

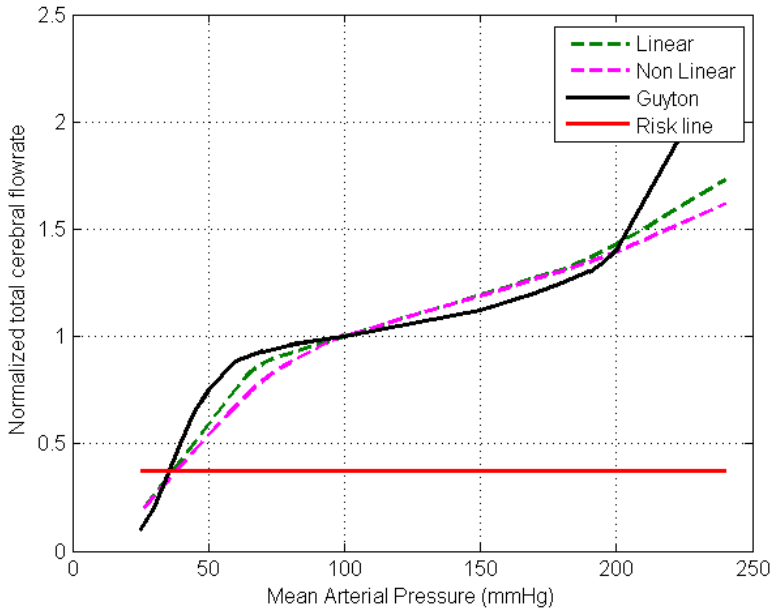

Figure 8.85 The total cerebral flowrate autoregulation plots of the simple metabolic model using linear and non-linear equations for a classical complete CoW under a left ICA occlusion.

Second, the model was run using the CoW special case described in Section 8.1.2.9. Here, the left ICA is 75% stenosed and the ACoA and ipsilateral PCoA are missing. This case combines the most common abnormality in the anterior and the most common abnormality in the posterior of the CoW. The most affected efferent arteries are the left ACA2 and MCA, while the rest of the efferent arteries experience almost no disturbance. Figures 8.87 and 8.88 show the autoregulation plots for the left and right MCAs respectively. The left MCA is affected enough to drive the autoregulation range well above the normal upper limit of autoregulation (ULA) for the linear model. The non-linear model cannot produce sufficient blood flow even at unrealistic high MAP. In this case, the other parts of the CoW cannot route the blood to where it is needed because of the missing communication arteries which play a vital role in these cases. Therefore, the left ACA2 and MCA suffer extreme blood loss as a result of the very

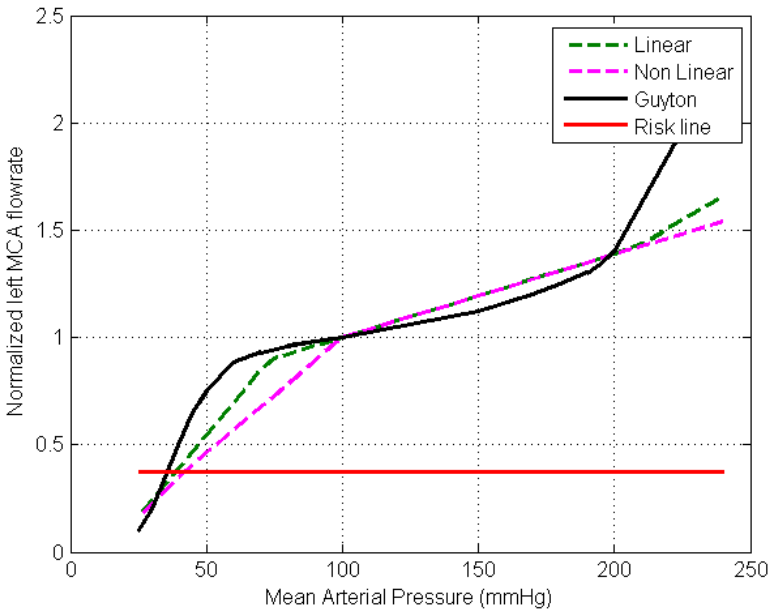

Figure 8.86 The left MCA autoregulation plots of the simple metabolic model using linear and non-linear equations for a classical complete CoW under a left ICA occlusion.

stenosed left ICA while the other efferent arteries are well supplied by the BA and right ICA. This predicts that, if this case were to occur in reality, the CoW will be unable to deliver enough blood to the ipsilateral anterior and middle parts of the cerebral mass, which may give rise to a stroke incident.

The non-linear model using Cieslicki et al.'s equation for losses was compared to the angle pressure losses model, where C was set to 100. Figures 8.89, 8.90, and 8.91 show the pressures and flowrates of the model with no losses and both losses models implemented above for different cases. In the first case (Figure 8.89), a normal classical complete CoW was used with no pathological conditions. The flowrates for all the three different models have the same normal values as under normal conditions. The pressure values using the angle pressure losses are almost the same as the no losses model; however, the pressure values for the non-linear model are well below the no losses model.

The second case (Figure 8.90) used a normal classical complete CoW under a unilateral ICA occlusion. Again, the flowrates for all the three different models had the same normal values experienced under normal conditions. The pressure values using the angle pressure losses were just below the no losses model; however, the pressures for the non-linear model significantly dropped to almost 50% of the normal pressure values at some of the nodes. In the last case (Figure 8.91), the pressures and flowrates of the angle pressure losses model were almost identical to the no losses model while the non-linear model was significantly lower in both pressure and flowrate plots.

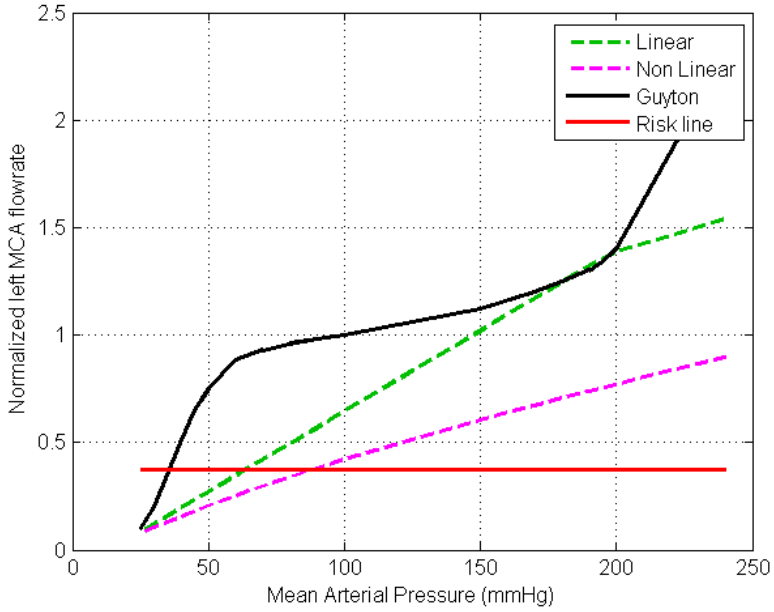

Figure 8.87 The left MCA autoregulation plots of the simple metabolic model using linear and non-linear equations in the CoW special case described in Section 8.1.2.9

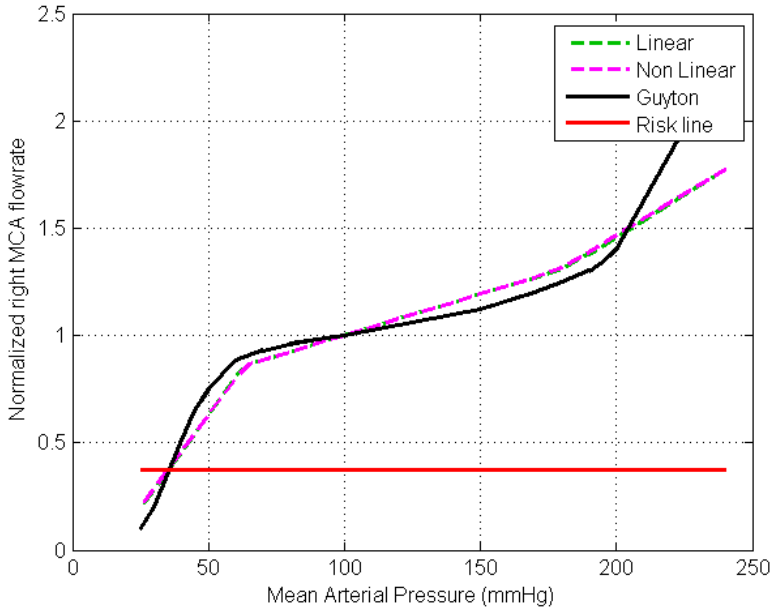

Figure 8.88 The right MCA autoregulation plots of the simple metabolic model using linear and non-linear equations in the CoW special case described in Section 8.1.2.9.

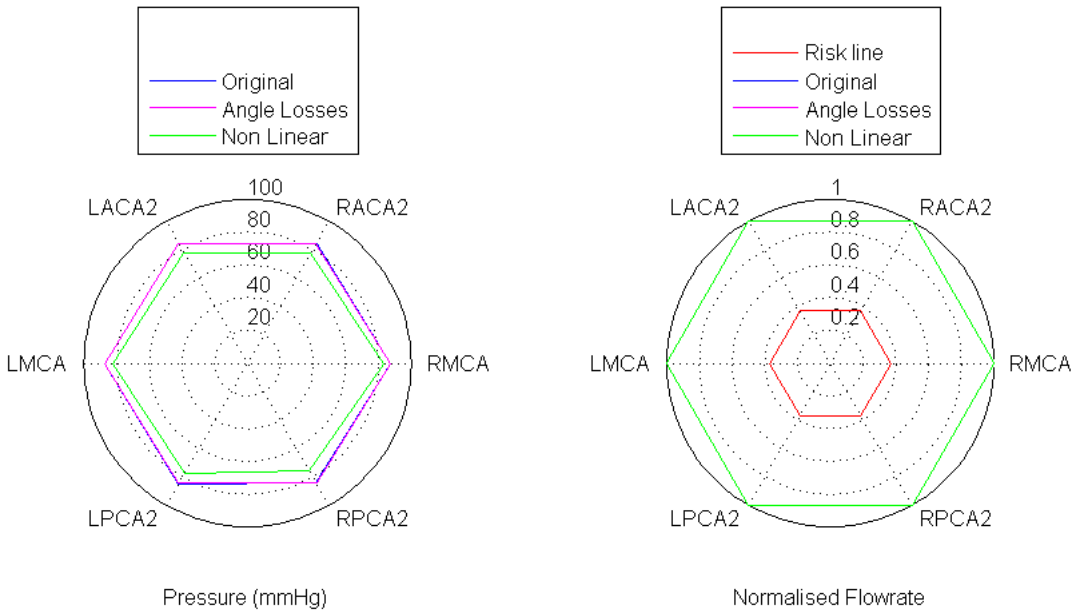

Figure 8.89 Efferent arteries' pressures and flowrates for no losses, angle pressure losses, and non-linear losses models in a classical complete CoW with no pathological conditions.

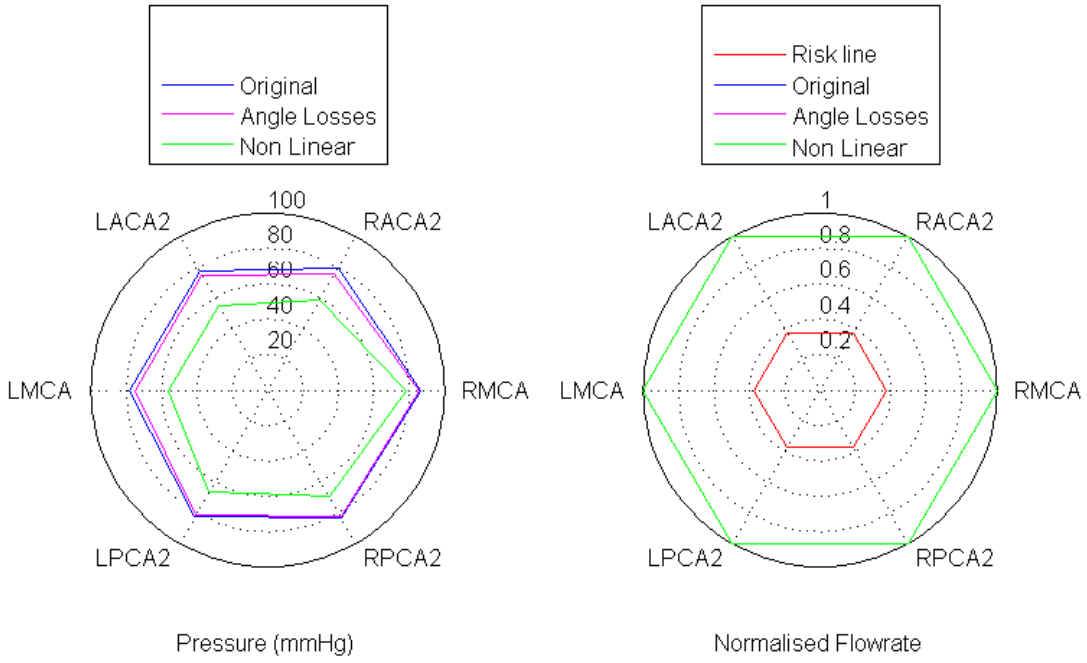

Figure 8.90 Efferent arteries' pressures and flowrates for no losses, angle pressure losses, and non-linear losses models in a classical complete CoW with a unilateral ICA.

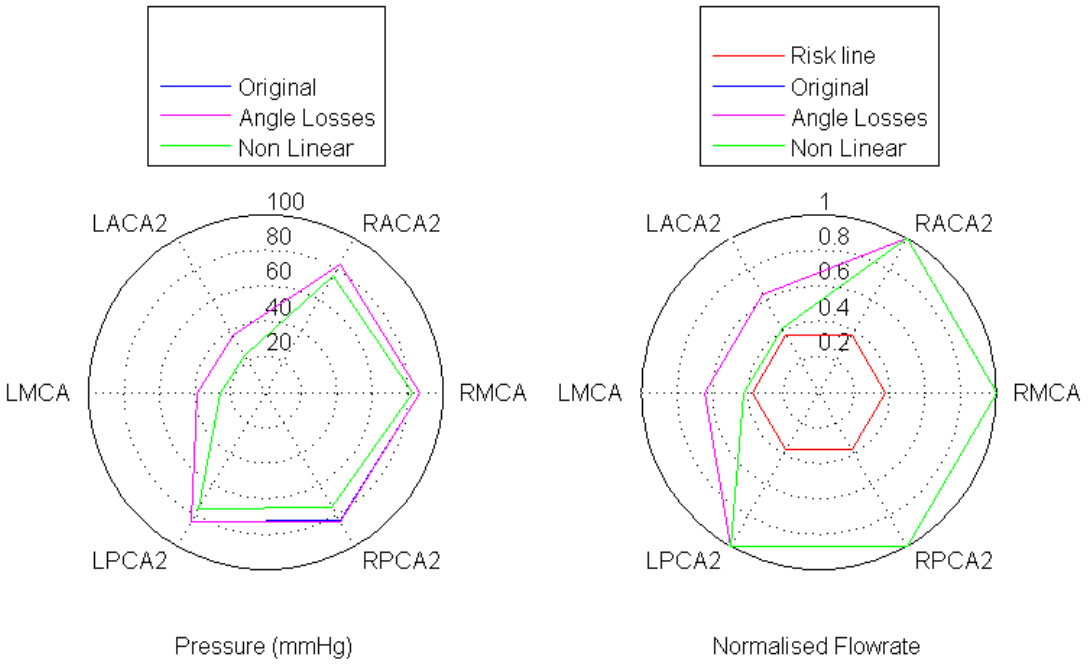

Figure 8.91 Efferent arteries' pressures and flowrates for no losses, angle pressure losses, and non-linear losses models in the CoW special case described in Section 8.1.2.9.

8.3.3 The New Metabolic Model

The simple metabolic model was developed further as discussed in Section 6.3. By this stage of the research, autoregulation graphs in the literature were well investigated. This led to adopting Panerai et al.'s conclusion [98], which is that the autoregulation graph is flat and does not have a slope as reported by Guyton et al. and that the autoregulation range is slightly lower than reported by Guyton et al. (as discussed in Chapter 2). The lower range of autoregulation of $50 - 150$ mmHg was used from this point onwards in this research replacing the range of $75 - 175$ mmHg (Figure 8.92).

The simulations for the new metabolic model were run for different cases using the linear and non-linear algorithms. Figure 8.93 shows the total cerebral flowrate autoregulation plot for a classical complete CoW under no pathological conditions using the linear and non-linear algorithms. As observed in Section 8.3.2, the non-linear autoregulation range is slightly narrower than the linear model. The non-linear model was used when setting up the new values of upper and lower vessels' resistances to achieve the ULA and LLA of 50 and150 mmHg respectively.

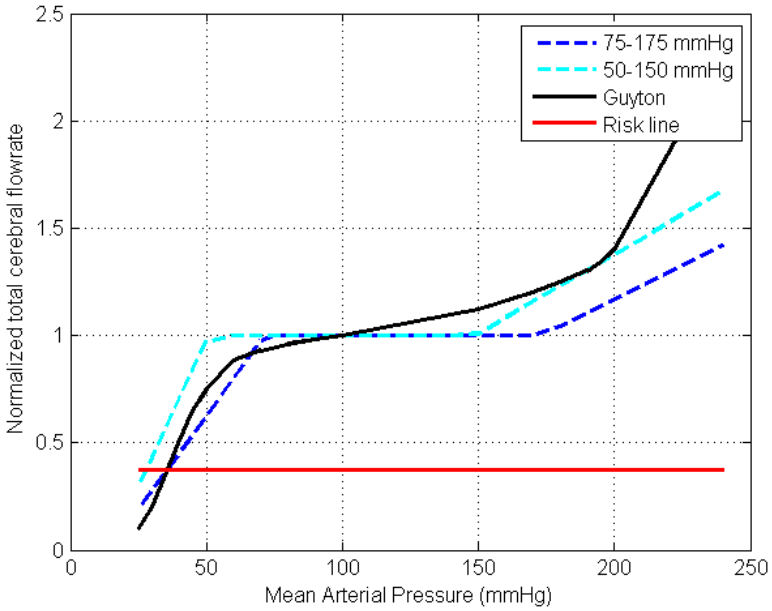

Figure 8.92 The old $(75 - 175$ mmHg) and new $(50 - 150$ mmHg) autoregulation ranges.

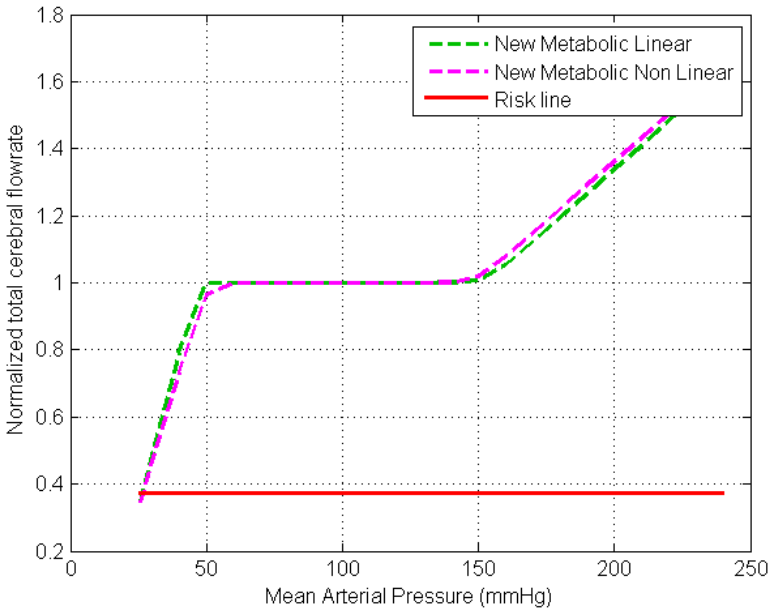

Figure 8.93 The total cerebral flowrate autoregulation plot of the new metabolic model using linear and non-linear equations for a classical complete CoW under no pathological conditions.

The differences between using the linear and non-linear algorithms in the new metabolic model are similar to the differences reported using the simple metabolic model presented in Section 8.3.2 above. In the case of a unilateral ICA occlusion, the total cerebral flowrate autoregulation plot using the non-linear algorithm is shifted upwards towards higher MAP values (Figure 8.94). This shift was observed to be higher for the left ACA2 and MCA efferent arteries, while other efferent arteries experienced smaller shifts of the autoregulation range. Figure 8.95 shows the left MCA autoregulation plot. In the special case described in Section 8.1.2.9, the linear algorithm produced a significantly higher range of autoregulation while the non-linear algorithm was unable to provide sufficient blood flow to the left ACA2 and MCA even at very high MAP, while other efferent arteries received almost undisturbed blood flow. The autoregulation plots for the left MCA and right MCA are shown in Figures 8.96 and 8.97 respectively.

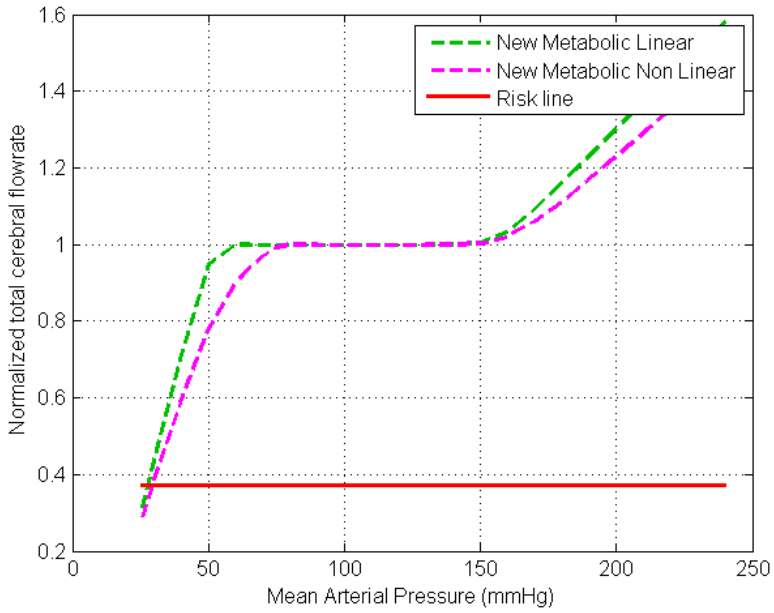

Figure 8.94 The total cerebral flowrate autoregulation plots of the new metabolic model using linear and non-linear equations for a classical complete CoW under a left ICA occlusion.

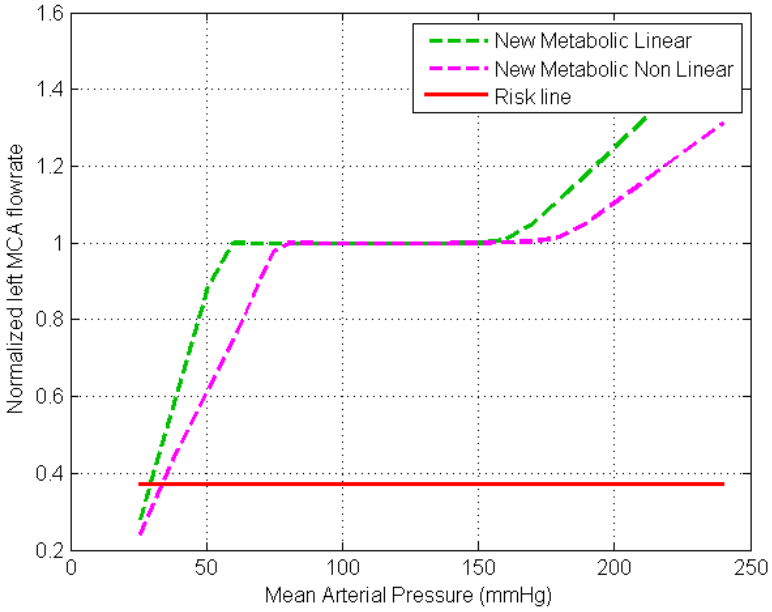

Figure 8.95 The left MCA autoregulation plots of the new metabolic model using linear and non-linear equations for a classical complete CoW under a left ICA occlusion.

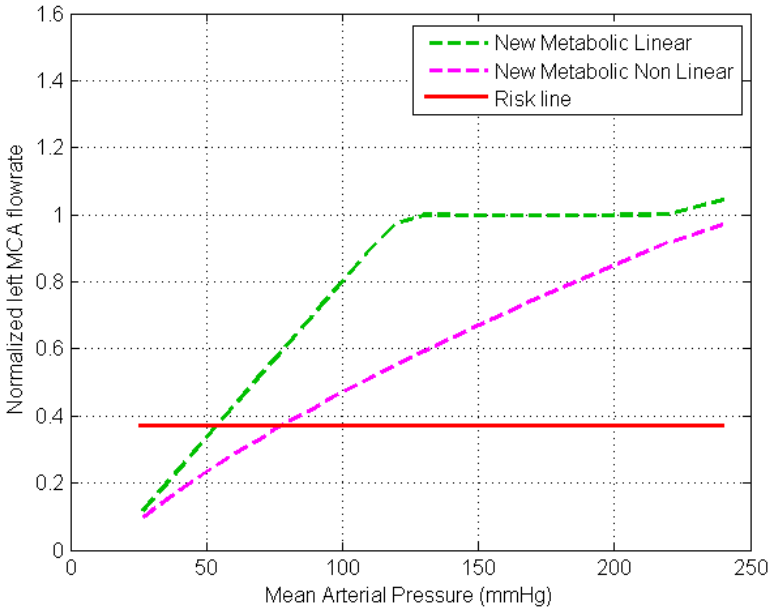

Figure 8.96 The left MCA autoregulation plots of the simple metabolic model using linear and non-linear equations in the CoW special case described in Section 8.1.2.9

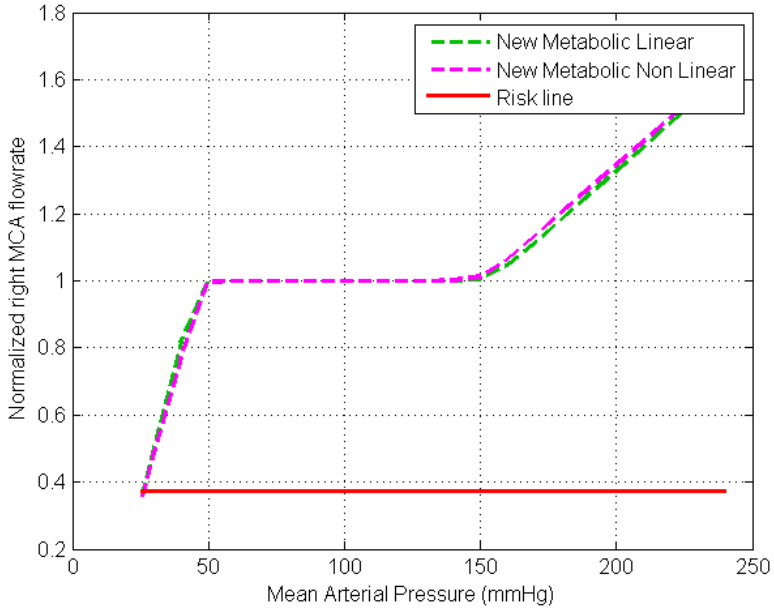

Figure 8.97 The right MCA autoregulation plots of the simple metabolic model using linear and non-linear equations in the CoW special case described in Section 8.1.2.9.

8.4 Arterial Tree Model

8.4.1 The Binary Arterial Tree

The binary arterial tree was created as described in Chapter 7. The code implementing this binary tree can accept any root vessel radius size and create an arterial tree that branches until all vessels reach the assumed terminal/pre-capillary size of 10 μm. For testing the properties of this binary tree, the root vessel was set to the radius of an MCA of 1.5 mm. The resulting binary tree was composed of 34 branching levels with more than $850,000$ vessels. More than $400,000$ out of these vessels are terminal vessels, each supplying a capillary bed consisting of approximately 7500 capillaries. Figure 8.98 shows the distribution of total number of vessels and the number of terminal vessels in each branching level of the tree. The number of vessels and terminal vessels reaches a maximum in the 20-25 branch level. There are no terminal vessels produced until the thirteenth branch level.

8.4.1.1 Tree vessels' properties

The relationship between the parent (or mother) vessel and the daughter vessels in the current binary arterial tree was compared to the experimental results by VanBavel et al. [136]. The experiment studies the porcine coronary arterial branching patterns.

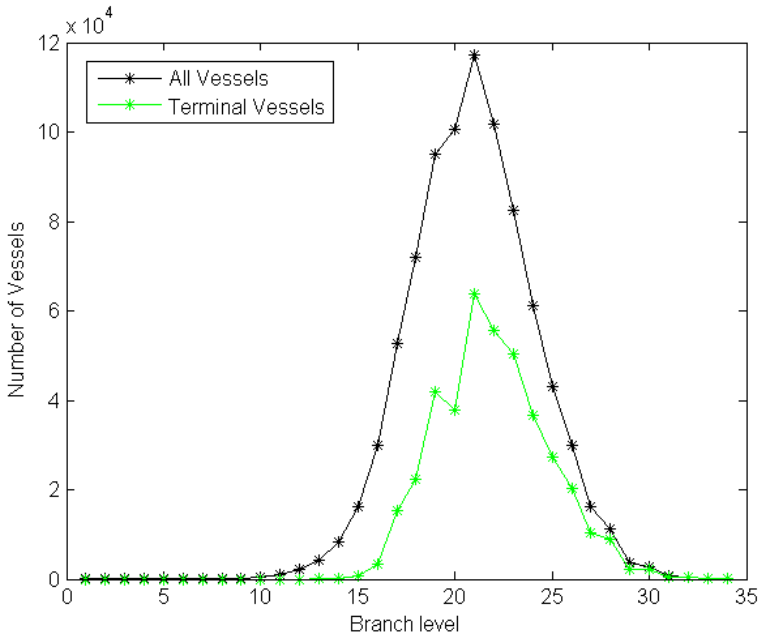

Figure 8.98 The total number of vessels (black) and the number of terminal vessels (green) per branching level in the arterial binary tree.

One of the branching patterns examined was the parent-daughter diameter relationship. Figure 8.99 (A,B) show the logarithmic plots of the daughter vessels' diameters as functions of the parent vessels' diameters for the experimental results by VanBavel et al. (black) and the binary tree created by the current model (blue). These plots show that the created binary arterial tree have a very close resemblance to vanBavel et al.'s experimental results. The logarithmic plots of the binary tree have a shift in slope at two different points, which is shown more clearly in the smaller daughter/ parent logarithmic plot in Figure 8.99 (C). This is because when the binary arterial tress is created, the power exponent (k) and the asymmetry ratio (γ) values change as the parent radius size decreases as given in Table 7.1.

The radius of the vessels in the binary arterial tree created was examined. Figure 8.100 shows the mean radius value of vessels of all sizes at each branch level, while Figure 8.101 show the mean radius of the terminal vessels only. The maximum and minimum values are shown as the bars in the plots. The terminal vessels plot does not present any values for the first 12 branches because there are none created at these levels. The terminal vessels in the remainder of the tree have a radius of $8 - 12\mu\ m$ where $10\mu\ m$ was set as the target radius in the code.

To evaluate these radii results physiologically, they were compared to the experimental study by Zamir et al. [142] where the network of the arterial tree was analysed using 1313 vessels in the arterial tree of a rat. Figure 8.102 shows the average diameter at each level for the experimental results by Zamir et al. (black) and the current binary

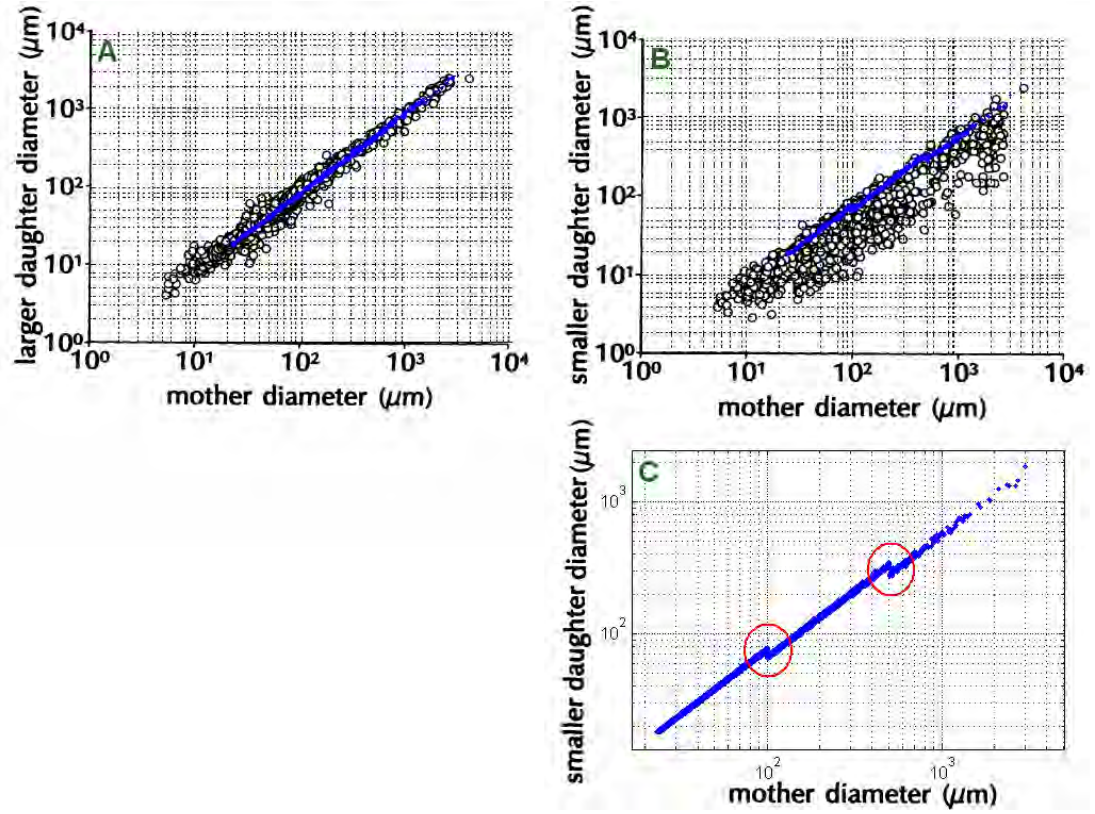

Figure 8.99 Logarithmic plots of the diameter of the larger (A) and smaller (B) daughter segments as functions of the diameter of the mother (parent) segment [136]. (C) A close up of the smaller daughter/ mother logarithmic plot highlighting the shifts observed in the slope.

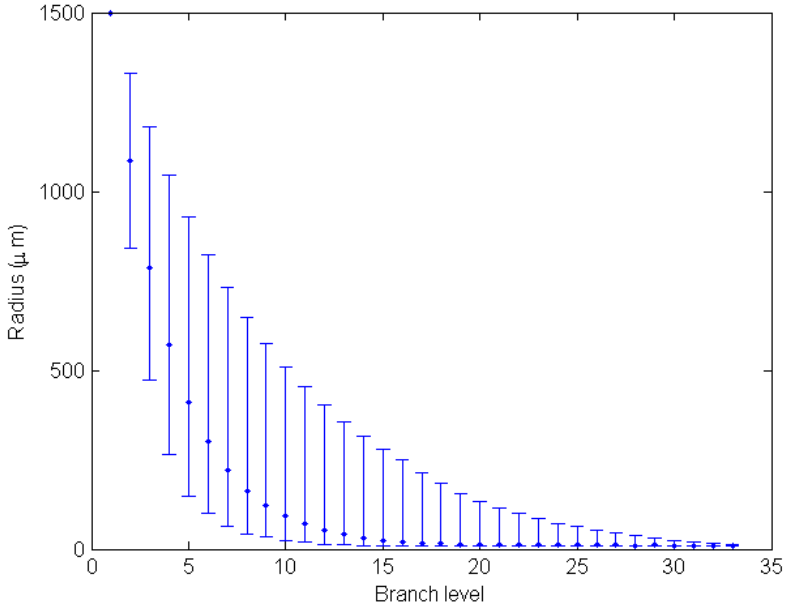

Figure 8.100 The mean (dots) radius of all vessels at each branch level with maximum and minimum values (bars).

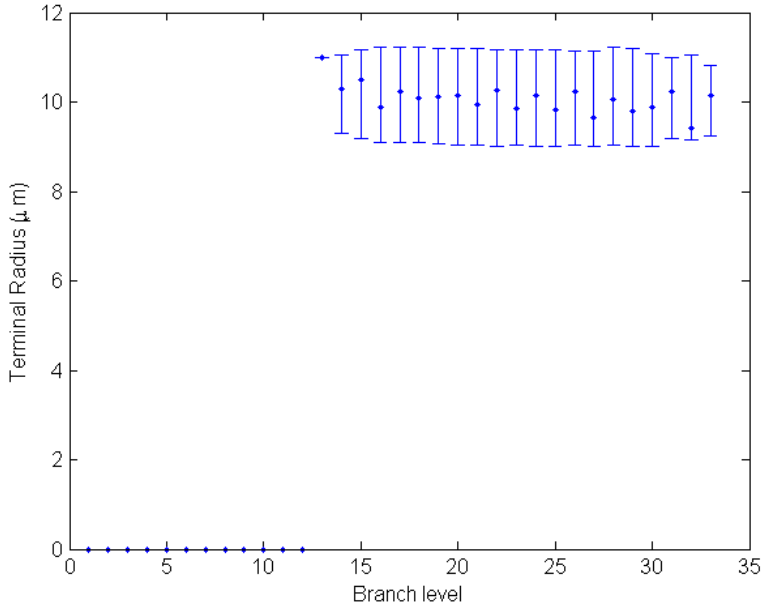

Figure 8.101 The mean (dots) radius of the terminal vessels at each branch level with maximum and minimum values (bars).

arterial tree (blue), with their ± standard deviations. For Zamir et al.'s experimental results, level 1 in the figure represents the segments of the aorta from its origin to the iliac bifurcation, and of the iliacs through to the end of the femoral arteries. This level is comparable to level 3 (assigned as level 1 in the same figure) in the binary arterial tree created in the current model using an MCA as the root vessel.

As mentioned in the Section 7.1.1, the normal distribution adopted from Lauwers et al.'s work was introduced into the current binary arterial tree. The parameters for the normal distributions were provided in Table 7.2. Figure 8.103 shows the distributions of the vessels' radii of the original binary tree without (A) and with (B) the transformation function mapping of the inverse square root of the diameter. These distributions were compared to the binary tree with the introduction of a random normal distribution (C, D). The normal distribution observed by Lauwers et al. (provided in Figure 7.4 (B)) was not achieved as expected when using the transformation function mapping. This is because the target terminal vessels were specified to be $10\mu\ m$, so the normal distribution was cut at around this value of the radius. However, the histogram in Figure 8.103 (D) does show a slightly smoother left side of the distribution compared to the original binary tree histogram (B).

The length of the vessels in the binary arterial tree was also subjected to the normal distribution properties adopted from Lauwers et al. (Table 7.2). Figure 8.104 shows the distribution of the vessels' lengths of the original binary tree with and without the transformation function mapping of the natural logarithm. These were also compared to

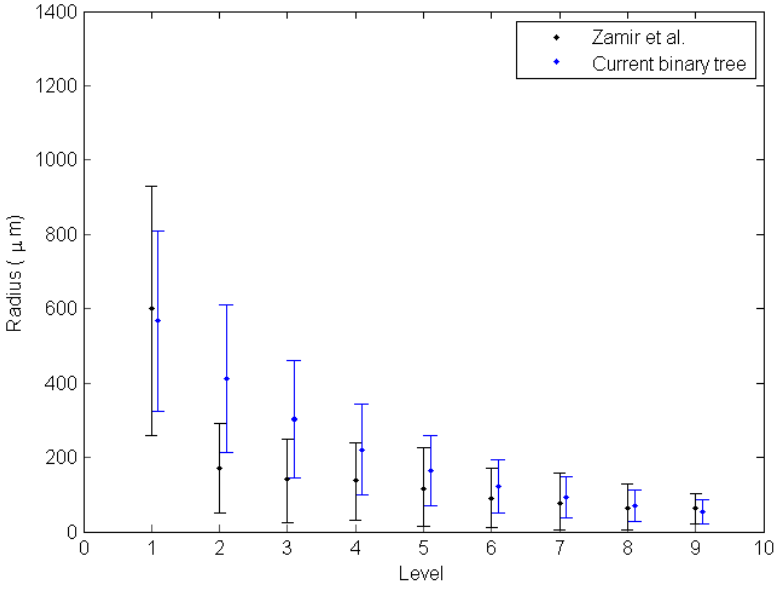

Figure 8.102 The average diameters of vessel segments at each level with ± standard deviation for Zamir et al.'s experimental results (black) and the current binary arterial tree (blue).

the binary tree with the introduction of random normal distribution. Figure 8.104 (D) shows that the normal distribution reported by Lauwers et al. was achieved using the natural logarithm transformation function. However, the mean of the vessels's lengths of the binary arterial tree created here was higher because the distribution does not take capillaries into account while Lauwers et al.'s distributions considers the complete network including the capillaries.

8.4.1.2 Resistances

The resistance of the arterial tree plays a vital role in the autoregulation in the cerebral mass. The blood flowrate delivered to the brain is based on the resistance of the cerebral vasculature. Figure 8.105 shows the cumulative resistance of the arterial tree as a function of branching level. The majority of resistance is obtained at approximately branch level 25. At this stage of the arterial tree, most of the vessels were created (see Figure 8.98). This shows that the majority of the tree's total resistance is contributed by the arterioles. The tree is extended beyond the 25th branch level even though it does not do so physiologically. This is to ensure that all vessels in the arterial tree had reached the terminal vessels size.

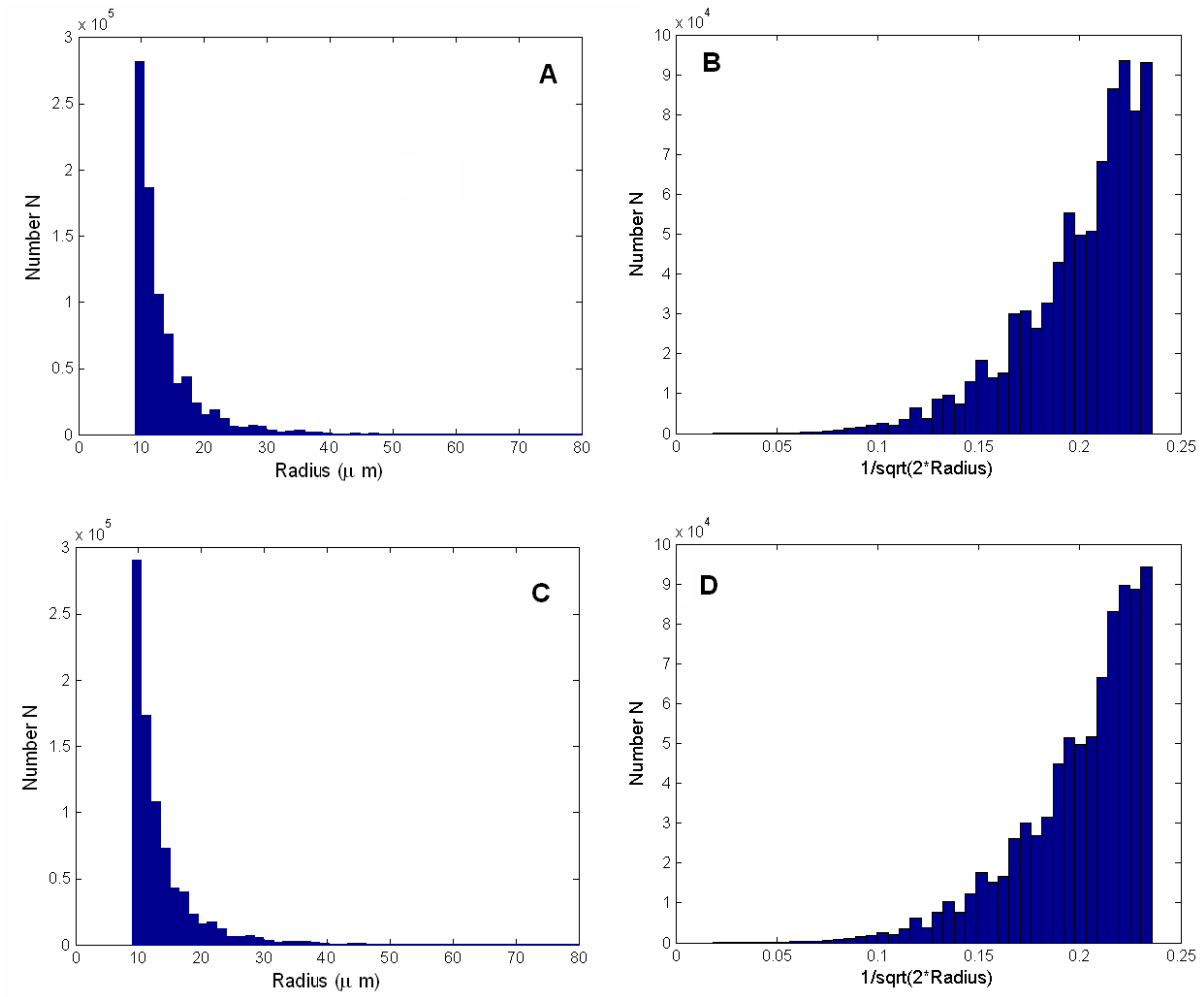

Figure 8.103 The distributions of the vessels' radii in binary arterial tree. A) Histogram of original tree radii. B) Histogram of the inverse square root mapping of original tree. C) Histogram of the tree with introduced normal distribution. D) Histogram of the inverse square root mapping of tree with introduced normal distribution.

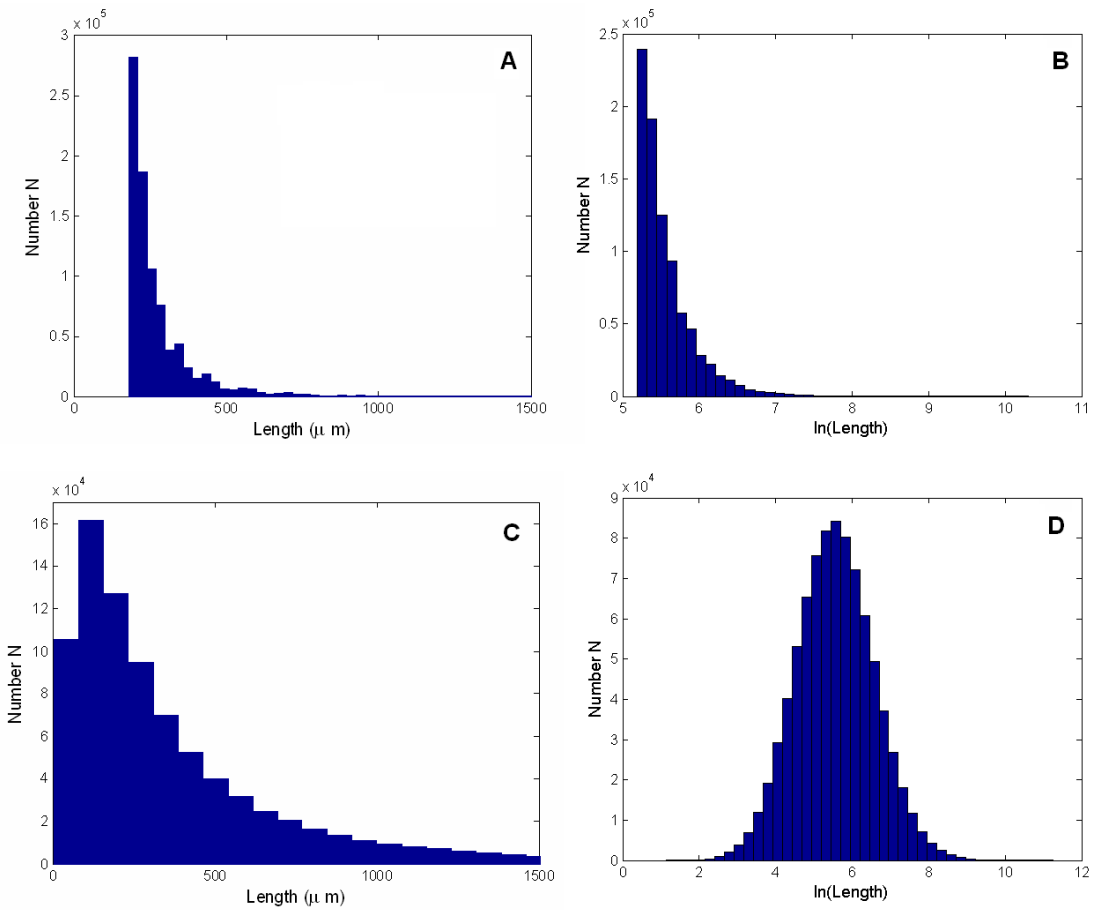

Figure 8.104 The distributions of the vessels' lengths in binary arterial tree. A) Histogram of original tree lengths. B) Histogram of the inverse square root mapping of original tree. C) Histogram of the tree with introduced normal distribution. D) Histogram of the normal logarithm mapping of tree with introduced normal distribution.

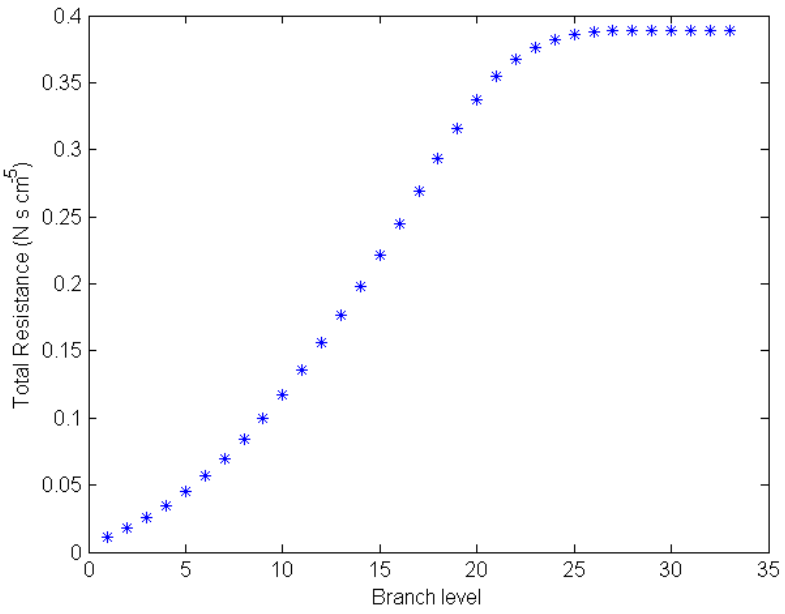

Figure 8.105 The cumulative resistance of the arterial tree as a function of branching level.

In order to implement the autoregulation in the arterial tree, it was important to investigate which vessels in the tree possess the greatest influence on the tree resistance, which consequently influences the blood flow. The tree vessels were classified into sections based on their radii. Then, the vessels' radius of each section were reduced by 25, 50 and 75% and the resistance of the tree was re-calculated. Figure 8.106 shows the percentage change in resistance that the arterial tree would experience as a result of a percentage reduction in radii at each of the radii-sections. The resistance of the arterial binary tree with the vessels' original radii was 0.286 $N\ s\ cm^{-5}$

The plots clearly show that the smaller vessels shown in Figure 8.106 have a greater impact on the vasculature resistance as they are reduced. These plots agree physiologically with experimental results of Kontos et al. [69], which examine the responses of cerebral vessels to acute hypotension. The experimental results of Kontos et al. in Figure 8.107 show that the smaller vessels in the cerebral vasculature change their radii the most in order to attain autoregulation. As a result, the first two radius ranges in Figure 8.106 that account for vessels equal to or below the radius size of 50 μm are selected in the arterial tree to implement autoregulation as a result of metabolic mechanisms, which is discussed in the sections below.

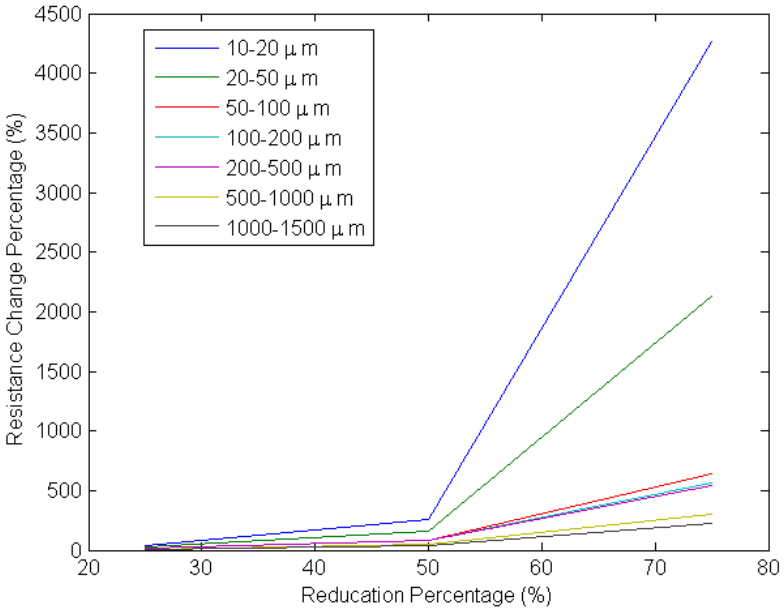

Figure 8.106 The percentage change in resistance as a result of reduction in vessels' radii by 25, 50 and 75%.

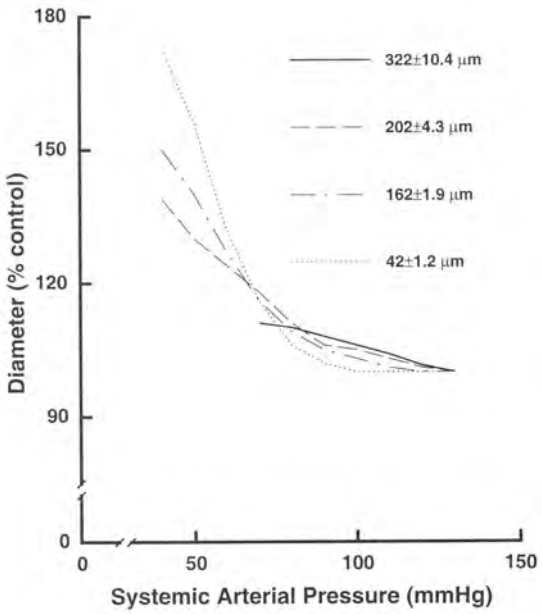

Figure 8.107 Steady state response of pial arteries and arterioles to induced hypotension [36, 69].

8.4.1.3 Pressures

The pressures at the arterial tree nodes and flowrates through all the vessels were calculated as described in Section 7.1.2. The inlet pressure for the MCA binary arterial tree created and tested here was set to 85 mmHg. This value was obtained from running the new metabolic model with the non-linear equations for a classical complete CoW under no pathological conditions, which was presented in Section 8.4.1 above. The average pressures were calculated at each branching level of the binary tree to evaluate the general drop of pressure as the arterial tree progresses as shown in Figure 8.108 (A). The plot clearly demonstrates that the average pressure drops steeply between branching levels 5 and 15. The pressures for the terminal vessels were also calculated separately and are presented in Figure 8.108 (C). The distribution of the pressure values at the tree nodes is shown in Figure 8.108 (B) where there is high occurrence of pressure between 10 and 20 mmHg because most of the terminal vessels have an inlet pressure in that range as shown in Figure 8.108 (D).

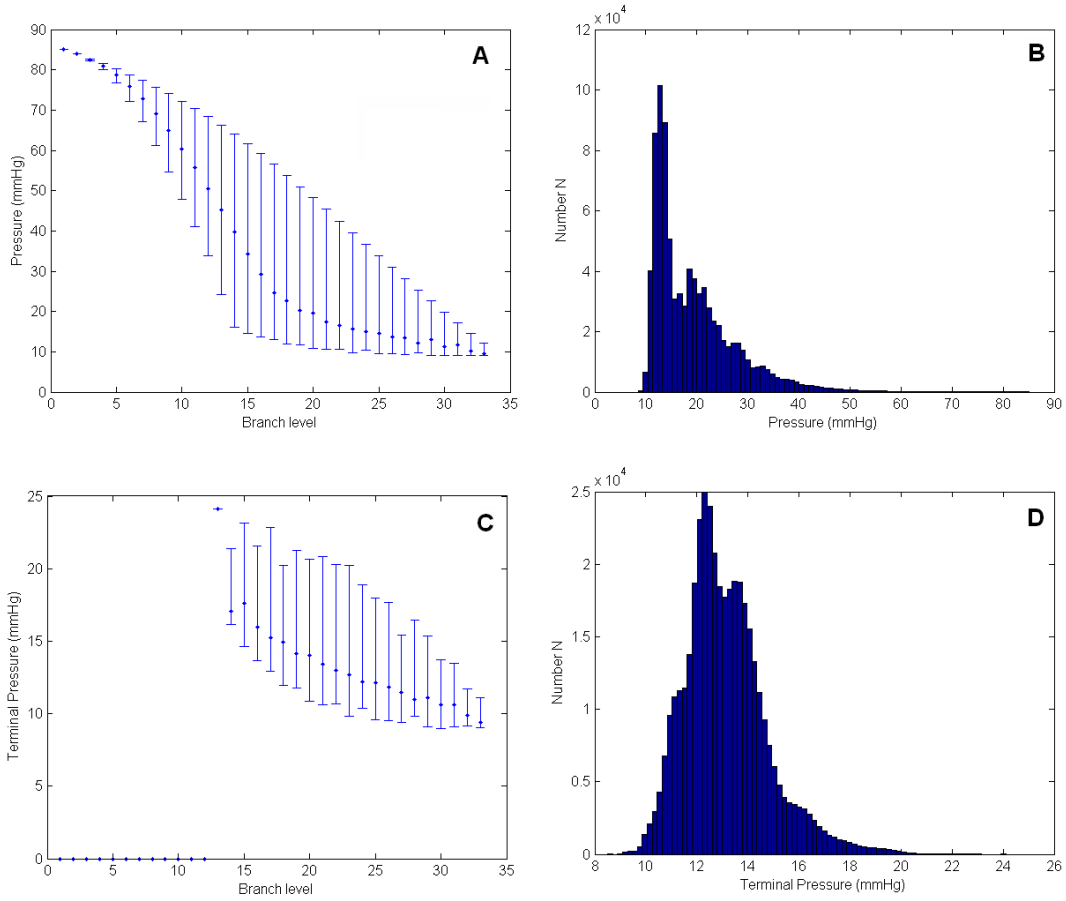

Figure 8.108 Pressures at the binary arterial tree nodes. A) Average pressure (dots) of all vessels per branching level with maximum and minimum values (bars). B) Pressure distribution of all vessels. C) Average pressure (dots) of terminal vessels per branching level with maximum and minimum values (bars). D) Pressure distribution of terminal vessels.

8.4.1.4 Flowrates

The blood flowrate through each of the vessels in the binary arterial tree was calculated as described in Section 7.1.2. Figure 8.109 shows the average flowrate at each branching level considering all vessels (A) and terminal vessels only (B). The flowrate through the smaller vessels in the arterial tree becomes very small due to the high total number of vessels in that tree. Figures 8.109 (C) shows the distribution of the flowrates through the terminal vessels of the tree. There is a high occurrence at 0.3-1.5 $\times 10^{-5}$ $ml\ s^{-1}$ due to the high number of terminal vessels which account for almost half of the binary arterial tree.

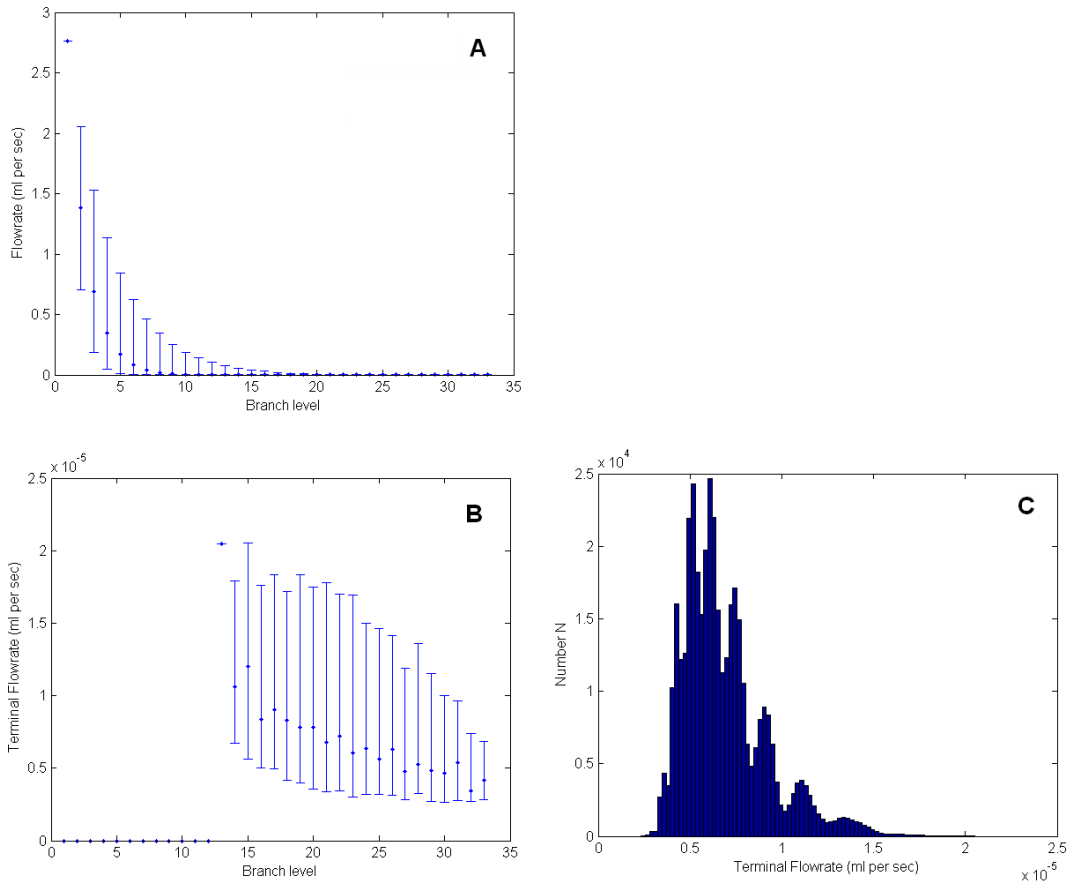

Figure 8.109 Flowrates through the binary arterial tree vessels. A) Average flowrate (dots) of all vessels per branching level with maximum and minimum values (bars). B) Average flowrate (dots) of terminal vessels per branching level with maximum and minimum values (bars). C) Flowrate distribution of terminal vessels.

8.4.1.5 Wall shear stress

The wall shear stress (WSS) in the vessels of the arterial tree was calculated using two formulae. First, using the Hagen-Poiseuille equation, which is the general equation used to calculate the wall shear stress. Second, using Lipowsky et al.'s equation generated from experiments studying the vasculature of the cat mesentery [77]. The two methods were discussed in Section 7.3.7 and presented in Equations 7.52 and 7.53. Figure 8.110 shows the average WSS at each of the branching levels and the distributions for all vessels in the tree using both methods. Figure 8.111 shows the same plots for the terminal vessels only. Both figures clearly indicate that there is a significant drop in the WSS values when using Lipowsky equation; however, the values are still much higher than what is expected physiologically, which have an average of 5 Pa and a maximum of 20 Pa.

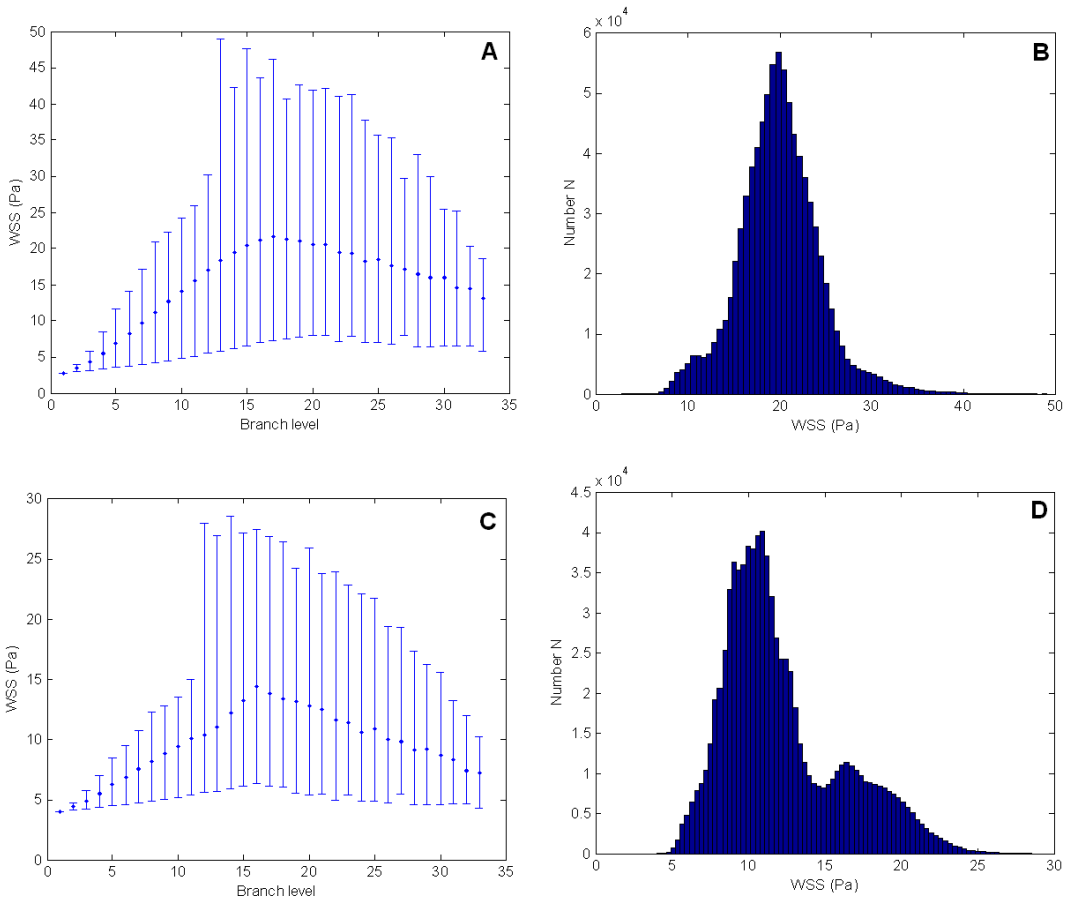

Figure 8.110 A) Average WSS (dots) of all vessels per branching level using Hagen-Poiseuille equation with maximum and minimum values (bars). B) WSS distribution of all vessels using Hagen-Poiseuille equation. C) Average WSS (dots) of all vessels per branching level using Lipowsky equation with maximum and minimum values (bars). D) WSS distribution of all vessels using Lipowsky equation.

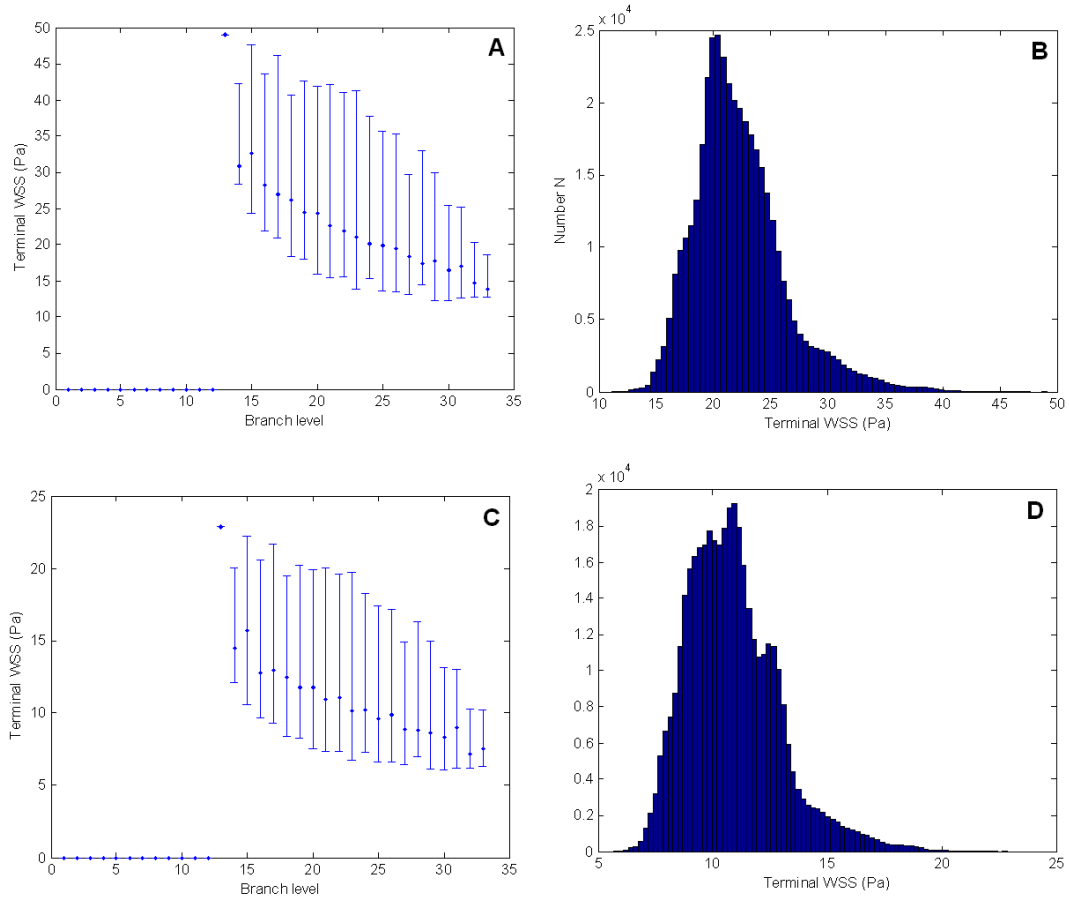

Figure 8.111 A) Average WSS (dots) of terminal vessels per branching level using Hagen-Poiseuille equation with maximum and minimum values (bars). B) WSS distribution of terminal vessels using Hagen-Poiseuille equation. C) Average WSS (dots) of terminal vessels per branching level using Lipowsky equation with maximum and minimum values (bars). D) WSS distribution of terminal vessels using Lipowsky equation.

8.4.2 Autoregulation

The myogenic mechanisms used to model the autoregulation behavior was implemented and tested before the metabolic autoregulation mechanisms. First, the results obtained by Gonzalez-Fernandez and Ermentrout [44] were reproduced. The hoop stresses acting on the cylindrical element inside the vessel wall described in Section 7.3.5 are shown in Figure 8.112. The response using the myogenic equations produced an oscillatory response as in Figure 8.113.

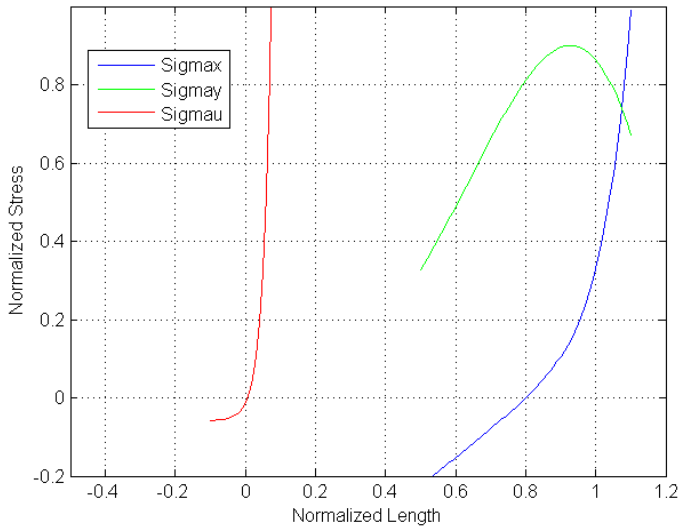

Figure 8.112 Normalised hoop stress of the components of the cylindrical element as a function of the components' normalised lengths.

The radius as a function of the transmural pressure was developed by Hannah Farr [37] using the non-dimensional equations discussed in Section 7.3.6. The response was implemented using different sizes of inner to outer radius ratios (R_r) as presented in Figure 8.114. Note that x is the average circumference of the vessel. Physiologically, the vessels' R_r varies between 0.5-0.7 depending on the radius size of the vessel. However, in order to simplify the non-dimensional myogenic mechanism, all vessels in the tree were assumed to have the same R_r value of 0.6. The plots correlate well with the results by Gonzalez-Fernandez and Ermentrout [44] where there is a passive dilation of the arterial wall at very low transmural pressure followed by an active contraction as the pressure increases.

The combined dimensionless myogenic and wall shear stress response for different values of β_e is shown in Figure 8.115. The β_e value of 1×10^{-4} was used here (see [29] for further detail regarding the value of β_e). The wall shear stress was assumed to be 1 Pa in this plot.

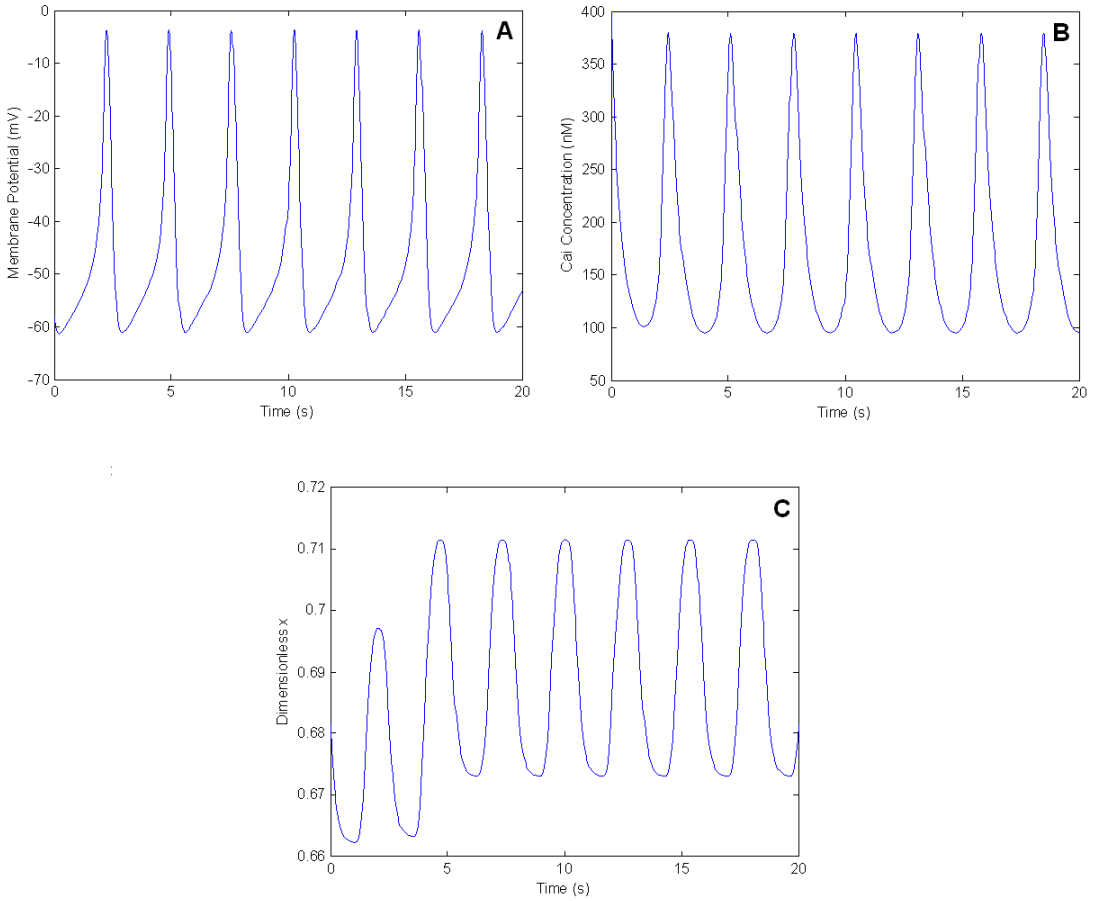

Figure 8.113 A) Membrane voltage. B) Free cytosolic calcium concentration. C) Dimensionless x.

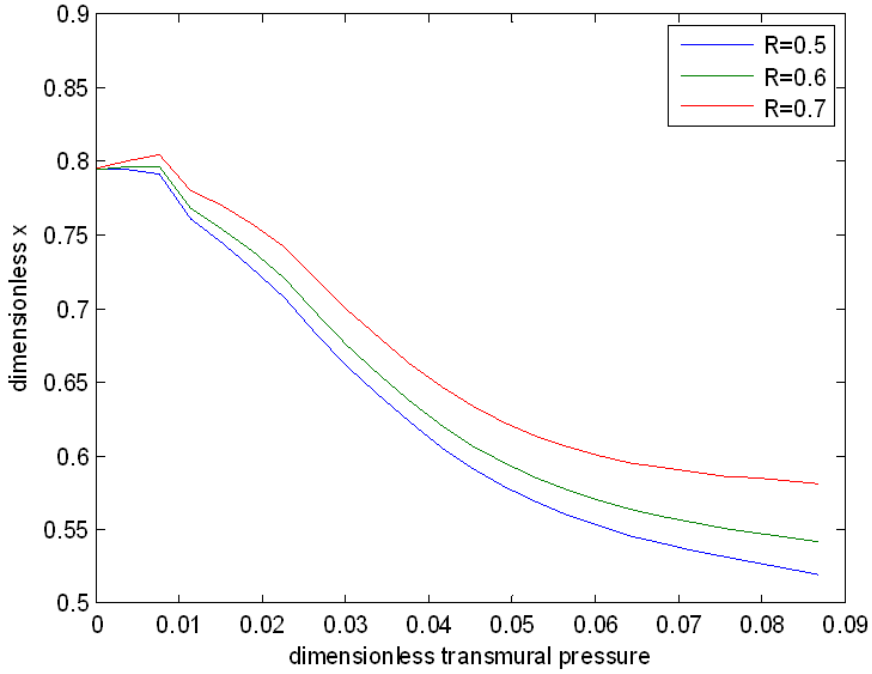

Figure 8.114 Dimensionless plot for the myogenic response for vessels with $R_r = 0.5$, 0.6 and 0.7 [37].

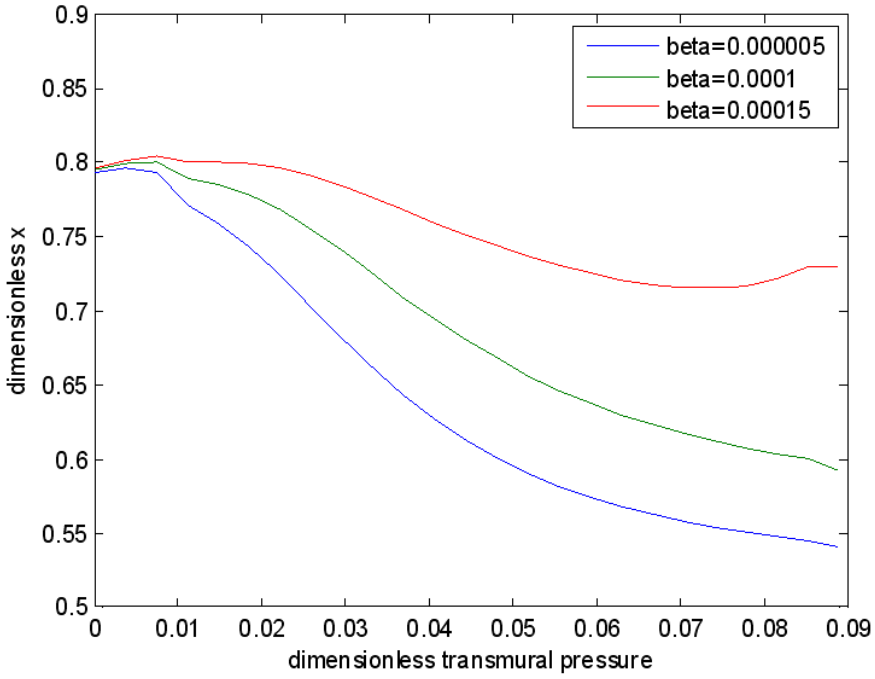

Figure 8.115 Effect of β_e on dimensionless myogenic and shear stress response [37].

The variation in the dimensionless response for the physiological range of wall shear stress is shown in Figure 8.116. These results were stored as a 3D look-up table consisting of non-dimensional x versus pressure and wall shear stress as shown in Figure 8.117. The look-up table was used in implementation of myogenic-forced autoregulation.

The myogenic mechanism was implemented in the binary arterial tree as presented in Section 7.5. It was set to be active in *all* vessels of the MCA arterial binary tree. Figure 8.118 shows the flowrate response as a result of a 20 mmHg drop in the inlet pressure. First, new pressures throughout the nodes of the tree are calculated. The myogenic mechanism is activated by using the 3D look-up table, which produces new values for the vessels' radii, and hence, new resistance. The flowrate is then calculated based on the new resistance of the tree. This process is repeated until the flowrate value converges after several iterations.

The autoregulation plot of flowrate perfusing the brain tissue supplied by the MCA arterial tree is presented in Figure 8.119. The ideal autoregulation (black line in Figure 8.119) should be achieved in the pressure range of 50 - 150 mmHg. If the vasculature has no autoregulation function, the response would be linear (red line). The influence of the myogenic mechanism on the autoregulating function was small as shown in the plot (blue line). This is because most of the arterioles, which account for the majority of resistance, have very low pressures. This results in very small changes in radii in those vessels when using the myogenic look-up table (see Figure 8.117) to implement autoregulation. The

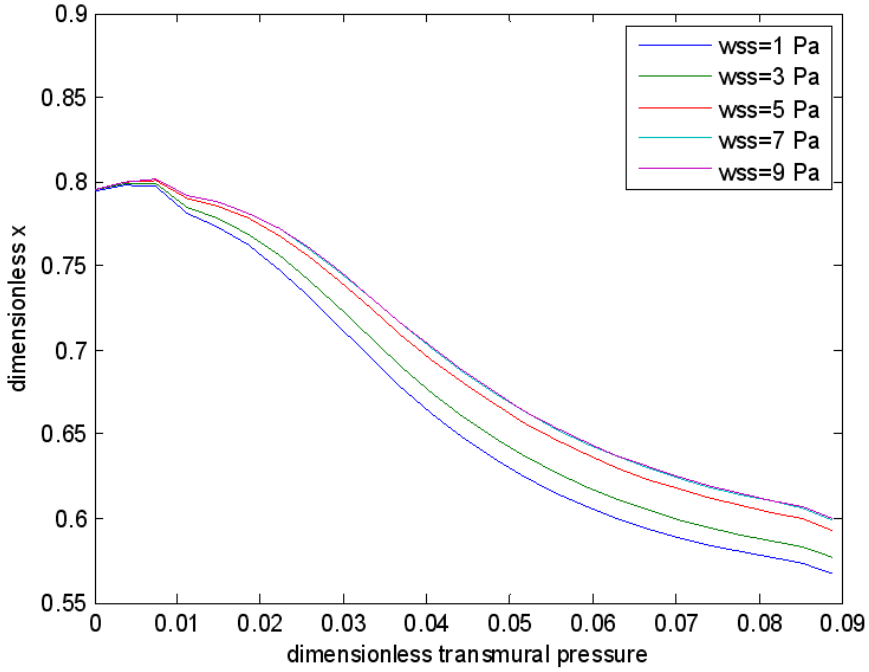

Figure 8.116 Dimensionless myogenic and shear stress response for WSS = 1-9 Pa [37].

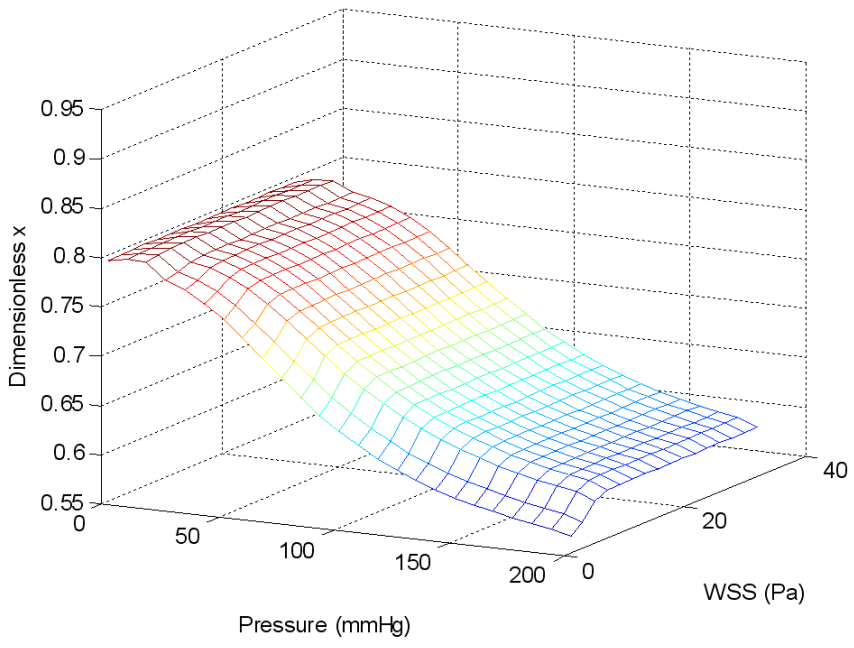

Figure 8.117 Myogenic response 3D plot.

vessels in the arterial tree with larger vessels experience high pressure values which decline dramatically as the tree branching level increases as shown in Figure 8.108. Even though these vessels will become very active under myogenic autoregulation, they contribute very little to the total resistance of the tree as presented earlier in Figure 8.105. The tree's resistance using the myogenic algorithm as a function of systemic pressure is shown in Figure 8.120, where the ideal behavior of the tree's resistance to maintain autoregulation and no autoregulation behavior are also plotted.

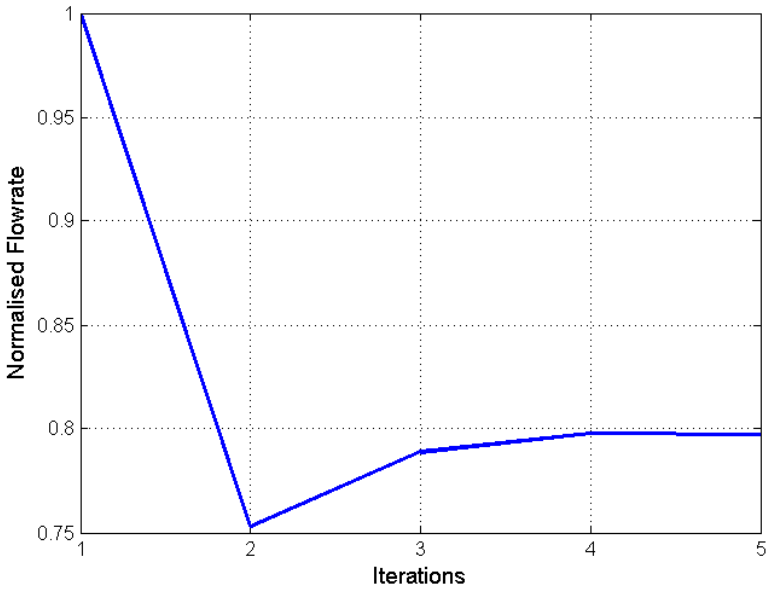

Figure 8.118 Flowrate response as a result of 20 mmHg drop in inlet pressure using myogenic mechanisms.

Figure 8.121 was plotted to give an indication of how much the arterioles are required to change their radii in order to achieve the ideal autoregulation. The arterioles tested here were in the range of $10 - 50\ \mu m$, as these are the ones which induce most of the change in resistance as presented above (Figure 8.106). The changes required cannot be achieved using the current myogenic mechanisms due to the low pressures experienced by arterioles with this radius range. As a result, the metabolic algorithm was substituted for the myogenic one.

The metabolic response of a vessel's radius was solved using the two ODEs presented in Section 7.2. The response as a function of disturbance in cerebral flowrate is shown in Figure 8.122. This result provided a look-up table consisting of non-dimensional x versus pressure, which was used in implementing the metabolic autoregulation.

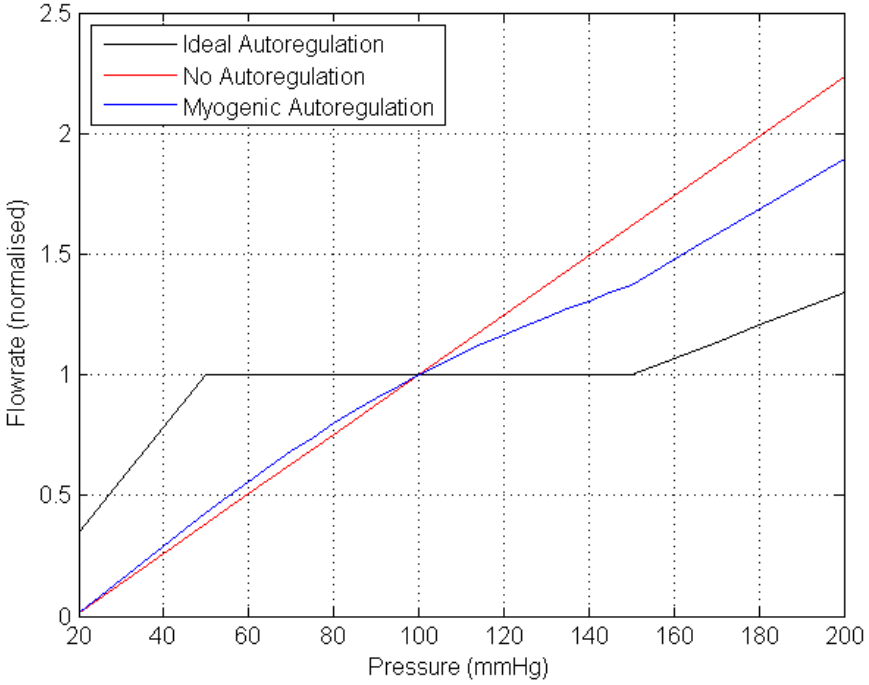

Figure 8.119 Autoregulation plots for the cerebral mass perfused by the MCA presenting ideal (black), myogenic (blue), and no (red) autoregulation.

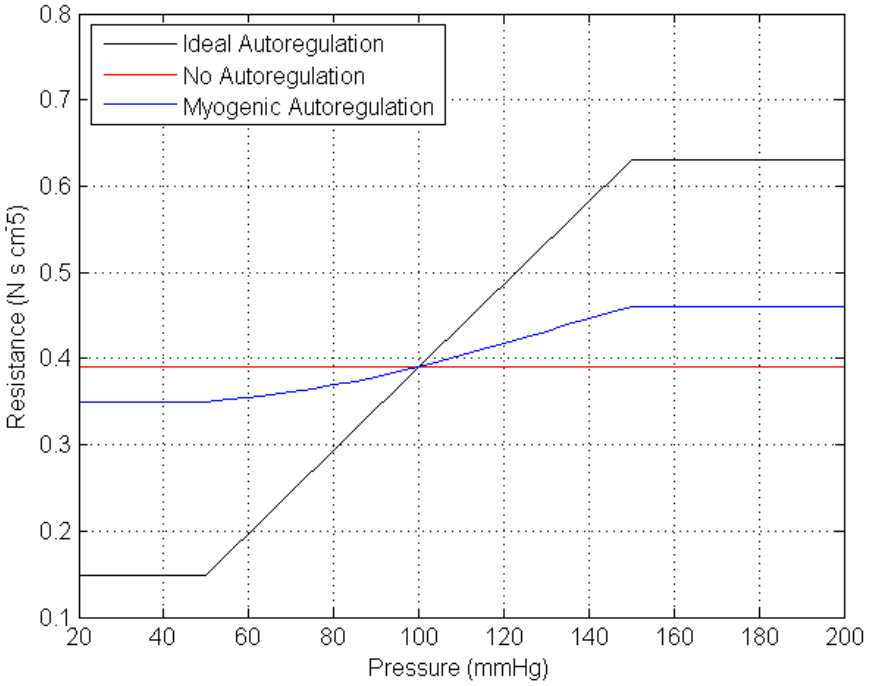

Figure 8.120 Resistance plots of the MCA vasculature for the ideal (black), myogenic (blue), and no (red) autoregulation.

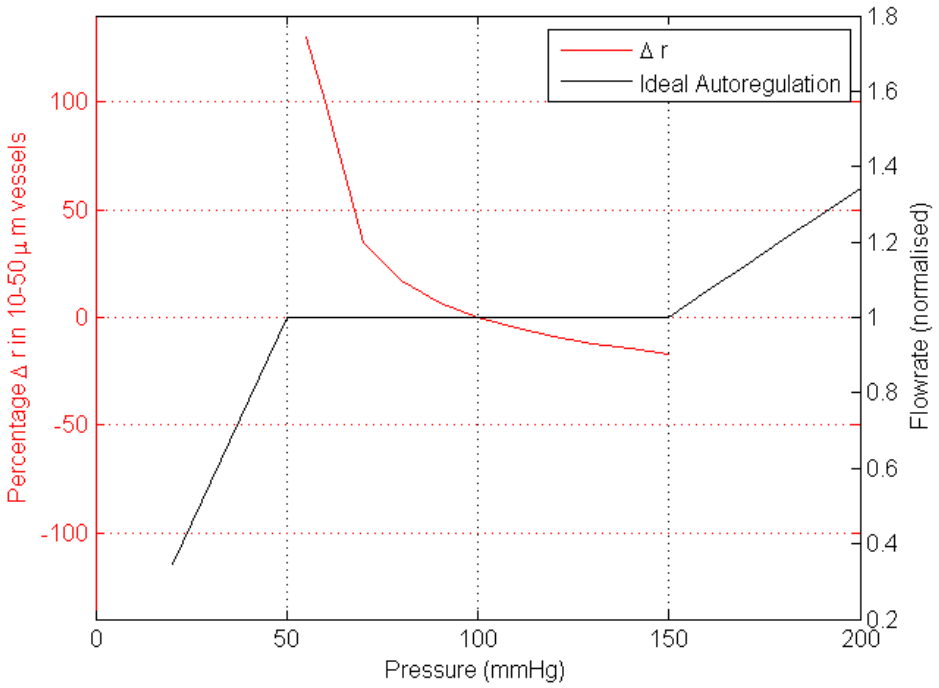

Figure 8.121 The percentage changes in the 50 μm radius arterioles to achieve ideal autoregulation.

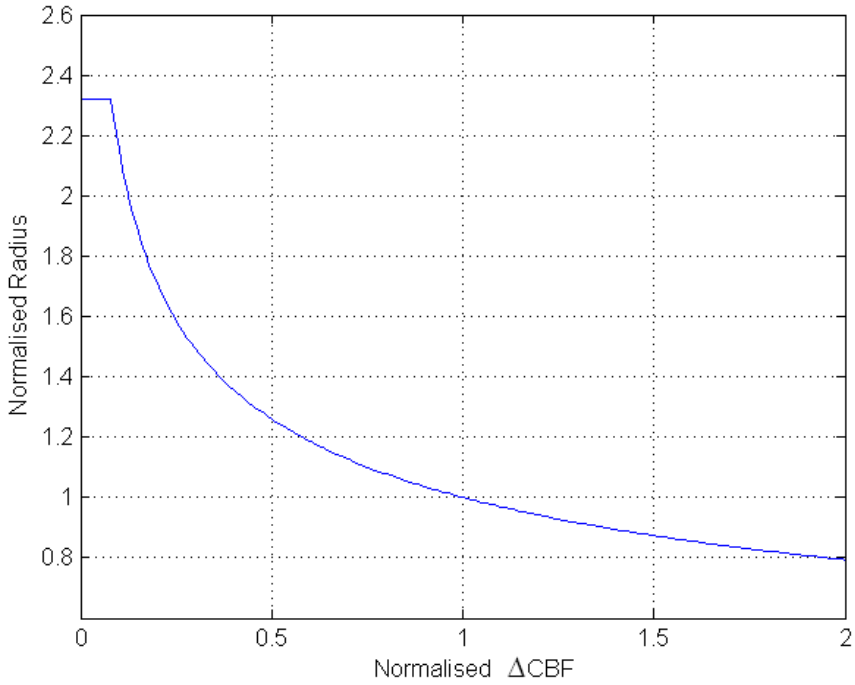

Figure 8.122 The dimensionless radius response as a function of cerebral blood flow using the metabolic mechanisms.

The metabolic mechanism was implemented in the binary arterial tree as presented in Section 7.5. It was set to be active in the $10-50\ \mu m$ radius vessels of the MCA arterial binary tree. The autoregulation plot of flowrate perfusing the brain tissue supplied by the MCA arterial tree is presented in Figure 8.123. The arterial tree resistance for the autoregulation range is shown in Figure 8.124. For each systemic pressure, the flowrate was calculated similarly to the myogenic implementation described above. The metabolic mechanism is activated by using the look-up table, which produces new values for the vessels' radii and the tree's resistance. This process is repeated until the flowrate value converges after several iterations. Figure 8.125 shows the flowrate response as a result of a 20 mmHg drop in inlet pressure.

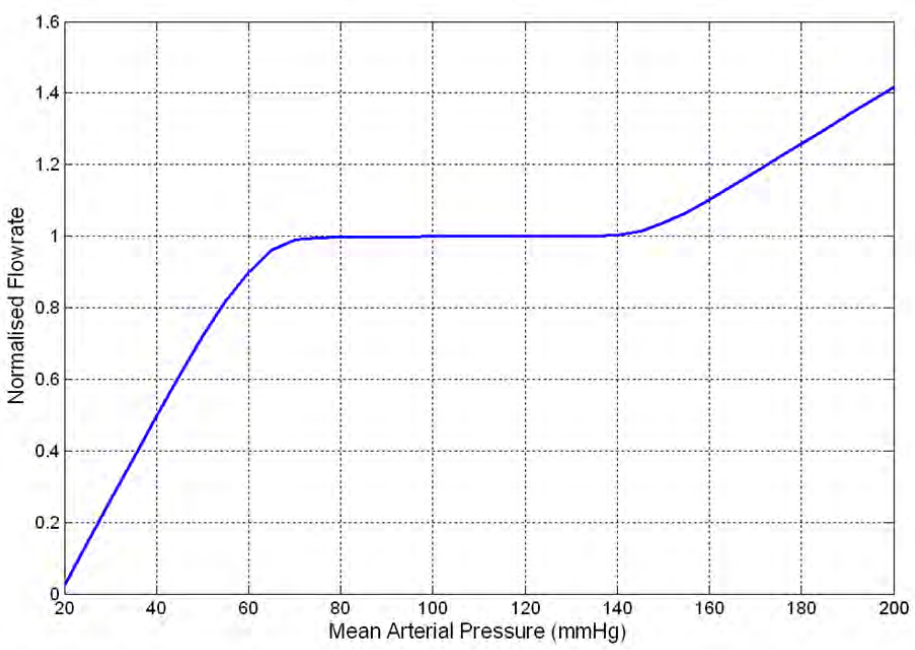

Figure 8.123 Autoregulation plot for the cerebral mass perfused by the MCA using metabolic mechanisms.

Figures 8.123 and 8.124 show that the autoregulation function was produced by using the correct tree resistance achieved through the variations in the vessels' radii. The upper and lower limits of autoregulation were maintained through defining a maximum and minimum limits of radius change, which were set to 230% and 80% respectively. These percentages were chosen by trial and error to try achieve the autoregulation limits at 50 and 150 mmHg respectively. The lower limit of autoregulation in Figure 8.123 does not occur at the expected pressure of 50 mmHg. This is because no matter how much the $10-50\ \mu m$ radius vessels dilate above the 230% limit, the tree's resistance fails to decrease low enough to maintain the autoregulation at that pressure. Vessels in the arterial binary tree with radius bigger than $50\ \mu m$ need to be incorporated when implementing the metabolic mechanism.

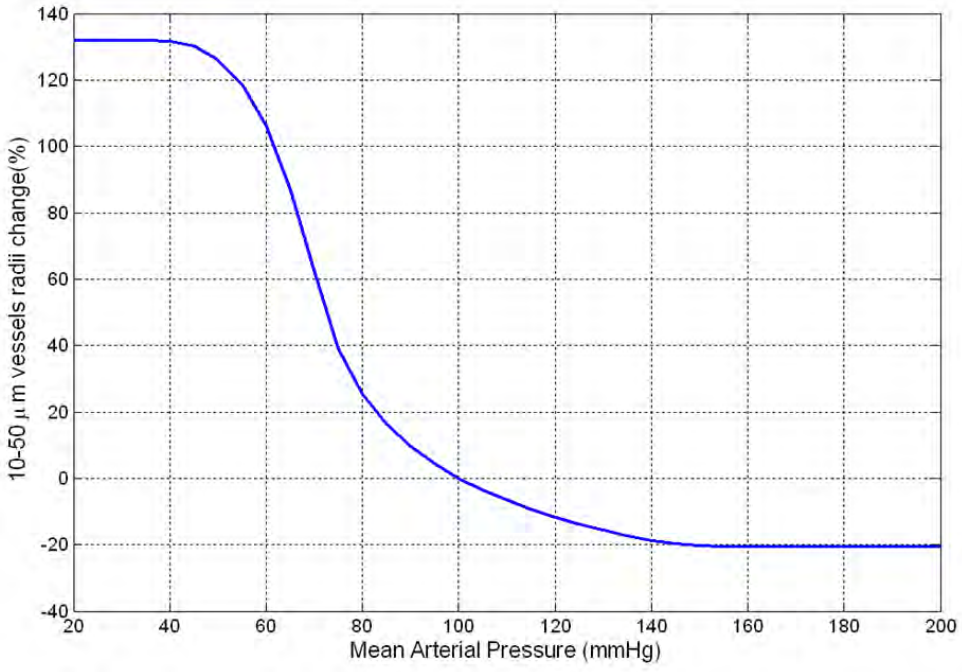

Figure 8.124 resistance plot for the cerebral mass perfused by the MCA using metabolic mechanisms.

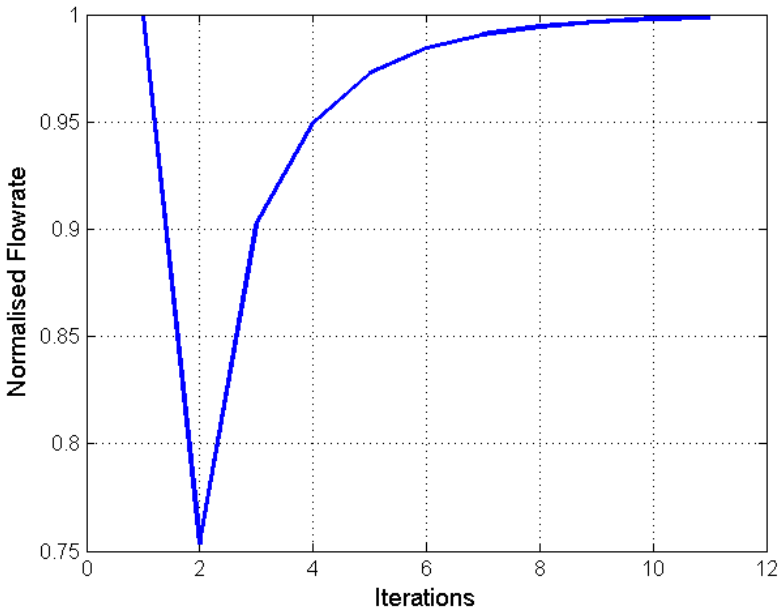

Figure 8.125 Flowrate response as a result of 20 mmHg drop in inlet pressure using metabolic mechanisms.

8.4.3 Oxygen Diffusion

The above results for the metabolic mechanism were executed while maintaining the metabolic rate of oxygen consumption ($CMRO_2$) as a constant (called $CMRO_{2,\ sp}$). The metabolic response presented in Figure 8.122 was re-calculated for different values of $CMRO_2$, defined as a factor ε multiplied by $CMRO_{2,\ sp}$. The response for the different ε values ranging from 0.1 to 5 is shown in Figure 8.126.

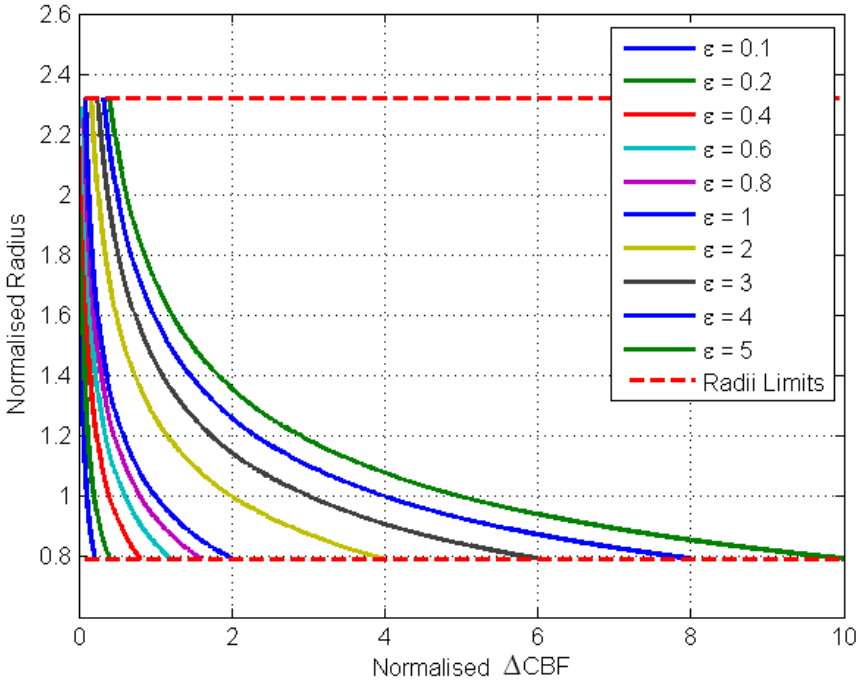

Figure 8.126 The metabolic response plots for different values of $CMRO_2$.

The different values of the $CMRO_{2,\ sp}$ were tested in a smaller binary arterial tree with root vessel radius size of 100 μm. Part of the cerebral tissue supplied by a section of the arterial tree was set to have the new $CMRO_2$ (which is a function of ε and $CMRO_{2,\ sp}$), while the rest of the cerebral tissue supplied by the rest of the arterial tree is set to have the normal metabolic rate $CMRO_{2,\ sp}$ (see Figure 8.127). This to model local change in neuronal activity in parts of the brain, which will experience an increase or decrease in the metabolic rate of oxygen consumption.

The tree with two different $CMRO_2$ values was tested under a 20 mmHg pressure drop for different values of ε. Due to the having different values of $CMRO_2$ in part of the tree, the vessels' radii response will differ. The radii distribution for the metabolically active vessels was plotted as shown in Figure 8.128.

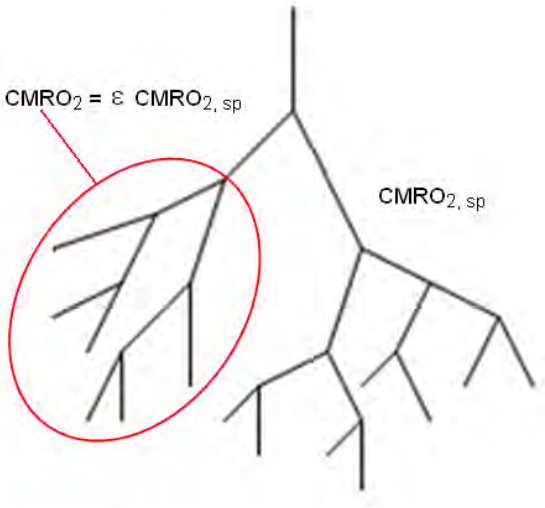

Figure 8.127 The binary arterial tree with two different $CMRO_2$ values.

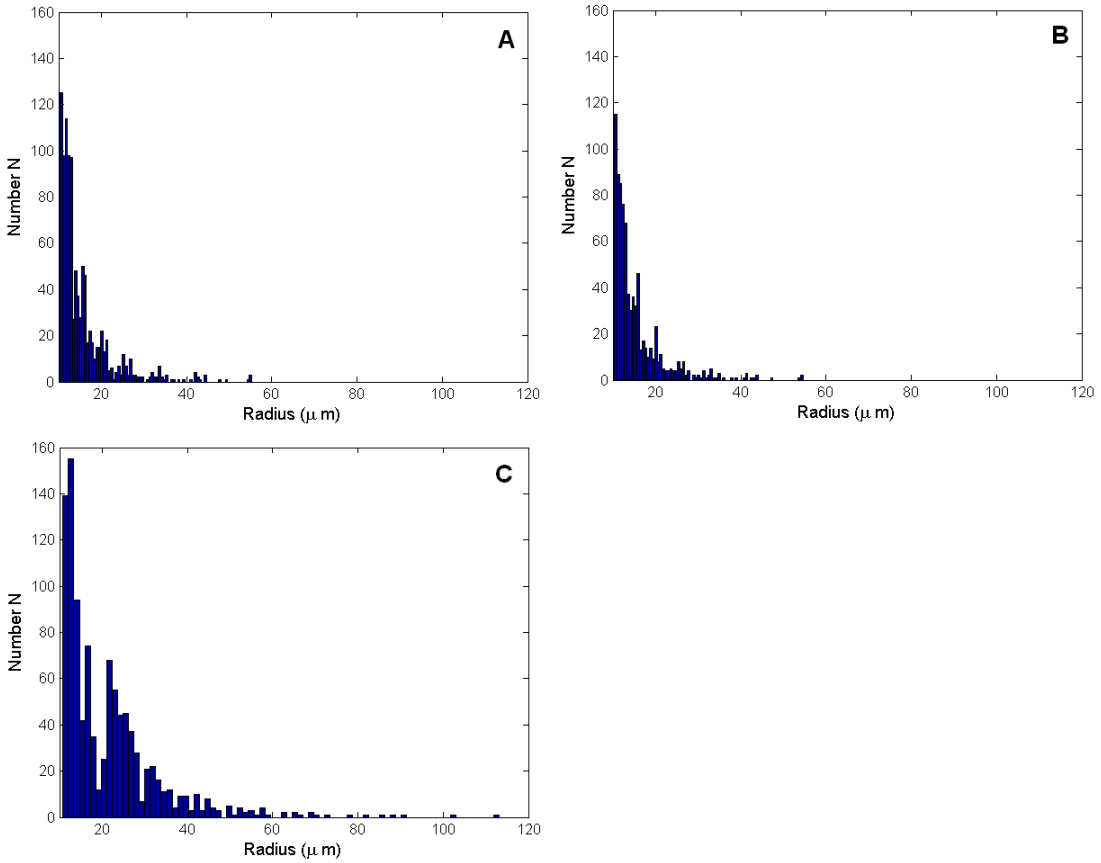

Figure 8.128 Radii distribution of metabolically active vessels in the small binary arterial tree with A) $\varepsilon = 1$, B) $\varepsilon = 0.1$ and C) $\varepsilon = 5$.

The statistical properties of the radii distributions is presented in Table 8.7. The results show that as the value of $CMRO_2$ increases, the vessels' radii need to dilate more to allow for more blood flow reach the cerebral tissue, which is what is expected physiologically.

Table 8.7 *Statistics of arterial binary tree as a result of changing the $CMRO_2$ in a small section of it.*

ε	**Mean**	**Median**	**Mode**	**S. D.**	**Skewness**	**Kurtosis**
0.1	13.95	12.29	8.72	6.29	2.50	11.81
0.2	13.95	12.29	8.72	6.29	2.50	11.81
0.4	13.91	12.22	7.43	6.22	2.53	11.90
0.6	14.60	12.60	8.56	6.28	2.61	12.02
0.8	15.12	12.86	9.55	6.37	2.64	11.99
1	15.61	13.07	10.36	6.53	2.65	11.96
2	18.10	15.76	10.59	8.30	2.61	12.83
3	20.71	17.04	25.48	11.24	2.58	13.65
4	21.20	17.64	25.48	11.63	2.51	13.00
5	21.55	17.70	25.48	12.00	2.49	12.79

Finally, when running the arterial tree MATLAB code, the oxygen diffusion is calculated by assuming that the cerebral tissue supplied by the MCA is divided into cylinders. Each tissue cylinder is supplied only by the capillary that it surrounds. The oxygen transport in the cerebral tissue was adopted from the work of McGuire et al. [83] as presented in Section 7.4. The oxygen partial pressure (PO_2) profile in the blood traveling a single capillary is shown in Figure 8.129.

The radial oxygen diffusion inside the tissue surrounding the capillary is presented at different points along the capillary in Figure 8.130, where Figure 8.131 shows the points along the capillary. These plots correlate well with McGuire et al.'s results.

An example of the oxygen profile in a small volume is shown in Figure 8.132 where the tissue is divided up into a number of cylinders aligned in parallel. The total oxygen consumption by the cerebral tissue supplied by the MCA was calculated to be 0.396 $mL\ O_2\ s^{-1}$. This is within the expected physiological data for the oxygen demand by the cerebral mass.

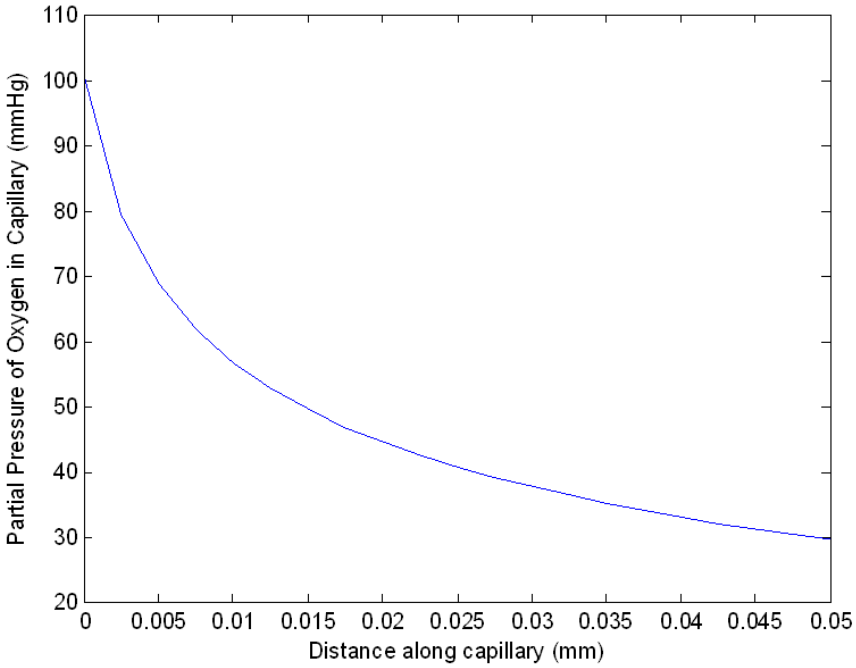

Figure 8.129 PO_2 profile in the blood stream.

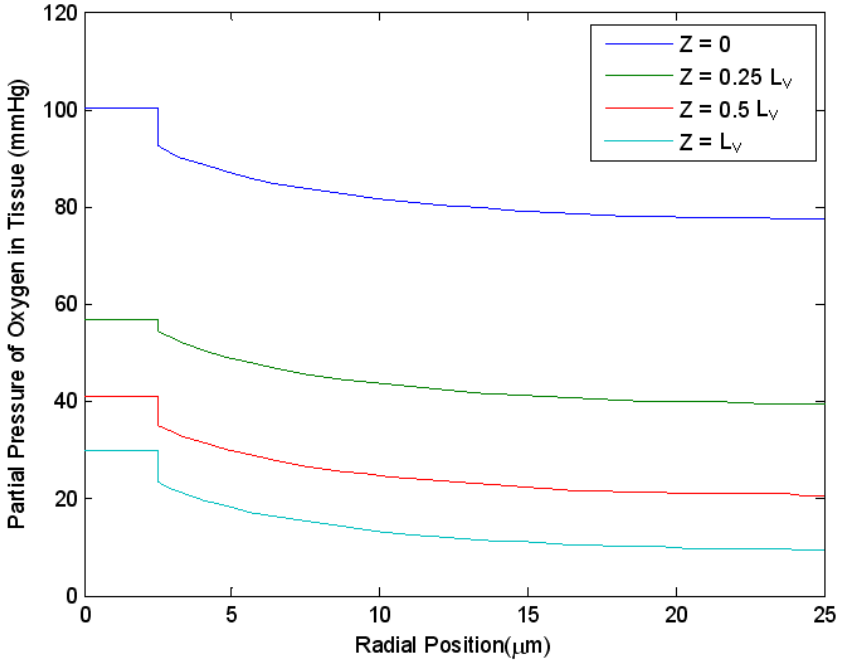

Figure 8.130 Tissue PO_2 radial profile at several points along the capillary.

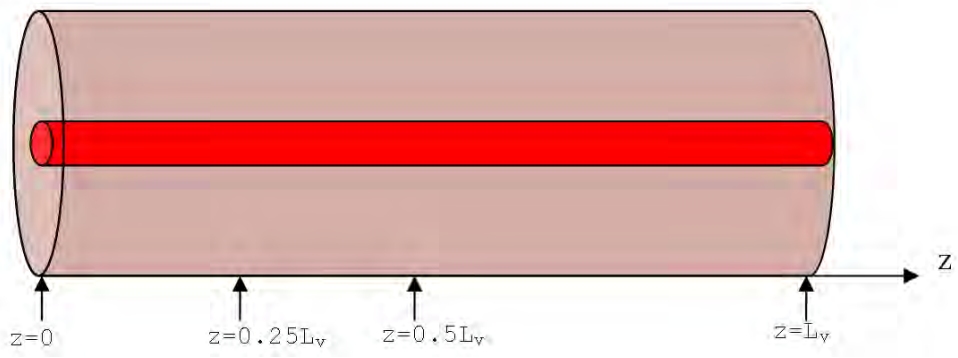

Figure 8.131 The capillary with tissue cylinder surrounding it.

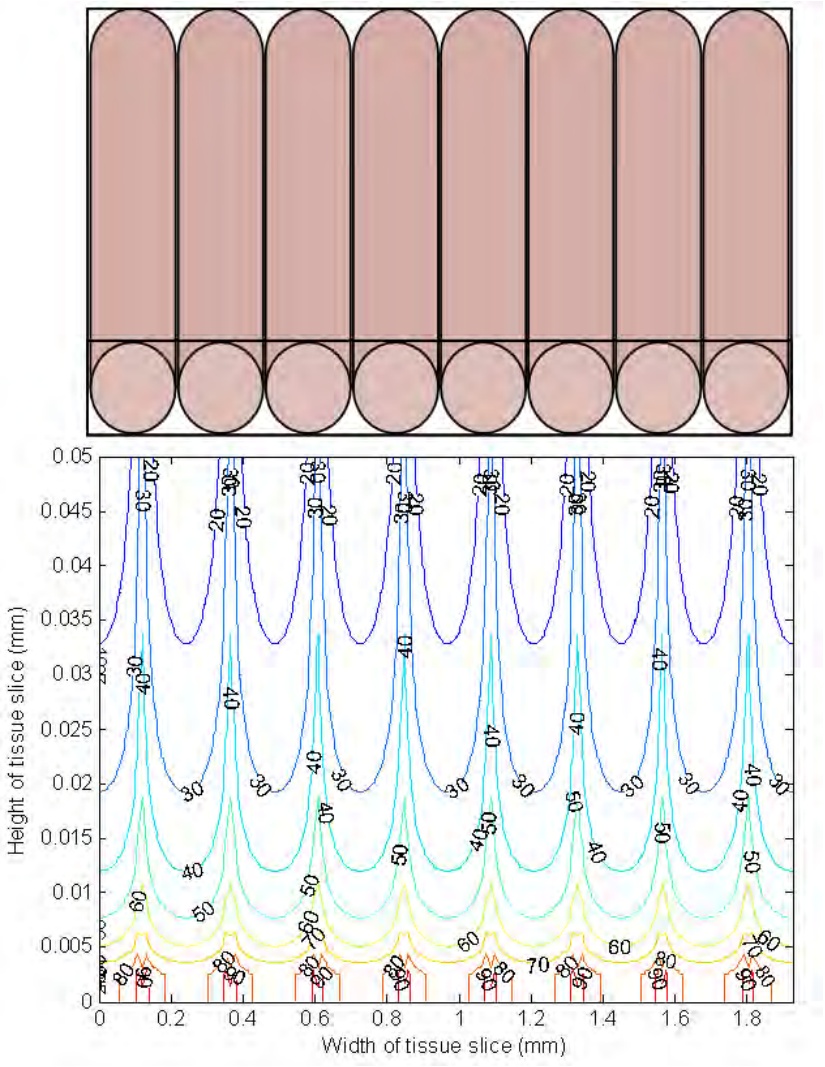

Figure 8.132 PO_2 profile for a small tissue volume.

Chapter 9

Graphical User Interface (GUI)

In order for the mathematical CoW models created from this research to become a useful tool for clinicians, results should be presented in a manner that can be recognized easily. A graphical user interface (GUI) had been generated using MATLAB to take input data and visualise results and information about the blood flow in the vessels and blood delivery to the cerebral mass. The GUI was designed to be used by clinicians or programmers to interact with the MATLAB code of the CoW models, setting parameters and entering inputs, without dealing with or changing the code itself.

There were several versions of the CoW GUI developed by different individuals in the Brain Group at the Centre of Bioengineering of the University of Canterbury. The first was based on the non-linear CoW model with metabolic model described in Chapter 6. The CoW model consisted of 27 vessels with 14 nodes. The vessels were represented as lines and the nodes as small circles in the GUI, where the lines and the small circles have the property to change colour according to the values of flowrates and pressure respectively. The width of the lines in the GUI represent the diameter of the CoW's vessels relative to the ICA diameter. When the GUI is launched, the window shown in Figure 9.1 is displayed with all the vessels and nodes values are set to zero.

The GUI provides for inputs at the right hand side of the image to run and control the simulation. Figure 9.2 shows the control panel where the user is able to start the simulation after setting the simulation parameters, pause the simulation anytime during running and then resume it, reset the parameter setting, or exit the GUI. The parameters panel shown in Figure 9.3 displays the flowrate, pressure and time inputs which can be set by the user. The colour of the flowrates of the CoW vessels displayed in the GUI can be presented as the absolute value of the flowrates, or values relative to the normal flowrates through these vessels. The mean arterial pressure (MAP) can be defined as a step change from one value to another which changes at a specific time. The pressure can also be defined by an array set as a function of time which is saved in a separate file before starting up the GUI. The time parameters including start time, finish time and time step can be set to default or be set by the user. The CoW geometry

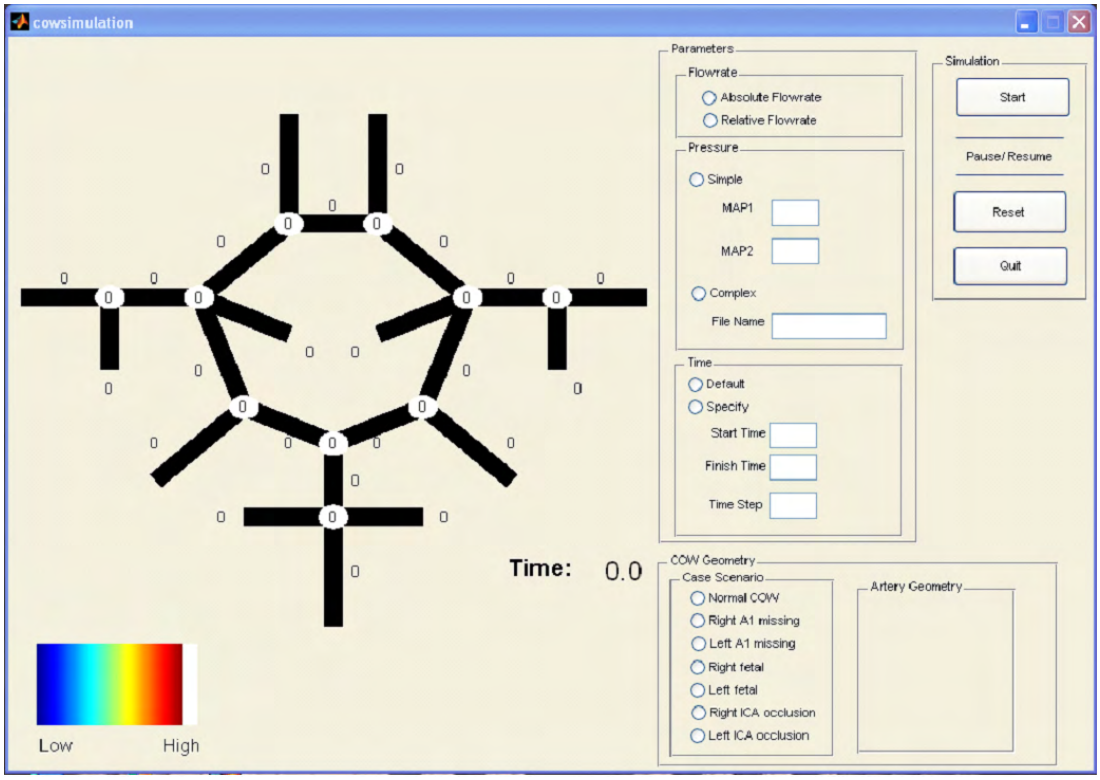

Figure 9.1 The GUI, version one, when it is launched.

panel shown in Figure 9.4 allows the user to define the anatomical variations that might be present in a patient's CoW such as a missing ACA1 segment or a fetal case. The user can also introduce an ICA occlusion at a specified time of running the occlusion to model different kinds of pathological conditions.

When the parameters are set using the GUI and the simulation is started, the MATLAB code is run in the background. The GUI interacts with the CoW model, which calculates the flowrates in 27 vessels and the pressure in 14 nodes in the CoW. There were 10 efferent arteries out of the total 27 arteries of the CoW. The matrix equation defined in Chapter 4 is solved with A of size 41×41. The SPECT colour scale was used for colour mapping, which ranges from dark blue (representing low values) to light blue, green, yellow, orange, red and then dark red (representing low values). The white colour was added to the colour range to represent extremely high values. Presenting results on terms of colour helps modellers understand the results generated more easily. The CoW diagram is updated at each time step by updating the colour of lines representing the flow rates in the arteries, and the nodes representing the pressure values. The actual values of flow rates and pressures are also represented by the numbers next to the lines and nodes. Also, time is updated at each time step as shown in the GUI window.

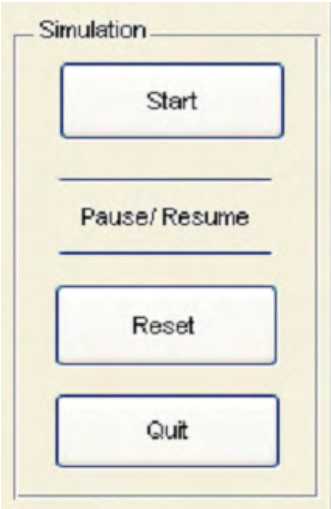

Figure 9.2 The control panel of the GUI.

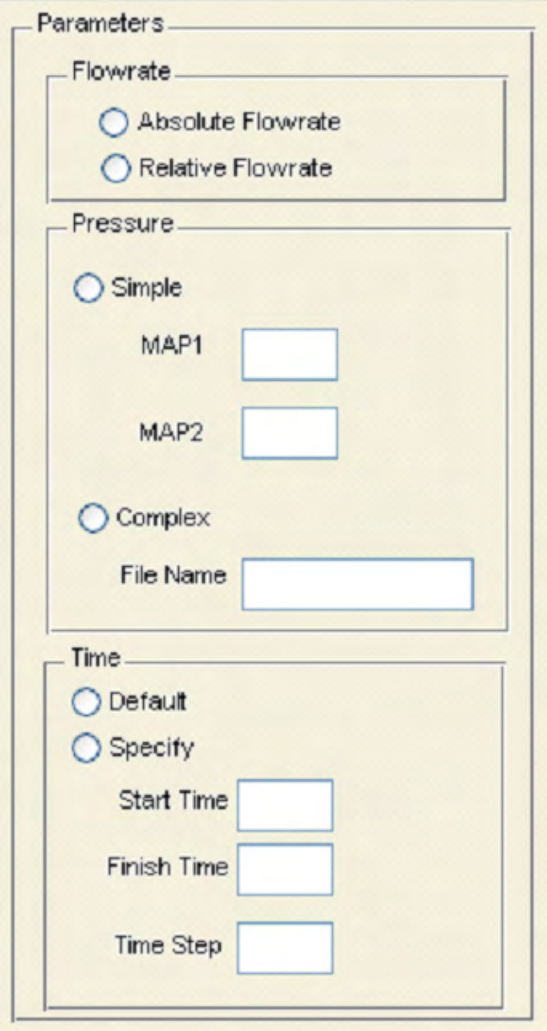

Figure 9.3 The parameters panel of the GUI.

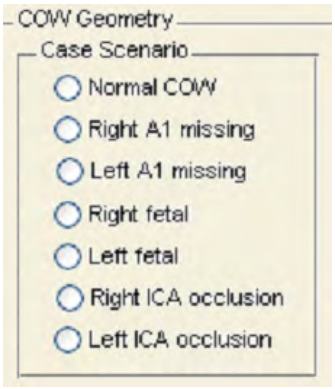

Figure 9.4 The CoW specification panel of the GUI.

Figure 9.5 shows the GUI while running a simulation for a classical complete CoW configuration under normal pathological conditions. When starting the simulation, the width of the lines representing the CoW vessels has changed compared to the CoW representation before a simulation was run. Figures 9.6 shows the GUI while running a simulation for a specific clinical scenario: missing left ACA1 segment with a contralateral (right) ICA occlusion occurring at half time. The right ICA in this figure has dropped to zero indicating the occlusion. As a result, the flowrates in the different vessels of the CoW has been affected greatly where the BA flowrate has increased (changing the vessel's colour from light blue to orange) to be able to sustain the same amounts of blood flow to the efferent arteries. Subsequently, the flowrates throw the right PCA1 and PCoA has changed value, and their lines changed colour in the GUI when compared to Figure 9.5. The pressure values have also dropped on the right side of the CoW as a result of the ICA occlusion.

This GUI was further developed in two stages by the Brain group at the University of Canterbury. First by Iain McIver, and then by Fabian Herzog [56, 84]. McIver added the visualisation of blood flow delivery to the different lobes of the cerebral mass. The efferent arteries of the CoW were also changed by introducing the smaller vessels to the vascular network, which branch off the main efferent arteries. Instead of having the original 10 efferent arteries, there were 38 smaller efferent arteries. Each ACA2 segment had 8 distal vessels and each MCA segment had 9 distal vessels. The total number of vessels in the network was 81. The vasculature was described as a system of equations similarly to version one. Each of the new smaller efferent arteries were represented by a variable resistance. The GUI developed by McIver allowed the user to view results in arteries or cerebral lobes. The user had the option of viewing results in some or all of the cerebral lobes. The GUI also maintained the original options available to the user. The SPECT colour scale was used for both the arteries' flowrates and the flow to the lobes. The colour of the lines representing the arteries in the GUI changed from dark blue, indicating low blood flow, to dark red, representing high blood flow. The

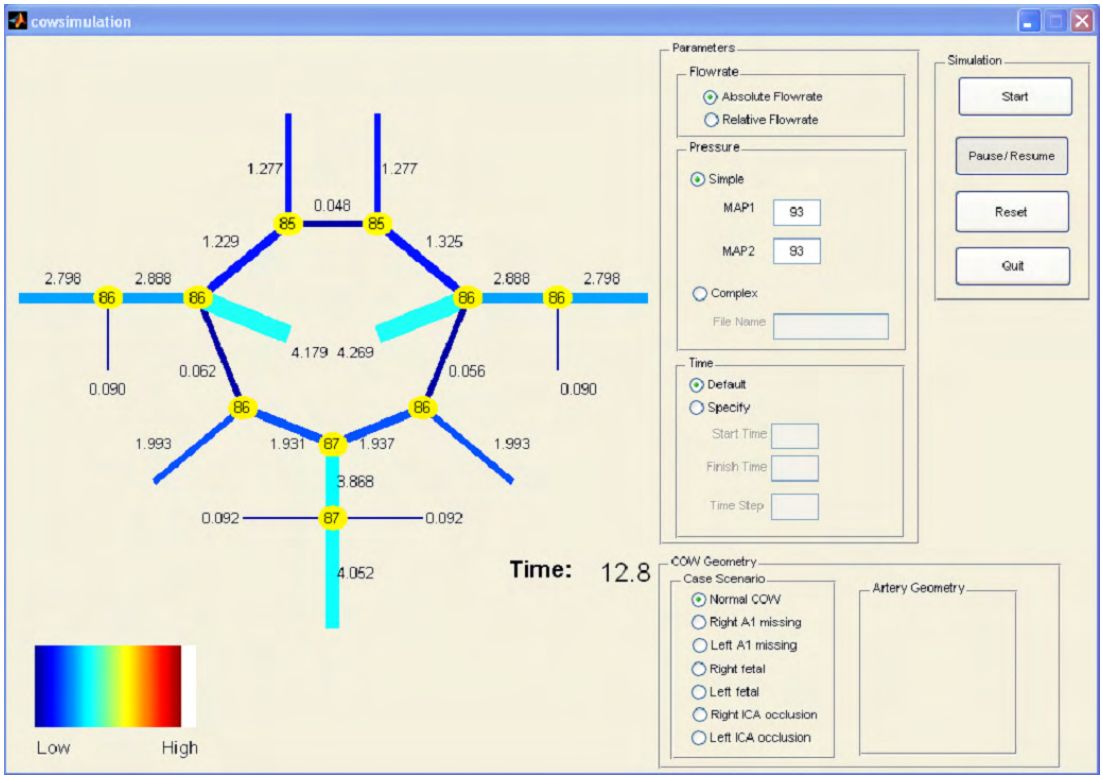

Figure 9.5 Running a simulation using the GUI with a classical complete CoW under normal conditions.

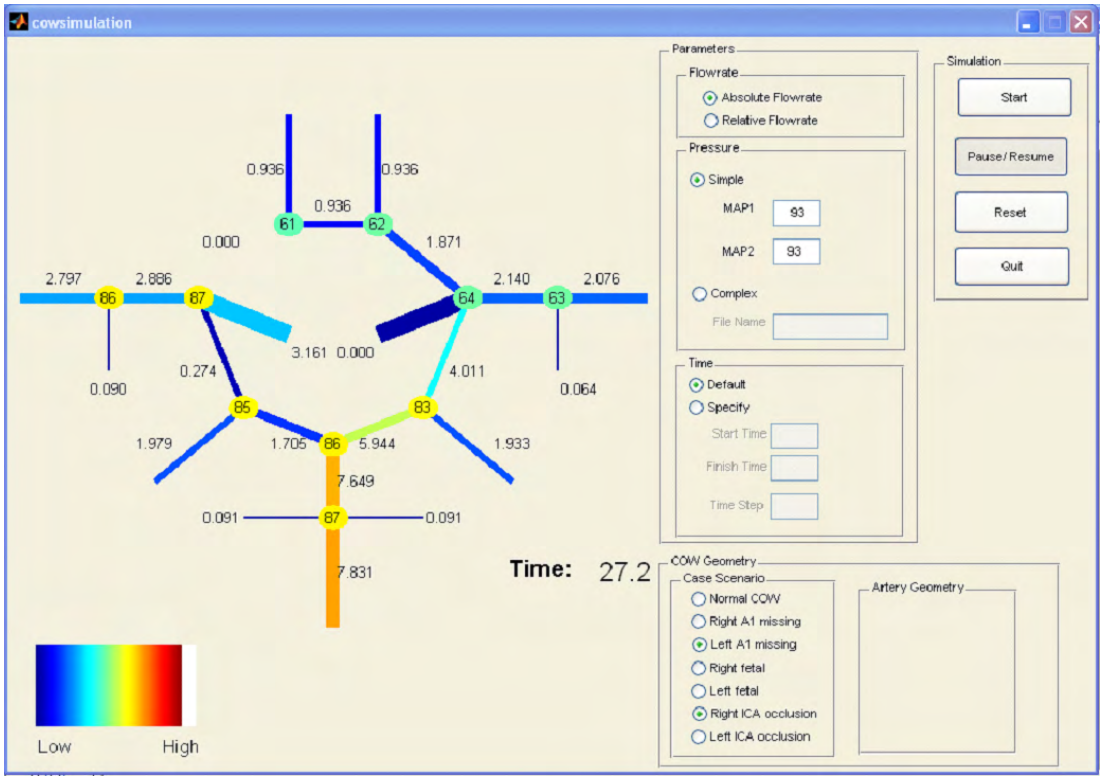

Figure 9.6 Running a simulation using the GUI using a CoW with a missing left ACA1 segment subjected to a contralateral ICA occlusion.

colour of the lobes ranged from dark red, representing low blood perfusion, to dark blue, representing high blood perfusion. Figure 9.7 shows the GUI when it is first run.

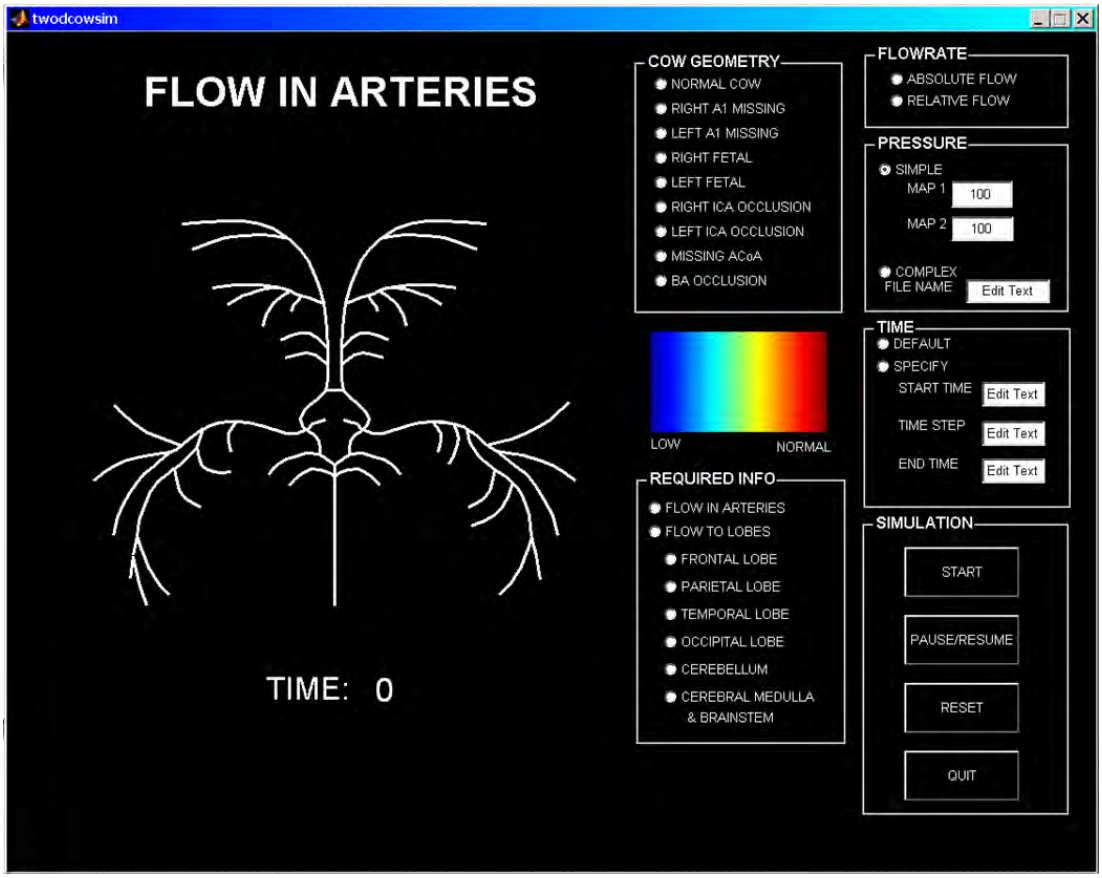

Figure 9.7 The GUI developed by Iain McIver [84], version 2, when it is launched.

Figure 9.8 shows the flowrates in the vessels while running a simulation. On the left the figure shows the simulation for a classical complete CoW under no pathological conditions. On the right, the simulation is run for a fetal case on the left side of the CoW with an ipsilateral (left) ICA occlusion. The ICA occlusion is modelled by setting its radius as a step function. This radius changes its value from normal to almost zero at a specific time. As a result of the occlusion in a CoW with an ipsilateral fetal case, the blood flow through the contralateral (right) ICA increases dramatically (changing its colour to red) to supply blood to the left side of the CoW. The blood delivery in this case is maintained through the anterior vessels of the CoW which also experience increase levels of flowrates. Figure 9.9 show the results in the different cerebral lobes under the same conditions in Figure 9.8. In the case of a COW with fetal condition undergoing an ipsilateral ICA occlusion, the blood perfusion to the ipsilateral cerebral lobes decreases, resulting in a change in colour in the GUI towards red shades. The running time was set to 50 seconds for most of the simulations. This value was chosen because it gives enough time for the peripheral arteries' response.

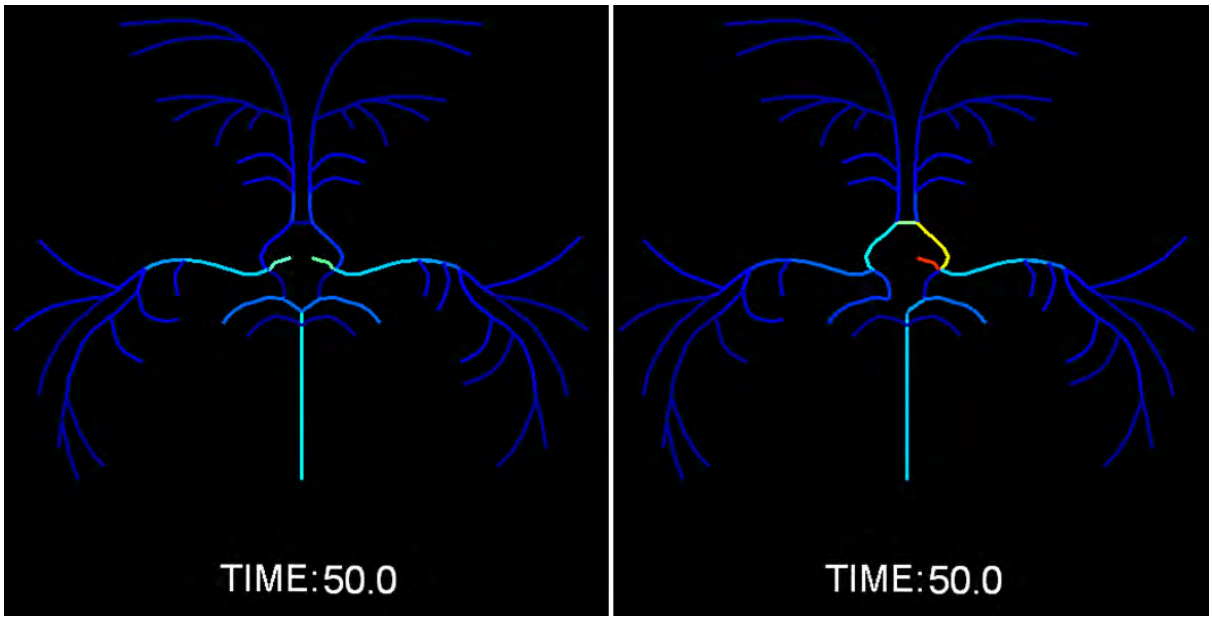

Figure 9.8 The CoW vessels when running a simulation using A) a classical complete CoW under normal conditions. B) a CoW with a left fetal case with ipsilateral ICA occlusion. [84].

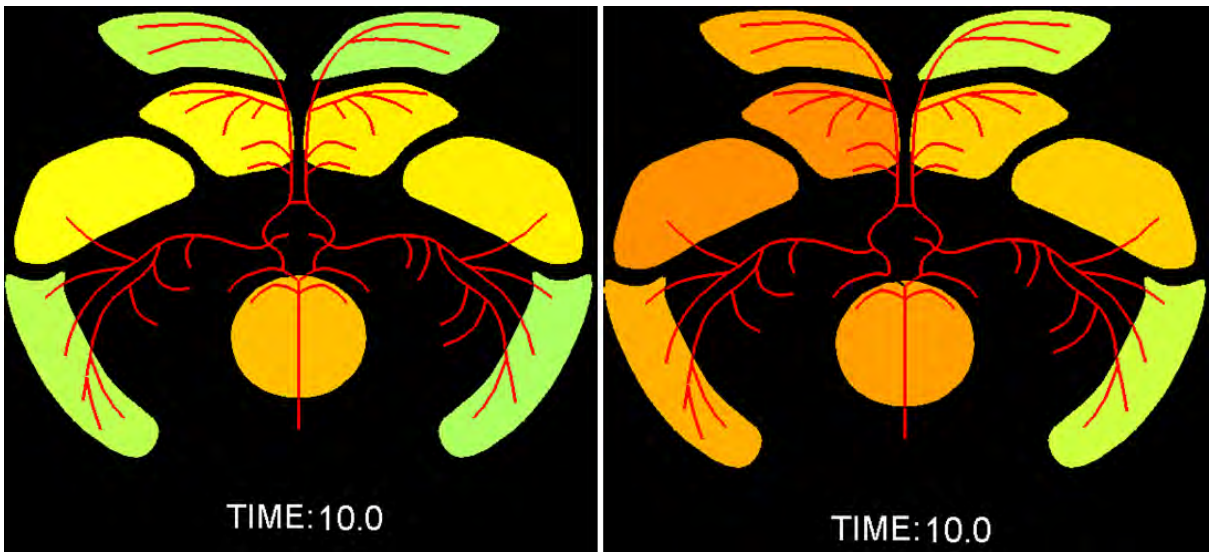

Figure 9.9 The cerebral lobes when running a simulation using A) a classical complete CoW under normal conditions. B) a CoW with a left fetal case with ipsilateral ICA occlusion. [84].

The GUI was further developed by Fabian Herzog [56]. Three smaller efferent arteries were added to each PCA2 segment, resulting in 42 efferent arteries. More cerebral sections supplied by the BA, PCA2 and MCA vessels were added as shown in Figure 9.10. Multiple functions were added to this latest version of the GUI. The user is given more options and can interact more easily with the GUI. For example, the user can define a missing vessel in the CoW using the *missing arteries* box, which lists the most common absent vessels cases. The user, can also set any vessel as absent by clicking on the vessel in the GUI window then using the *Edit* menu. The *File*, *Simulation* and *?* menus at the top of the GUI window give the user more options.

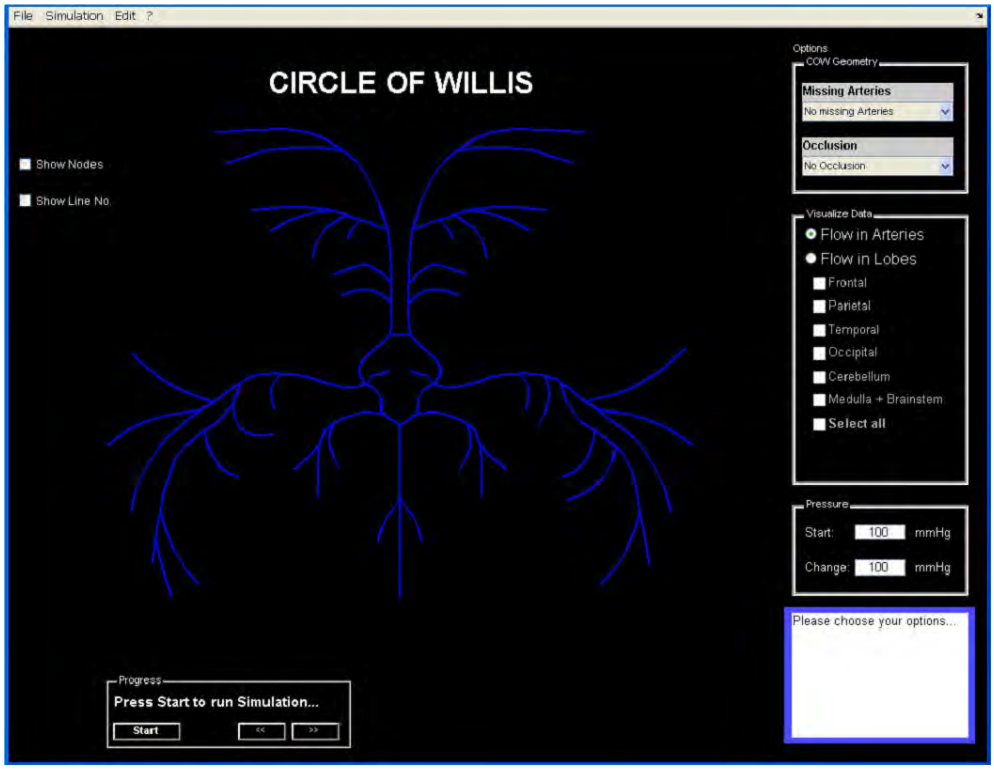

Figure 9.10 The GUI developed by Fabian Herzog [56], version 3, when it is launched.

The arterial binary tree algorithm with the metabolic and myogenic autoregulation mechanisms described in Chapter 7 were also implemented in this latest version of the GUI. The binary arterial tree was created for each of the small efferent arteries. Having a smaller root radius leads to a smaller number of bifurcations in the tree, resulting in smaller number of vessels and levels in the tree. The overall system of running this GUI and the computations required is represented by Figure 9.11.When the GUI is launched, a data structure of the system, *Data Generator*, is created. When the simulation is started, the data processor file, *Process Data*, obtains data from the user inputs and the data structure files. Then the *Initial Solver* is called, where an initial solution is calculated for the CoW arteries' resistances, flowrates and pressures.

The resistances of the peripheral arteries including the vasculature downstream of the CoW are calculated using the estimated values of flowrates through the efferent arteries. The *Matrix Generator*, then the *Matrix Solver* are used to calculate the solution. The flowrates are evaluated by assessing the volume of each lobe in the brain and how much flowrate is required under normal conditions. At this stage, the complete set of the CoW resistances, flowrates and pressures are set as the default conditions.

The occlusion in arteries, if any, are then taken into consideration, where the system solves for new flowrates and pressures using the *Matrix Generator* and the *Matrix Solver*. If there is a change in the inlet pressure, the system is solved again using the same process. Then a loop is used to calculate an arterial tree, *Tree*, for each efferent artery in the CoW. After each tree is calculated, the total resistance is modified using the autoregulation mechanisms, described in Section 7.5, until autoregulation is maintained.

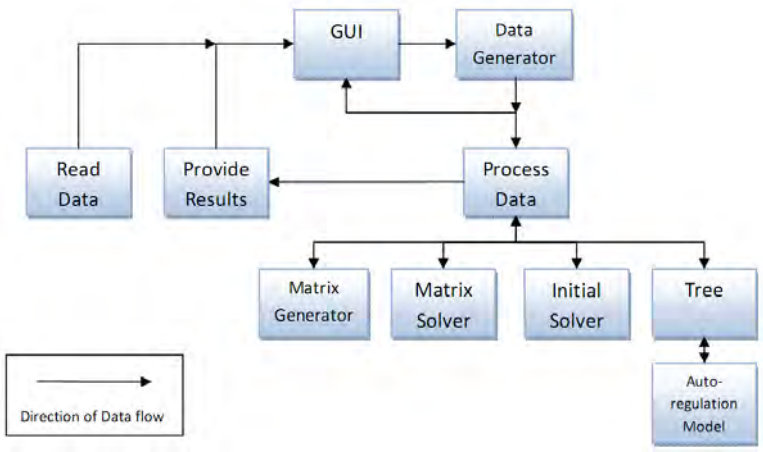

Figure 9.11 Flow diagram for computations involved in running the GUI developed by Fabian Herzog [56].

The simulation results of a classical complete CoW geometry with no pathological conditions is shown in Figure 9.12. The colour scale used for the flowrates in vessels and blood perfused in tissue is different to previous versions. For flowrates in the vessels, the colour scale ranges from blue (for low blood flow) to red (for high blood flow), where brownish purple is the normal flowrate through the vessels. For blood delivered to the cerebral lobes, the colour also ranges from blue to red, where yellow is the normal perfusion.

The user can get more information about a particular vessel or cerebral section by clicking on it. The information is then displayed in the *results window* at the bottom right of the GUI window. An example is given in Figure 9.13, where the selected vessel's information of artery ID, radius, flowrate and the tissue perfused are displayed.

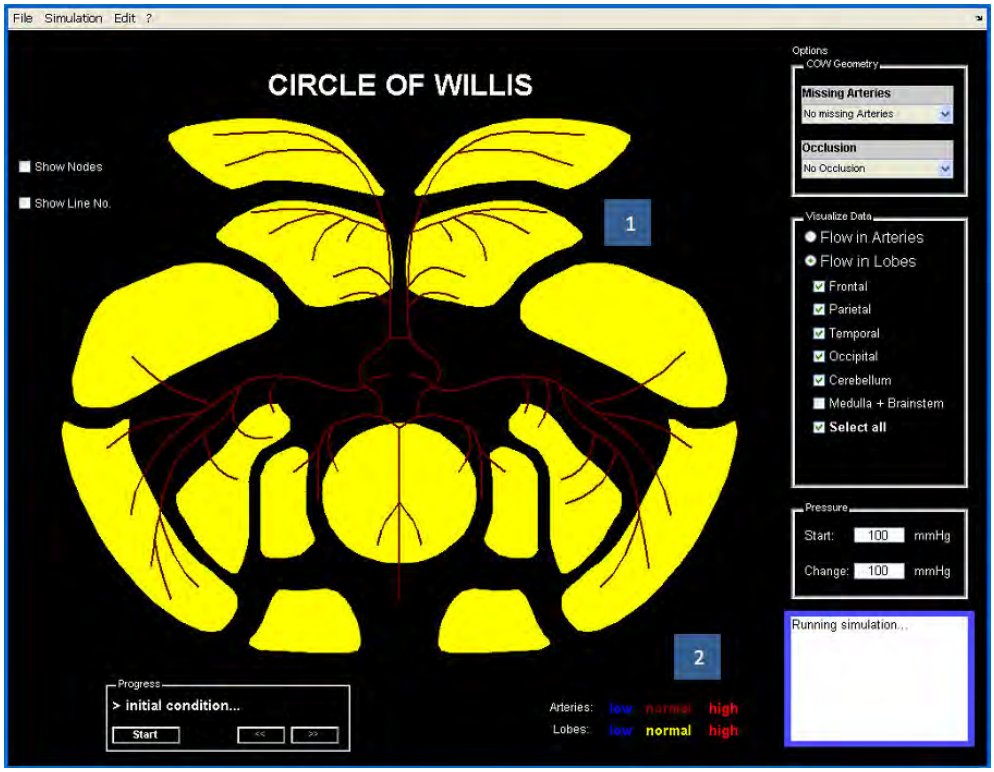

Figure 9.12 The CoW vessels and cerebral lobes when running a simulation using a classical complete CoW under normal conditions [56].

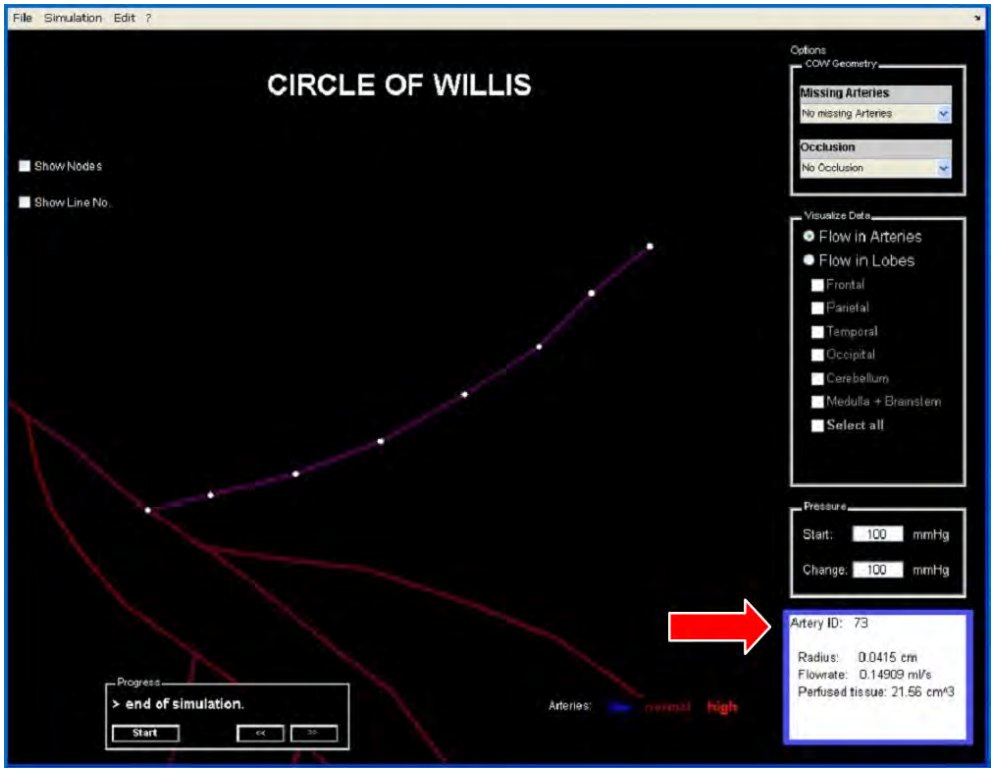

Figure 9.13 The GUI allows the user to zoom in and select a vessel to display its properties in the results window [56].

Figures 9.14 and 9.15 show the results for the CoW vessels and cerebral lobes for the case of a classical complete CoW under a unilateral ICA occlusion. As a result of the occlusion, the GUI is showing that there is more blood flow traveling through the BA and contralateral ICA, which are represented by having the lines change their colour to bright red as in Figure 9.14. The cerebral lobes on the ipsilateral side of the ICA occlusion experience a drop in blood perfusion, and therefore, change their colour to greyish yellow in the GUI as in Figure 9.15.

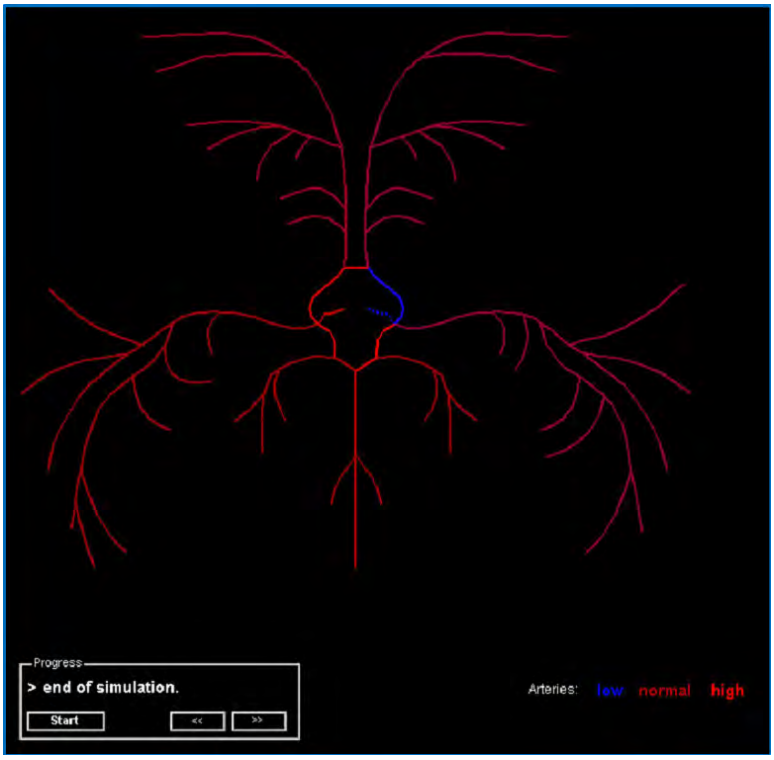

Figure 9.14 The CoW vessels when running a simulation using a classical complete CoW with a unilateral ICA occlusion [56].

9.1 Collaborative Environment for Visualisation of the Circle of Willis (CEVCoW)

The work developed in this thesis was also part of a joint project with the University of Leeds to develop a collaborative environment for visualisation of the CoW (CEVCoW). The aim was to create an interface that is accessible from a web browser. For example, a clinician at the hospital and a modeller at the Centre of Bioengineering interested in examining together the the effects of a particular configuration over web interface. The aim was for the clinician at the hospital and a modeller at the Bioengineering Centre to be able to work independently, but also be able to share their results at the same or different times.

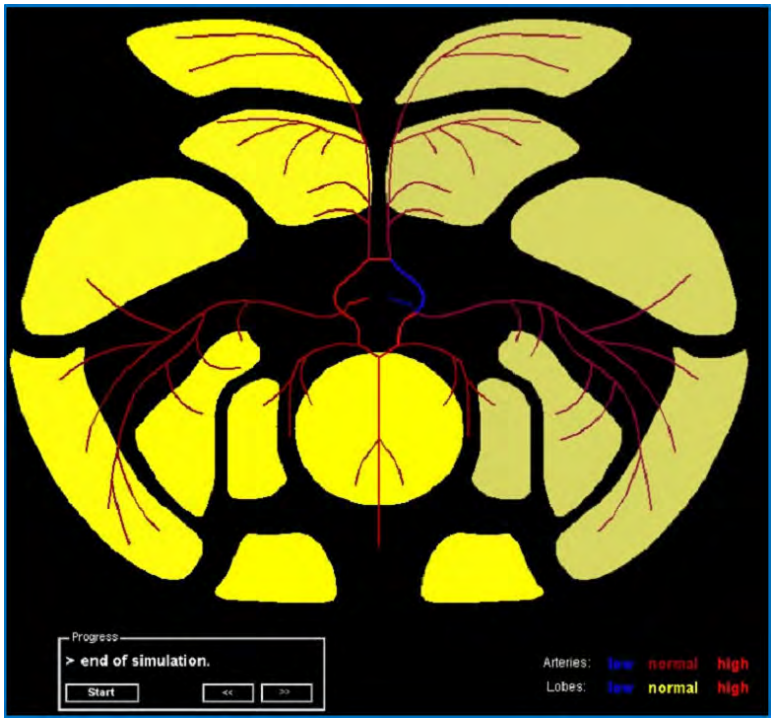

Figure 9.15 The cerebral lobes when running a simulation using a classical complete CoW with a unilateral ICA occlusion [56].

The collaborative environment (CE) was developed by Robert Hayford from the University of Leeds [53]. It was based on version one of the GUI described above. The web interface shown in Figure 9.16 was designed so only registered members can access and use it.

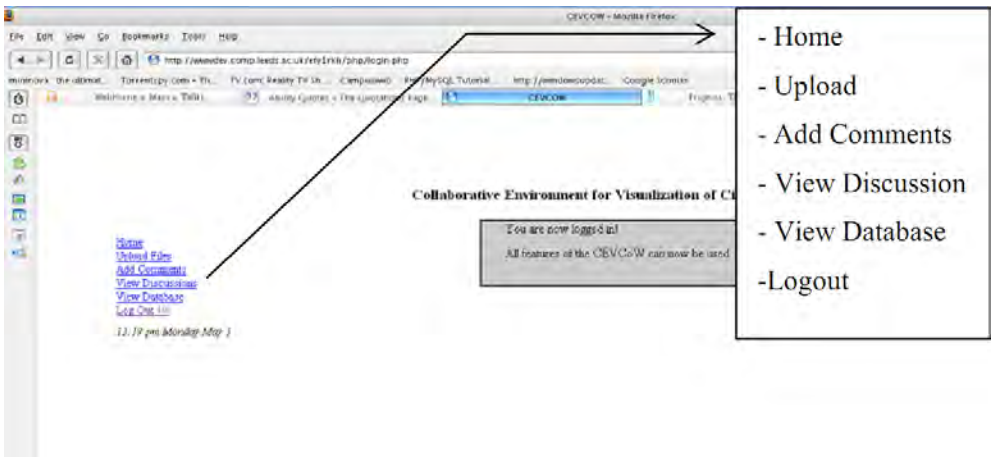

Figure 9.16 The collaborative environment created using a web interface for authorised users [53].

The collaborative environment has three main functions. First, the *store* function, where the user is allowed to save the results of a simulation to a file store. Users are presented with dialog by clicking the store button. Second, the *fetch* function, where

the user is allowed to retrieve previous simulations. Users are presented with a dialog box allowing them to save and open a file. Third, the *publish* function, where users are allowed to publish files onto the CE by clicking the publish button that starts up a browser. This function serves as a gateway from the CoW GUI to the CE. Figure 9.17 shows an example of publishing a set of results onto the web interface. On the RHS, the new buttons are added to the GUI system to be able to interact with the CE. The overall CE system designed and implemented by the University of Leeds group is summerised in Figure 9.18. This CE system is not completed and was under development with possibility of continuation and further improvement and expansion in the future.

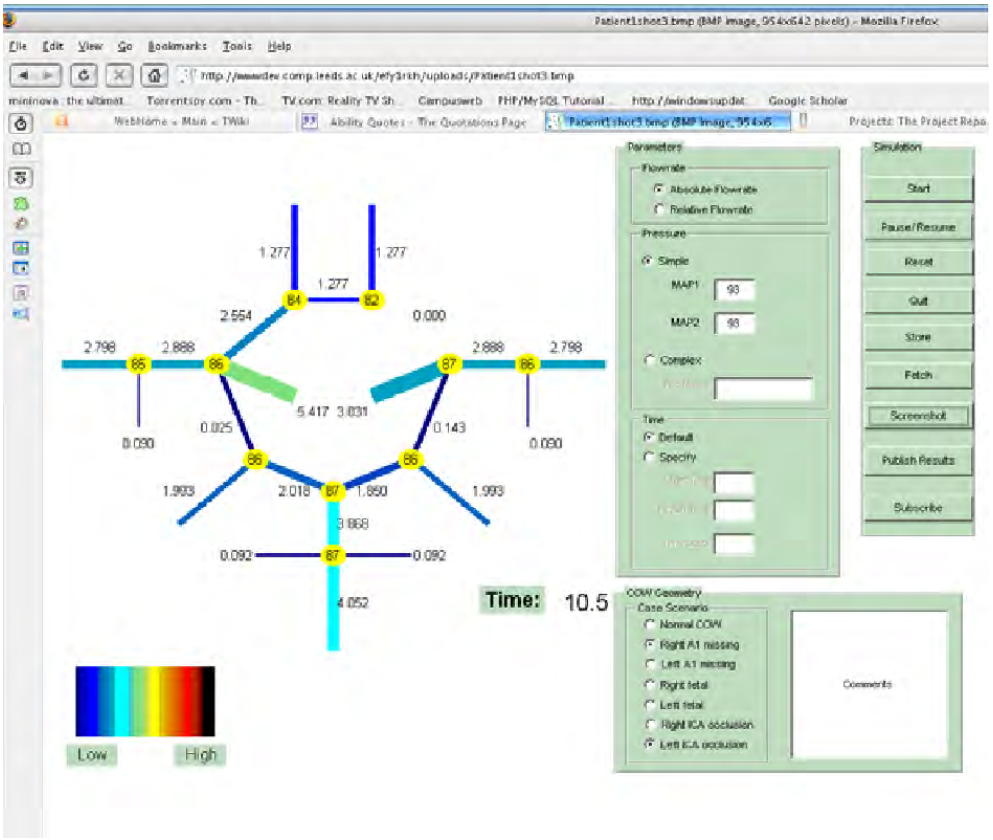

Figure 9.17 The CE illustrating the *publish* function available to users present results of a CoW simulation [53].

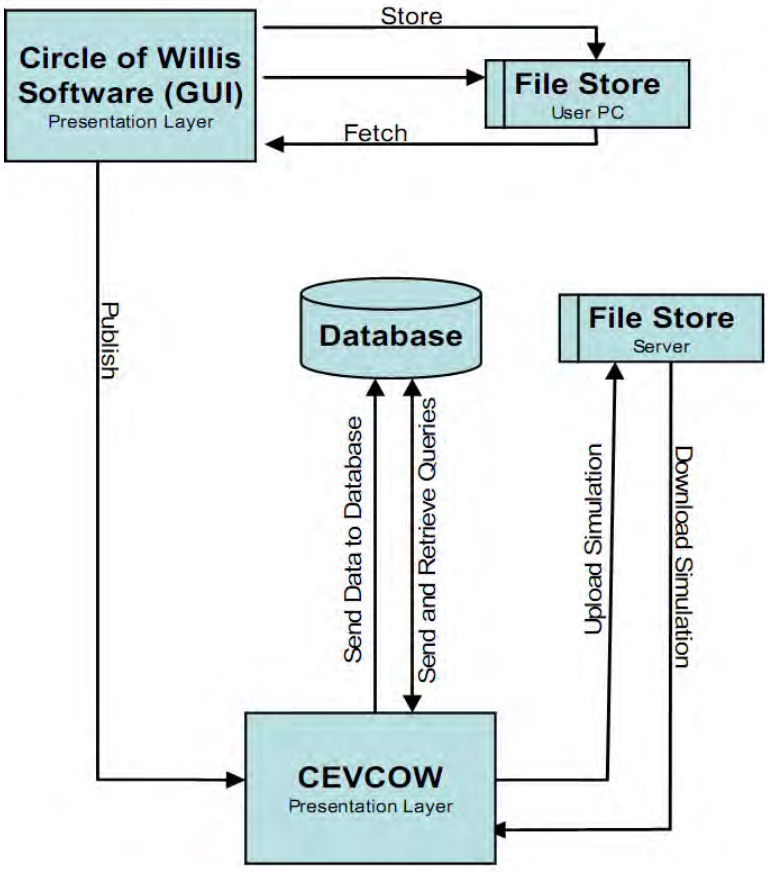

Figure 9.18 The CE system architecture [53].

Chapter 10

Conclusions & Future Work

This thesis presents the work performed to develop the mathematical model of the cerebral vasculature and its autoregulation function, which transformed it from a phenomenological based model to a more physiological one. The final model consists of the cerebral vasculature comprising the CoW and its peripheral arteries which branch down to the capillary level. This vascular network incorporates the autoregulation function, where the myogenic and metabolic regulation mechanisms are activated in the vasculature downstream of the CoW.

The original CoW model described in Chapter 4 consisted of the basic algorithm where the efferent arteries were modelled as variable resistances that replicate the autoregulation mechanism. The flowrates through the efferent arteries were based on Hillen's ratio [58], and the autoregulation response was based on the experimental work of Newell et al. [91]. The original model was modified in several stages. First, the emphasis was based on replicating the autoregulation slope observed in Guyton et al. [47]. This was done using the phenomenological model of the memory algorithm and then by the more physiological model of the simple metabolic rate algorithm. Both the models produced the autoregulation curve desired. However, because of its physiological basis, the simple metabolic model was developed further to be included in the non-linear CoW model, where the cerebral mass CO_2 concentration was the main driver for the response in the CoW efferent arteries. The non-linear model was created to include the extra losses encountered as a result of velocity profile development along the CoW vessels and the centripetal forces in tortuous vessels.

Numerous simulations were run using both the linear and non-linear models. The initial linear model with the 10 efferent arteries was used to simulate a large range of clinical scenarios. These scenarios included cases where the most common CoW configurations experienced a unilateral ICA occlusion or stenosis. The results outline the important role that the internal CoW vessels play in order to re-route blood to the efferent arteries affected most. The anterior and posterior communicating arteries, which are usually anatomically small in radius, play a very significant role in delivering

blood in these clinical scenarios. The communicating arteries experience a significant increase of blood flow through them and/or reversed flow direction when one of the afferent CoW arteries is occluded or heavily stenosed. Under conditions where the CoW was no longer able to redirect blood to the suffering efferent arteries, a shift in autoregulation range to higher values was observed.

A selection of the clinical scenarios was chosen to be simulated using the various developments made to the CoW model. The non-linear model which accounted for additional losses in the CoW vessels showed that the cerebral vasculature is more susceptible to pathological conditions, such as an ICA occlusion or stenosis. A significant shift in autoregulation was observed when the different CoW configurations were simulated using different pathological conditions.

As mentioned above, the simple metabolic model presented in Chapter 5 was further developed as described in Chapter 6. The new range of autoregulation was adopted at the same time after more research in the literature was carried out, where the range was observed to be generally lower than assumed at an earlier stage of this thesis research. In addition, the autoregulation slope was observed to be flat. The gradient in the slope reported by some researchers was due to the averaging of the autoregulation range of several individuals.

The leptomeningeal arteries (LMAs) were added to the linear CoW model because of their compensatory capacity significance. Even though the flowrate through the LMAs was assumed to be only 5% of the MCA flowrate under normal conditions, the simulations showed that there is a difference in response, however minor, compared to a CoW with no LMAs. More data on the size and variability of the LMAs is needed in order to define the amount of flowrate that normally travel through them. The implementation of the LMAs were later removed because of their great variations from one individual to another in terms of number and size. Once more data is available, the LMA can be incorporated back into the final model of the CoW along with the binary arterial trees.

The most significant work of this thesis was the implementation of vasculature trees that replace the distal resistance of the CoW efferent arteries and their autoregulation function. The arterial binary tree was based on Steele et al.'s fractal vascular network [112] where each efferent artery is specified as a root vessel of the tree that branches numerous times before reaching the terminal (pre-capillary) radius size. Using the MCA radius as the root radius, the binary arterial tree created extended to 34 levels in order for all vessels in the tree to reach the assumed terminal (pre-capillary) radius size. Anatomically, arterial trees normally do not extend to more than 25 levels. However, the binary tree's cumulative resistance plot as a function of branching level showed that the majority of the resistance was attained at level 25. This indicates that the binary

tree's vessels created at branching levels higher than 25 are of small significance.

The total resistance of the binary tree created with the MCA radius was close to the resistance experienced physiologically. However, the binary tree parameters (γ and k) were modified slightly in order to achieve a total resistance that matches the value expected physiologically. The same method was used in the latest version of the graphical user interface to create binary arterial trees for the CoW efferent arteries that have the same distal resistance experienced physiologically. Other properties of the binary arterial tree, such as the mother-daughter diameters logarithmic plots, were found to be similar to experimental data.

The metabolic and myogenic mechanisms were implemented to reproduce the autoregulation behavior. The vessels' radii response for these mechanisms were summarised as look-up tables, where they were used to implement a time steady state response at each iteration step of the autoregulation. At each iteration step, the tree experienced changes in the total resistance as a result of the change in vessels' radii. The computation of the resistances, flowrates and pressures of the tree were performed every time some or all the binary tree's vessels change their radii. The myogenic mechanism, which is hypothesised by multiple researchers as the main driver of autoregulation, did not provide enough variation in the vessels' radii, hence, did not provide enough change in the tree's resistance to maintain autoregulation. This is because the myogenic mechanism is highly active at high pressure which are only experienced by vessels with larger radius at the lower levels of the binary tree. these vessels do not contribute much to the resistance of the total resistance of the tree. The metabolic mechanism was based on the CO_2 diffusion from venules to arterioles, resulting in the dilatation and contraction of the arterioles' radii. These arterioles contribute to the majority of the tree's resistance, and therefore, were able to maintain the autoregulation of blood flow for the desired range of mean arterial pressures. This leads to the conclusion that the metabolic mechanism is the dominant mechanism in maintaining cerebral autoregulation.

The properties of the mathematical models were tested throughout this research. The sensitivity of the linear CoW model was first tested by varying the time constant λ. This parameter represents the smooth muscle contraction time of the vessels' walls, which become slower with aging. The linear CoW model was also tested by varying the radii of some of the CoW arteries that have a vital impact on the the blood flow rerouting to where it is needed most. The results of the simulations show that the linear CoW model has low sensitivity when varying its parameters. However, in the case of a unilateral ICA occlusion, there was a significant affect on the efferent arteries supplied through a connecting vessel, when the radius of this connecting vessel was decreased by several standard deviations. The properties of the arterial binary tree were tested by Boudewijn Deurloo in the Brain Group [32]. Changing the γ and k parameters resulted

in changes in the number of vessels, number of terminal vessels, number of branching levels, resistance and blood flow through the binary arterial tree.

The graphical user interface was developed at different stages as the CoW model was developed. It was created to provide an interface that can be used by clinicians without the need to interact with the code of the model. The simulations of the models are executed based on average data of a human cerebral properties. However, patient-specific data can be incorporated into the model.

This research succeeded in developing a model of the cerebral vasculature coupled with the different forms of autoregulatory mechanisms. A number of cerebral autoregulation models exist in the literature, however, no model combines a fully populated arterial tree with dynamic autoregulation. The final model presented in this thesis simulates an asymmetric binary arterial vascular tree with myogenic and metabolic regulation mechanisms implemented in the small arteries and arterioles of the tree. The model has the capacity to account for the local variation in metabolic demand as a result of an increase in the neuronal activity. This work has the potential of being a significant clinical tool to evaluate patient-specific cases when combined with the graphical user interfaces provided.

10.1 Future Work

Further developments can be added to the model to produce an enhanced and more accurate tool that could be used in a clinical environment. One of the aspects that should be considered for development is the modelling of the capillary bed and its contribution to autoregulation. Currently, the capillary beds are modelled as capillaries lined up in parallel while anatomically the capillary beds are aligned in a net-like arrangement [75]. The capillary beds also take part in the autoregulation process by the opening and closure of the pre-capillary sphincters supplying these capillary beds [71]. The capillary beds' autoregulation function is currently being developed by Navid Safaeian in the Brain Group.

In this thesis, the oxygen diffusion in the cerebral tissue was implemented using the krogh cylinder where the oxygen consumption rate was assumed to be constant. Boudewijn Deurloo [32] implemented the flow dependence of the metabolic rate of oxygen where analytical steady state solutions for concentration patterns in and around the capillary were used depending on the flow through the capillary. The modelling also included a numerical method which was used to include the time dependence for the concentration patterns in and around the capillary. This can be introduced to the model created for this thesis, however, it will require a large amount of computation

and computer memory to do so because of the large number of capillaries in the cerebral mass.

One of the difficulties faced in implementing the binary arterial tree with the autoregulation behavior was the computational cost. The binary arterial tree created using the MCA radius for the root radius has more than $850,000$ vessels, where more than $400,000$ are terminal vessels, each supplying a capillary bed consisting of approximately 7500 capillaries. The number of all vessels and terminal vessels in the tree can increase to more than $1,000,000$ and $500,000$ respectively when the normal distribution is applied to the tree. The memory required to create the binary tree and compute its properties such as the resistances, flowrates and pressures take a significant amount of memory on the PC used, which has an Intel(R) Pentium(R) 4 processor (2.40 GHz) and 1 GB memory (RAM). The metabolic and myogenic mechanisms were implemented through the use of look-up tables. It was necessary to avoid implementing the metabolic and myogenic responses in real time. This is because the amount of computation required for the response of all vessels in the tree will be large and not possible to be done on a PC, especially that the computation is done in serial. If the model is to be developed further, the use of a supercomputer is necessary.

Plans are made to use the BlueFern supercomputer at the University of Canterbury. The use of the BlueFern will provide enough space to create a binary tree for all the efferent arteries of the CoW. Also, will provide the computation power required to calculate the metabolic and myogenic response in real time, where the tree's resistance is calculated upwards and the flowrates and pressures are calculated downwards in the tree. The computations will be done in parallel at each time step instead of using serial computation in quasi time. The first step to use the supercomputer is convert the code from MATLAB to C++ language. This is being done by another member of the Brain Group of the University of Canterbury, Svava Kristinsdottir.

The work performed for this thesis resulted in developing a model representing the cerebral vasculature and its autoregulatory function. This model can be used to replicate clinical scenarios by using the graphical user interface. The asymmetric binary arterial tree is planned to be the fundamental framework for further work into the cellular processes that determine how our brain regulates its blood supply - a crucial step into understanding the homeostasis of the body.

Appendix A

Fluid Dynamics

The Force balance equation acting on the cylindrical body of blood

$$P\pi r^2 - (P + dP)\pi r^2 - \tau(2\pi r)dx \;=\; 0 \tag{A.1}$$

The shear stress equation

$$\tau = -\mu\frac{du}{dr} \tag{A.2}$$

Simplified force balance equation A.1

$$\tau = -\frac{r}{2}\frac{dP}{dx} \tag{A.3}$$

Equating A.3 and A.2 results in

$$\frac{du}{dr} = \frac{r}{2\mu}\frac{dP}{dx} \tag{A.4}$$

Integrating the above equation

$$u(r) = \frac{r^2}{4\mu}\frac{dP}{dx} + B \tag{A.5}$$

Accounting for no-slip boundary condition by assuming that the velocity is zero ($u = 0$) at the vessel radius ($r = r_v$)

$$u(r) = \frac{1}{4\mu}\frac{dP}{dx}(r^2 - r_v^2) \tag{A.6}$$

Which shows that velocity profile is a parabola. The average flowrate through the

vessel is obtained by integrating the velocity times area over the vessel cross section

$$Q = \int_0^{r_v} u(r) \cdot 2\pi r \cdot dr \tag{A.7}$$

The integrated average flowrate equation using A.6 results in

$$Q = -\frac{\pi}{8\mu}\frac{dP}{dx}r_v^4 \tag{A.8}$$

Since $\frac{dP}{dx}$ is a constant for developed flow, use the following representation where l_v is the vessel length

$$\frac{dP}{dx} = -\frac{\Delta P}{l_v} \tag{A.9}$$

Substituting A.9 in equation A.8 results in the final simplified Poiseuille equation

$$Q = \frac{\pi r_v^4}{8\mu l_v}\Delta P \tag{A.10}$$

Appendix B

CoW Complete Set of Equations

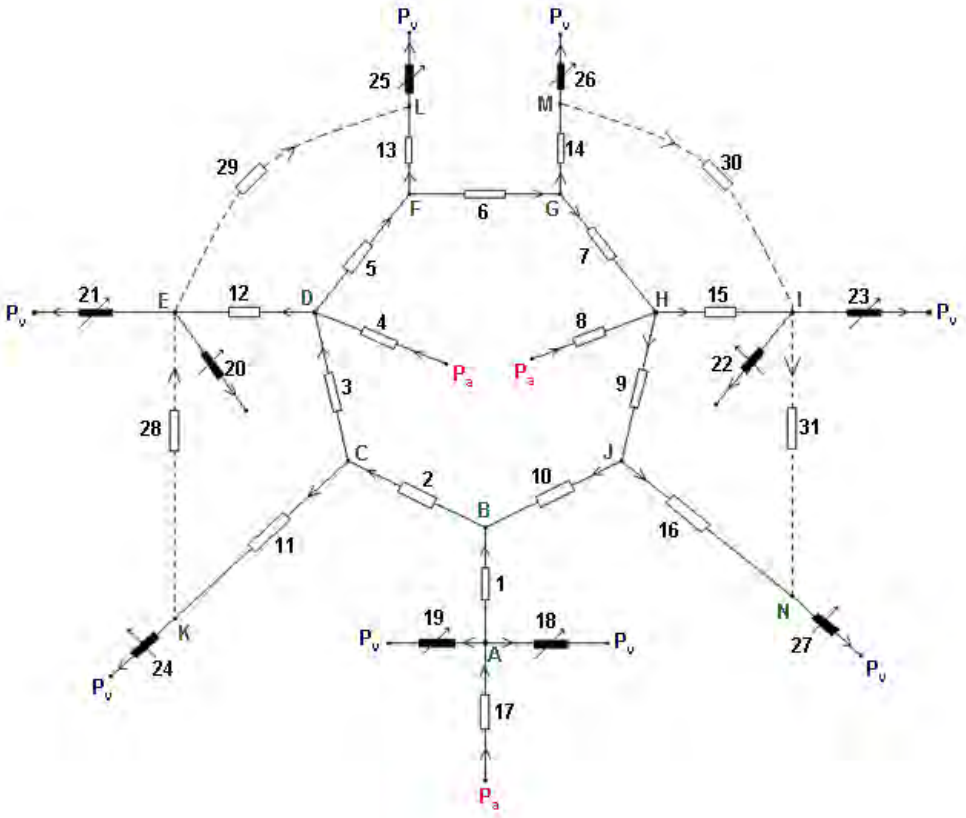

Figure B.1 The CoW network. Dashed vessels represent LMA vessels' resistance implemented in Chapter 5.

Table B.1 *CoW network numbering key.*

Number	Artery	Abbreviation
Afferent and internal arteries		
1	Basilar Artery - Segment 1	BA1
2	Left Posterior Cerebral Artery - Segment 1	LPCA1
3	Left Posterior Communications Artery	LPCoA
4	Left Internal Carotid Artery	LICA
5	Left Anterior Cerebral Artery - Segment 1	LACA1
6	Anterior Communication Artery	ACoA
7	Right Anterior Cerebral Artery - Segment 1	RACA1
8	Right Anterior Cerebral Artery - Segment 1	RICA
9	Right Posterior Communications Artery	RPCoA
10	Right Posterior Cerebral Artery - Segment 1	RPCA1
11	Left Posterior Cerebral Artery - Segment 2	LPCA2
12	Left Middle Cerebral Artery	LMCA
13	Left Anterior Cerebral Artery - Segment 2	LACA2
14	Right Anterior Cerebral Artery - Segment 2	RACA2
15	Right Middle Cerebral Artery	RMCA
16	Right Posterior Cerebral Artery - Segment 2	RPCA2
17	Basilar Artery - Segment 2	BA2
Efferent arteries		
18	Right Superior Cerebellar Artery	RSCbA
19	Left Superior Cerebellar Artery	LSCbA
20	Left Anterior Choroidal Artery	LAChA
21	Left Middle Cerebral Artery VARIABLE	LMCAvar
22	Right Anterior Choroidal Artery	RAChA
23	Right Middle Cerebral Artery VARIABLE	RMCAvar
24	Left Posterior Cerebral Artery - Segment 2 VARIABLE	LPCA2var
25	Left Anterior Cerebral Artery - Segment 2 VARIABLE	LACA2var
26	Right Anterior Cerebral Artery - Segment 2 VARIABLE	RACA2var
27	Right Posterior Cerebral Artery - Segment 2 VARIABLE	RPCA2var
LMA arteries		
28	LMA between LMCA and LPCA2	
29	LMA between LACA2 and LMCA	
30	LMA between RACA2 and RMCA	
31	LMA between RMCA and RPCA2	

Table B.2 *CoW network equations with no LMA vessels. Note that the symbol Q is used instead of CBF (flowrate) and the symbol R is used instead of CVR (resistance) for simplicity.*

Vessel/Node	Equation
Poiseuille Equations	
1	$Q_1 \times R_1 - P_A + P_B = 0$
2	$Q_2 \times R_2 - P_B + P_C = 0$
3	$Q_3 \times R_3 - P_C + P_D = 0$
4	$Q_4 \times R_4 + P_D = P_a$
5	$Q_5 \times R_5 - P_D + P_F = 0$
6	$Q_6 \times R_6 - P_F + P_G = 0$
7	$Q_7 \times R_7 - P_G + P_H = 0$
8	$Q_8 \times R_8 + P_H = P_a$
9	$Q_9 \times R_9 - P_H + P_J = 0$
10	$Q_10 \times R_10 - P_J + P_B = 0$
11	$Q_11 \times R_11 - P_C + P_K = 0$
12	$Q_12 \times R_12 - P_D + P_E = 0$
13	$Q_13 \times R_13 - P_F + P_L = 0$
14	$Q_14 \times R_14 - P_G + P_M = 0$
15	$Q_15 \times R_15 - P_H + P_I = 0$
16	$Q_16 \times R_16 - P_J + P_N = 0$
17	$Q_17 \times R_17 + P_A = P_a$
18	$Q_18 \times R_18 - P_A = -P_v$
19	$Q_19 \times R_19 - P_A = -P_v$
20	$Q_20 \times R_20 - P_E = -P_v$
21	$Q_21 \times R_21 - P_E = -P_v$
22	$Q_22 \times R_22 - P_I = -P_v$
23	$Q_23 \times R_23 - P_I = -P_v$
24	$Q_24 \times R_24 - P_K = -P_v$
25	$Q_25 \times R_25 - P_L = -P_v$
26	$Q_26 \times R_26 - P_M = -P_v$
27	$Q_27 \times R_27 - P_N = -P_v$
Conservation of Flow Equations	
A	$Q_1 - Q_{17} + Q_{18} + Q_{19} = 0$
B	$Q_1 - Q_2 + Q_{10} = 0$
C	$Q_2 - Q_3 - Q_{11} = 0$
D	$Q_3 + Q_4 - Q_5 - Q_{12} = 0$
E	$Q_{12} - Q_{20} - Q_{21} = 0$
F	$Q_5 - Q_6 - Q_{13} = 0$
G	$Q_6 - Q_7 - Q_{14} = 0$
H	$Q_7 + Q_8 - Q_9 - Q_{15} = 0$
I	$Q_{15} - Q_{22} + Q_{23} = 0$
J	$Q_9 - Q_{10} - Q_{16} = 0$
K	$Q_{11} - Q_{24} = 0$
L	$Q_{13} - Q_{25} = 0$
M	$Q_{14} - Q_{26} = 0$
N	$Q_{16} - Q_{27} = 0$

Table B.3 *Additional and modified equations for the CoW network with LMA vessels. Note that the symbol Q is used instead of CBF (flowrate) and the symbol R is used instead of CVR (resistance) for simplicity.*

Vessel/Node	Equation
Poiseuille Equations	
28	$Q_28 \times R_28 - P_K - P_E = 0$
29	$Q_29 \times R_29 - P_E - P_L = 0$
30	$Q_30 \times R_30 - P_M - P_I = 0$
31	$Q_31 \times R_31 - P_I - P_N = 0$
Conservation of Flow Equations	
E	$Q_{12} - Q_{20} - Q_{21} + Q_{28} - Q_{29} = 0$
I	$Q_{15} - Q_{22} + Q_{23} + Q_{30} - Q_{31} = 0$
K	$Q_{11} - Q_{24} - Q_{28} = 0$
L	$Q_{13} - Q_{25} - Q_{29} = 0$
M	$Q_{14} - Q_{26} - Q_{30} = 0$
N	$Q_{16} - Q_{27} + Q_{31} = 0$

Appendix C

Memory Algorithm

$$\int_0^{T+h} err(t)dt \;=\; err(T) \times h \;+\; exp(-\zeta h) \int_0^{T} err(t)dt \tag{C.1}$$

Let I(T) represent the error integral $\int_0^T err(t)dt$

$$I(T+h) \;=\; err(T) \times h \;+\; exp(-\zeta h)\; I(T) \tag{C.2}$$

Subtract the term I(T) to both sides of the equation

$$I(T+h) \;-\; I(T) \;=\; err(T) \times h \;+\; exp(-\zeta h)\; I(T) \;-\; I(T) \tag{C.3}$$

Rearrange

$$I(T+h) \;-\; I(T) \;=\; I(T)[exp(-\zeta h) \;-\; 1] \;+\; err(T) \times h \tag{C.4}$$

Divide by the time step (h)

$$\frac{I(T+h) \;-\; I(T)}{h} = \frac{I(T)[exp(-\zeta h) \;-\; 1]}{h} \;+\; err(T) \tag{C.5}$$

Rewrite

$$\frac{dI}{dT} = I(T) \lim_{h \to 0} \frac{exp(-\zeta h) \;-\; 1}{h} \;+\; err(T) \tag{C.6}$$

Simplify

$$\frac{dI}{dT} = I(T)(-\zeta) \;+\; err(T) \tag{C.7}$$

Rearrange

$$\frac{dI}{dT} \;+\; \zeta I(T) = err(T) \tag{C.8}$$

Rewrite

$$\frac{dI}{dT}\ exp(\zeta T) = err(T)\ exp(\zeta T) \tag{C.9}$$

Integrate

$$I(T) = exp(-\zeta T) \int_0^T err(\gamma)\ exp(\zeta\gamma) d\gamma \tag{C.10}$$

Rearrange

$$\int_0^T err(t)dt = \int_0^T\ exp(-\zeta(T-\gamma))\ err(\gamma)d\gamma \tag{C.11}$$

Appendix D

Metabolic Rate Autoregulation Equation

The three basic equations for implementing the brain metabolism are used to describe the Poiseuille equation defined in Equation D.1, the cerebral oxygen consumption defined by Equation D.2, and the cerebrovascular resistance defined by Equation D.3.

$$P_a - P_v = CVR \cdot CBF \tag{D.1}$$

$$(C_aO_2 - C_vO_2)CBF = CMRO_2 \tag{D.2}$$

$$CVR = CVR_{sp}(1 + S_R \cdot C_vO_2) \tag{D.3}$$

The above equations are rewritten as functions of CVR, $CMRO_2$, and CBF as follows

$$CVR = \frac{P_a - P_v}{CBF} \tag{D.4}$$

$$CBF = \frac{CMRO_2}{(C_aO_2 - C_vO_2)} \tag{D.5}$$

$$C_vO_2 = \frac{1}{S_R}\left(\frac{CVR}{CVR_{sp}} - 1\right) \tag{D.6}$$

Insert Equation D.6 into Equation D.5

$$CBF = \frac{CMRO_2}{\left(C_aO_2 - \frac{1}{S_R}\left(\frac{CVR}{CVR_{sp}} - 1\right)\right)} \tag{D.7}$$

Rearrange and replace the CVR term in Equation D.7 by Equation D.4

$$CBF = \frac{CMRO_2 \cdot S_R}{1 + S_R \cdot C_aO_2 - \frac{P_a - P_v}{CBF \cdot CVR_{sp}}} \tag{D.8}$$

Rearrange

$$\frac{CMRO_2 \cdot S_R}{CBF} + \frac{P_a - P_v}{CBF \cdot CVR_{sp}} = 1 + S_R \cdot C_aO_2 \tag{D.9}$$

Simplify

$$\frac{1}{CBF}\left(CMRO_2 \cdot S_R + \frac{P_a - P_v}{CVR_{sp}}\right) = 1 + S_R \cdot C_aO_2 \tag{D.10}$$

Rearrange as a function of CBF

$$CBF = \frac{1}{1 + S_R \cdot C_aO_2}\left(CMRO_2 \cdot S_R + \frac{P_a - P_v}{CVR_{sp}}\right) \tag{D.11}$$

The parameters S_R and CVR_{sp} are evaluated by first normalising Equation D.11 by CBF_{sp}

$$\frac{CBF}{CBF_{sp}} = \frac{CMRO_2 \cdot S_R}{CBF_{sp}(1 + S_R \cdot C_aO_2)} + \frac{P_a - P_v}{CBF_{sp} \cdot CVR_{sp}(1 + S_R \cdot C_aO_2)} \tag{D.12}$$

This is set to equal the autoregulation range slope given in Equation D.12.

$$\frac{CBF}{CBF_{sp}} = \frac{2}{3} + \frac{1}{3}\frac{P_a - P_v}{P_{a_{sp}} - P_v} \tag{D.13}$$

The first term on the RHS of Equation D.12 is equated with the first term on RHS of Equation D.13 resulting in the equation for S_R

$$S_R = \frac{2CBF_{sp}}{3CMRO_2 - 2C_aO_2 \cdot CBF_{sp}} \tag{D.14}$$

Similarly, the second term on the RHS of Equation D.12 is equated with the second term on RHS of Equation D.13 resulting in the equation for CVR_{sp}

$$CVR_{sp} = \frac{3(P_{a_{sp}} - P_v)}{CBF_{sp}(1 + S_R \cdot C_aO_2)} \tag{D.15}$$

Appendix E

Matrix A Transformations

The poiseuille and conservation of flow equations are represented in matrix form.

$$Ax = b \tag{E.1}$$

To solve for the unknowns in vector x, the equation is solved by rewriting as

$$x = A^{-1}b \tag{E.2}$$

To include the effect of varying the radius of a specific vessel in the CoW, the matrix ∂A is introduced, which contains the change in the artery's resistance.

$$x = (A + \partial A)^{-1}b \tag{E.3}$$

Rearrange

$$x = (I + A^{-1}\partial A)^{-1}A^{-1}b \tag{E.4}$$

The term $(I + A^{-1}\partial A)^{-1}$ is written as

$$(I + A^{-1}\partial A)^{-1} = I - A^{-1}\partial A + O(\partial A)^2 \tag{E.5}$$

Considering the term $O(A^{-1}\partial A)$ is negligible results in

$$x = (I - A^{-1}\partial A)A^{-1}b \tag{E.6}$$

Rearrange

$$x = (A^{-1} - A^{-1}\partial A A^{-1})b \tag{E.7}$$

The ∂A matrix is all zeros matrix except for the term representing the difference in resistance of a particular vessel as a result of change in its radius. The following is the evaluation of this matrix.

First evaluate the resistance with new radius $r_v + dr_v$

$$R = \frac{8\mu l_v}{\pi(r_v + dr_v)^4} \tag{E.8}$$

Let the constant C_R be defined as $C_R = \frac{8\mu l_v}{\pi}$, then simplify

$$R = C_R(r_v + dr_v)^{-4} \tag{E.9}$$

Rewrite as

$$R = C_R\ r_v^{-4}(1 + \frac{dr_v}{r_v})^{-4} \tag{E.10}$$

Use the binomial series defined below to evaluate the term $(1 + \frac{dr_v}{r_v})^{-4}$

$$(1+x)^m = 1 + \sum_{k=1}^{\infty} \frac{m(m-1)...(m-k+1)}{k!}\ x^k \tag{E.11}$$

The binomial series is used up to the tenth term to evaluate $(1 + \frac{dr_v}{r_v})^{-4}$

$$(1+\frac{dr_v}{r_v})^{-4} = 1-4\frac{dr_v}{r_v}+\frac{20}{2!}\left(\frac{dr_v}{r_v}\right)^2-\frac{120}{3!}\left(\frac{dr_v}{r_v}\right)^3+...+\frac{1037836800}{10!}\left(\frac{dr_v}{r_v}\right)^{10} \tag{E.12}$$

Implement this in the resistance equation

$$R = C_R\ r_v^{-4}\left(1 - 4\frac{dr_v}{r_v} + \frac{20}{2!}\left(\frac{dr_v}{r_v}\right)^2 - \frac{120}{3!}\left(\frac{dr_v}{r_v}\right)^3 + ...\right) \tag{E.13}$$

After multiplying out the terms on the RHS of equation E.13 we can rearrange to define the resistance of matrix A to be the first term only on the RHS while the resistance of the ∂A Matrix is defined by the rest of the terms on the RHS of Equation E.14. These are placed in Equation E.7 for computation.

$$R = C_R\ r_v^{-4} - 4C_R\ r_v^{-4}\frac{dr_v}{r_v} + C_R\ r_v^{-4}\frac{20}{2!}\left(\frac{dr_v}{r_v}\right)^2 - C_R\ r_v^{-4}\frac{120}{3!}\left(\frac{dr_v}{r_v}\right)^3 + ... \tag{E.14}$$

Bibliography

[1] http://www.heartandstroke.com. The Heart and Stroke Foundation of Canada, viewed May 2008.

[2] http://www.strokecenter.org. The Stroke Centre at Washington University in St. Louise, viewed May 2008.

[3] J. Alastruey, S. Moore, K.H. Parker, J. Peiro, T David, and S.J. Sherwin. Reduced modelling of blood flow in the cerebral circulation: Coupling 1-d, 0-d and cerebral auto-regulation models. *International Journal for Numerical Methods in Fluids*, 56(8):1061–1067, 2008.

[4] J. Alastruey, K. H. Parker, J. Peiro, S. M. Byrd, and S. J. Sherwin. Modelling the circle of willis to assess the effects of anatomical variations and occlusions on cerebral flows. *Journal of Biomechanics*, 40(8):1794–1805, 2007.

[5] B. J. Alpers and R. G. Berry. Circle of willis in cerebral vascular disorders. *Arch Neurol*, 8:398–402, 1963.

[6] J. Arnold, J. Fink, T David, J. G. Chase, S. Moore, K.T. Moorhead, and S. S. Alzaidi. Anatomical variations of the circle of willis and magnetic resonance measurement techniques. In *Annual Conference of the Australian College of Physical Scientists and Engineers in Medicine (ACPEM)*, Christchurh, 2004.

[7] A. Avolio. Input impedance of distributed arterial structures as used in investigations of underlying concepts in arterial haemodynamics. *MEDICAL AND BIOLOGICAL ENGINEERING AND COMPUTING*, 47(2):143–151, 2009.

[8] A. Avolio, B. E. Westerhof, M. Siebes, and J. V. Tyberg. Arterial hemodynamics and wave analysis in the frequency and time domains: an evaluation of the paradigms. *MEDICAL AND BIOLOGICAL ENGINEERING AND COMPUTING*, 47(2):107–110, 2009.

[9] A. P. Avolio. Multi-branched model of the human arterial system. *Medical and Biological Engineering and Computing*, 18(6):709–718, 1980.

[10] Murad Banaji, Ilias Tachtsidis, David Delpy, and Stephen Baigent. A physiological model of cerebral blood flow control. *Mathematical Biosciences*, 194(2):125–173, 2005.

[11] J. C. Baron. Perfusion thresholds in human cerebral ischemia: Historical perspective and therapeutic implications. *Cerebrovascular Diseases*, 11(SUPPL. 1):2–8, 2001.

[12] E. Belardinelli, G. Gnudi, and M. Ursino. A simulation study of physiological mechanisms controlling cerebral blood in venous hypertension. *IEEE Transactions on Biomedical Engineering*, BME-32(10):806–16, 1985.

[13] Ingram Bloch. Some theoretical considerations concerning the interchange of metabolites between capillaries and tissue. *The Bulletin of Mathematical Biophysics*, 5, 1943.

[14] J. J. Blum. Concentration profiles in and around capillaries. *American Journal of Physiology*, 198(5):991–998, 1960.

[15] D.J. Brown. Input impedance and reflection coefficient in fractal-like models of asymmetrically branching compliant tubes. *IEEE Transactions on Biomedical Engineering*, 43(7):715–722, 1996.

[16] M. Brozici, A. van der Zwan, and B. Hillen. Anatomy and functionality of leptomeningeal anastomoses - a review. *Stroke*, 34(11):2750–2762, 2003.

[17] A. Burton. *Physiol Rev.*, 34:619, 1954.

[18] Jerrold T. Bushberg, J. Anthony Seibert, Edwin M. Jr. Leidholdt, and John M. Boone. *The Essential Physics of Medical Imaging.* Lippincott Williams and Wilkins, Philadelphia, Pa., 2nd edition, 2002.

[19] F. Cassot, V. Vergeur, P. Bossuet, B. Hillen, M. Zagzoule, and J. P. Marc-Vergnes. Effects of anterior communicating artery diameter on cerebral hemodynamics in internal carotid artery disease: A model study. *Circulation*, 92(10):3122–3131, 1995.

[20] F. Cassot, M. Zagzoule, and J. P. Marc-Vergnes. Hemodynamic role of the circle of willis in stenoses of internal carotid arteries. an analytical solution of a linear model. *Journal of Biomechanics*, 33(4):395–405, 2000.

[21] J. Cebral, R. Lohner, P. L. Choyke, and P. J. Yim. Parallel patient-specific computational haemodynamics. In *Applied Parallel Computing*, volume 2367 of *Lecture Notes in Computer Science*, pages 18–34. 2002.

[22] J. Cebral, R. Lohner, P. J. Yim, and J. E. Burgess. Blood flow predictions during neuro-surgery and carotid artery stenting. *International Journal of Bioelectromagnetism*, 3(2):1âĂŞ12, 2001.

[23] J. R. Cebral, M. A. Castro, O. Soto, R. Lohner, and N. Alperin. Blood-flow models of the circle of willis from magnetic resonance data. *Journal of Engineering Mathematics*, 47(3-4):369–386, 2003.

[24] J. R. Cebral, M. Hernandez, and A. F. Frangi. Computational analysis of blood flow dynamics in cerebral aneurysms from cta and 3d rotational angiography image data. *Proc. ICCB'03*, 1:191–198, 2003.

[25] F. T. Charbel, M. Zhao, S. Amin-Hanjani, W. Hoffman, X. Du, and M. E. Clark. A patient-specific computer model to predict outcomes of the balloon occlusion test. *Journal of Neurosurgery*, 101(6):977–988, 2004.

[26] K. Cieslicki and D. Ciesla. Investigations of flow and pressure distributions in physical model of the circle of willis. *Journal of Biomechanics*, 38(11):2302–2310, 2005.

[27] A. Comerford, M.J. Plank, and T. David. Endothelial nitric oxide synthase and calcium production in arterial geometries: an integrated fluid mechanics/cell model. *Journal of biomechanical engineering*, 130(1):011010, 2008.

[28] Neal R. Cutler, C. G. Gottfries, and Klaudius Siegfried. *Alzheimer's disease : clinical and treatment perspectives*. J. Wiley and Sons, New York, 1995.

[29] T David, S. S. Alzaidi, and H Farr. Coupled autoregulation models in the cerebrovasculature. *Journal of Engineering Mathematics*, 2008.

[30] T David, M. Brown, and A. Ferrandez. Auto-regulation and blood flow in the cerebral circulation. *Int. Jour. Num. Methods Fluids*, 43:701–713, 2003.

[31] Frank H. DeLand. *Cerebral Radionuclide Angiography*. W. B. Saunders Company, 1976.

[32] Boudewijn Deurloo. Metabolic regulation of the blood-flow through the brain. Technical report, University of Canterbury, 2008.

[33] S. Dimmeler, I. Fleming, B. Fisslthaler, C. Hermann, R. Busse, and A.M. Zeiher. Activation of nitric oxide synthase in endothelial cells by akt- dependent phosphorylation. *Nature*, 399(6736):601–605, 1999.

[34] A. Dokoumetzidis and P. Macheras. A model for transport and dispersion in the circulatory system based on the vascular fractal tree. *Annals of Biomedical Engineering*, 31(3):284–293, 2003.

[35] A. R. Douglas, N. L. Jones, and J. W. Reed. Calculation of whole-blood co2 content. *Journal of Applied Physiology*, 65(1):473–477, 1988.

[36] Lars Edvinsson and Diana N Krause. *Cerebral blood flow and metabolism*. Lippincott Williams and Wilkins, Philadelphia, 2nd edition, 2002.

[37] H. Farr. Dimensionless auto regulation model for the human cerebrovasculature - summer research project report. Technical report, University of Canterbury, 2008.

[38] A. Ferrandez, T. David, and M. Brown. Numerical models of auto-regulation and blood flow in the cerebral circulation. *Comput Methods Biomech Biomed Engin*, 5(1):7–19, 2002.

[39] William S. Fields, Martin E. Bruetman, and Jorge Weibel. *Collateral circulation of the brain*. Williams and Wilkins Co., Baltimore, 1965.

[40] Sumio Fukuda, Keisuke Mizuno, Hiroki Kakita, Takenori Kato, Mohamed Hamed Hussein, Tetsuya Ito, Ghada A. Daoud, Ineko Kato, Satoshi Suzuki, and Hajime Togari. Late circulatory dysfunction and decreased cerebral blood flow volume in infants with periventricular leukomalacia. *Brain and Development*, In Press, Corrected Proof, 2008.

[41] Masashi Fukui. Current state of study on moyamoya disease in japan. *Surgical Neurology*, 47(2):138–143, 1997.

[42] Y. C. Fung. *Biomechanics : mechanical properties of living tissues*. Springer-Verlag, New York, 2nd edition edition, 1993.

[43] E. Gao, W. L. Young, J. Pile-Spellman, E. Ornstein, and Q. Ma. Mathematical considerations for modeling cerebral blood flow autoregulation to systemic arterial pressure. *American Journal of Physiology - Heart and Circulatory Physiology*, 274 (43):H1023–H1031, 1998.

[44] Jose M. Gonzalez-Fernandez and Bard Ermentrout. On the origin and dynamics of the vasomotion of small arteries. *Mathematical Biosciences*, 119(2):127–167, 1994.

[45] Henry Gray. *Gray's Anatomy of the Human Body*. Bartleby.com, New York, 20th edition, 2000.

[46] Guillermo Gutierrez. A mathematical model of tissueâĂŞblood carbon dioxide exchange during hypoxia. *American Journal of Respiratory and Critical Care Medicine*, 169:525–533, 2004.

[47] Arthur C. Guyton and John E. Hall. *Textbook of medical physiology*. W.B. Saunders Company, tenth edition, 2000.

[48] J. H. Halsey Jr and S. McFarland. Oxygen cycles and metabolic autoregulation. *Stroke*, 5(2):219–225, 1974.

[49] D.R. Harder. Pressure-dependent membrane depolarization in cat middle cerebral artery. *Circulation Research*, 55(2):197–202, 1984.

[50] D.R. Harder. Pressure-induced myogenic activation of cat cerebral arteries is dependent on intact endothelium. *Circulation Research*, 60(1):102–107, 1987.

[51] A. Murray Harper and Sheila Jennett. *Cerebral blood flow and metabolism*, volume 5 of *Physiological Society study guides*. Manchester University Press, Manchester and New York, 1990.

[52] David R. Hay. Cardiovascular disease in new zealand, 2004: A summary of recent statistical information. Technical Report 82, The National Heart Foundation of New Zealand, 2004.

[53] Robert Kwesi Hayford. Collaborative environment for visualisation of the circle of willis (cevcow). Technical report, University of Leeds, 2006.

[54] W. D. Heiss, A. Thiel, M. Grond, and R. Graf. Which targets are relevant for therapy of acute ischemic stroke? *Stroke*, 30(7):1486–1489, 1999.

[55] Donald D. Heistad and Hermes A. Kontos. Cerebral circulation. In J. T. Shepherd, F. M. Abboud, and S. R. Geiger, editors, *Handbook of Physiology, section 2*, volume 3, page 137âĂŞ182. American Physiological Society, Bethesda, 1983.

[56] F. Herzog. Further development on the computer model and graphical user interface to investigate cerebral blood flow in the circle of willis and surrounding. Technical report, University of Canterbury, 2008.

[57] B. Hillen, T. Gaasbeek, and H. W. Hoogstraten. A mathematical model of the flow in the posterior communicating arteries. *Journal of Biomechanics*, 15(6): 441–448, 1982.

[58] B. Hillen, H. W. Hoogstraten, and L. Post. A mathematical model of the flow in the circle of willis. *Journal of Biomechanics*, 19(3):187–194, 1986.

[59] A. G. Hudetz, J. H. Halsey, C. R. Horton, K. A. Conger, and D. D. Reneau. Mathematical simulation of cerebral blood-flow in focal ischemia. *Stroke*, 13(5): 693–700, 1982.

[60] A.G. Hudetz, A.S. Greene, G. Feher, D.E. Knuese, and A.W. Cowley Jr. Imaging system for three-dimensional mapping of cerebrocortical capillary networks in vivo. *Microvascular Research*, 46(3):293–309, 1993.

[61] A.S. Iberall. Anatomy and steady flow characteristics of the arterial system with an introduction to its pulsatile characteristics. *Mathematical Biosciences*, 1(3): 375–395, 1967.

[62] A. Jung, R. Faltermeier, R. Rothoerl, and A. Brawanski. A mathematical model of cerebral circulation and oxygen supply. *Journal of Mathematical Biology*, 51 (5):491–507, 2005.

[63] R. Karch, F. Neumann, and W. Schreiner. Staged growth of optimized arterial model trees. *Annals of Biomedical Engineering*, 28(5):495–511, 2000.

[64] D. Katritsis, L. Kaiktsis, A. Chaniotis, J. Pantos, E. P. Efstathopoulos, and V. Marmarelis. Wall shear stress: Theoretical considerations and methods of measurement. *Progress in Cardiovascular Diseases*, 49(5):307–329, 2007.

[65] James P. Keener and James. Sneyd. *Mathematical physiology*, volume 8 of *Interdisciplinary applied mathematics*. Springer, New York, 1998.

[66] C. S. Kim, C. Kirist, D. Kwak, and T. David. Numerical models of human circulatory system under altered gravity: Brain circulation. In *AIAA Paper*, pages 6794–6806, 2004.

[67] Hannah C. Kinney. The near-term (late preterm) human brain and risk for periventricular leukomalacia: A review. *Seminars in Perinatology*, 30(2):81–88, 2006.

[68] M. Koenigsberger, R. Sauser, J. L. Beny, and J. J. Meister. Role of the endothelium on arterial vasomotion. *Biophysical Journal*, 88(6):3845–54, 2005.

[69] H. A. Kontos, E. P. Wei, R. M. Navari, J. E. Levasseur, W. I. Rosenblum, and J. L. Patterson Jr. Responses of cerebral arteries and arterioles to acute hypotension and hypertension. *The American journal of physiology*, 234(4), 1978.

[70] M. J. Krabbe-Hartkamp, J. Van Der Grond, F. E. De Leeuw, J. C. De Groot, A. Algra, B. Hillen, M. M. B. Breteler, and W. P. T. M. Mali. Circle of willis: Morphologic variation on three-dimensional time-of- flight mr angiograms. *Radiology*, 207(1):103–112, 1998.

[71] A. Krogh. The supply of oxygen to the tissues and the regulation of the capillary circulation. *J. Physiol.*, 52:457–474, 1919.

[72] August Krogh. The number and distribution of capillaries in muscles with calculations of the oxygen pressure head necessary for supplying the tissue. *Jouranl of Physiology*, 52(6):409–415, 1919.

[73] August Krogh. The rate of diffusion of gases through animal tissues, with some remarks on the coefficient of invasion. *Jouranl of Physiology*, 52(6):391–408, 1919.

[74] R. H. Kufahl and M. E. Clark. A circle of willis simulation using distensible vessels and pulsatile flow. *Journal of Biomechanical Engineering*, 107(2):112–122, 1985.

[75] Frederic Lauwers, Francis Cassot, Valerie Lauwers-Cances, Prasanna Puwanarajah, and Henri Duvernoy. Morphometry of the human cerebral cortex microcirculation: General characteristics and space-related profiles. *NeuroImage*, 39(3): 936–948, 2008.

[76] J. R. Levick. *An introduction to cardiovascular physiology*. Butterworths, London; Boston, 1991.

[77] H. H. Lipowsky, S. Kovalcheck, and B. W. Zweifach. The distribution of blood rheological parameters in the microvasculature of cat mesentery. *Circulation Research*, 43(5):738–749, 1978.

[78] C. A. Lodi, A. Ter Minassian, L. Beydon, and M. Ursino. Modeling cerebral autoregulation and co2 reactivity in patients with severe head injury. *Am J Physiol*, 274(5 Pt 2):H1729–41, 1998.

[79] C. A. Lodi and M. Ursino. Hemodynamic effect of cerebral vasospasm in humans: a modeling study. *Ann Biomed Eng*, 27(2):257–73, 1999.

[80] Judith Mackay and George Mensah. Atlas of heart disease and stroke. Technical report, World Health Organization (WHO), September 2004.

[81] E. Magosso and M. Ursino. A mathematical model of co2 effect on cardiovascular regulation. *American Journal of Physiology - Heart and Circulatory Physiology*, 281(5 50-5):H2036–H2052, 2001.

[82] Frederic H. Martini. *Fundamentals of Anatomy and Physiology*. Pearson Education, 2006.

[83] B.J. McGuire and T.W. Secomb. A theoretical model for oxygen transport in skeletal muscle under conditions of high oxygen demand. *Journal of Applied Physiology*, 91(5):2255–2265, 2001.

[84] Iain McIver. Computer model and graphical user interface: investigating blood flowin the circle of willis and surrounding arteries - summer research project report. Technical report, University of Canterbury, 2008.

[85] Stanley Middleman. *Transport phenomena in the cardiovascular system.* Wiley Interscience series on biomedical engineering. Wiley-Interscience, New York, 1972.

[86] Donald S. Miller. *Internal flow systems.* BHRA fluid engineering series. BHRA Fluid Engineering, 1978.

[87] G. D. Mitsis, R. Zhang, B. D. Levine, and V. Z. Marmarelis. Modeling of nonlinear physiological systems with fast and slow dynamics. ii. application to cerebral autoregulation. *Annals of Biomedical Engineering*, 30(4):555–565, 2002.

[88] S.M. Moore, T David, J. G. Chase, J. Arnold, and J. Fink. 3d models of blood flow in the cerebral vasculature. *Journal of Biomechanics*, 39(8):1454–1463, 2006.

[89] Stephen Moore. *Computational 3D modelling of hemodynamics in the circle of Willis.* PhD thesis, University of Canterbury, 2007.

[90] Katherine Tracey Moorhead. *Autoregulation modelling of cerebral haemodynamics.* PhD thesis, University of Canterbury, 2005.

[91] D. W. Newell, R. Aaslid, A. Lam, T. S. Mayberg, and H. R. Winn. Comparison of flow and velocity during dynamic autoregulation testing in humans. *Stroke*, 25 (4):793–797, 1994.

[92] John Nolte. *THE HUMAN BRAIN: An introduction to its functional anatomy.* The C. V. Mosby Company, 1981.

[93] K. S. Olsen, L. B. Svendsen, F. S. Larsen, and O. B. Paulson. Effect of labetalol on cerebral blood flow, oxygen metabolism and autoregulation in healthy humans. *British Journal of Anaesthesia*, 75(1):51–54, 1995.

[94] M. S. Olufsen. Structured tree outflow condition for blood flow in larger systemic arteries. *American Journal of Physiology - Heart and Circulatory Physiology*, 276 (1 45-1), 1999.

[95] M. S. Olufsen, A. Nadim, and L. A. Lipsitz. Dynamics of cerebral blood flow regulation explained using a lumped parameter model. *American Journal of Physiology - Regulatory Integrative and Comparative Physiology*, 282(2 51-2):R611–R622, 2002.

[96] Mette Olufsen, Ali Nadim, and Lewis Lipsitz. Autoregulation of cerebral blood flow. In *Bioengineering, Proceedings of the Northeast Conference*, pages 41–42, 2000.

[97] S. B. Pai, R. G. Varma, and R. N. Kulkarni. Microsurgical anatomy of the middle cerebral artery. *Neurology India*, 53(2):186–190, 2005.

[98] R. B. Panerai. Assessment of cerebral pressure autoregulation in humans - a review of measurement methods. *Physiological Measurement*, 19(5):305–338, 1998.

[99] R. B. Panerai, M. Chacon, R. Pereira, and D. H. Evans. Neural network modelling of dynamic cerebral autoregulation: assessment and comparison with established methods. *Medical Engineering and Physics*, 26(1):43–52, 2004.

[100] R. B. Panerai, S. L. Dawson, and J. F. Potter. Linear and nonlinear analysis of human dynamic cerebral autoregulation. *American Journal of Physiology - Heart and Circulatory Physiology*, 277(46):H1089–H1099, 1999.

[101] R. B. Panerai, A. W. R. Kelsall, J. M. Rennie, and D. H. Evans. Analysis of cerebral blood flow autoregulation in neonates. *IEEE Transactions on Biomedical Engineering*, 43(8):779–788, 1996.

[102] R. Parri and V. Crunelli. An astrocyte bridge from synapse to blood flow. *NATURE NEUROSCIENCE*, 6(1):5–6, 2003.

[103] G. Pawlik, A. Rackl, and R.J. Bing. Quantitative capillary topography and blood flow in the cerebral cortex of cats: An in vivo microscopic study. *Brain Research*, 208(1):35–58, 1981.

[104] C. Peers and P. J. Kemp. Ion channel regulation by chronic hypoxia in models of acute oxygen sensing. *Cell Calcium*, 36(3-4):341–348, 2004.

[105] M.J. Plank, D.J.N. Wall, and T. David. Atherosclerosis and calcium signalling in endothelial cells. *Progress in Biophysics and Molecular Biology*, 91(3):287–313, 2006.

[106] Merle C. Potter and D. C. Wiggert. *Mechanics of fluids*. CA : Brooks Cole /Thompson Learning, Pacific Grove, 2002.

[107] A. R. Pries, T. W. Secomb, T. GeÃ§ner, M. B. Sperandio, J. F. Gross, and P. Gaehtgens. Resistance to blood flow in microvessels in vivo. *Circulation Research*, 75 (5):904–915, 1994.

[108] J. P. Schade. *The Human Brain: Structure and Function*. F. Hoffmann-La Roche and Co. Limited Company, 1980.

[109] W. Schreiner, F. Neumann, M. Neumann, R. Karch, A. End, and S. M. Roedler. Limited bifurcation asymmetry in coronary arterial tree models generated by constrained constructive optimization. *Journal of General Physiology*, 109(2): 129–140, 1997.

[110] Rod R. Seeley, Trent D. Stephens, and Philip Tate. *Anatomy and Physiology*. McGraw-Hill Companies, New York, 6th edition, 2003.

[111] T. F. Sherman. On connecting large vessels to small - the meaning of murray law. *JOURNAL OF GENERAL PHYSIOLOGY*, 78(4):431–453, 1981.

[112] B. N. Steele, M. S. Olufsen, and C. A. Taylor. Fractal network model for simulating abdominal and lower extremity blood flow during resting and exercise conditions. *Computer Methods in Biomechanics and Biomedical Engineering*, 10 (1):39–51, 2007.

[113] Roger B. Stephens and Donald L. Stilwell. *Arteries and veins of the human brain*. Charles C Thomas Publisher, 1969.

[114] S. Strandgaard. Autoregulation of cerebral blood flow in hypertensive patients. the modifying influence of prolonged antihypertensive treatment on the tolerance to acute, drug induced hypotension. *Circulation*, 53(4):720–727, 1976.

[115] S. Strandgaard, J. Olesen, E. SKINHOJ, and N. A. LASSEN. Autoregulation of brain circulation in severe arterial hypertension. *BRITISH MEDICAL JOURNAL*, 1(5852):507–510, 1973.

[116] K. Suyama, K. Yoshida, H. Takahata, K. Toda, H. Baba, Y. Ishikawa, M. Hirose, and I. Nagata. Pediatric moyamoya disease presenting with intracerebral hemorrhage-report of three cases and review of the literature. *Clinical Neurology and Neurosurgery*, 110(3):270–275, 2008.

[117] W. J. Thoman, S. Lampotang, D. Gravenstein, and J. Van Der Aa. A computer model of intracranial dynamics integrated to a full-scale patient simulator. *Computers and Biomedical Research*, 31(1):32–46, 1998.

[118] W. James Thoman, Dietrich Gravenstein, Jan van der Aa, and Samsun Lampotang. Autoregulation in a simulator-based educational model of intracranial physiology. *Journal of Clinical Monitoring and Computing*, 15(7-8):481–491, 1999.

[119] F.P. Tiecks, A.M. Lam, R. Aaslid, and D.W. Newell. Comparison of static and dynamic cerebral autoregulation measurements. *Stroke*, 26(6):1014–1019, 1995.

[120] Gerard J. Tortora and Sandra Reynolds Grabowski. *Principles of anatomy and physiology*. Wiley, Hoboken, N.J., 10th edition, 2003.

[121] Thomas Truelsen, Stephen Begg, and Colin Mathers. The global burden of cerebrovascular disease. Technical report, World Health Organization (WHO), 2003.

[122] M. Ursino. A mathematical study of human intracranial hydrodynamics. part 1 - the cerebrospinal fluid pulse pressure. *Annals of Biomedical Engineering*, 16(4): 379–401, 1988.

[123] M. Ursino. A mathematical study of human intracranial hydrodynamics. part 2 - simulation of clinical tests. *Annals of Biomedical Engineering*, 16(4):403–416, 1988.

[124] M. Ursino. A mathematical model of overall cerebral blood flow regulation in the rat. *IEEE Trans Biomed Eng*, 38(8):795–807, 1991.

[125] M. Ursino, P. Di Giammarco, and E. Belardinelli. A mathematical model of cerebral blood flow chemical regulation–part i: Diffusion processes. *IEEE Trans Biomed Eng*, 36(2):183–91, 1989.

[126] M. Ursino, P. Di Giammarco, and E. Belardinelli. A mathematical model of cerebral blood flow chemical regulation–part ii: Reactivity of cerebral vascular bed. *IEEE Trans Biomed Eng*, 36(2):192–201, 1989.

[127] M. Ursino and M. Giulioni. Quantitative assessment of cerebral autoregulation from transcranial doppler pulsatility: a computer simulation study. *Medical Engineering and Physics*, 25(8):655–666, 2003.

[128] M. Ursino and C. A. Lodi. A simple mathematical model of the interaction between intracranial pressure and cerebral hemodynamics. *J Appl Physiol*, 82(4): 1256–69, 1997.

[129] M. Ursino and E. Magosso. Acute cardiovascular response to isocapnic hypoxia. i. a mathematical model. *American Journal of Physiology - Heart and Circulatory Physiology*, 279(1 48-1):H149–H165, 2000.

[130] M. Ursino and E. Magosso. Acute cardiovascular response to isocapnic hypoxia. ii. model validation. *American Journal of Physiology - Heart and Circulatory Physiology*, 279(1 48-1):H166–H175, 2000.

[131] M. Ursino, A. Ter Minassian, C. A. Lodi, and L. Beydon. Cerebral hemodynamics during arterial and co2 pressure changes: In vivo prediction by a mathematical model. *American Journal of Physiology - Heart and Circulatory Physiology*, 279 (5 48-5):H2439–H2455, 2000.

[132] A. Van Der Zwan and B. Hillen. Araldite f as injection material for quantitative morphology of cerebral vascularization. *Anatomical Record*, 228(2):230–236, 1990.

[133] A. Van der Zwan and B. Hillen. Review of the variability of the territories of the major cerebral arteries. *Stroke*, 22(8):1078–1084, 1991.

[134] A. F. van Raamt, Wptm Mali, P. J. van Laar, and Y. van der Graaf. The fetal variant of the circle of willis and its influence on the cerebral collateral circulation. *Cerebrovascular Diseases*, 22(4):217–224, 2006.

[135] D.A. van Riper, N.L. McDaniel, and C.M. Rembold. Myosin light chain kinase phosphorylation in nitrovasodilator induced swine carotid artery relaxation. *Biochimica et Biophysica Acta - Molecular Cell Research*, 1355(3):323–330, 1997.

[136] E. VanBavel and J. A. E. Spaan. Branching patterns in the porcine coronary arterial tree: Estimation of flow heterogeneity. *Circulation Research*, 71(5):1200–1212, 1992.

[137] A. Viedma, C. Jimenez-Ortiz, and V. Marco. Extended willis circle model to explain clinical observations in periorbital arterial flow. *Journal of Biomechanics*, 30(3):265–272, 1997.

[138] T.F. Wiesner, B.C. Berk, and R.M. Nerem. A mathematical model of the cytosolic-free calcium response in endothelial cells to fluid shear stress. *Proceedings of the National Academy of Sciences of the United States of America*, 94(8): 3726–3731, 1997.

[139] J. Yang, J. W. Clark Jr, R. M. Bryan, and C. Robertson. The myogenic response in isolated rat cerebrovascular arteries: Smooth muscle cell model. *Medical Engineering and Physics*, 25(8):691–709, 2003.

[140] M. Zagzoule and J. P. Marc-Vergnes. A global mathematical model of the cerebral circulation in man. *Journal of Biomechanics*, 19(12):1015–1022, 1986.

[141] M. Zamir. On fractal properties of arterial trees. *Journal of Theoretical Biology*, 197(4):517–526, 1999.

[142] M. Zamir and S. Phipps. Network analysis of an arterial tree. *Journal of Biomechanics*, 21(1):25–34, 1988.

[143] Carl Zimmer. *Soul made flesh : the discovery of the brain - and how it changed the world*. Heinemann, London, 2004.

[144] Klaus Joachim Zulch. *Cerebral circulation and stroke*. Springer, Berlin, 1971.